University of Nottingham

School of Mathematical Sciences

The interfacial dynamics of Amari type neural field models on finite domains

Aytül Gökçe

A thesis submitted to the University of Nottingham for the degree of

Doctor of Philosophy

August 2017

Dedicated to my family...

Abstract

Continuum neural field models mimic the large scale spatio-temporal dynamics of interacting neurons on a cortical surface. For smooth Mexican hat kernels, with short-range excitation and long-range inhibition, they support various localised structures as well as travelling waves similar to those seen in real cortex. These non-local models have been extensively studied, both analytically and numerically, yet there remain open challenges in their study. Here we provide new numerical and analytical treatments for the study of spatio-temporal pattern formation in neural field models. In this context, the description of spreading patterns with a well identified interface is of particular interest, as is their dependence on boundary conditions.

This Thesis is dedicated to the analyses of one- and two-dimensional localised states as well as travelling waves in neural fields. Firstly we analyse the effects of Dirichlet boundary conditions on shaping and creating localised bumps in one- dimensional spatial models, and then on the development of labyrinthine structures in two spatial dimensions. Linear stability analysis is used to understand how spatially extended patterns may develop in the absence and presence of boundary conditions. For the case without boundary conditions we recover the results of Amari, namely the widest bump among two branches of solutions is stable. However, new stable solutions can arise with an imposed Dirichlet boundary condition. For a Heaviside non-linearity, the Amari model allows a description of solutions using an equivalent interface dynamics. We generalise this reduced, yet exact, description by deriving a normal velocity rule that can account for boundary conditions. We extend this approach to further treat neural field models with spike frequency adaptation. These can exhibit breathers and travelling waves. The latter can take

the form of spiral waves, to which we devote particular attention. We further study neural fields on feature spaces in the primary visual cortex (V1), where cells respond preferentially to edges of a particular orientation. Considering a general form of the synaptic kernel which includes an orientation preference at each spatial point, we present the construction and stability of orientation bumps, as well as stripes.

To date there has been surprisingly little analysis of spatio-temporal pattern formation in neural field equations described on curved surfaces. Finally, we study travelling fronts and pulses on non-flat geometries, where we consider the effects of inhomogeneities on the propagation velocity of these waves. In all sections, theoretical results for pattern formation are shown to be in excellent agreement with simulations of the full neural field models.

Acknowledgements

I would first like to express my deep thanks to my supervisors Stephen Coombes and Daniele Avitabile for their constant support and guidance for my academic development throughout my postgraduate experience. Without their supervision and patience, this thesis would not have succeeded. I am really grateful not only for their guidance but also for their friendship and personal advice on many issues all these years.

I was very lucky to have great friends in the maths department: the most special thanks goes to Agne, Andrea, Mayte, Alban, Lisa and Joshua; you all have made the maths department a pleasure to work in. I am grateful to many people inside the maths department for their friendship, but unfortunately I cannot name all of them here. I thank my lovely friends Tayyibe, Seda and Rukiye for always being encouraging and supportive throughout my PhD.

I would also like to thank the Ministry of Turkish Education for giving me financial and social support during my studies in the past 6 years.

The most special thanks goes to my beloved parents, Melek and Zeynal, and my brother Ergin and sister-in-law Nihal, for their encouragement, support, patience and infinite love.

CONTENTS

1

INTRODUCTION

In the 20th century, two ground-breaking findings shed light on the foundations of mathematical neuroscience: (i) large-scale dynamics in real cortical tissue depends on the activity of individual cells, whose anatomical structure comprises axons (sending signals) and dendrites (receiving signals), (ii) these cells are seen as electrical units: their task is to conduct signals by reacting to electrical current. Since Hodgkin & Huxley [1] described the generation and propagation of an action potential in the giant axon of the squid (1952) via a conductance based model (an electrical circuit representation of a cell membrane), the field of computational neuroscience motivated by experimental studies as well as mathematical and numerical methods has been an increasingly popular research area. The development of multi-electrode technology in the late 1950s enabled the characterisation of resting (non-signalling) membrane voltage of cells in living tissue slices [2]. Shortly after that, the advent of such tissue slice techniques opened new research routes for the electro-physiological studies of synaptic transmission, as well as whole cell recording techniques in the 1980*s* [3]. Hence, research on neural networks and large-scale neural dynamics, which were relatively unrecognised by the scientific community until the 1980s, have now been one of the main sources for progress in the field of mathematical neuroscience. In particular, neural field models describing the coarse-grained spatio-temporal dynamics of real cortical tissue are now widely studied in

this field. These models, initially conceived in the late 1970s by Wilson and Cowan [4, 5], Amari [6, 7], and Nunez [8], are non-linear spatially extended systems typically cast as continuum integro-differential equations. Neural field models are motivated by anatomical and physiological findings, and are commonly used to describe large-scale cortical dynamics in neuro-imaging experiments.

The research in this Thesis addresses three important aspects of the dynamics of Amari type neural field models: (i) imposition of Dirichlet boundary conditions, (ii) the use of an interface dynamics approach to construct solution and analyse stability, (iii) modelling and analysis of neural fields on non-flat geometries.

Dirichlet boundary conditions

In many partial differential equation models, boundary conditions are usually needed for describing how activity spreads and how a model interacts with its environment. Neural field models are typically expressed in the form of integro-differential equations, whose associated Cauchy problems do not require the specification of boundary conditions. Hence, the activity of neural dynamics are often developed on finite as well as infinite domains without regard to the role of boundary conditions in shaping or creating patterns.

Since the size of the brain is evolutionarily restricted by the skull, the cortex has a limited surface area. In this sense, the importance of imposing boundary conditions is evidenced by the fact that the neural circuits of the neocortex are adapted to many different tasks, giving rise to functionally distinct areas such as the prefrontal cortex (for problem solving), motor association cortex (for coordination of complex movement), the primary sensory cortices (for vision, hearing, somatic sensation), Wernicke's area (language comprehension), Broca's area (speech production and articulation), and so on. Thus it would seem reasonable to parcellate their functional activity by the use of appropriate boundaries and boundary conditions. Previous work by Daunizeau et al. [9] on dynamic causal modelling for evoked responses using neural field equations has used Dirichlet boundary conditions. Hence, one

major topic here is to study the effect of a Dirichlet boundary condition that clamps neural activity at the boundary to a specific value. Of course other choices are possible, though this one is one way to enforce a functional separation between cortical areas [9].

Dimensionally reduced system of equations

Many solutions of neural field models can be described using the notion of an *interface*. An interface denotes the boundary between high and low states of neural activity, and can be mathematically defined by a level set condition [10]. It is quite easy to track an interface in the one-dimensional Amari model with Heaviside firing rate as the activity reduces to a point or a set of points at threshold crossings. In two-dimensional systems, we expect the interface dynamics to be more complicated, as in the work of Coombes *et al.* [11], where the activity reduces to a closed curve. Here we extend the work in [11] to treat neural field models with boundary conditions for a generic synaptic kernel.

Outline of the Thesis

Chapter 2

To understand the dynamics of neurons at the macro-level, one should first be familiar with their function, what they do, how they function individually and how they interact collectively. Hence, in order to better understand the dynamics of neuron populations, the first Chapter of this Thesis is concerned with the properties and models of single neurons. We first describe some of the well known single neuron models; from the Hodgkin & Huxley model to the analytically more tractable leaky integrate and fire model. We then illustrate the main components and basic properties of neural field models, for which there is a substantial and growing body of knowledge with various refinements including threshold accommodation, axonal

delays, and synaptic plasticity. This Chapter provides the relevant physiological background for interpreting the neural field models that are treated throughout this Thesis.

Chapter 3

Neural field models with short-range excitation and long-range inhibition support spatially localised solutions in the form of spots in two spatial dimensions (known as bumps in one dimension) [12]. In Chapter 3, we extend the standard Amari model to study the dynamics of pattern formation (labyrinthine structures) arising from azimuthal instabilities of a spot, posed on a bounded domain with a Dirichlet boundary condition. Extending ideas from Coombes *et al.* [11], we develop a numerical scheme to evolve the interface dynamics to highlight how a Dirichlet boundary condition can limit the growth of spreading spatio-temporal patterns. Studying such models with a Heaviside firing rate non-linearity often allows a better understanding of the stability of stationary solutions via the construction of certain integrals over synaptic kernels. Amari's seminal work developed an approach for analysing localised solutions of neural field models posed on the real line, and has recently been extended to the flat planar domain by Coombes et al. [11], albeit assuming that the synaptic connectivity can be expressed in terms of a linear combination of zeroth order modified Bessel functions of the second kind. Here, we remove this restriction and show that the interface dynamics can be described for more general synaptic kernel functions. Moreover, motivated by the work of Herrmann *et al.* [13], the last part of the Chapter 3 is devoted to neural field models with piece-wise constant interactions, to allow for analytical progress.

Chapter 4

Adaptation is a negative feedback process that diminishes the firing rate activity of neurons. With the addition of spike frequency adaptation, neural field models can exhibit activity states such as breathers, travelling waves, and rotating spiral waves. In this Chapter, we develop a theory for interface dynamics in neural fields

with adaptation, and show that they are in excellent numerical agreement with direct numerical simulations for localised non-oscillatory labyrinthine structures and oscillatory breathers. Spiral waves are one of the most common rotating travelling waves that occur throughout nature: from galaxies with millions of light-years across in diameter, to seashells that are only a couple of centimetres across [14]. These waves also appear in various biological systems, for example, in cardiac muscle during ventricular fibrillation [15]. In Chapter 4, we concentrate on the properties of neural fields with a recovery variable, that can also subserve the generation of planar rigidly rotating spiral waves in cortical tissue [16]. The behaviour of such travelling waves has previously been analysed for equivalent partial differential equation models (PDE) on bounded domains with a smooth sigmoidal firing rate function [16, 17]. We study spiral waves in neural fields using equivalent PDE models with Dirichlet boundary conditions and very steep sigmoidal firing rate (that mimics the Heaviside firing rate), and perform their numerical continuation under parameter variation.

Chapter 5

Another natural extension of the work presented in Chapter 3 and Chapter 4 is to analyse neural fields on feature spaces. In the first half of this Chapter, we focus on neural fields of primary visual cortex (the first cortical region that processes visual information from the eyes), where cells respond preferentially to lines and edges of a particular orientation [18]. A standard Amari type neural field model (in one spatial and one orientation dimension) is studied with a generalised synaptic weight kernel, for which $w(\boldsymbol{r}, \boldsymbol{r'})$ is modified according to $w(\boldsymbol{r}, \boldsymbol{r'}) = w(\boldsymbol{r}, \boldsymbol{r'}|\theta, \theta')$ to produce orientation preference at each spatial location. The neural field dynamics of primary visual cortex has recently been studied by Bressloff *et al.* [18] with a Heaviside firing rate, and is thus appropriate for a further analysis using an interface approach. Stationary bump solutions that are found to be organised via a snaking bifurcation structure are also discussed in detail. The second half of this

Chapter is concerned with the existence and stability of stripes that are relevant to understanding visual hallucinations.

Chapter 6

There is no substantial difficulty in formulating neural field models on curved surfaces, though to date there has not been much analysis of spatio-temporal pattern formation in this context. In Chapter 6, we discuss the pertinent differences between the planar neural field models discussed in previous Chapters and the well known folded characteristics of real cortex, with its sulci and gyri. We then investigate the model with different levels of complexity and heterogeneity. In the presence of adaptation and a piece-wise constant modulation function (describing a curved cortex), we observe the reflection and compression of waves. Since local cortical and cortico-cortical interactions in the brain are highly dependent on the degree of gyrification, we study travelling fronts in neural fields with various constraints in terms of the degree of excitability (stronger or weaker synaptic connections) varying between gyri and sulci. We also treat the effect of curvature on wave speed.

Chapter 7

We end this Thesis in Chapter 7 by briefly reviewing the previous Chapters and discussing some potential future work on extending neural field equations.

Publications

- A Gökçe, D Avitabile and S Coombes 2017, The dynamics of neural fields on bounded domains: an interface approach for Dirichlet boundary conditions, Journal of Mathematical Neuroscience, under revision.
- A Gökçe, S Coombes and D Avitabile 2017, Neural fields: Localised states with piece-wise constant interactions, NeuroMath, INdAM (Istituto Nazionale di Alta Matematica) Series, Springer, to appear.

Talks

- "*Interface dynamics in bounded neural fields: Dirichlet boundary conditions*", 4th International Conference on Neural Field Theory (ICNFT) - The Interplay of Models and Data Assimilation, Reading, UK, 3- 5 July, 2017.
- "*Reduced dynamics of pattern formation in a mean-field cortical model*", INdAM Meeting, NeuroMath, Mathematical and Computational Neuroscience: cell, network and data analysis, Cortona, Italy, 11- 17 July, 2016.
- "*Interface Dynamics in Neural Fields*", Complex Systems with Interfaces (COSI) workshop, The University of Birmingham, 17 September, 2015.
- "*Spiral Waves: Interface Analysis in a Neural Field*", The Centre for Mathematical Medicine and Biology, The University of Nottingham, 11 November 2014.

Presentations

- "*Reduced dynamics of pattern formation in a mean-field cortical model*", Poster session presented at: European Conference for Mathematical and Theoretical Biology (ECMTB), 11-15 July 2016, Nottingham, UK.

◇ This poster was also presented at (i) Woman in Mathematics Day, London Mathematical Society, 30 March 2017, London, UK 2017, (ii) MASS/MMB Poster Showcase, 7 June 2017, Nottingham, UK (Awarded for best poster prize) .

- "*Spiral Waves: Interface Analysis in a Neural Field*", Poster session presented at: The First International Conference on Mathematical NeuroScience (ICMNS), 8-10 June 2015, Antibes, France.

◇ (This poster was also presented in (i) Neuroscience Nottingham Poster & Lecture Day (2016), (ii) in Post-Graduate Open Day (2016), the University of Nottingham.

- "*An interface approach to planar neural fields: from spots to spirals*", Registration fee waived and poster session presented at: Integrated Systems Neuroscience workshop, 23-24 March 2015, Manchester, UK.

2

MATHEMATICAL MODELS: FROM NEURONS TO NEURON POPULATIONS

Due to the high complexity of the nervous system, mathematical models of brain activity have been developed over a wide range of spatio-temporal scales: from microscopic (single neurons) to meso- and macroscopic (neural networks). Since the dynamics of the brain can never be fully understood without understanding the way neurons exchange information, models for analysing the behaviour and structure of single neurons at the micro level are of great importance. In contrast to highly chaotic and non-linear dynamics of neurons at the micro-scale, the emergence of smoother and more regular dynamics, in which the constituent particles are arranged together, is often observed in large-scale systems [19]. The study of such dynamics allows substantial insights into not only neural functions in various brain regions but also the basis of complex processes such as cognition, spatial navigation and memory.

Since neurons are the essential units for information processing, it is worth beginning this Chapter by familiarising ourselves with their elementary structure and function in §2.1. We then review some of the most common single neuron models in §2.2 and take an introductory step to networks of neurons for analysing collective behaviour of spiking neurons. Since neural field modelling is a very well-known framework that captures spatio-temporal activity on the macroscopic scale, in §2.3,

we expand our review by exploring the properties of these models. Neural field models will be the main focus of this Thesis.

2.1 BIOLOGICAL MOTIVATION: THE CELLS OF THE BRAIN

The central nervous system consists of two major types of cells: glial cells and neurons. Glial cells were discovered in the mid 19th century and are believed to comprise more than half of the cells in the brain [20]. The name glia comes from the Greek word 'glue', implying that these cells hold neurons together and allow chemical and electrical impulses to travel faster [21]. Unlike neurons, these cells do not have an ability to carry electrical impulses. Depending on their function, there are a couple of types of glial cells in the nervous system, yet the scientific community has mostly focused on the largest group called *astrocytes*, particularly after the 1980s, when experiments performed by Diamond showed that Einstein's brain had more astrocytes than neurons [22]. Although the percentage, classification and function of the glial cells relative to those of neurons are still under debate, recent findings suggest that these cells play many important roles ranging from homoeostasis to plasticity in the brain [23]. We refer the reader to [24–27] for further discussion about glial cells, and concentrate only on the mathematical models of neurons and their networks.

A typical human brain comprises at least 10^{10} neurons, each of which has thousands of nerve endings, from which special chemical messengers called *neurotransmitters* are released into a small gap called the *synaptic cleft* allowing communication with neighbouring neurons [28]. At a synapse *pre-synaptic neuron* and *post-synaptic neurons* communicate with one another by releasing and receiving neurotransmitters, respectively.

Since neurons are distinguished from other cells by their remarkable wiring system (specialised for each neuronal type), it is worth familiarising ourselves with the

elementary structure of an individual neuron, that can be roughly divided into three parts: *dendrite* which detects and processes the neurotransmitters emitted by pre-synaptic neurons, *soma* (cell body) which processes the signals received from dendrites, and *axon* which generates output and transmits the information from the neuron to other neurons [29]. Although their morphological and chemical properties may change depending on their task in the nervous system, almost all neurons have these three main structures. In Figure 2.1, neurons with various size and morphology are shown.

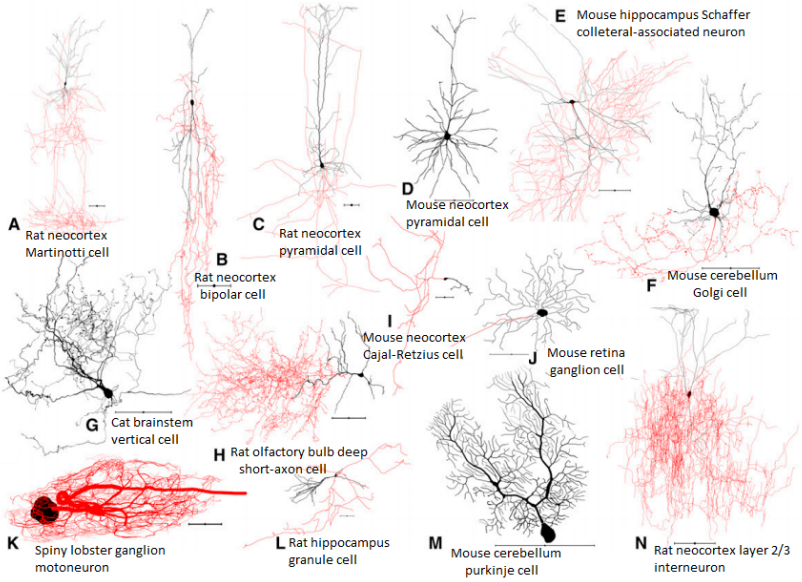

Fig. 2.1: Examples of neurons with different morphologies. Some neurons may have large and widely branched dendritic structures yet a small and unbranched axon, meaning that these neurons send information to a few places in the nervous system but receive information from a wide range of sources. It is also true the other way around: receiving inputs from a few sources and sending them to many places require a large axon and a small dendritic tree, e.g a Purkinje cell. Scale bars represent 100 μm. Soma and dendrites are represented in black and axons are represented in red. Image modified from [30].

2.1.1 *Mechanism of Action Potential and Sub-cellular Processes*

Neurons are specialised for receiving and processing information coming from other cells, as well as conducting and transmitting information to other cells via electrical currents known as *nerve impulses* or *action potentials*, which propagate regeneratively along the axon [31]. This process of signal transmission is extremely complex, involving many types of ions (predominantly Na^+, K^+, Ca^{2+}, Cl^-) with various intra- and extra-cellular concentrations. Almost all action potentials for a given neuron look similar to each other, implying that the timing of these impulses matter (not the shape or form). The duration of an action potential is usually $1-3$ ms. In Fig. 2.2, the first row shows cartoons for resting (**A**) and depolarised (**B**) states of a cell and the second row shows a schematic of a neuron (**C**), where an electrical pulse (**D**) is measured using an electrode placed in the axon (sometimes soma).

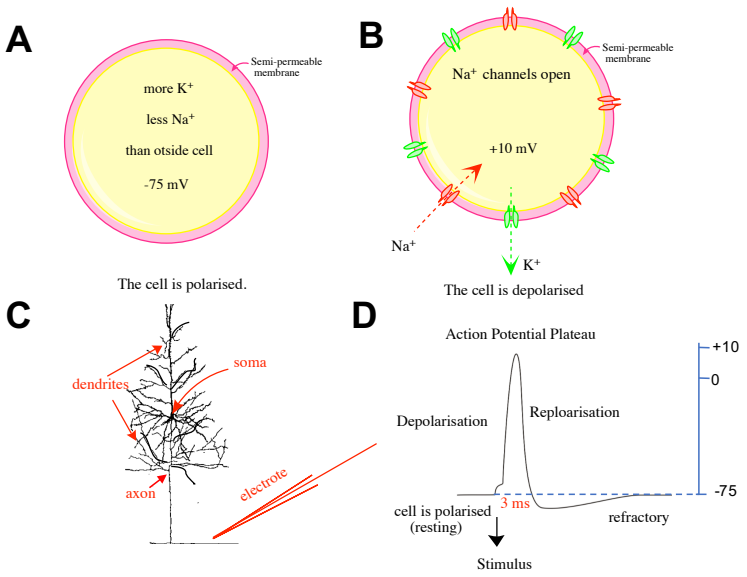

Fig. 2.2: An illustration of a cell in its polarised resting state (**A**) and stimulated depolarised state (**B**). Basic structures of a neuron is shown in (**C**) and an example for a mechanism of an action potential is shown in (**D**).

Broadly speaking, the change in the electrical potential is completed in four main stages, see Fig. 2.2**D**. Without any input, in the *resting state*, the inside of a neuron is more negatively charged relative to outside of the cell leading to a membrane potential typically ~ -75 mV (polarisation) [29], shown in Fig. 2.2**A**. After an external stimulus is applied, the permeability of the cell membrane changes due to the opening of ion channels, allowing an influx of Na^+ into the cell and a flow of K^+ the outside of the cell [29]. This avalanche effect is called *depolarisation*, shown in Fig. 2.2**B**. The cell stays in a depolarised state for a certain time period before it returns back to its resting state, and this is called *repolarisation*, where sodium Na^+ channels are deactivated. Since sodium Na^+ channels which are responsible for depolarisation of the membrane need to recover from the deactivation, a neuron can not be excited immediately after an action potential. Thus, membrane potential resting, depolarisation and repolarisation states are followed by a *refractory* period, where a neuron becomes unresponsive after the undershoot of the potential.

After this complex chain of biochemical processes and the propagation of an action potential along an axon, a chemical synapse can be activated in the synaptic cleft between a pre-synaptic and post-synaptic neuron. Note that, although it is not in the scope of this Thesis, neurons can also be connected electrically via *gap junctions*, providing direct communication between cells through hemi-channels (connexin proteins) [32].

Now we expand our perspective to treat neuron populations, and try to give a glimpse of how large-scale brain dynamics may differ from that of a single neuron.

2.1.2 *From Noisy Neurons to Deterministic Neural Networks and Populations*

Although the latest advances in mathematical neuroscience have led to a great understanding about the interplay between cellular (detailed single neuron dynamics) and complex functions (cognitive and behavioural states), developing a general the-

ory of the brain function is still a long way off. In this context, mathematical and numerical techniques to gain insight into the connection between the microscopic and macroscopic dynamics are key to understand the complexity of the brain. A recent book by Acton [33] includes an interesting discussion about *top-down* and *bottom-up* approaches in brain modelling. Both approaches emphasise the idea of bidirectionally: the *top-down* approach refers to the generation of cellular dynamics from neural networks in the macroscopic level and the *bottom-up* approach refers to the generation of large-scale spatio-temporal dynamics from cell-to-cell interactions [33]. Although noisy and heterogeneous firing patterns are common features of individual neurons, it has not been fully understood how heterogeneity at the cell level translates into heterogeneity at the population level [34]. Neural field models that predict macroscopic brain activity only take mean firing rate proportion into account, ignoring all forms of heterogeneity and higher order statistics. This may seem overly simplistic, yet scientists have revealed that macro-scale activity may be relatively homogeneous and deterministic, and such homogeneity may result from a high of single cells being in the same state [35, 36]. For instance, individual neurons that are physically separated from each other fail to keep synchrony with the circadian clock; however, the intact cortical tissue demonstrates a robust 24 hour rhythm [36, 37]. This rhythm is driven by the central circadian pacemaker in the suprachiasmatic nucleus that resides in the ventral hypothalamus and stays in synchrony with the outside world [38, 39]. See [35, 36, 40, 41] for an overview various deterministic and homogeneous factors in cell-cell variability, which have been linked to population dynamics.

In this Thesis, we will ignore complex cellular mechanisms and concentrate only on the dynamics of network activity using a non-linear and deterministic coarse-grained model of the neural field, whose synaptic kernels are associated with the spatial distribution of neuronal synaptic interactions. See [10, 18, 42] for further discussion.

2.1.3 *Motivation: Columnar Structure of the Cortex*

The structure of the cortex can be viewed as a large number of micro- and macro-columns, each comprising laminar substructures. Due to this laminar organisation, cortical tissue is often regarded as a two-dimensional structure. For example there are about a million cortical columns in humans, each of which is considered as an elementary unit of organisation in the cortex [43]. Perhaps the first steps taken in understanding the columnar organisation in the cortex can be attributed to Mountcastle's work on the cat's somatosensory cortex in the middle of the twentieth century, when vertical electrode recordings showed that vertical clusters of neurons extend through the cortical layers of the brain and form cylinders (columns) of $200 - 500$ μm width [2, 44, 45]. Using electrical recordings, Mouncastle showed that neurons that are inside these columns respond to the same stimulation with similar electrical activity, meaning that these neurons have common receptive field properties. This is illustrated in Fig. 2.3. In the last few decades, the studies motivated by the idea of cortical columns and their functional organisation have been associated with various physiological [46, 47] and anatomical [48] bases. For example, columnar organisation of the cortex has been comprehensively studied in somatosensory and visual systems [49].

Following Mountcastle's pioneering work, in the 1970s, Hubel and Wiesel [50, 51] showed that neurons with identical receptive fields in cat and monkey visual cortex are grouped in the vertical direction (known as hypercolumns) and share the same orientation preference for bars of light. Despite having rather discrete behaviour in primary somatosensory cortex [49] with no apparent shifts in the receptive fields in vertical directions, orientation columns in visual cortex smoothly vary in a direction parallel to the surface of the visual cortex. The columnar structure of the visual cortex and the mechanism of orientation preference will be studied in Chapter 5. Several studies have shown that because of the radial migration of cortical neurons

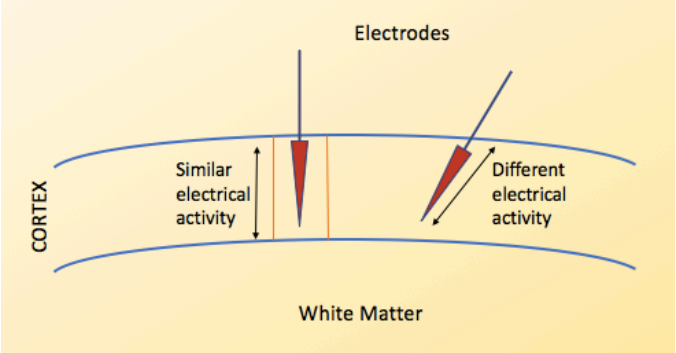

Fig. 2.3: An illustration of Mountcastle's seminal experiment, where moving an electrode perpendicular to the cortical surface he observed neurons with similar responses to a precise stimulation; whereas moving the electrode laterally to the cortical surface he observed neurons responding to the same stimulation with a different electrical activity.

during brain development, there are also smaller columns, so called *micro-columns*, with a diameter $20 - 50$ μm, each comprising up to a hundred neurons [2, 52, 53]. We will ignore these definitional issues and focus on the broad aspects of columnar organisation in the cortex. Our aim throughout this Thesis is not to construct a detailed model of cortical columns, but to study the macro-scale neural activity inside these columns, and networks of these columns. For further information about columnar structure of the cortex we refer the reader to a number of reviews in [2, 43, 44, 54].

2.2 NEURON MODELS: SINGLE NEURONS

As mentioned in §2.1.2, numerous physiological and anatomical hypotheses have been clarified with the help of experimental findings at the single neuron level. Therefore it is worthwhile to revisit some of the more popular single neuron models before we pay attention to models of neuron populations, and neural field models in particular. Single neuron models can be broadly classified into three main types:

binary neurons, integrate and fire neurons, and conductance based systems [41]. Binary neurons can have only two states with two outputs: firing or non-firing. Integrate and fire models are the simplest and most well known examples of the models that captures the essence of excitable behaviour of the membrane, leading to action potential (spike) generation with a discontinuous fire/reset process.

We start this section by giving some essential properties for electro-physiological models of cell membrane (usually treated as a capacitor). Then, in §2.2.2, we overview the Hodgkin & Huxley model [1], that is the most well-known biophysical model of excitable cells. A considerable number of models remain at levels of complexity in between Hodgkin & Huxley and the Binary models (mentioned above), including the Fitzhugh-Nagumo [55] and Integrate and Fire models [56, 57]. The Fitzugh-Nagumo model is a two-dimensional simplification of the Hodgkin & Huxley model, and the one-dimensional integrate and fire model is popular in the computational neuroscience community for its simplicity. Here the dimension of the dynamical system is defined by the number of state variables.

2.2.1 *Electrical Properties of Cell Membranes: an Introduction*

The dynamic properties of the cell membrane are modelled by a capacitor. Figure 2.4 shows a simplified example of a cellular circuit. Here, ionic current can flow through channels that open or close. These channels are modelled by (non-linear) resistance. Using Kirchoff's laws (current balance) the equation describing the evolution of membrane potential is

$$C\frac{\mathrm{d}V}{\mathrm{d}t} + I_R = I. \tag{2.2.1}$$

Here I is an externally injected current and I_R is the ionic current. Note that we only consider the simplest mechanism where only external currents are taken into

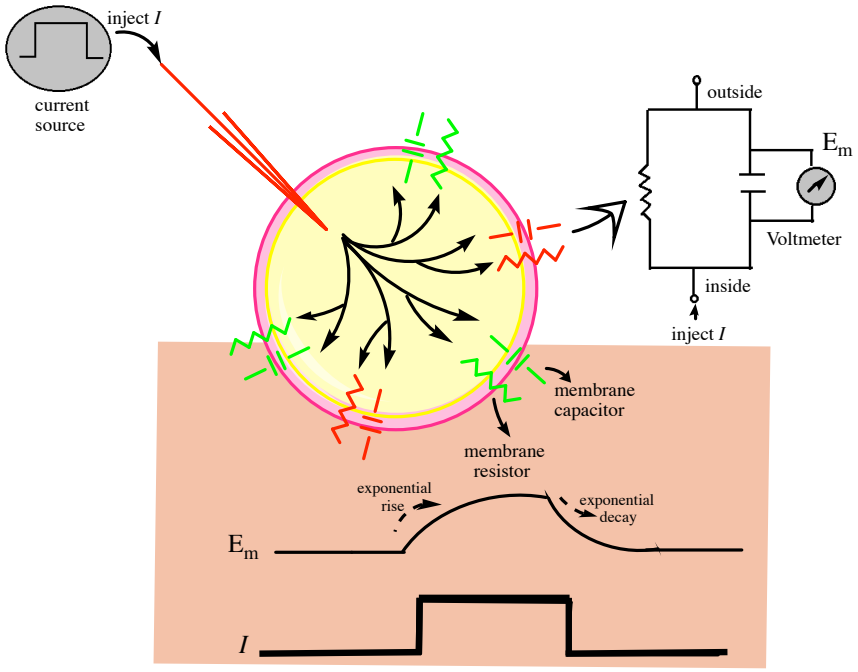

Fig. 2.4: An illustration of a cellular circuit for an isolated cell, where the membrane voltage exponentially increases during the injection of a constant current, and decreases when the current is inactivated. Note that all charge flows into the cell at the onset of current injection, and gives rise to an accumulated response. Figure is redrawn from [58].

account. However, there are many factors that influence the overall membrane current, including the changes in the synaptic currents as well as various ion channels.

2.2.2 *The Hodgkin-Huxley Model*

Since it is extremely complicated to study a model that illustrates all the ionic basis of complex neuron membrane, one should decide the most important factors for understanding the information processing in a model neuron. Knowing that ion channels play a crucial role for electrical signal transmission across the cell membrane, the first and most comprehensive experiments for understanding the role of three main ion channels and their role in generating action potential mechanism were performed by Hodgkin & Huxley on the giant axon of the squid in 1952 [1]. In addition to sodium (Na^+) and potassium (K^+) ionic currents, a third ionic current was considered (mostly due to Cl^-). Hodgkin & Huxley obtained the dynamics of the membrane currents in terms of a system of four non-linear ordinary differential equations [1]. Their model has motivated the construction of many single neuron models, some of which are presented in the following sub-sections.

In the setting of the model developed by Hodgkin & Huxley [1], the total current flowing through membrane is given as

$$C\frac{\mathrm{d}V}{\mathrm{d}t} + \sum_i I_i = I, \tag{2.2.2}$$

where

$$\sum_i I_i = n^4 g_{K^+}(V - V_{K^+}) + m^3 h g_{Na^+}(V - V_{Na^+}) + g_L(V - V_L). \tag{2.2.3}$$

Here the V_i, $i \in \{K^+, Na^+, L\}$ are reversal potentials for potassium, sodium and leak respectively. These can be determined using the formula for the Nernst potential [10]. In addition, g_{K^+}, g_{Na^+} and g_L denote constant conductance values, and I denotes any externally injected current. The equations describing m, n, h satisfy

$$\frac{\mathrm{d}y}{\mathrm{d}t} = \alpha_y(1 - y) - \beta_y y, \qquad y = \{m, n, h\}, \tag{2.2.4}$$

$$\alpha_n = \frac{0.01(V+10)}{e^{(V+10)/10}-1}, \qquad \alpha_m = \frac{0.1(V+25)}{e^{(V+25)/10}-1}, \qquad \alpha_h = 0.07\,e^{V/20}, \tag{2.2.5}$$

$$\beta_n = 0.125\,e^{V/80}, \qquad \beta_m = 4\,e^{V/18}, \qquad \beta_h = \frac{1}{e^{(V+30)/10}+1}, \tag{2.2.6}$$

where the activation of potassium channels (n), activation of sodium channels (m), and inactivation of sodium channels (h) are dimensionless quantities [1]. Figure 2.5 shows the dynamics of the Hodgkin & Huxley model obtained numerically with an injected current varied from $I = 0$ (panels **A** & **B**) to $I = 80$ (panels **D** & **E**), as well as its bifurcation diagram (panel **C**) and the dynamics of dimensionless quantities (panel **D**). For more information on biophysical and mathematical aspects of Hodgkin & Huxley model, we refer reader to comprehensive reviews in [59–61].

In the middle of 1950*s*, Fitzhugh made the important observation that while the voltage V and gating variable m evolve on a similar time scale for an action potential, the gating variables n and h evolve at much slower time scales [62]. This resulted in a two-variable slow-fast phase plane model, showing quantitatively similar behaviours to four-dimensional Hodgkin & Huxley model. We now visit this dimensionally reduced polynomial model for analysing the dynamics of single neurons.

2.2.3 *The Fitzhugh-Nagumo Model*

The Fitzhugh-Nagumo model (FHN) which effectively captures the fundamental properties of action potentials in a single neuron was independently constructed by Fitzhugh (1961) [55] and Nagumo *et al.* (1962) [63]. This model not only allows a simplification of the mathematically more complicated Hodgkin & Huxley equations [64], but also allows for phase plane methods to gain a better understanding of spike generation [65, 66]. A second order differential equation introduced by Fitzhugh [55] is

$$x'' + f(x)x' + g(x) = 0, \tag{2.2.7}$$

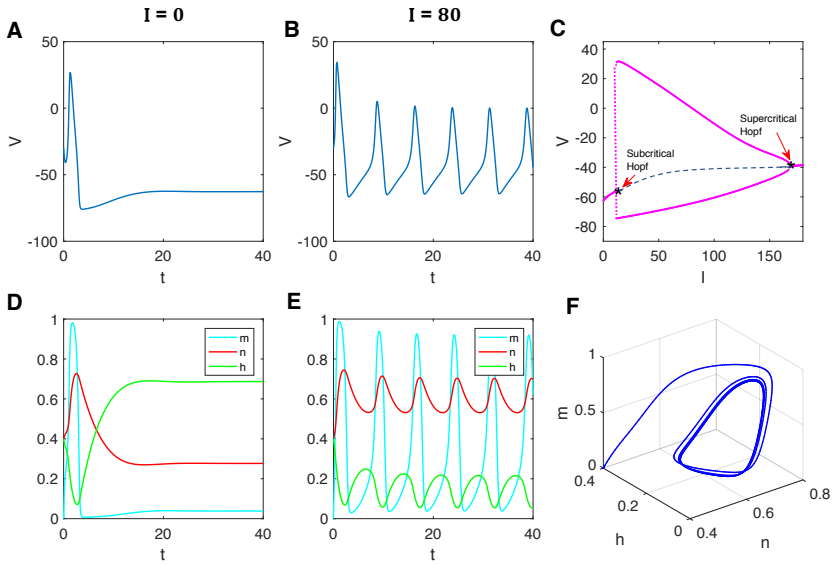

Fig. 2.5: Dynamics of membrane potential and gating variables for the Hodgkin & Huxley model are shown. Membrane potentials (panels **A** & **B**) and the behaviour of the gating variables (panels **D** & **E**) are plotted for $I = 0\ \mu A$ and $I = 80\ \mu A$ respectively. Considering the injected current I as a bifurcation parameter, sub- and super-critical Hopf bifurcations that respectively result in stable or unstable limit cycles are observed, as seen in panel **C**. Lastly, panel **F** shows the dynamics of dimensionless quantities (n, m, h). Parameters are $g_{K^+} = 36$ mmho cm^{-2}, $g_{Na^+} = 120$ mmho cm^{-2}, $g_L = 0.3$ mmho cm^{-2}, $V_{Na^+} = 50$ mV, $V_{K^+} = -77$ mV, $V_L = -54.4$ mV, $C = 1\ \mu$F cm^{-2}.

where x' denotes the derivative of x with respect to time. Here g represents the oscillatory quantity and f is often regarded as a damping coefficient that controls the degree to which oscillations are decayed for harmonic oscillators. Replacing the damping constant with a quadratic function $f(x) = \widetilde{p}(x^2 - 1)$ (even), $\widetilde{p} > 0$ and considering $g(x) = x$ (odd), a simplified model of Van der Pol's equation [67] is obtained, and hence the qualitative properties for a wide class of non-linear relaxation oscillators can be explored [68]. Since $f(x) = \widetilde{p}(x^2 - 1)$ is an even function, Lienard transformation [69] can be applied to equation (2.2.7) to obtain a pair of first order equation given by

$$x_1 = x, \qquad x_2 = \int_0^x f(s)\mathrm{d}s = \widetilde{p}\left(x^3/3 - x\right). \tag{2.2.8}$$

After dropping intermediate steps and rescaling $x_2 = x_2/\widetilde{p}$, (2.2.8) becomes

$$x_1' = \widetilde{p}\left(x_1 + x_2 - x_1^3/3\right), \tag{2.2.9}$$

$$x_2' = -x_1/\widetilde{p}. \tag{2.2.10}$$

Several terms can be added to explore various dynamics in the model [68]:

$$x_1' = \widetilde{p}\left(x_1 + x_2 - x_1^3/3 + x_3\right), \tag{2.2.11}$$

$$x_2' = -\left(x_1 - a + bx_2\right)/\widetilde{p}, \tag{2.2.12}$$

where $0 < a < 1$, $1 - 2b/3 < a < 1$ and $b < \widetilde{p}^2$. In fact, this system of equations can be rewritten with a commonly used FHN notation ($x_1 = V$, $x_2 = W$, $x_3 = I$)

$$\widetilde{p}V' = h(V) - W + I, \tag{2.2.13}$$

$$W' = V - \beta W, \tag{2.2.14}$$

where $h(V) = V(a - V)(V - 1)$ with $\beta, \widetilde{p} > 0$. Note that I is the magnitude of the applied current and the two variables in the model represent membrane voltage (V) and recovery (or refractoriness) (W), respectively. Here if the external input I exceeds some activity threshold, the stable singular point (the brown star in Fig. 2.6**B** & 2.6**E**) in the model destabilises via a Hopf bifurcation, as seen in Fig. 2.6**E**, &

2.6**F**. Thus, for sufficiently large values of current input I, the voltage variable V exhibits oscillatory behaviour with a series of spikes, (shown in Fig. 2.6**D**), and with a further increase in I these oscillations drop to the steady state (not shown). The

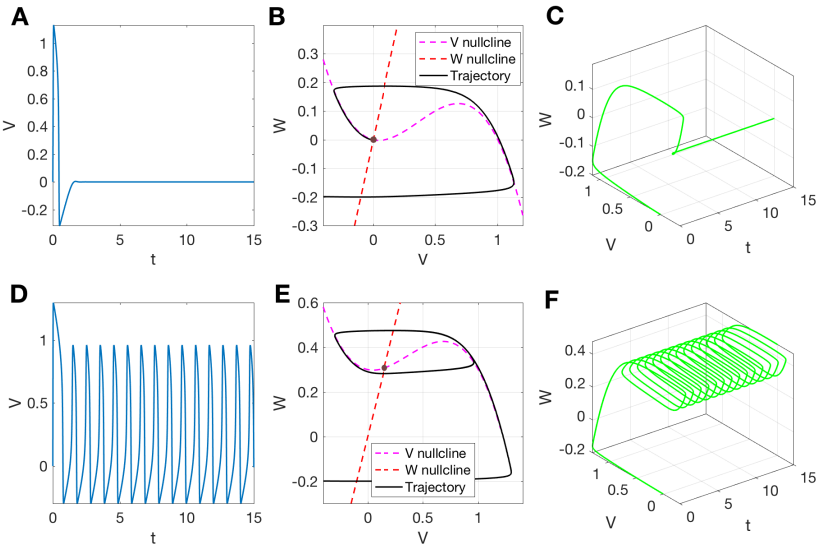

Fig. 2.6: Time evolution and phase plane diagram for the FHN model with two different values of the constant drive I. Membrane voltage V (panels **A** & **D**), phase plane diagram with nullclines (dashed lines) of potential V and recovery W variables (panels **B** & **E**) and their cycling behaviour in time (panels **C** & **F**) are shown for $I = 0$ and $I = 0.3$ respectively. First row $(I = 0)$: in the absence of external input, the fixed point (brown dot) is stable. Second row $(I = 0.3)$: a repetitive spiking activity is seen with a sufficiently large constant external current, where the stable fixed point loses its stability. The fixed point loses stability in favour of a stable limit cycle. Parameters are $a = 0.1$, $\beta = 0.5$ and $\widetilde{p} = 100$.

essential feature of the FHN model is that not only does it allow a detailed phase plane analysis of limit cycles but also captures the main physiological features of a neuron. Comprehensive reviews on the derivation of the Hodgkin & Huxley model and its simplified forms, including various forms of FHN model, can be found in [41, 70].

2.2.4 *Integrate and Fire Model*

The integrate and fire (IF) neuron model is based upon equation (2.2.2) with the inclusion of a threshold condition, where a spike is characterised only through its firing times. In other words, after exceeding some firing threshold via either an external current or an input signal from neighbouring pre-synaptic neurons, a spike is generated and the membrane voltage V is reset to a resting state which is usually taken to be zero for simplicity. Although various linear and non-linear forms of IF models exist in the literature, the best known version is the leaky IF model (LIF) [57]. Initially proposed by Lapicque (1907) [56], the leaky model has a long history with wide application in computational and mathematical neuroscience due to its analytical tractability and ability to capture the qualitative behaviour of a real neuron [57, 71]. The LIF model is based on equation (2.2.1) where

$$CV'(t) = -V(t) + I, \qquad t^m < t < t^{m+1}. \tag{2.2.15}$$

Here, the external input I may be constant as well as time dependent. After reaching a certain threshold, a spike is generated at time t^m and membrane voltage immediately resets to a resting value V_0, $\lim_{t \to t^m} V(t) = V_0$. In Figure 2.7, the time evolution of a LIF model with a constant (**A**) and time dependent (**B**) currents is shown. Considering a time dependent input $I(t)$, one can find an analytical solution for the voltage:

$$V(t) = V_0 e^{-t/C} + \frac{1}{C} \int_0^t e^{-(t-s)/C} I(s)\, ds, \tag{2.2.16}$$

where V_0 denotes the resting value. For simplicity, the spiking time t^m is set to zero.

The IF models have been successfully applied to many problems in neuroscience, including the estimation of neuron response in sensory and motor behaviours, as well as their firing rate behaviour [72, 73]. In this context IF neurons have been suc-

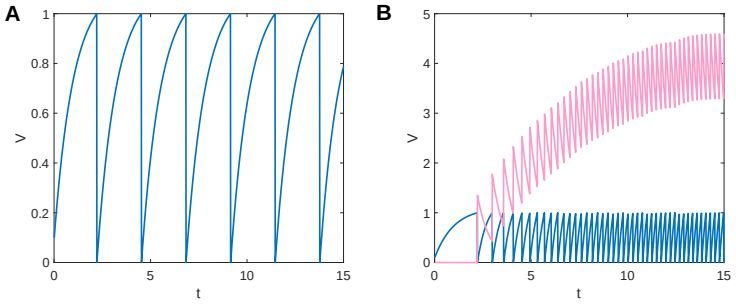

Fig. 2.7: A representation of the voltage (blue) and post-synaptic current (pink) of a single neuron. Panel (**A**): voltage with a constant current $I = 1.01$. Reset value is chosen to be zero for simplicity. Panel (**B**): voltage with a time dependent current in the form $I(t) = I_1 + I_2 e^{-\beta t}$, where β controls the rate of drop of signal. Parameters are $\beta = 1.5$, $I_1 = I_2 = 1.01$.

cessfully expanded to the network level [41], where the dynamics of $i = 1, 2, ..., N$ identical neurons can be described by

$$\tau V_i' = -V_i + I_i(t), \qquad I_i(t) = \sum_{j=1}^{N} W_{ij} \sum_m \eta(t - t_j^m), \tag{2.2.17}$$

where neuron j is a post-synaptic neuron connecting its axons to the dendrites of pre-synaptic neuron i. Here t_j^m denotes mth the firing time for neuron j, W_{ij} denotes synaptic strength from neuron j to neuron i. The sum over m on the right hand side of (2.2.17) represents the total post-synaptic response. This model has been widely studied in the literature to include important aspects of pattern formation, including travelling waves, spirals, and spots [74, 75]. Since the model given by (2.2.17) can be challenging for analysing large values of N, one can study average voltage activity in a neuron population using a continuous approximation with a mean firing rate, namely using neural field models.

We now introduce a short time averaging over an arbitrary function v :

$$\langle v \rangle = \frac{1}{T} \int_{t-T}^{t} v(s) \mathrm{d}s, \tag{2.2.18}$$

and a property of delta function in the form of

$$\int_{-\infty}^{\infty} \eta(s)\delta(x-s)\mathrm{d}x = \eta(x). \tag{2.2.19}$$

Here one can write the sum over m on the right hand side of (2.2.17) as

$$\frac{1}{T}\int_{t-T}^{t} \mathrm{d}t' \sum_m \eta(t'-t_j^m) = \frac{1}{T}\int_{t-T}^{t} \mathrm{d}t' \sum_m \int_{-\infty}^{\infty} \mathrm{d}s\eta(s)\delta(t'-t_j^m-s). \tag{2.2.20}$$

Introducing a function

$$f_i(t) = \frac{1}{T}\int_{t-T}^{t} \sum_m \delta(t'-t_i^m)\mathrm{d}t', \tag{2.2.21}$$

the average of total input over a short time scale is given by

$$\langle I_i(t)\rangle = \sum_{j=1}^{N} W_{ij} \int_0^{\infty} \mathrm{d}s\eta(s)f_j(t-s). \tag{2.2.22}$$

Here, f_j represents the firing rate of neuron j. We can express the short time average of synaptic voltage in equation (2.2.17) by an activity term $u_i = \langle V_i\rangle$, so that the firing rate of neuron j can be written by its average activity $f_j(t-s) = f(u_j(t-s))$ [76]. Replacing the connectivity W_{ij} by a continuous kernel $w(x,x')$ due to characteristic spatial structure of the cortex [18], and considering $\eta \to 0$ for a slow synaptic process [76], equation (2.2.17) can be rewritten in the form of

$$u(x,t) = \int_0^{\infty} \mathrm{d}s\eta(s) \int_{\mathbb{R}} dx' w(x,x')f(u(x',t-s)), \tag{2.2.23}$$

where $\eta(t)$ is commonly chosen as $\alpha-$function $\eta(t) = \alpha \mathrm{e}^{-\alpha t}H(t)$ and can be expressed using Green's function of a linear operator, for which we find $\left(1+\frac{1}{\alpha}\frac{\mathrm{d}}{\mathrm{d}t}\right)\eta = \delta$ [10, 18]. This leads to a generic form of a continuum neural field equation in the form

$$\frac{1}{\alpha}u_t(x,t) = -u(x,t) + \int_{-\infty}^{\infty} \mathrm{d}x' w(x,x')f(u(x',t)). \tag{2.2.24}$$

2.3 NEURAL FIELD MODELS

Although single neuron models are able to predict dynamical activity of real neurons with a wide variety of spiking behaviour, such models are difficult to analyse because of their complexity and thus they are not well suited to describe the behaviour of a tissue on the mesoscopic or macroscopic cortical scale [41, 77]. Neural field modelling is a well known framework that captures spatio-temporal activity on the macroscopic scale, so that the patterns over large parts of the brain, e.g. cortex, can be explored. The history of neural fields can be traced back to the work of Beurle in the 1950s, who pioneered the analysis of masses of cells in the brain considering only excitatory neurons [78]. The first attempt at analysing more realistic neural populations was made by Griffith who studied spatio-temporal neural activity with a partial differential equation approach [79, 80]. The seminal papers written later on, by Amari [7] and Wilson & Cowan [4, 5], provide the basis for modern day neural field models, where inhibitory and excitatory populations are both represented.

2.3.1 *The Model: Non-local Integro-differential Equations*

Initially described by Brodmann in 1909, a real cortex has a six layered structure [81]. These layers are the molecular layer (layer I), external granular layer (layer II), external pyramidal layer (layer III), internal granular layer (layer IV), internal pyramidal layer (layer V), and polymorphic or multiform layer (layer VI), from outside to inside [82]. In 1973, using a one-dimensional two-layer (excitatory and inhibitory layers) population model, Wilson and Cowan [4, 5] studied synaptic activity of excitatory and inhibitory coupled populations. Later in 1977, assuming that inhibition is linear and faster than excitation in Wilson and Cowan's model, Amari [7] simplified their work by constructing a one-dimensional single layer mean field model

with lateral inhibition (as an approximation of the two-layer model). However, depending on the functional organisation of neurons in each layer of a cortical tissue, one may write Amari's reduced neural field model for each layer. For example, see Pinto and Ermentrout's work on a one-dimensional two-layer Amari type model for single bump solutions (spatially localised patterns associated with working memory) [83].

Here, focusing on one spatial dimension, we present a one-layer Amari type neural field that is typically expressed in the form of an integro-differential equation:

$$\frac{\partial u(x,t)}{\partial t} = -u(x,t) + \psi(x,t), \quad \psi(x,t) = \int_{-\infty}^{\infty} w(|x-x'|)H(u(x,t)-\kappa)\mathrm{d}x', \quad (2.3.1)$$

where u is average membrane voltage, or synaptic activity, at a position x and time t. Here w is a distance dependent connectivity function, that is often called as the synaptic kernel.

Synaptic kernel: The kernel w in (2.3.1) represents the spatial distribution of synaptic interactions, where positive and negative connection strengths can be considered as excitatory and inhibitory synaptic strengths, respectively. Typical functional forms for the kernel are often chosen using exponential functions; considered in such a way that $w(x) \to 0$ as the distance $x \to \infty$. The most popular used forms are known as Wizard hat and Mexican hat functions; for example one can study

$$w(x) = (1 - a|x|)\mathrm{e}^{-|x|}, \quad (2.3.2)$$

for a Wizard hat kernel ($a > 0$) as shown in Fig. 2.8**B**, where neurons communicate with short-range excitatory and long-range inhibitory interactions (also known as lateral inhibition), or for a purely excitatory kernel ($a = 0$) as shown in Fig. 2.8**A**.

Interestingly, labeling studies [84] have shown that spatially periodic stripes are formed by an extensive network of connections in the primate prefrontal cortex[1] [85, 86]. Hence, a periodically modulated synaptic connectivity with a decaying oscillatory behaviour allows a better representation of the interactions which are

1 A specialised cortical area encoding the information for working memory.

believed to exist in prefrontal cortex. For example Laing *et al.* [87] studied the Amari model with the effects of the coupling function:

$$w(x) = \mathrm{e}^{-b|x|}\left(b\sin(|x|) + cos(x)\right), \tag{2.3.3}$$

to study short term working memory, see Fig. 2.8**D**. In fact, principal pyramidal cells in a cortical tissue are often surrounded by local inhibitory interactions with a lateral excitation [88, 89], implying that inverted Mexican hat kernel with short-range inhibition and long-range excitation (Fig. 2.8**C**) is another natural choice for representing synaptic interactions.

Firing rate function : The firing rate evoked by the membrane voltage was taken to be Heaviside function by Amari. That is

$$f(u) = H(u-\kappa) = \begin{cases} 1, & \text{if} \quad u \geq \kappa \\ \\ 0, & \text{if} \quad u < \kappa \end{cases}, \tag{2.3.4}$$

where κ is firing threshold. Studying Amari type models with a Heaviside firing rate non-linearity often allows substantial insight into solution properties (existence and stability) via the construction of integrals over kernels. In his original work, Amari found two bump solutions, the wider of which is always stable. Later in 1979, Kishimoto and Amari [90] showed the existence of a bump solution for a smooth and monotonically increasing non-linear firing rate function which satisfies the conditions $\lim_{x\to-\infty} f(u(x,t)) = 0$ and $\lim_{x\to\infty} f(u(x,t)) = 1$. An example of such a firing rate is the sigmoid:

$$f(u) = \frac{1}{1+\mathrm{e}^{-\mu(u-\kappa)}}, \tag{2.3.5}$$

where μ is the gain parameter and κ is the threshold parameter. Heaviside and smooth sigmoidal firing rate functions are plotted in Fig. 2.8**E** and Fig. 2.8**F** respectively.

Since their initial inception in the 1970s by Wilson and Cowan [4, 5], Amari [6, 7], and Nunez [8], neural field models have been extensively studied in one-dimensional

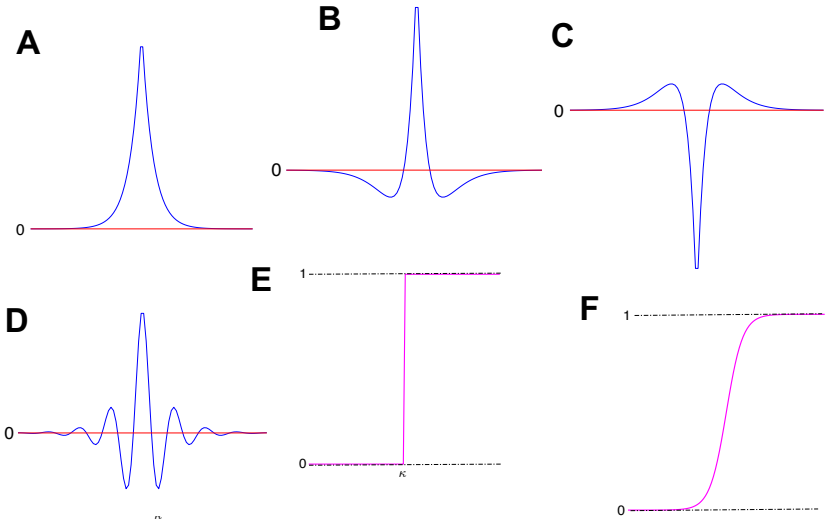

Fig. 2.8: Various synaptic kernels and firing rate functions that have been studied in the literature to mimic interactions in the brain. **A**: excitatory kernel, **B**: Wizard hat kernel, **C**: inverted Wizard hat kernel, **D**: oscillatory kernel, **E**: Heaviside firing rate and **F**: smooth sigmoidal firing rate.

as well as in two-dimensional (planar) settings. This has included both the mathematical and numerical analysis of spatio-temporal patterns, and much has been learnt about localised states, global periodic patterns, and travelling waves. To list just a few of the common application areas, neural field modelling has shed light on large-scale brain rhythms [42], geometric visual hallucinations [91, 92], mechanisms for short term memory [93–95], motion perception [96–98], binocular rivalry [99, 100], and anaesthesia [101]. There are also a number of reviews summarising work to date, such as [102–106]. For the most recent perspective on the use of neural field modelling we refer reader to a comprehensive book by Coombes *et al*. [10]. As mentioned in section 2.2.4, large networks of IF neurons support the dynamics of pattern formation of bumps as well as travelling waves. Here we will study similar types of structures in a continuum neural field framework.

In addition to partial integro-differential equations (PIDE) for neural field models given by (2.3.1) for certain synaptic kernels w, one can describe an equivalent system of partial differential equations (PDEs) for a more straight forward numerical

implementation. Now we quickly overview the link between neural PDE models and neural PIDE models.

2.3.2 *Neural Fields with Partial Differential Equations*

Due to the convolution structure on the right hand side of (2.3.1), several techniques have been developed to transform the system of PIDE into an equivalent form of PDE [95]. One of these techniques is to apply the Fourier transform to the convolution structure, manipulate and then to take an inverse Fourier transform. This method can be especially useful for exploiting many standard tools from dynamical systems [103], as well as for facilitating the numerical analysis of the neural field model [76]. Following the ideas presented by Laing [95], one can write equation (2.3.1) in the form

$$F\left[u_t + u\right] = F\left[w\right](s) F\left[f(u)\right](s), \tag{2.3.6}$$

where s is a transform variable (spectral parameter) and $F\left[\cdot\right]$ denotes the Fourier transform. This transformation is achieved assuming that u and w are square integrable functions. Here a specific connectivity function whose Fourier transform can be written in the form of a rational function of s^2 is given by $F\left[w\right](s) = G(s^2)/Q(s^2)$, where G and Q are any polynomial functions. For example, considering the connectivity function $w(x) = \mathrm{e}^{-|x|/2}$ and its Fourier transform $F\left[w\right](s) = (1+s^2)^{-1}$, (2.3.6) takes the form

$$(1+s^2) F\left[u_t + u\right](s) = F\left[f(u)\right](s). \tag{2.3.7}$$

Here taking the inverse Fourier transform we obtain the PDE form as

$$(1 - \partial_{xx})(u_t + u) = f(u). \tag{2.3.8}$$

See [17, 76, 95, 103] and Chapter 4 for further details on PDE methods for one- and two- dimensional neural field models.

Although we mostly focus on the solutions of neural field models with spatially homogeneous dynamics throughout this Thesis, neural field models can be analysed with various heterogeneities and complex feedback mechanisms. Now we will overview some forms of the heterogeneities which can be described in a neural field framework.

2.3.3 *Neural Field Models with Adaptation and Heterogeneities*

Neuronal activity is determined not only by the interactions between neurons but also by metabolic processes and negative feedback mechanisms. This includes spike frequency adaptation, axonal delay, threshold accommodation and synaptic plasticity. We now briefly describe models of these processes, some of which will be studied further in later Chapters.

Adaptation: Spike frequency adaptation, which brings neural tissue back to its resting state after high activity periods, is a common choice to modulate population response [107]. This modulation is particularly important for disinhibited cortices (where inhibition is blocked) for dampening the effects of high excitation. Investigating a large group of cellular mechanisms, Benda and Herz developed an universal model to investigate the role of spike frequency adaptation on the mechanism of signal processing at the single-neuron level [108]. The first analysis of a population model with adaptation was performed by Pinto and Ermentrout, who added a slow recovery variable to the Wilson-Cowan equations to describe the dynamics in disinhibited cortex [83]. This can give rise to travelling pulses in one dimension, and spiral waves in two dimension. Many theoretical studies of pattern

formation have been motivated by Pinto and Ermentrout's model, which can be written as

$$\tau \frac{\partial u(x,t)}{\partial t} = -u(x,t) + \psi(x,t) - ga(x,t), \tag{2.3.9}$$

$$\frac{\partial a(x,t)}{\partial t} = u(x,t) - a(x,t), \tag{2.3.10}$$

where the variable a denotes the linear spike frequency adaptation, ψ is the synaptic input given in (2.3.1), g is coupling parameter, and τ represents a synaptic or membrane time constant. The recovery variable (2.3.10) is comprehensively discussed in Chapter 4.

Neural fields in feature spaces: Neural field models can be described in feature spaces, whose geometry is tuned to edge orientation or motion direction [109]. In the primary visual cortex (V1), cells respond preferentially to lines and edges of a particular orientation. The model (2.3.1) can be reformulated with an additional orientation component to obtain a coupled ring model of feature space given by

$$\frac{\partial u(x,\theta,t)}{\partial t} = -u(x,\theta,t) + \int_{\mathbb{R}} \int_{S} w(x,\theta|x',\theta') F(u(x',\theta',t) - \kappa) \mathrm{d}\theta' \mathrm{d}x', \tag{2.3.11}$$

where a standard neural field model that connects points at x and x' with a weight $w(x|x') = w(|x - x'|)$, is replaced by a more general form $w(x|x') \to w(x,\theta|x',\theta')$, where θ represents an orientation preference at x. This model has recently been studied for the choice of a Heaviside firing rate [92], and is discussed further in Chapter 5.

Threshold accommodation: Although standard neural field models are often studied using a constant threshold that depends neither on the state of the tissue nor on its history, Hill [110] has argued that this threshold changes gradually depending on the local synaptic activity. Coombes and Owen called this state dependant dynamic threshold *threshold accommodation* [111], and studied neural fields (2.3.1) using a time and activity dependent threshold in the form

$$\frac{\partial \kappa(x,t)}{\partial t} = -\kappa(x,t) + \kappa_0 + g_0 \widehat{g}(u(x,t) - \widetilde{\kappa}), \tag{2.3.12}$$

where $\widehat{g}(u)$ is a non-linear function which controls the accommodation process, g_0 is a constant scale, and $\widetilde{\kappa}$ denotes a constant threshold value. We will mostly focus on constant firing thresholds, yet briefly discuss a piece-wise constant synaptic threshold that alters in between brain folds in Chapter 6.

Axonal delays: Although many of the scientific papers written on dynamical neural networks have assumed that there is an instant communication between different regions of the brain, the importance of the effects of time delays due to the finite propagation speed of axons has also been demonstrated in the neural field framework [17, 112]. Here, the firing rate f may include time delays due to finite propagation speed [111], by which the synaptic input on the right hand side of (2.3.1) becomes

$$\psi(x,t) = \int_{\Omega} \mathrm{d}y w(|x-y|) f(u(y, t-|x-y|/v)), \tag{2.3.13}$$

where v denotes the propagation speed of the membrane voltage. For further discussion on neural field models with axonal delays we refer reader to [76, 111, 113]. We will only discuss neural field equations without axonal delays throughout this thesis.

Synaptic depression and potentiation: Synaptic connections in the brain are not fixed. Indeed, all types of synapses are regulated by a variety of short lived and long lasting processes, some of these lead to a decrease in synaptic strength (depression), while others lead to synaptic potentiation [114]. However, in most cases, multiple processes are present. This results in a combination of recovery and depression in which synaptic strength is highly dependent on details of the cellular environment and of stimulation. This phenomenon is referred to as *synaptic plas-*

ticity. Following the basic mechanism of the neural field model, Kilpatrick and Bressloff [113, 115] reformulated (2.3.10) such that

$$\begin{aligned}
\tau\frac{\partial u(x,t)}{\partial t} &= -u(x,t) + \int_{\Omega} w(|x-x'|)q(x',t)f(u(x',t)-\kappa)\mathrm{d}y - ga(x,t),\\
\frac{\partial q(x,t)}{\partial t} &= -\beta q(x,t)f(u(x,t)-a(x,t)) - \frac{1-q(x,t)}{\alpha},\\
\epsilon\frac{\partial a(x,t)}{\partial t} &= -a(x,t) + \gamma f(u(x,t)-a(x,t)).
\end{aligned} \tag{2.3.14}$$

Here equation (2.3.14) describes synaptic activity u with a synaptic depression and adaptation [115]. The variable a denotes adaptation and variable q denotes synaptic scaling factor, by which present synaptic resources can be depleted by $\beta f(u)$ and can be also recovered by constant rate α, see [113, 115] for details.

2.4 CONCLUSION & DISCUSSION

In this Chapter we have given an overview of how to model dynamics of neurons at the cellular level, as well as at the population level. Although we have taken several well known neuron models into account, this is not the whole picture. For example, there are continuum models such as Morris & Lecar model [116] and Hindmarsh & Rose model [117], as well as discrete models such as Galves & Löcherbach model [118] for single neurons, that have been successfully applied for studying the dynamical properties of neurons. We have given an overview of some of the popular single neuron models and discussed their transformation to neural field models. Here, rather than considering individual neuronal properties, the average activity is studied along with natural assumptions and simplifications such as firing rate functions and synaptic kernels shown in Fig. 2.8. For example, neural field equations are usually chosen to be translation-invariant, namely the synaptic kernel depends on the Euclidean distance between two points. Neural field models are well-developed frameworks whose qualitative and quantitative properties successfully describe large-scale brain dynamics such as motion perception, binocular

rivalry, hallucinations, and anaesthesia to mention a few of the applications. See reviews [10, 88, 102] summarising work to date. Throughout this Thesis, we will work with spatio-temporal pattern formation in neural field models, and analyse the existence and stability for localised patterns (bumps), and for travelling waves. Bumps (or spots), in one- (and two-) dimensional neural fields, are usually linked to orientation dependent activity in primary visual cortex [119], short term memory in prefrontal cortex [18, 87, 120], and motion perception [96]. On the other hand, travelling waves are associated with spreading neural activity in the cortex [16, 121].

Neural field models have been extensively studied in idealised one- dimensional or planar settings. The value attained by the activity variable at the boundary is determined by the initial condition and by the non-local synaptic input. Considering neural field models on bounded as well as unbounded domains without boundary conditions has included both the mathematical and numerical analysis of spatio-temporal patterns, and much has been learnt about localised states, global periodic patterns, and travelling waves mentioned above. Moreover, ignoring the synaptic activity on the boundary has been seen as a reasonable argument in the literature to date. However, the imposition of different boundary conditions may affect the spatio-temporal evolution of a pattern.

Knowing that very little work has been done on the enforcement of boundary conditions in neural fields, or on their effect in inducing patterned states, we will revisit the seminal work of Amari (2.3.1) on neural field models and show how to incorporate Dirichlet boundary conditions in the next Chapter.

3

THE DYNAMICS OF NEURAL FIELDS ON BOUNDED DOMAINS: AN INTERFACE APPROACH FOR DIRICHLET BOUNDARY CONDITIONS

Following the original approach of Amari [7], a substantial amount of work on various neurobiological phenomena (see §2.3), both analytically and numerically, has been developed in one-dimensional neural field models with a great success for analysing coarse-grained dynamics of interconnected cortical neurons. However, due to its large surface area ($\sim 1600 - 4000\,\mathrm{cm}^2$ in total) with a small thickness ($\sim$ 3mm), the cortex is often regarded as a two-dimensional laminar structure [122, 123]. Hence, Amari's seminal work for analysing localised solutions in one spatial dimensions has recently been extended to two spatial dimension by Coombes *et al.* [11], see also [12, 124, 125]. As mentioned in Chapter 2, the Amari type neural field models are not only able to describe localised solutions, often called bumps in one dimensions and spots in two dimensions, but also dynamic states such as travelling pulses and their transients as well as spreading labyrinthine patterns.

Neural field models have been considered for describing the behaviour of tissue in bounded as well as unbounded domains; however, studying the role of boundary conditions in shaping and creating patterns in bounded domains has drawn very little attention. The exception to this is the work of Laing and Troy [17], but even here the use of an equivalent PDE formulation means that boundary conditions

are not chosen to impose any biophysical constraint. Instead, they are chosen to ensure the smooth decay of localised solutions [17].

Moreover, the Amari approach with a Heaviside firing rate, in either one or two spatial dimension, effectively tracks the boundary between a high and low state of neural activity, giving rise to so called *interface dynamics*, see Chapter 1. Requiring no information away from the interface, this approach gives a reduced description of solutions to a neural field model without any approximation. An interface description for two-dimensional case was originally developed by Coombes *et al.* [11], where using a special choice of synaptic connectivity kernel, it was possible to formulate interface dynamics in terms of the shape of an active region, giving rise to a reduced, yet exact, model.

This Chapter delivers a new interface modelling approach for analysing the solutions of Amari type neural field models with Dirichlet boundary conditions.

3.1 THE MODEL

The scalar neural field model that we consider is given by

$$\frac{\partial u(\boldsymbol{x},t)}{\partial t} = -u(\boldsymbol{x},t) + \int_{\Omega} \mathrm{d}\boldsymbol{y} w(|\boldsymbol{x}-\boldsymbol{y}|) H[u(\boldsymbol{y},t)-\kappa], \tag{3.1.1}$$

with Dirichlet boundary conditions

$$u(\boldsymbol{x},t)|_{\boldsymbol{x}\in\partial\Omega} = u_{\mathrm{BC}}, \tag{3.1.2}$$

where u_{BC} represents the activity prescribed on the domain boundary. Here Ω is a planar domain and $\partial\Omega$ is the boundary of the domain $\Omega \subseteq \mathbb{R}^2$, with $\boldsymbol{x} \in \Omega$ and $t \in \mathbb{R}^+$. The variable u denotes synaptic activity and the function w denotes anatomical connectivity, for simplicity we only study the case where this depends on the Euclidean distance $\| \boldsymbol{x}-\boldsymbol{y} \|$. The function H is the firing rate of the cortical tissue and will be considered to be a Heaviside function so that the parameter κ

is interpreted as a firing threshold. It was the essential insight of Amari that the choice of a Heaviside function allows the explicit construction of localised states (stationary bumps and travelling pulses) on bounded as well as unbounded domains without regarding the role of boundary conditions. Our key observation that allows the extension of the Amari approach to handle the boundary condition (3.1.2) is to impose this constraint by writing the state variable of the system in terms of a line integral given by

$$u(\boldsymbol{x},t) = u_{\mathrm{BC}} + \int_{\Gamma(\boldsymbol{x})} \boldsymbol{z}(\boldsymbol{y},t)\cdot \mathrm{d}\boldsymbol{y}, \tag{3.1.3}$$

where $\boldsymbol{z} = \nabla_{\boldsymbol{x}} u \in \mathbb{R}^2$ is the gradient of u.

Here $\Gamma(\boldsymbol{x})$ denotes an arbitrary path that connects a point on the domain boundary $\partial\Omega$ to the point $\boldsymbol{x}$ within its interior. An evolution equation for $\boldsymbol{z}$ is easily constructed taking the gradient of (3.1.1) to give

$$\frac{\partial \boldsymbol{z}(\boldsymbol{x},t)}{\partial t} = -\boldsymbol{z}(\boldsymbol{x},t) + \int_{\Omega} \mathrm{d}\boldsymbol{y}\, \nabla_{\boldsymbol{x}} w(|\boldsymbol{x}-\boldsymbol{y}|) H[u(\boldsymbol{y},t)-\kappa]. \tag{3.1.4}$$

Namely the reformulation of the original scalar model in terms of the evolution of its gradient reconstruction using (3.1.3) allows for an interface description that respects Dirichlet boundary conditions. Here, we shall consider equations (3.1.3) and (3.1.4) as the neural field model with Dirichlet boundary conditions. In the following sections we develop the extension of Amari's interface dynamics to encapsulate Dirichlet boundary conditions.

To illustrate the approach, we first treat the example of localised states in a one-dimensional model in §3.2. This provides a useful primer before we develop a theory for interface dynamics that encapsulates neural activity at the boundary in a two-dimensional model, presented in §3.3. As mentioned earlier, Amari's seminal work has recently been extended to the two-dimensional case by Coombes *et al.* [11], albeit assuming that the synaptic connectivity is restricted to a linear combination of zeroth order modified Bessel functions of the second kind. The first part of §3.3 also shows how to generalise the original treatment in [11], for infinite domains

without imposing boundary conditions, to handle arbitrary choices of the synaptic connectivity function (removing the restriction to Bessel functions). In §3.4 we extend this approach to treat Dirichlet boundary conditions, and in §3.5 we show explicitly how this approach can be used to handle (circularly symmetric) spots and their azimuthal instabilities. We consider a standard choice of a Mexican hat synaptic kernel in §3.2 to §3.5. However, in §3.6 we focus on neural fields with piece-wise constant kernels, for which calculations simplify. We also develop a numerical scheme to evolve the interface dynamics in §3.7 and use this to highlight how Dirichlet boundary conditions can limit the growth of a spreading pattern arising from the azimuthal instability of a spot. Finally in §3.8 we discuss possible extensions of the work presented in this Chapter.

3.2 ONE SPATIAL DIMENSION: A PRIMER

Before we develop the analysis for a two-dimensional neural field model in a bounded domain with Dirichlet boundary conditions imposed, we first start with a discussion for the more tractable one-dimensional case. This gives the main components of our mathematical analyses, as well as that of its equivalent interface dynamics. The one-dimensional version of (3.1.3) and (3.1.4) on finite domain $[-L, L]$ with a Dirichlet boundary condition is given by

$$z_t(x,t) = -z(x,t) + \int_{-L}^{L} \mathrm{d}y\, w_x(|x-y|) H[u(y,t)-\kappa], \tag{3.2.1}$$

with

$$u(x,t) = u_{\mathrm{BC}} + \int_{-L}^{x} \mathrm{d}y\, z(y,t). \tag{3.2.2}$$

Here $x \in [-L, L]$, $z = \partial_x u \in \mathbb{R}$, $t \in \mathbb{R}^+$, and u_{BC} denotes boundary value imposed on the left end of the interval, namely $u(-L) = u_{\mathrm{BC}}$. Note that, using the second

fundamental theorem of calculus, the integral on the right hand side of equation (3.2.2) is

$$\int_{-L}^{x} \partial_x u(y,t)\,\mathrm{d}y = u(x,t) - u_{BC}. \tag{3.2.3}$$

In this setting $u(L)$ is determined by the fixed value of $u(-L)$. Hence some choices of u_{BC} can result in an even bump, for which $u(L) = u(-L) = u_{BC}$.

One-dimensional neural field models with long-range inhibition and short-range excitation are known to support bump solutions. Hence we now focus on a bump solution, where the edges of the bump $x_i(t)$, $i = 1, 2$, are defined by a level set condition that takes the form

$$u(x_i(t), t) = \kappa, \qquad i = 1, 2. \tag{3.2.4}$$

We shall refer to the two bump edges as the interface, as they naturally separate regions of high and low activity. The differentiation of the level set condition (3.2.4) and using (3.2.2) generates a rule for the evolution of the interface for a pulse with a boundary condition according to

$$\dot{x}_i = -\frac{u_t(x,t)}{z(x,t)}\bigg|_{x=x_i(t)} = -\frac{1}{z(x,t)} \int_{-L}^{x} \partial_t z(y,t)\mathrm{d}y\bigg|_{x=x_i(t)}, \quad i = 1, 2. \tag{3.2.5}$$

Once again, applying the second fundamental theorem of calculus for a continuous function z, we find that the velocity rules for the interface can be written

$$\dot{x}_i = \frac{(\kappa - u_{\mathrm{BC}}) - \psi(x,t) + \psi(-L,t)}{z(x,t)}\bigg|_{x=x_i(t)}, \qquad i = 1, 2, \tag{3.2.6}$$

where

$$\psi(x,t) = \int_{-L}^{L} \mathrm{d}y\, w(|x-y|) H[u(y,t) - \kappa] = \int_{x_1(t)-x}^{x_2(t)-x} \mathrm{d}y\, w(|y|). \tag{3.2.7}$$

A closed form expression for $z(x,t)$ may also be found by integrating (3.2.1) to give

$$z(x,t) = \eta(t) z_0(x) + \int_0^t \mathrm{d}s\, \eta(t-s) \left[w(|x_1(s) - x|) - w(|x_2(s) - x|) \right], \tag{3.2.8}$$

where $\eta(t) = \mathrm{e}^{-t} H(t)$ and $z_0(x) = \partial_x u(x, 0)$.

Together with (3.2.8) and (3.2.7), equation (3.2.6) determines the interface dynamics for a time-dependent spatially localised bump solutions that respects the Dirichlet boundary condition at $x = -L$.

Since the Amari model supports a stationary bump solution when the synaptic connectivity has a Mexican hat shape we now revisit this scenario and choose

$$w(x) = \frac{1}{\sqrt{c\pi}}\left[\frac{a_1}{\sqrt{b_1}}\mathrm{e}^{-x^2/b_1} - \frac{a_2}{\sqrt{b_2}}\mathrm{e}^{-x^2/b_2}\right], \tag{3.2.9}$$

where $b_1, b_2, c > 0$. Moreover, we will focus on the case that the stationary bump is symmetric about the origin. In this case, a null interface velocity implies that the numerator in (3.2.6) vanishes. The formula for ψ given by (3.2.7) will also become time independent, and if we let

$$\mathcal{P}(x) = \int_{x_1}^{x_2} w(|x-y|)\mathrm{d}y, \tag{3.2.10}$$

then we have that

$$\kappa = u_{\mathrm{BC}} + \mathcal{P}(-\Delta/2) - \mathcal{P}(-L), \tag{3.2.11}$$

where we have set $x_1 = -\Delta/2$ and $x_2 = \Delta/2$ so that the bump width is given by $\Delta = x_2 - x_1$. The formula for $\mathcal{P}$ is easily calculated as $\mathcal{P}(x) = p(x; a_2, b_2) - p(x; a_1, b_1)$, where

$$p(x; a, b) = \frac{1}{\sqrt{c\pi}}\int_{x_1}^{x_2}\frac{a}{\sqrt{b}}\mathrm{e}^{-x^2/b}\mathrm{d}x, \tag{3.2.12}$$

$$= \frac{a}{2\sqrt{c}}\left[\mathrm{erf}\left(\frac{x_1 - x}{\sqrt{b}}\right) - \mathrm{erf}\left(\frac{x_2 - x}{\sqrt{b}}\right)\right]. \tag{3.2.13}$$

Hence, the bump width is determined implicitly by the single equation (3.2.11), and the bump shape, $q(x)$, is calculated from (3.2.2) as

$$q(x) = u_{\mathrm{BC}} + \mathcal{P}(x) - \mathcal{P}(-L). \tag{3.2.14}$$

In Fig. 3.1, we plot the bump width Δ as a function of time (solid blue and gray lines in each Fig. 3.1**A**), and indicate bump shapes (Fig. 3.1**B**) for direct numerical simulations (blue) as well as their corresponding interface dynamics (gray) at selected times along the trajectories in each Fig. 3.1**A**. Comparing direct numerical

simulations and their corresponding interface dynamics for profiles, only a very small difference in bump widths is seen (typically less than 0.8%).

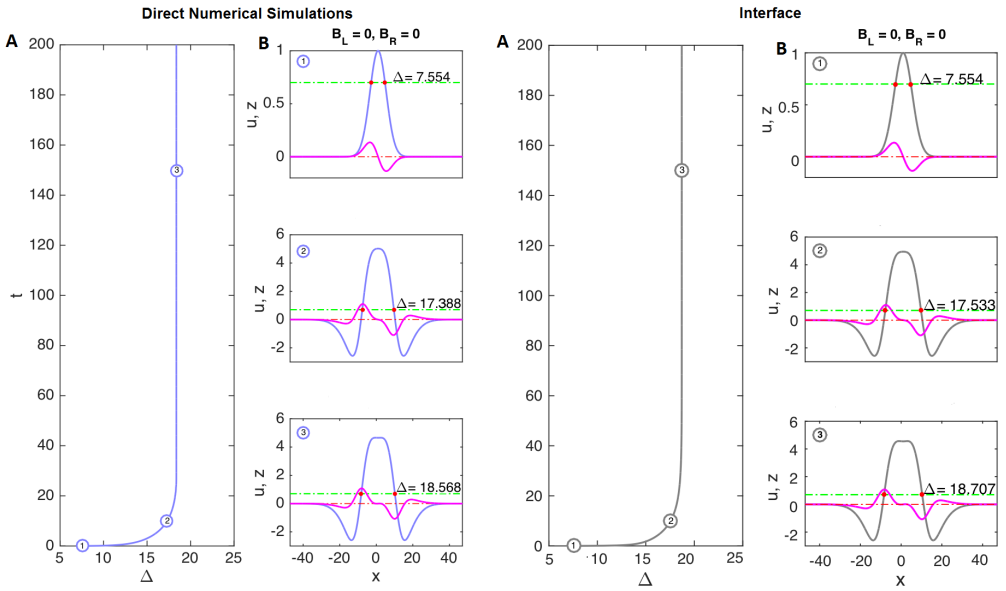

Fig. 3.1: A comparison of the results of direct numerical simulations (blue) for a bump solution of equations (3.2.1), (3.2.2) and (3.2.9) and its equivalent interface dynamics (gray) with a Dirichlet boundary condition $u_{\mathrm{BC}} = 0$ using equations (3.2.6), (3.2.7) and (3.2.9). The solution profiles (gray) for interface dynamics are plotted using equations (3.2.14) and (3.2.13). Panel (**A**): change in the bump width Δ over time posed on a domain of $\Omega = [-L, L]$. Panel (**B**): shape of the bumps at $\kappa = 0.7$ for $q(x)$ (blue) and $z(x)$ (magenta) for selected times along the branches in each (**A**). Parameters are $a_1 = 14$, $a_2 = 13$, $b_1 = 24$, $b_2 = 150$, $c = 5$, $L = 15\pi$.

To determine the stability of the bump solution we can follow the original approach of Amari and linearise the interface dynamics around the stationary values for x_i. Alternatively we can follow the Evans function approach, reviewed in [126], which considers perturbations at all values of x (rather than just at the bump edges). Here we pursue the latter approach, though it is straight forward to check that the former approach gives the same answer.

To determine the linear stability of a bump we write $u(x,t) = q(x) + e^{\lambda t}\widetilde{u}(x)$ where $\widetilde{u} \ll 1$. In this case the corresponding change to z is given by $z(x,t) = dq(x)/dx + e^{\lambda t}\widetilde{z}(x)$, where $\widetilde{z}(x) = d\widetilde{u}(x)/dx$. Expanding (3.2.1) to first order gives

$$(\lambda+1)\frac{d\widetilde{u}(x)}{dx} = \int_{-L}^{L} w_x(|x-y|)H'(q(y)-\kappa)\widetilde{u}(y)\,dy. \tag{3.2.15}$$

For the Dirac-delta function occurring under the integral, we can use the formal identity

$$H'(q(x)-\kappa) = \delta(q(x)-\kappa) = \frac{\delta(x-x_1)}{|q'(x_1)|} + \frac{\delta(x-x_2)}{|q'(x_2)|}, \tag{3.2.16}$$

where integrating (3.2.15) from $-L$ to x and demanding that perturbations on the edge of the domain vanish, namely $\widetilde{u}(-L) = 0$, we obtain

$$\begin{aligned}(\lambda+1)\widetilde{u}(x) = &\frac{\widetilde{u}(x_1)}{|q'(x_1)|}\left[w(|x-x_1|) - w(|L+x_1|)\right] \\ &+ \frac{\widetilde{u}(x_2)}{|q'(x_2)|}\left[w(|x-x_2|) - w(|L+x_2|)\right].\end{aligned} \tag{3.2.17}$$

Here $q'(x) = \mathcal{P}'(x) = w(|x-x_1|) - w(|x-x_2|)$.

From (3.2.17) we may generate two equations for the amplitudes $(\widetilde{u}(x_1), \widetilde{u}(x_2))$ by setting $x = x_1$ and $x = x_2$. This gives a linear system of equations that we can write in the form

$$[\mathcal{A} - (\lambda+1)I](\widetilde{u}(x_1), \widetilde{u}(x_2)) = (0,0), \tag{3.2.18}$$

where I is a 2×2 identity matrix and

$$\mathcal{A} = \begin{bmatrix} \dfrac{w(0)-w(L+x_1)}{|q'(x_1)|} & \dfrac{w(\Delta)-w(L+x_2)}{|q'(x_2)|} \\ \dfrac{w(\Delta)-w(L+x_1)}{|q'(x_1)|} & \dfrac{w(0)-w(L+x_2)}{|q'(x_2)|} \end{bmatrix}. \tag{3.2.19}$$

For the stability analysis of the Amari neural field model [11], equation (3.2.18) has two eigenvalues, one of which is always zero due to the translational invariance. However, boundary conditions break this translational invariance.

Requiring non-trivial solutions gives a formula for the spectrum as $\det[\mathcal{A} - (\lambda+1)I] = 0$, which yields

$$\lambda_\pm = -1 + \frac{\operatorname{Tr}\mathcal{A} \pm \sqrt{(\operatorname{Tr}\mathcal{A})^2 - 4\det\mathcal{A}}}{2}. \tag{3.2.20}$$

Hence a bump solution will be stable provided $\mathrm{Re}\,\lambda_\pm < 0$. In Fig. 3.2, we plot the bump width as a function of the threshold κ. We also indicate whether a branch of solutions is stable by plotting it with a solid (stable) or dashed (unstable) line. Insets show the shapes of the bumps, albeit the inset in Fig. 3.2**B** is shown with a Dirichlet boundary condition $u_{BC} = 0$. For the case of bounded domain with no boundary conditions (Fig. 3.2**A**) we recover the expected Amari result, namely that there are two branches of solutions and it is the one with widest bump width that is stable. However, with a posed boundary condition (Fig. 3.2**B**) we see that new solutions can arise, and that it is possible for these to be stable with widths that occupy a large portion of the domain. Here, four coexisting bumps are found for some values of κ, and two of these bumps are stable. Direct numerical simulations (not shown) show excellent agreement with the theoretical predictions.

3.3 TWO SPATIAL DIMENSIONS WITHOUT BOUNDARY CONDITIONS

Before discussing the extension of §3.2 to two spatial dimensions, it is first instructive to revisit the scenario without regard to the imposition of boundary conditions. In this case, the model (3.1.1) with Heaviside firing rate is written in the form

$$\frac{\partial u(\boldsymbol{x},t)}{\partial t} = -u(\boldsymbol{x},t) + \psi(\boldsymbol{x},t), \quad \psi(\boldsymbol{x},t) = \int_{\Omega_+(t)} \mathrm{d}\boldsymbol{y} w(|\boldsymbol{x}-\boldsymbol{y}|), \tag{3.3.1}$$

where $\Omega_+ \subseteq \mathbb{R}^2$ is where the domain is active, $\Omega_+ = \{\boldsymbol{x}|\boldsymbol{u}(\boldsymbol{x},t) > \kappa\}$. Similar to one-dimensional case, excited and quiescent regions in a two-dimensional neural field model are distinguished by determining if synaptic activity is above or below the firing threshold, namely by an *interface* between these two states. An interface description for (3.3.1) was originally developed in [11], albeit for a special choice of synaptic connectivity kernel. Using properties of Bessel functions, it was possible to compute two-dimensional integrals in terms of one-dimensional line integrals.

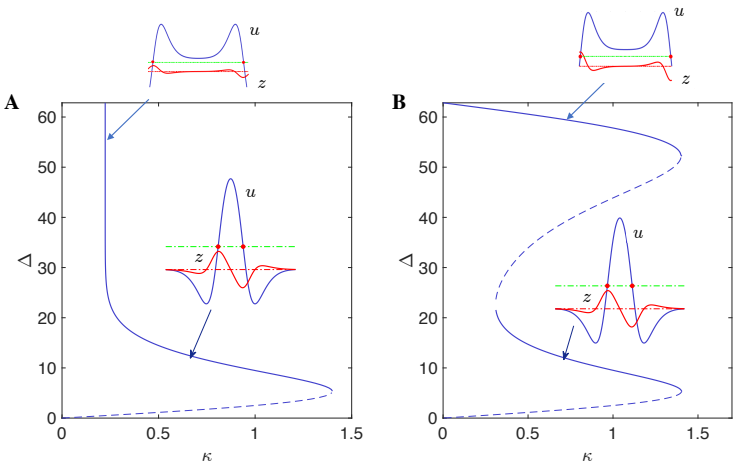

Fig. 3.2: Effect of Dirichlet boundary condition $u_{BC} = 0$ on the bifurcation diagram of a bump solution. Panel (**A**): bump solutions for equation (3.1.1) with $\Omega = [-10\pi, 10\pi]$. Here the bump width is plotted as a function of threshold using equations (3.2.7) and (3.2.10). Panel (**B**) : bump solutions for equations (3.1.3)–(3.1.4) posed on $\Omega = [-10\pi, 10\pi]$ with the Dirichlet boundary condition $u_{BC} = 0$, where the bump width is plotted as a function of threshold using equation (3.2.11). Stable (unstable) solutions are indicated with solid (dashed) lines. The insets show the shapes of the lower (stable) bumps at $\kappa = 0.7$ for $q(x)$ (blue) and $z(x)$ (red). The insets that show the shapes of the bumps near boundary are plotted at $\kappa = 0.23$ (**A**) and $\kappa = 0.7$ (**B**) for $q(x)$ and $z(x)$. Parameters are $a_1 = 14$, $a_2 = 13$, $b_1 = 24$, $b_2 = 150$, $c = 5$.

This allowed the interface dynamics to be expressed solely in terms of the shape of the active region, namely a one-dimensional closed curve.

Here we revisit this approach, together with extension that allows for a far more general class of synaptic connectivity kernels. This allows us to treat the natural extension of (3.2.9), namely a radially symmetric difference of Gaussians, giving rise to the two-dimensional Mexican hat connectivity as shown in Fig. 3.3.

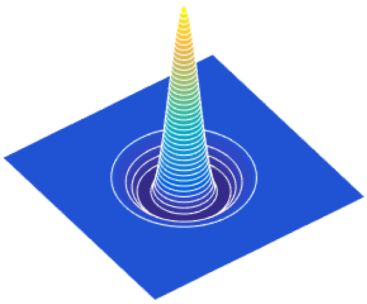

Fig. 3.3: An illustration of a Mexican hat connectivity function with local (short-range) excitation and lateral (long-range) inhibition using a kernel of radially symmetric difference of Gaussians given by (3.2.9).

We consider the integro-differential equation given by (3.1.1). We decompose the domain Ω by writing $\Omega = \Omega_+ \cup \partial\Omega_+ \cup \Omega_-$ where $\partial\Omega_+$ represents the level-set which separates Ω_+ (excited) and Ω_- (quiescent) regions. These regions are given explicitly by $\Omega_+ = \{\boldsymbol{x} \mid u(\boldsymbol{x}) > \kappa\}$, $\Omega_- = \{\boldsymbol{x} \mid u(\boldsymbol{x}) < \kappa\}$, and $\partial\Omega_+ = \{\boldsymbol{x} \mid u(\boldsymbol{x}) = \kappa\}$. We shall assume that $\partial\Omega_+$ is a closed contour or the union of a finite number of disjoint contours, for all $t \in R_+$.

In Fig. 3.4 we show a direct numerical simulation of the full space-time model to illustrate that a Mexican hat synaptic connectivity function can support a spreading labyrinthine pattern. Similar patterns have previously been reported and discussed in [11, 127] for both Heaviside and steep sigmoidal firing rate functions. A description of the numerical scheme used to evolve the full space-time model is given later in §3.7.1.

Differentiation of $u(\boldsymbol{x}, t) = \kappa$ along the contour $\partial\Omega_+(t)$ yields

$$\nabla_{\boldsymbol{x}} u \cdot \frac{\mathrm{d}}{\mathrm{d}t}\partial\Omega_+ + \frac{\mathrm{d}u}{\mathrm{d}t}\bigg|_{\boldsymbol{x}=\partial\Omega_+} = 0, \tag{3.3.2}$$

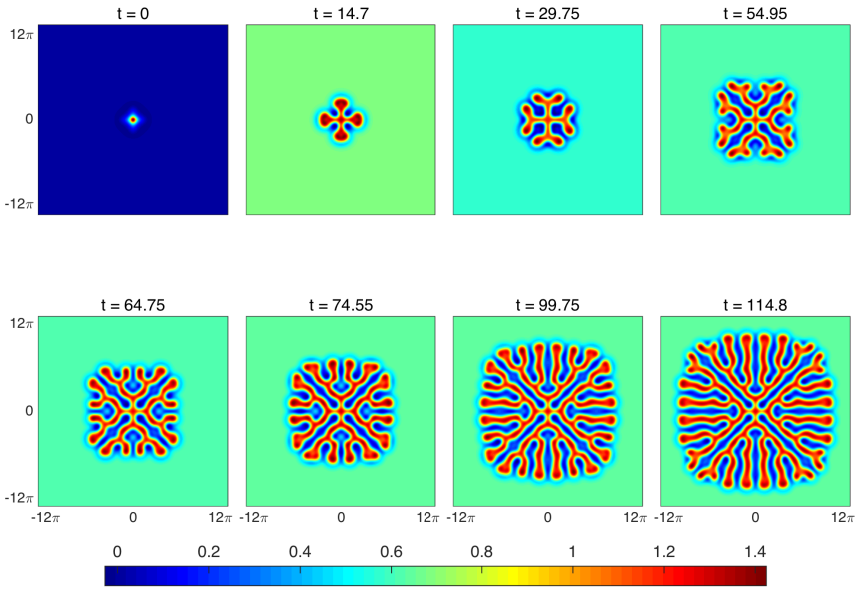

Fig. 3.4: Space time simulations of the field $u(\boldsymbol{x}, t)$ showing a spreading labyrinthine structure in a two-dimensional Amari model (3.3.1) (on a large domain $[-L, L] \times [-L, L]$) with a radially symmetric difference of Gaussians connectivity, namely $w(\boldsymbol{r}) = w(r)$, with $w(r)$ given by (3.2.9) and a Heaviside firing rate. The colorbar below indicates the values of u. Parameters are $\kappa = 0.03$, $a_1 = 3.55$, $a_2 = 3$, $b_1 = 2.4$, $b_2 = 3.2$, $c = 10$, and $L = 12\pi$.

and this gives the normal velocity rule:

$$c_n \equiv \boldsymbol{n} \cdot \frac{\mathrm{d}}{\mathrm{d}t}\partial\Omega_+ = \left.\frac{u_t(\boldsymbol{x},t)}{\nabla_x u(\boldsymbol{x},t)}\right|_{\boldsymbol{x}=\partial\Omega_+}, \tag{3.3.3}$$

where we have introduced the normal vector $\boldsymbol{n} = -\nabla_x u/|\nabla_x u|$ along $\partial\Omega_+$. Let us first consider the denominator in (3.3.3). The temporal integration of (3.1.4) from 0 to t (dropping intermediate steps) gives

$$\boldsymbol{z}(\boldsymbol{x},t) = \eta(t)\boldsymbol{z}_0(\boldsymbol{x}) + \int_0^t \mathrm{d}t'\eta(t')\nabla_x\psi(\boldsymbol{x},t-t'), \tag{3.3.4}$$

where $\eta(t) = \mathrm{e}^{-t}H(t)$, $\boldsymbol{z}_0(\boldsymbol{x}) = \nabla_x u(\boldsymbol{x},0)$ denotes gradient information at $t = 0$, and

$$\left.\frac{\partial u(\boldsymbol{x},t)}{\partial t}\right|_{\boldsymbol{x}=\partial\Omega_+(t)} = -\kappa + \psi(\boldsymbol{x},t)|_{\boldsymbol{x}=\partial\Omega_+(t)}, \tag{3.3.5}$$

with

$$\psi(\boldsymbol{x},t) = \int_{\Omega_+(t)} \mathrm{d}\boldsymbol{y} w(|\boldsymbol{x}-\boldsymbol{y}|). \tag{3.3.6}$$

Describing the double integral (3.3.6) in terms of a dimensionally reduced line integral, we show that the interface dynamics require no knowledge away from the contour $\partial\Omega_+(t)$. In this context, the key mathematical idea is to write a radially symmetric weight kernel w in such a way that Green's first identity for a two-dimensional vector field (two-dimensional Divergence theorem) can be applied. Hence, a relationship between a double integral and a line integral can be written symbolically as

$$\int_{\Omega_+(t)} (\nabla\cdot\boldsymbol{F})\mathrm{d}\boldsymbol{x} = \oint_{\partial\Omega_+(t)} \boldsymbol{F}\cdot\boldsymbol{n}\mathrm{d}s, \tag{3.3.7}$$

where $\nabla\cdot\boldsymbol{F}$ is the Divergence operator of a vector field $\boldsymbol{F}$ and $\boldsymbol{n}$ is the unit normal vector along $\partial\Omega_+$. Therefore, the term $\nabla_x\psi$ in (3.3.4) can be constructed as a line integral using integral vector identity:

$$\nabla_x\psi(\boldsymbol{x},t) = \int_{\Omega_+(t)} \mathrm{d}\boldsymbol{y}\nabla_x w(|\boldsymbol{x}-\boldsymbol{y}|) = -\oint_{\partial\Omega_+(t)} \mathrm{d}s\boldsymbol{n}(s)w(|\boldsymbol{x}-\boldsymbol{y}(s)|). \tag{3.3.8}$$

Thus the denominator in (3.3.3) can be expressed solely in terms of a line integral around the contour. The same is true for the numerator of (3.3.3),

$$u_t(\partial\Omega_+(t), t) = -\kappa + \psi(\partial\Omega_+(t), t),$$

provided that we evaluate ψ using the following identity

$$\psi(\boldsymbol{x}, t) = \oint_{\partial\Omega_+(t)} \varphi(|\boldsymbol{x} - \boldsymbol{\gamma}(s)|) \frac{\boldsymbol{x} - \boldsymbol{\gamma}(s)}{|\boldsymbol{x} - \boldsymbol{\gamma}(s)|} \cdot \boldsymbol{n}(s) \mathrm{d}s + \mathcal{K}C, \tag{3.3.9}$$

where

$$\varphi(r) = \frac{1}{r} \int_{\infty}^{r} x w(x) \mathrm{d}x, \tag{3.3.10}$$

and

$$\mathcal{K} = \int_{\mathbb{R}^2} \mathrm{d}\boldsymbol{x}\, w(\boldsymbol{x}), \qquad C = \begin{cases} 1 & \text{if } \boldsymbol{x} \in \Omega_+ \\ 1/2 & \text{if } \boldsymbol{x} \in \partial\Omega_+ \\ 0 & \text{if } \boldsymbol{x} \in \Omega_- \end{cases}. \tag{3.3.11}$$

Here s is a parametrisation for points on the contour $\boldsymbol{\gamma} \in \partial\Omega_+$. For details of the derivation of ψ (3.3.9) see Appendix A1. Hence the normal velocity rule (3.3.3) can be expressed solely in terms of one-dimensional line integrals involving the shape of the active region Ω_+ (which is prescribed by $\partial\Omega_+$). This is a substantial reduction in description as compared to the full space-time model, yet is exact.

Once again we emphasise that the techniques developed here generalise the original treatment by Coombes *et al.* [11] to tackle any choice of radially symmetric synaptic kernel. For example, for a synaptic kernel in the form $w(x) = K_0(\beta x)$, where K_0 denotes the modified Bessel function of the second kind zeroth order, we find that $\varphi(r) = -K_1(\beta r)/\beta$ using equations (3.3.9), (3.3.10) and (3.3.11). This recovers the results for dimensionally reduced equations obtained by Coombes *et al.* [11].

In the rest of the Chapter, we consider a difference of Gaussians with $w(r)$ given by (3.2.9). A simple calculation for this choice shows that

$$\mathcal{K} = \sqrt{\pi/c}[a_1\sqrt{b_1} - a_2\sqrt{b_2}], \tag{3.3.12}$$

and

$$\varphi(r) = \frac{1}{2r\sqrt{c\pi}}\left[a_2\sqrt{b_2}\mathrm{e}^{-r^2/b_2} - a_1\sqrt{b_1}\mathrm{e}^{-r^2/b_1}\right]. \tag{3.3.13}$$

In Fig. 3.5 we show a numerical simulation obtained by the interface method, with initial data equivalent to that from the full space-time simulation shown in Fig. 3.4. The excellent agreement between the two figures is easily observed. The full details

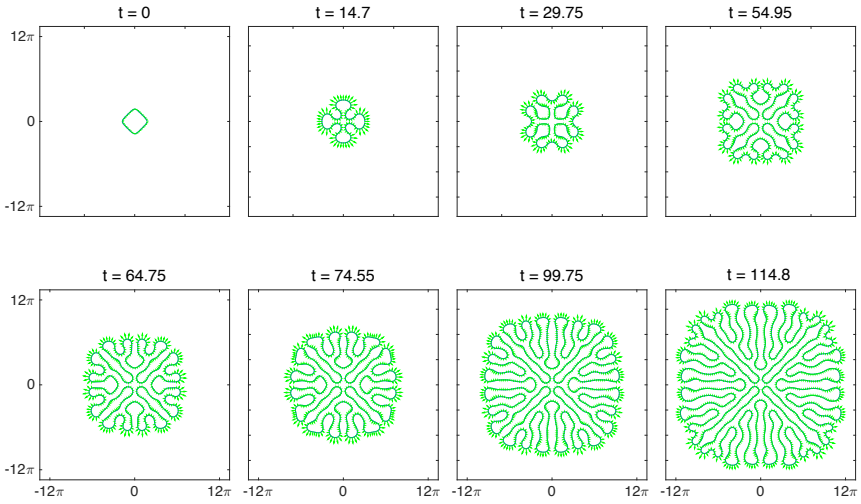

Fig. 3.5: A numerical simulation of the interface dynamics for the same scenario as Fig. 3.4, using (3.3.3) and (3.3.9). Here the threshold condition where $u = \kappa$ is given by the solid blue line, whilst the green arrows show the normal velocity of the moving interface. All parameters as in Fig. 3.4.

of our numerical scheme for implementing interface dynamics are given in §3.7.2. Here we have shown that the full two-dimensional non-linear integro-differential system of equations can be reduced to line integrals of vector fields, and thus the evolution of a full space-time simulation is reduced to the evolution of its interface, driven by a velocity in the normal direction, seen in Fig. 3.5.

It is worth mentioning that a downside of the technique we develop here for interface dynamics is that one needs to track self interactions, namely *splitting* activity on the contour boundary. In this case pinching behaviour in the contour may result in multiple irregular and disjointed curves. Direct numerical simulations with

(3.3.1) can break into multiple patterns each with an independent boundary. Thus an improved numerical algorithm would be needed to cope with the evolution of merging and splitting patterns. On a positive note, such *contour surgery* algorithms have previously been developed for describing fluid models [76, 128].

3.4 TWO SPATIAL DIMENSIONS WITH BOUNDARY CONDITIONS

Using the notation of §3.3 we now show how to extend the one-dimensional approach of §3.2 to develop an interface dynamics for a planar Amari model on a bounded domain with Dirichlet boundary conditions. Revisiting equation (3.1.4) for the evolution of z, that is

$$\frac{\partial z(\boldsymbol{x},t)}{\partial t} = -z(\boldsymbol{x},t) + \nabla_x \psi(\boldsymbol{x},t), \tag{3.4.1}$$

with ψ given by (3.3.6), the state of the activity with a Dirichlet boundary condition is given by

$$u(\boldsymbol{x},t) = u_{BC} + \int_{\Gamma(\boldsymbol{x})} \boldsymbol{z}(\boldsymbol{y},t)\cdot \mathrm{d}\boldsymbol{y}. \tag{3.4.2}$$

Here $\boldsymbol{z}(\boldsymbol{x},t) = \nabla_x u(\boldsymbol{x},t)$ is a continuous vector field for a differentiable scalar function $u(\boldsymbol{x},t)$, and Γ denotes a path that connects a point on the domain boundary $\partial\Omega$ to the point $\boldsymbol{x}$ on the contour $\partial\Omega_+$. As for the one-dimensional case, u_{BC} is the value attained by the activity variable at the boundary. Using the second fundamental theorem of calculus in two-dimensions, we can write

$$\int_{\Gamma(\partial\Omega_+(t))} \boldsymbol{z}(\boldsymbol{y},t)\cdot \mathrm{d}\boldsymbol{y} = u(\partial\Omega_+(t),t) - u(\zeta(\partial\Omega_+(t)),t), \tag{3.4.3}$$

where $\zeta : \partial\Omega_+(t) \to \partial\Omega$ is a mapping from points on the boundary of the active region to points on the boundary $\partial\Omega$ for a particular choice of path Γ. One consequence of this theorem is that, since the vector field $\boldsymbol{z}$ is conservative, the line integral over $\boldsymbol{z}$ does not actually depend on the path taken by Γ, but depends only on the end points of Γ.

Now using (3.1.3), the level set condition becomes

$$\kappa - u_{\mathrm{BC}} = \int_{\Gamma(\partial\Omega_+(t))} \boldsymbol{z}(\boldsymbol{r},t)\cdot \mathrm{d}\boldsymbol{r}. \tag{3.4.4}$$

Using Leibniz's rule:

$$\frac{\mathrm{d}}{\mathrm{d}t}\int_{\Gamma(\partial\Omega_+(t))} z(\boldsymbol{r},t)\cdot \mathrm{d}\boldsymbol{r} = \boldsymbol{z}(\partial\Omega_+(t),t)\cdot\frac{\mathrm{d}}{\mathrm{d}t}\partial\Omega_+ + \int_{\Gamma(\partial\Omega_+(t))} z_t(\boldsymbol{r},t)\cdot \mathrm{d}\boldsymbol{r}, \tag{3.4.5}$$

we may differentiate (3.4.4) with respect to t to obtain the normal velocity rule:

$$c_n \equiv \boldsymbol{n}\cdot\frac{\mathrm{d}}{\mathrm{d}t}\partial\Omega_+ = \frac{1}{|\boldsymbol{z}(\boldsymbol{x},t)|}\int_{\Gamma(\boldsymbol{x})} \boldsymbol{z}_t(\boldsymbol{r},t)\cdot \mathrm{d}\boldsymbol{r}\Big|_{\boldsymbol{x}=\partial\Omega_+(t)}. \tag{3.4.6}$$

Here the normal vector is given by $\boldsymbol{n} = -\boldsymbol{z}/|\boldsymbol{z}|$ along the contour $\partial\Omega_+$. An alternative derivation of the normal velocity rule is given in Appendix A2. Using (3.4.1) and (3.4.3) we may write the numerator in the normal velocity rule (3.4.6) as

$$\int_{\Gamma(\partial\Omega_+(t))} \boldsymbol{z}_t(\boldsymbol{r},t)\cdot \mathrm{d}\boldsymbol{r} = u_{\mathrm{BC}} - \kappa + \psi(\partial\Omega_+(t),t) - \psi(\zeta(\partial\Omega_+(t)),t). \tag{3.4.7}$$

Hence, using the formulas for $\boldsymbol{z}$ and ψ from §3.3, namely equations (3.3.4), (3.3.8), and (3.3.9), then all of the terms in the normal velocity rule (3.4.6) may be expressed as one-dimensional line integrals. This yields the interface dynamics for Dirichlet boundary conditions, and once again we see that it is a reduced yet exact alternative formulation to the full space-time model. The numerical method for implementing the interface dynamics can be based upon that for an unbounded domain, with a specific choice for the paths Γ. Each of the paths Γ connects a point $\boldsymbol{x}$ in the interior of the domain to a point on the boundary, and we set $\zeta(\partial\Omega_+(t))$ to be the end point of $\Gamma(\partial\Omega_+(t))$, see §3.7.2 for details on the numerical scheme.

We do not have to numerically integrate along this path (to determine the normal velocity), and we need only to determine the values of $\psi(\boldsymbol{x},t)$ at the two endpoints. We choose the paths Γ to be straight lines connecting $\boldsymbol{x}$ to its closest point on the boundary. Figure 3.6 shows a direct numerical simulation computed using the evolution of the gradient $\boldsymbol{z} = \nabla_{\boldsymbol{x}} u$ as well as the corresponding interface dynamics. We see excellent agreement between the two approaches. The obvious advantage

of the interface dynamics is that one need only evolve the shape of the active region to fully reconstruct the full space-time dynamics using (3.1.3) and (3.3.8). We see

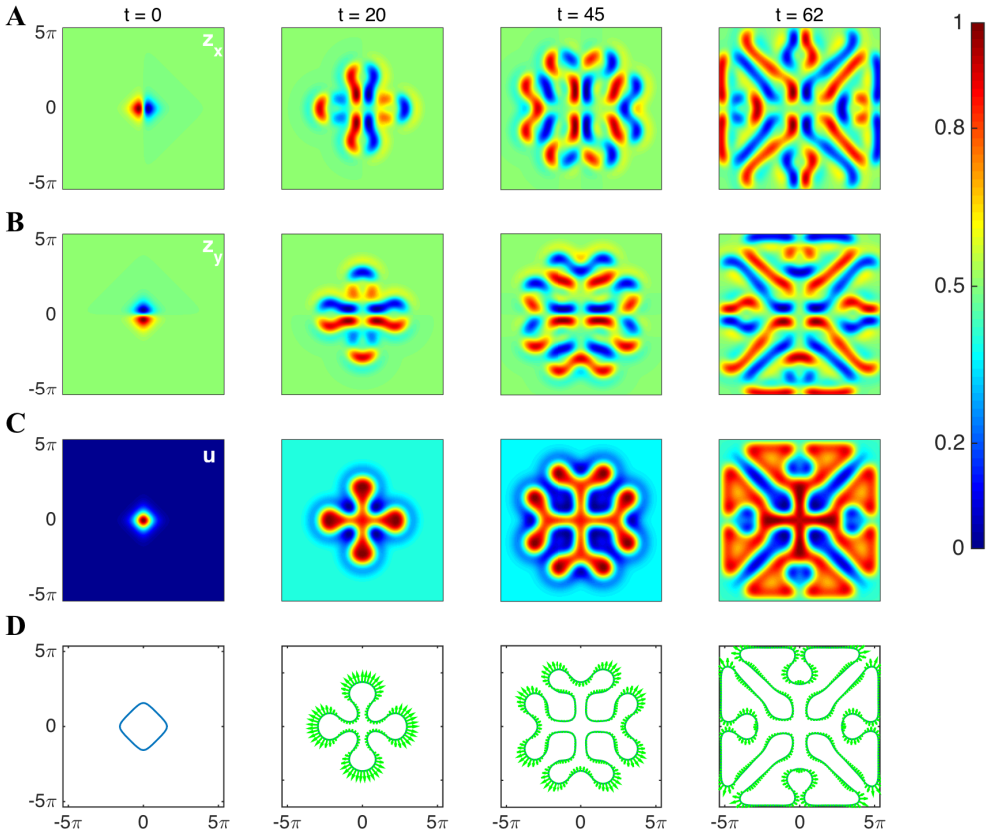

Fig. 3.6: A spreading pattern (**C**) governed by the space-time model (3.1.3) and (3.1.4) with a radially symmetric synaptic connectivity kernel given by (3.2.9) and a Dirichlet boundary condition $u_{\text{BC}} = 0$ on a domain of size $\Omega = [-L, L] \times [-L, L]$. The corresponding interface dynamics is shown in (**D**). Rows (**A**) and (**B**) that show the components of the gradient $\boldsymbol{z}$ in the x and y directions, and these are used to compute the activity of the neuronal tissue shown in row (**C**). Parameters are $\kappa = 0.05$, $a_1 = 3.55$, $a_2 = 3$, $b_1 = 2.4$, $b_2 = 3.2$, $c = 10$, and $L = 5\pi$.

from Fig. 3.6 that the main effect of the Dirichlet boundary condition is to limit the spread of a labyrinthine structure and ultimately induce a highly structured stationary pattern, as expected.

3.5 SPOTS IN A CIRCULAR DOMAIN: DIRICHLET BOUNDARY CONDITION

Given the large amount of historical interest in spot solutions of neural field models on unbounded domains [12, 124, 127, 129, 130] it is worthwhile to revisit this specific class of solutions on a finite disc. We shall consider radially symmetric synaptic connectivity kernels and a disc of radius D with a spot (circularly symmetric) solution of radius R. In this case $u(\boldsymbol{r},t) = q(r)$ with $r = |\boldsymbol{r}|$ for all t, and $q(D) = u_{\rm BC}$, with $q(R) = \kappa$ and $q(r) > \kappa$ for $r < R$ and $q(r) < \kappa$ for $R < r < D$. We shall denote the corresponding stationary field for ψ by $\psi(r)$, and this is conveniently constructed from (3.3.9). In the following, self-consistent equations for stationary solutions of spots are explicitly constructed and their stability determined.

3.5.1 *Construction*

To construct circular solutions, we first consider a standard parametrisation for a circle in the form

$$\boldsymbol{r}(\theta) = \begin{bmatrix} r\cos\theta \\ r\sin\theta \end{bmatrix}, \qquad \boldsymbol{n}_{\boldsymbol{r}}(\theta) = \begin{bmatrix} \cos\theta \\ \sin\theta \end{bmatrix}, \qquad \theta \in [0.2\pi),$$

where the normal vector is obtained by rotating the tangent vector $\boldsymbol{t}_{\boldsymbol{r}}(\theta) = \mathrm{d}\boldsymbol{r}(\theta)/\mathrm{d}\theta$ by $\pi/2$, in the clockwise direction according to $\boldsymbol{n}_{\boldsymbol{r}} = [0\ 1; -1\ 0]\boldsymbol{t}_{\boldsymbol{r}}$. Using the difference between displacement vectors:

$$\boldsymbol{r}(\theta) - \boldsymbol{r}'(\theta') = \begin{bmatrix} r\cos\theta - r'\cos\theta' \\ r\sin\theta - r'\sin\theta' \end{bmatrix},$$

and considering an arbitrary choice of $\theta = 0$, we may write the integral term (3.3.9) with specific choice of a difference of Gaussians given by (3.2.9) in the form

$$\psi(r) = \frac{a_1}{\sqrt{c\pi b_1}}\rho(r;b_1) - \frac{a_2}{\sqrt{c\pi b_2}}\rho(r;b_2) + \mathcal{K}C, \tag{3.5.1}$$

with

$$\rho(r;\alpha) = -\frac{\alpha}{2}\int_0^{2\pi} \mathrm{d}\theta \frac{\mathrm{e}^{-\mathcal{Q}(\theta)^2/\alpha}}{\mathcal{Q}(\theta)^2} R(r\cos\theta - R), \tag{3.5.2}$$

and $\mathcal{Q}(\theta) = \sqrt{R^2 + r^2 - 2Rr\cos\theta}$. Here we also demand that $C = 1/2$ for points on the boundary of the spot solution of radius R.

An implicit equation for the radius of the bump is obtained after setting the normal velocity to zero. Using (3.4.6) and (3.4.7) this yields

$$\kappa = u_{\mathrm{BC}} + \psi(R) - \psi(D). \tag{3.5.3}$$

Equations (3.5.2) and (3.5.3) determine interface dynamics for a time-dependent spot solution that respects the Dirichlet boundary condition $\psi(D) = u_{BC}$.

3.5.2 *Stability Analysis*

The stability of spots on unbounded domains has been treated by several authors, and see [130] for a recent overview. Here we extend this approach to treat a bounded domain with an imposed Dirichlet boundary condition following very similar arguments to those presented in §3.2. To determine the linear stability of a spot we write

$$u(\boldsymbol{r}, t) = q(r) + \mathrm{e}^{\lambda t}\cos(m\theta)\widetilde{u}(r), \tag{3.5.4}$$

where $\boldsymbol{r} = (x, y)$, $r = |\boldsymbol{r}|$, $\widetilde{u} \ll 1$ and $m \in \mathbb{N}$. In this case the corresponding change to $\boldsymbol{z}$ is given by

$$\boldsymbol{z}(\boldsymbol{r}, t) = \nabla_{\boldsymbol{r}} q(r) + \mathrm{e}^{\lambda t}\cos(m\theta)\widetilde{\boldsymbol{z}}(\boldsymbol{r}), \tag{3.5.5}$$

where $\widetilde{\boldsymbol{z}}(\boldsymbol{r}) = \nabla_{\boldsymbol{r}}\widetilde{u}(r)$. Expanding (3.1.4) to first order gives

$$(\lambda + 1)\widetilde{\boldsymbol{z}}(\boldsymbol{r}) = \int_0^{2\pi} \mathrm{d}\theta\cos(m\theta)\int_0^{\infty} r'\mathrm{d}r'\nabla_{\boldsymbol{r}} w(|\boldsymbol{r} - \boldsymbol{r}'|)\delta(q(r') - \kappa)\widetilde{u}(r'), \tag{3.5.6}$$

where $|\boldsymbol{r}-\boldsymbol{r}'| = \sqrt{r^2+r'^2-2rr'\cos\theta}$. Using properties of the Dirac-delta distribution we find

$$\nabla_{\boldsymbol{r}}\left[(\lambda+1)\widetilde{u}(r)-\widetilde{u}(R)\frac{R}{|q'(R)|}\int_0^{2\pi}\mathrm{d}\theta\cos(m\theta)\;w(|\boldsymbol{r}-\boldsymbol{r}'|)\big|_{r'=R}\right]=0. \tag{3.5.7}$$

Since the term in square brackets in (3.5.7) is radially symmetric we may integrate in the radial direction, considering that perturbations vanish on the domain boundary, namely $\widetilde{u}(D)=0$, to obtain

$$(\lambda+1)\frac{\widetilde{u}(r)}{\widetilde{u}(R)}=\frac{R}{|q'(R)|}\int_0^{2\pi}\mathrm{d}\theta\cos(m\theta)\left[w(|\boldsymbol{r}-\boldsymbol{r}'|)\big|_{r'=R}-w(|\boldsymbol{r}-\boldsymbol{r}'|)\big|_{\substack{r'=R\\r=D}}\right]. \tag{3.5.8}$$

Setting $r=R$ in (3.5.8) and demanding non-trivial solutions gives an equation for the eigenvalues λ in the form $\mathcal{E}_m(\lambda)=0$, $m\in\mathbb{N}$, where

$$\mathcal{E}_m(\lambda)=\lambda+1-\frac{R}{|q'(R)|}\int_0^{2\pi}\mathrm{d}\theta\cos(m\theta)\left[w(|\boldsymbol{r}-\boldsymbol{r}'|)\big|_{\substack{r'=R\\r=R}}-w(|\boldsymbol{r}-\boldsymbol{r}'|)\big|_{\substack{r'=R\\r=D}}\right]. \tag{3.5.9}$$

Thus a spot solution will be stable provided $\lambda_m<0$ for all $m\in\mathbb{N}$ where λ_m is a zero of $\mathcal{E}_m(\lambda)$.

Using the above analysis we find that for a Mexican hat function, given by (3.2.9), that for large domains a wide and narrow spot can coexist for a sufficiently low value of the threshold κ. Moreover, the narrow spots are always unstable (to modes with $m=0$, reflecting uniform changes of size), whilst the wider spots can develop instabilities to modes with $m\geq 2$. This is entirely consistent with previous results for Mexican hat connectivities on an unbounded domain, as reviewed in [130].

We note that on an infinite domain the mode with $m=1$ is always expected to exist due to translational invariance (and would give rise to a zero eigenvalue for all parameter values). However, on a finite size disc and with a Dirichlet boundary condition further spots can be induced, with sizes commensurate that of the radius of the disc. These in turn can be unstable to modes with $m\geq 2$. Both of these scenarios are summarised with the use of Fig. 3.7. Note that, although (3.5.2) is in closed form, it is a challenge to perform the integral analytically. Thus it is also of

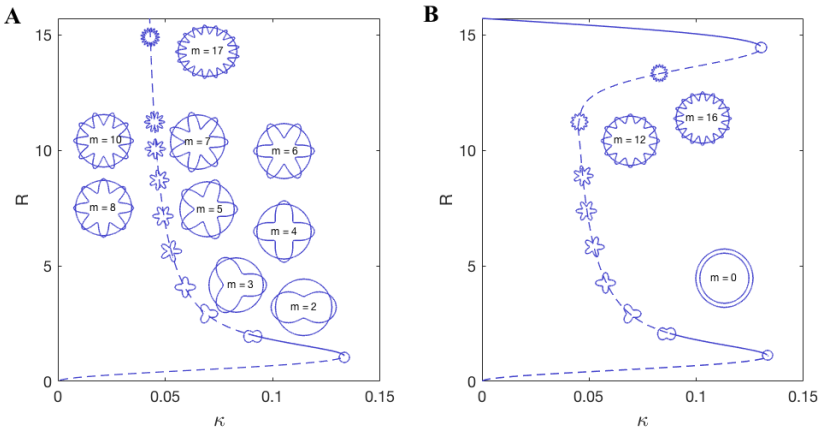

Fig. 3.7: Spot radius R as a function of κ for a smooth Mexican hat connectivity given by (3.2.9), with parameters as in Fig. 3.6. Panel (**A**): infinite domain. Panel (**B**): finite domain that is a disc of radius $D = 5\pi$, with Dirichlet boundary condition $q(D) = u_{\text{BC}} = 0$. Linear stability analysis shows that solid (dashed) lines are stable (unstable). Azimuthal instabilities with various modes are indicated by the mode shapes.

interest to consider synaptic connectivity kernels for which more explicit progress can be made. A case in point is that of piece-wise constant functions, that will be given in the next section.

3.6 PIECE-WISE CONSTANT INTERACTIONS

In the previous sections, we analysed a neural field with a Mexican hat connectivity (3.2.9), as shown in Fig. 3.3. In contrast to this smooth choice of synaptic kernel, here we concentrate on neural fields with a piece-wise constant kernel, which have been far less studied. The exception to this statement being the work of Herrmann *et al.* [13], where a piece-wise constant Top hat synaptic kernel was considered. Therefore, it is now of particular interest to consider piece-wise constant synaptic kernels for which explicit analytical progress can be made. In the first instance,

let us consider a piece-wise constant rotationally symmetric Top hat connectivity defined by

$$w(r) = \begin{cases} w_+ > 0, & r \leq \sigma \\ \\ w_- < 0, & r > \sigma \end{cases}, \qquad r = |\boldsymbol{r}|, \tag{3.6.1}$$

where w_+ and w_- are constant positive and negative synaptic strength factors respectively.

Another natural piece-wise constant choice is the piece-wise constant Mexican hat shape given by

$$w(r) = \begin{cases} w_+ > 0, & r \leq \sigma_1 \\ \\ w_- < 0, & \sigma_1 < r \leq \sigma_2, \\ \\ 0, & r > \sigma_2 \end{cases} \qquad \sigma_1 < \sigma_2 \,. \tag{3.6.2}$$

An illustration of a piece-wise constant Top hat and piece-wise constant Mexican hat functions are shown in Fig. 3.8.

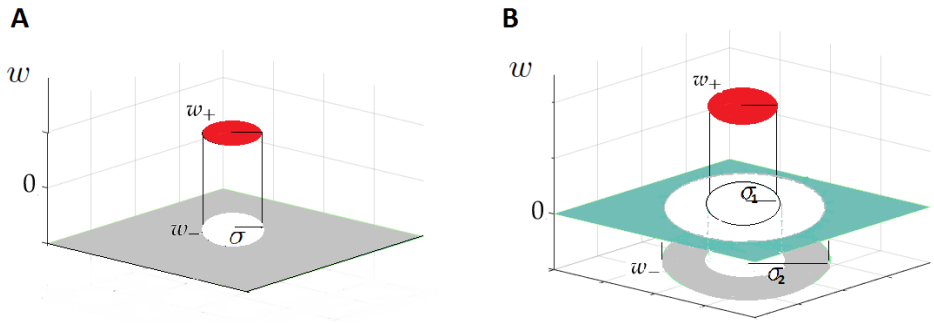

Fig. 3.8: An illustration of a piece-wise constant Top hat (3.6.1) (**A**) and piece-wise constant Mexican hat (3.6.2) (**B**) kernels. Panel (**A**): synaptic interactions are positive up to a distance σ ($w_+ > 0$) and negative beyond this distance ($w_- < 0$). Panel (**B**): synaptic interactions are positive up to a distance σ_1 ($w_+ > 0$), negative between σ_1 and σ_2 ($w_- < 0$), and zero beyond distance σ_2.

In the following, we show how piece-wise constant caricatures of synaptic connectivity allow simplified calculations for localised solutions of neural fields in

two-dimensions. We find that localised spots obtained using piece-wise constant Mexican kernels can destabilise to azimuthal instabilities, which in turn can lead to the generation of labyrinthine structures. Interestingly, a piece-wise constant Top hat kernel is more robust to these instabilities.

3.6.1 *Construction: No Boundary Conditions*

Considering the area $\Omega_+ = \{\boldsymbol{r} \,|\, \psi(\boldsymbol{r}) > \kappa\}$ over which the local field is excited, we revisit stationary solutions of spots (circularly symmetric solutions) of radius R as $\psi(\boldsymbol{r}) = q(r)$, where

$$q(r) = \iint_{|\boldsymbol{r}'|<R} \mathrm{d}\boldsymbol{r}' w(|\boldsymbol{r} - \boldsymbol{r}'|), \quad q(R) = \kappa. \tag{3.6.3}$$

For the Top hat kernel given by equation (3.6.1), we may split the above integral as

$$q(r) = w_+ \iint_{\substack{|\boldsymbol{r}'|<R \\ |\boldsymbol{r}-\boldsymbol{r}'|<\sigma}} \mathrm{d}\boldsymbol{r}' + w_- \iint_{\substack{|\boldsymbol{r}'|<R \\ |\boldsymbol{r}-\boldsymbol{r}'|>\sigma}} \mathrm{d}\boldsymbol{r}'. \tag{3.6.4}$$

Introducing the area $A_+(R,\sigma)$ as follows

$$A_+(R,\sigma) = \iint_{\substack{|\boldsymbol{r}'|<R \\ |\boldsymbol{r}-\boldsymbol{r}'|<\sigma}} \mathrm{d}\boldsymbol{r}' \Big|_{r=R}, \tag{3.6.5}$$

means that the self-consistent equation for a spot without a boundary condition takes the form

$$\kappa = (w_+ - w_-)A_+(R,\sigma) + w_- \pi R^2. \tag{3.6.6}$$

Here, the area $A_+(R,\sigma)$ can be calculated in terms of the area of the intersection between two disks, one of center $(0,0)$ and radius R, and the other of center $\boldsymbol{r}$ and radius σ subject to the constraint $|\boldsymbol{r}| = R$. Using the results from Appendix A3 we find

$$A_+(R,\sigma) = A(R,\theta_0(R,\sigma)) + A(\sigma,\theta_1(R,\sigma)), \tag{3.6.7}$$

where $A(r,\theta) = r^2(\theta - \sin\theta)/2$ and

$$\theta_0(R,\sigma) = 2\cos^{-1}\left(\frac{2R^2-\sigma^2}{2R^2}\right), \qquad \theta_1(R,\sigma) = 2\cos^{-1}\left(\frac{\sigma}{2R}\right), \qquad R > \frac{\sigma}{2}. \tag{3.6.8}$$

For example, for the special case that $R = \sigma$ and $\kappa = 0$, it is easy to show

$$A_+(R,\sigma) = 2A(R, 2\pi/3) = R^2(2\pi/3 - \sqrt{3}/2), \tag{3.6.9}$$

and using equation (3.6.6), we obtain the ratio

$$\frac{w_+}{w_-} = 1 - \frac{\pi}{(2\pi/3 - \sqrt{3}/2)}, \tag{3.6.10}$$

which recovers the result obtained by Herrmann *et al.* [13].

Another natural piece-wise constant choice for synaptic connectivity is the piece-wise constant Mexican hat shape given by (3.6.2). Using a similar argument to the one used for the Top hat connectivity, we find the self consistent equation for a localised spot

$$\kappa = (w_+ - w_-)A_+(R,\sigma_1) + w_- A_+(R,\sigma_2). \tag{3.6.11}$$

In Figure 3.9, we show the results of direct numerical simulations at fixed times for a neural field with a piece-wise constant Mexican hat kernel. These simulations show the emergence of an exotic mazelike pattern with the symmetries of a square, and suggest that the spot is unstable to an azimuthal instability with $m = 4$. Similar

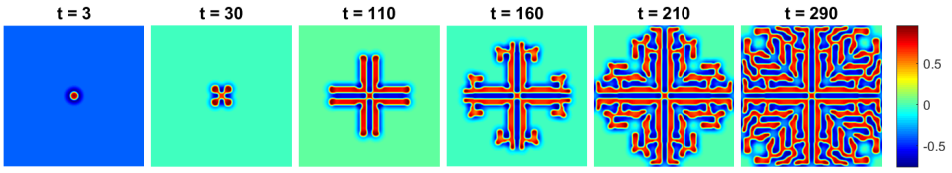

Fig. 3.9: Direct numerical simulations of a spreading pattern governed by the space-time model (3.3.1) with a radially symmetric piece-wise constant Mexican hat kernel on a domain of size $[-L, L] \times [-L, L]$. Parameters are $w_+ = 0.1$, $w_- = -0.004$, $\kappa = 0.1$, $\sigma_1 = 2$, $\sigma_2 = 10$, $L = 100$. Here, red and blue regions represent the excited (high activity) and quiescent states (low activity), respectively.

exotic patterns with a smooth Mexican hat connectivity (3.2.9) have been found and discussed in §3.3, and see [11, 88, 127] for further discussion.

3.6.2 *Stability Analysis*

To determine the linear stability of a spot with a piece-wise constant Top hat kernel, we follow the ideas in §3.5.2. Using equation (3.5.9) for $D \to \infty$, once again we obtain $\mathcal{E}_1(0) = 0$ is always true since a radial solution is rotationally invariant, and once more we emphasise that the nature of constant piece-wise kernels substantially simplifies the mathematical expressions presented above. For example for the Top hat function given by (3.6.1) and using the expressions in equation (3.6.8) it is simple to show that

$$q'(R) = (w_- - w_+)\left[A'(R, \theta_0(R,\sigma)) + A'(\sigma, \theta_1(R,\sigma))\right], \tag{3.6.12}$$

$$= \frac{\sigma(w_- - w_+)}{R}\sqrt{4R^2 - \sigma^2}. \tag{3.6.13}$$

Using the results in Appendix A3 yields

$$\theta_0(r,\sigma) = 2\cos^{-1}\left(\frac{R^2 - \sigma^2 + r^2}{2Rr}\right) \quad \text{and} \quad \theta_1(r,\sigma) = 2\cos^{-1}\left(\frac{\sigma^2 - R^2 + r^2}{2\sigma r}\right). \tag{3.6.14}$$

Furthermore, we obtain

$$\int_0^{2\pi} \mathrm{d}\theta \cos(m\theta)\; w(|\boldsymbol{r} - \boldsymbol{r}'|)\big|_{r'=r=R} = 2\left(\frac{w_+ - w_-}{m}\right)\sin m\theta^*, \tag{3.6.15}$$

where θ^* is the smaller of the two roots of the equation $R\sqrt{2(1-\cos\theta)} = \sigma$ for $\theta \in [0, 2\pi)$.

As for the piece-wise constant Top hat kernel, the calculations also simplify for the piece-wise constant Mexican hat kernel, where we find

$$q'(R) = (w_+ - w_-)\left[A'(R, \theta_0(R,\sigma_1)) + A'(\sigma_1, \theta_1(R,\sigma_1))\right] + w_-\left[A'(R, \theta_0(R,\sigma_2)) + A'(\sigma_2, \theta_1(R,\sigma_2))\right], \tag{3.6.16}$$

with

$$\int_0^{2\pi} \mathrm{d}\theta \cos(m\theta)\; w(|\boldsymbol{r} - \boldsymbol{r}'|)\big|_{r'=r=R} = \frac{2}{m}\left[(w_+ - w_-)\sin m\theta_1^* + w_- \sin m\theta_2^*\right], \tag{3.6.17}$$

where θ_1^* and θ_2^* are the smaller roots of equations $R\sqrt{2(1-\cos\theta)} = \sigma_1$, and $R\sqrt{2(1-\cos\theta)} = \sigma_2$ respectively, with $\theta \in [0, 2\pi)$.

In Figure 3.10, plots of the radius R as a function of the threshold parameter κ, and the spectra of selected profiles are shown for a neural field model without boundary conditions, with a piece-wise constant Top hat (Fig. 3.10**A**) and a piece-wise constant Mexican Top hat (Fig. 3.10**B**) kernels. Our linear stability analysis of the stationary circular solutions for the Top hat kernel shows that lower (dashed) branch of solutions is unstable to uniform changes (expansion or contraction) of size ($m = 0$) and the upper (solid) branch is stable. Here, it is straightforward to show that solutions of spots with Top hat kernels can not lead to azimuthal instabilities of modes $m \geq 2$. In this case, substituting equations (3.6.13) and (3.6.15) into (3.5.9) for the case where there is no boundary conditions ($D \to \infty$), we obtain

$$\lambda = -1 + \frac{2R^2}{\sigma m\sqrt{4R^2 - \sigma^2}} \sin m\theta, \tag{3.6.18}$$

where $\lambda < 0$ for all $\theta \in [\pi(2n-1), 2\pi n]$, $n \in \mathbb{Z}$. Considering the maximum value of $\sin m\theta$ is 1, let us assume that $\lambda > 0$. Hence we find

$$\frac{2R^2}{\sigma m\sqrt{4R^2 - \sigma^2}} > 1, \tag{3.6.19}$$

which means $2\sigma < R$. This statement is contradictory with the constraint $R > \sigma/2$ given in (3.6.8).

However, the piece-wise constant Mexican Top hat kernel readily supports azimuthal instabilities of various modes ($m \geq 2$). These results are consistent with those previously found in §3.5.2 and also studied by several authors for smooth Mexican hat kernels, as in [12, 107, 127, 130].

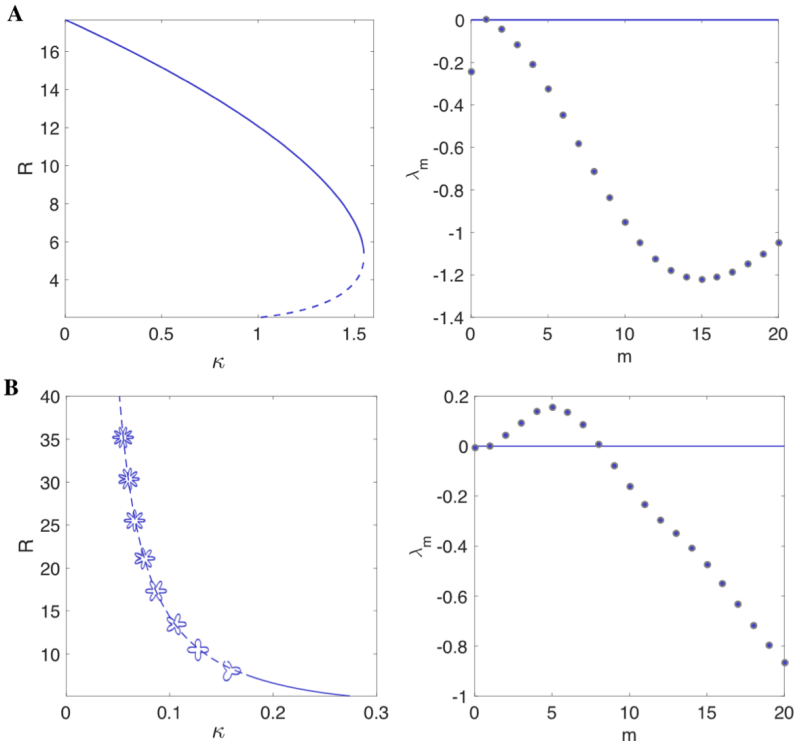

Fig. 3.10: Spot radius R as a function of threshold κ for piece-wise constant Top hat and piece-wise constant Mexican hat kernels using equations (3.6.6) and (3.6.11), respectively. Panel (**A**): piece-wise constant Top hat kernel, with the right panel showing the spectrum for $\kappa = 0.1$. Parameters are $w_+ = 0.08$, $w_- = -0.002$, $\sigma = 4$ with constraint $2R > \sigma$. Panel (**B**): piece-wise constant Mexican hat kernel, with the right panel showing the spectrum for $\kappa = 0.1$. Parameters are $w_+ = 0.1$, $w_- = -0.004$, $\sigma_1 = 2$, $\sigma_2 = 10$ with constraint $2R > \sigma_2 > \sigma_1$.

3.6.3 *Construction: Dirichlet Boundary Condition*

We can also extend this approach to treat a finite domain with an imposed Dirichlet boundary condition ($u_{BC} = 0$), following very similar techniques to those presented in §3.5.2. In this case the self consistent equation for a localised spot for a piece-wise constant Top hat kernel with a Dirichlet boundary condition takes the form

$$\kappa = u_{BC} + (w_+ - w_-)\left(A_+(R,\sigma) - A_+(D,\sigma)\right), \tag{3.6.20}$$

and, using a similar argument, we find that for a localised spot for a piece-wise constant Mexican hat kernel with a Dirichlet boundary condition as

$$\begin{aligned}\kappa = u_{BC} &+ (w_+ - w_-)\left(A_+(R,\sigma_1) - A_+(D,\sigma_1)\right) \\ &+ w_-\left(A_+(R,\sigma_2) - A_+(D,\sigma_2)\right),\end{aligned} \tag{3.6.21}$$

where D is the radius of the disc. Here, $A_+(r,\sigma) = A(R,\theta_0(r,\sigma)) + A(\sigma,\theta_1(r,\sigma))$ with $\theta_0(r,\sigma)$ and $\theta_1(r,\sigma)$ given by Equation (3.6.14).

In Fig. 3.11, we show the neural field model with boundary conditions ($u_{BC} = 0$) for a piece-wise constant Top hat (3.11**A**) and a piece-wise constant Mexican hat (3.11**B**) functions given in (3.6.1) and (3.6.2); where both support only stable solutions for large values of radii.

3.7 NUMERICAL SCHEME

3.7.1 *Numerical Scheme for the Full Space-time Model*

We discretise the space into 2^9 points in each of the x and y spatial directions, and evolve the resultant set of ordinary differential equations using MATLAB 2015a with its standard non-stiff `ode45` routine. The numerical simulation of the full

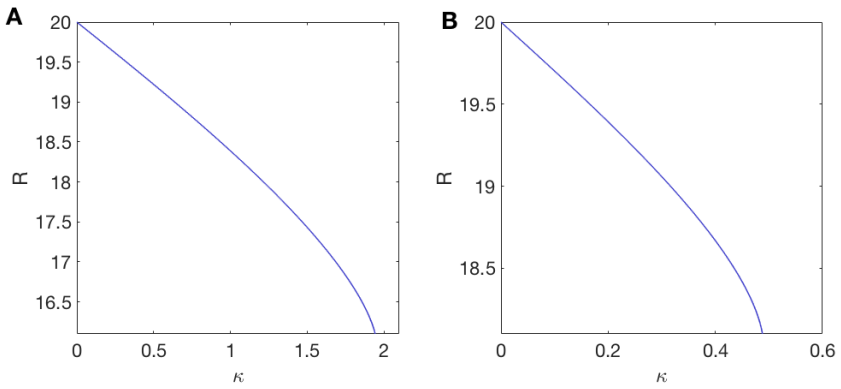

Fig. 3.11: Spot radius R as a function of κ for a piece-wise constant Top hat (**A**) and a piece-wise constant Mexican hat (**B**) connectivities given by (3.6.1) and (3.6.2) in a finite domain, that is a disk of radius $D = 20$ with Dirichlet boundary condition $q(D) = u_{\text{BC}} = 0$. Parameter values are as in Fig. 3.10. Linear stability analysis shows that solutions are stable (solid lines). Here the figures are plotted considering the constraint $R > D - \sigma$ for the piece-wise constant Top hat kernel and $R > D - \sigma_1$, where $\sigma_2 > \sigma_1$ for the piece-wise constant Mexican hat kernel.

space-time model (3.1.1) without boundary conditions was performed by discretising the domain on an N by N tensor grid, which requires N^4 operations. Due to the convolution structure of equation (3.1.1), it is possible to decrease the computational cost of each function evaluation by performing a pseudo-spectral evaluation of the convolution, using a Fast Fourier Transform (FFT), followed by an inverse Fast Fourier Transform (IFFT). This reduces the number of operations to $O(N^2 \log N^2)$ and allows to simulate full space-time neural fields efficiently. For a further discussion on direct numerical simulations of neural fields using FFTs, see the numerical schemes presented in [11, 131]. It is worth pointing out that we have studied neural field models for a Heaviside firing rate throughout this Chapter.

Note that Fourier methods can only be exploited for periodic domains. Since the model in (3.1.3) and (3.1.4) is not periodic, we used conventional matrix-vector multiplication for the convolution structure of (3.1.4). In this context, on a N by N grid, N^4 operations is precomputed and stored prior to the time stepping, with the synaptic kernel given by (3.2.9). Because of the memory constraints, the grid size for the model in (3.1.3) and (3.1.4) was limited to 2^7 points. Discretising (large) domains with a small number of grid points may not always be accurate for numerical simulations of the full space-time model. Therefore, the interface dynamics, which requires no knowledge away from contour, becomes a practical alternative for a robust and efficient description of a neural activity.

3.7.2 *Numerical Scheme for the Interface Dynamics*

Numerical evolution of the interface dynamics is performed based on the computation of the normal velocity by approximating the numerator and denominator of equations (3.3.3) and (3.3.9) for unbounded domains, and also that of (3.4.6) and (3.4.7) for bounded domains with an imposed Dirichlet boundary condition. For both cases, the interface between the active and quiescent regions is discretised into

a set of points (see Fig. 3.4), the number of which is proportional to the desired accuracy and smoothness of the solution. For a neural field model with a Dirichlet boundary condition, one also needs to discretise the domain boundary to compute the line integral (3.1.3) with a specific choice for the paths Γ, that connect points on the domain boundary to the points on the contour. For simplicity, we have used a shortest path (3.4.2) which starts on the contour $\partial\Omega_+$ and ends on the boundary $\partial\Omega$. Note that, since the evolution of the interface is driven by the normal velocity, it is also natural to choose paths in the normal direction. However, this would require more computational time for full space-time simulations, as well as that for interface dynamics.

Normal and tangent vectors along the interface are efficiently computed using spectral methods via numerical FFT and IFFT [132], allowing very robust and fast computation of the line integrals given by equations (3.3.8) and (3.3.9). Note that, for the spectral methods, the points along the contour must be evenly spaced at every time step. This requirement is fulfiled by an interpolation [133]. The contour is displaced in the normal direction, where a standard trapezoidal rule is used to calculate components of the normal velocity. Here, we obtain the new contour using a Forward Euler method, where $\partial\Omega_+(s, t + \Delta t) = \partial\Omega_+(s, t) + c_n \Delta t$ with $c_n(s) = c \cdot \boldsymbol{n}(s, t)$. As a pattern grows or shrinks, additional points are added or eliminated to fix the arclength between points on the contour. We emphasise that the time evolution for these equi-spaced interface dynamics requires data from the full history of $\partial\Omega_+(t)$, in the interval $[0, t]$, see equation (3.3.4). Since saving the history of all contours is computationally expensive, we always store the last 50 contours, and any other previously stored data is deleted as its effect on the system vanishes over time, since $\eta(t)$ in (3.3.4) is a decaying function. Singular points in the line integral given by equation (3.3.9) can be either skipped according to a *Plemelj*-type argument described in [134] or set to zero. In fact, the contribution of a single (singular) point to the solution is very small, so that we can ignore this when we compute the line

integrals. For a relatively smooth evolution, we consider a time step size of 0.05 (or smaller) to calculate the line integrals.

3.8 CONCLUSION & DISCUSSION

In this Chapter we have introduced a new approach for studying localised solutions of a neural field model on a bounded domain. Focusing on Dirichlet boundary conditions, we have developed a key mathematical idea, namely reformulating the model using the evolution of its gradient. We have reformulated the normal velocity rule for an interface framework that respects Dirichlet boundary conditions, and used this to highlight how a Dirichlet boundary condition can limit the growth of a spreading pattern. Hence, one major topic here is to study the effect of a Dirichlet boundary condition that clamps neural activity at the boundary to a specific value. It is also appreciated that continuum neural field models can be extended to include different properties that can strongly influence the spatio-temporal dynamics of waves and patterns. For example, heterogeneities may give rise to wave scattering [135] or even extinction [106]. Therefore another way for studying biological constraints at the boundary of a bounded domain would be to impose spatial heterogeneities as in the work of Goulet *et al.* [135]. The topic we address in this paper is to ponder the role that a Dirichlet boundary condition can have on spatio-temporal patterning. Considering Neumann boundary conditions would be another route; however, we do not pursue this here as localised states with Neumann boundary conditions could take on the value of the threshold at the boundary, making mathematical analysis harder (for handling the level set on the boundary). We have also reproduced the work of Coombes *et al.* [11] to develop an interface dynamics approach for both one- and two-dimensional systems, additionally removing the restrictions to Bessel functions in the synaptic kernel. In this setting, we have focused on localised states, as well as their instabilities. Com-

pared to the full space-time model for neural dynamics the interface description is reduced, but it is exact. For all results obtained from numerical simulations, we have highlighted the excellent agreement between the full space-time model and the equivalent interface approach in the absence and presence of boundary conditions. Although we mainly focused on the generation of labyrinthine structures (from unstable spots) with a four fold symmetry, suggesting that the spot is unstable to an azimuthal instability with 4-mode, the technique we have developed in this Chapter can treat other simple structures, including stripes and ring structures. The interface approach studied in this Chapter has been developed for Heaviside firing rates. An extension of the techniques for developing an interface dynamics approach to treat smooth sigmoidal firing rates (2.3.5) is a challenge, yet combining the mathematical techniques we discussed for interface dynamics in this Chapter with the results presented by Coombes *et al.* [136] for the approximate solutions of neural fields with sigmoidal firing rates may allow one to reformulate a normal velocity rule for a neural field model with a Dirichlet boundary condition and smooth sigmoidal firing rate function.

We have also shown that the analysis of the Amari model simplifies even further for the choice of piece-wise constant synaptic kernels. These kernels allow the analysis of localised states in the form of spots as well as their azimuthal instabilities. Using piece-wise constant kernels the interface approach becomes quasi-analytical, and the normal velocity of the interface can be calculated by hand rather than having to be found numerically. Compared to the original model of Amari, we find that localised states can be induced by the imposition of Dirichlet boundary conditions on a bounded domain, yet all are shown to be stable near the domain boundary. Another extension would be to consider doubly periodic solutions with $u(\boldsymbol{r}+\boldsymbol{l}_{1,2},t)=u(\boldsymbol{r},t)$, for linearly independent vectors $\boldsymbol{l}_{1,2}\in\mathbb{R}^2$. Because of the possible contour interactions (splitting and merging behaviour in periodic contours), developing an interface theory for these periodic (and interacting) solutions is a challenge. The ideas for a further analysis of doubly periodic solutions, and their

instabilities will be presented in Chapter 7. Furthermore, given that heterogeneities can strongly influence the behaviour of neural fields, e.g. giving rise to wave scattering [135] or even extinction [106], it would be interesting to further investigate the role that a boundary can have on patterning.

In the next Chapter, we study neural field models with a linear form of spike frequency adaptation (SFA) to mimic a negative feedback process to diminish sustained firing. The effects of an adaptation variable cause a travelling front to transition to a travelling pulse [83], or allow the generation of planar spiral waves [16]. Since the adaptation is linear, we generalise the interface approach presented in this Chapter.

4

INTERFACE DYNAMICS IN NEURAL FIELDS WITH ADAPTATION

Experiments on disinhibited cortex slices suggest that there are various metabolic processes, apart from inhibition, which restrain the excitatory activity of large scale neural networks [107, 108]. *M-type currents*, *AHP-type currents* and *slow recovery currents* are three major types of spike frequency adaptation currents [108]. *M-type currents* increase the firing threshold of an action potential in voltage-gated potassium (K^+) channels [108, 137], *AHP-type currents* are involved in inactivation of calcium-gated potassium channels [138], and *slow recovery currents* are linked to the inactivation of voltage-gated sodium (Na^+) channels [107, 139].

Perhaps the first comprehensive analysis of neural field models with adaptation was developed by Pinto and Ermentrout in Pinto's PhD thesis in the late 1990s [107, 140]. Concurrently, the existence of travelling pulses in the presence of adaptation on a ring domain was reported by Hansel and Sompolinsky [141]. Since then, the slow linear spike frequency adaptation, which brings neurons back to their resting state after high activity periods, has been a popular choice to modulate neural response in neural field models.

Prior to this Chapter, we have only studied neural fields for analysing the dynamics of localised patterns. As indicated earlier, these planar models with the addition of a linear adaptation component are known to support not only localised states but

also a wide range of travelling waves, including spiral waves. Here, we begin with an overview of neural fields with adaptation in §4.1. Coombes *et al.* [11] outlined how planar neural field models with linear adaptation could support a range of travelling waves and breathers. However, they did not develop an equivalent interface description of these models. Next in §4.2 we develop a theory for interface dynamics in neural fields with adaptation in an unbounded domain, and show that they are in an excellent numerical agreement with direct numerical simulations for localised non-oscillatory labyrinthine structures in §4.3 and oscillatory breathers in §4.4. Then, following Laing's work [16], we study rotating spiral waves in neural fields using a partial differential equation (PDE) on a circular domain with a Dirichlet boundary condition and steep sigmoidal firing rate in §4.6.3, and we perform their numerical continuation in §4.6.4.

4.1 THE MODEL: INTEGRO-DIFFERENTIAL EQUATIONS

A standard two-dimensional neural field with adaptation that we consider is given by

$$\frac{\partial u(\boldsymbol{x},t)}{\partial t} = -u(\boldsymbol{x},t) + \int_{\Omega} w(\boldsymbol{x}-\boldsymbol{x}')f[u(\boldsymbol{x}',t)-\kappa]\mathrm{d}\boldsymbol{x}' - ga(\boldsymbol{x},t), \tag{4.1.1}$$

$$\tau\frac{\partial a(\boldsymbol{x},t)}{\partial t} = \widetilde{\alpha}u(\boldsymbol{x},t) - a(\boldsymbol{x},t), \tag{4.1.2}$$

where $\Omega \subseteq \mathbb{R}^2$, $\boldsymbol{x} \in \mathbb{R}^2$ and $t \in \mathbb{R}^+$. The field a represents a local slow negative feedback ($g > 0$) mechanism that modulates synaptic activity, and τ controls the time course for the change in recovery variable relative to the change in synaptic drive. Further, we shall work with a rotationally invariant isotropic choice of synaptic kernel, that is $w(\boldsymbol{x}) = w(|\boldsymbol{x}|)$. Other variables are as in previous Chapters.

In this setting, for a Heaviside firing rate, it is convenient to recall equation (3.3.6):

$$\psi(\boldsymbol{x},t) = \int_{\Omega_+(t)} \mathrm{d}\boldsymbol{x}'\, w(|\boldsymbol{x}-\boldsymbol{x}'|). \tag{4.1.3}$$

Here we decompose the domain as $\Omega = \Omega_+ \cup \partial\Omega_+ \cup \Omega_-$, where $\Omega_+ = \{\boldsymbol{x} \in \mathbb{R}^2 | u(\boldsymbol{x},t) > \kappa\}$, $\Omega_- = \{\boldsymbol{x} \in \mathbb{R}^2 | u(\boldsymbol{x},t) < \kappa\}$, and $\partial\Omega_+ = \{\boldsymbol{x} \in \mathbb{R}^2 | u(\boldsymbol{x},t) = \kappa\}$. The system (4.1.1) and (4.1.2) is recast as

$$\frac{\partial X(\boldsymbol{x},t)}{\partial t} = AX(\boldsymbol{x},t) + B(\boldsymbol{x},t), \tag{4.1.4}$$

with $X(\boldsymbol{x},t) = (u(\boldsymbol{x},t), a(\boldsymbol{x},t))^T$, and

$$A = \begin{bmatrix} -1 & -g \\ \widetilde{\alpha}/\tau & -1/\tau \end{bmatrix}, \qquad B(\boldsymbol{x},t) = \begin{bmatrix} \psi(\boldsymbol{x},t) \\ 0 \end{bmatrix}. \tag{4.1.5}$$

Here the system of differential equations in (4.1.4) can be solved using the matrix exponential. Thus, the solution of the system in equation (4.1.4) can be written as

$$X(\boldsymbol{x},t) = G(t)X(\boldsymbol{x},0) + \int_0^t G(t-t')B(\boldsymbol{x},t')\mathrm{d}t', \qquad G(t) = \mathrm{e}^{At}. \tag{4.1.6}$$

The G matrix in equation (4.1.6) can be computed with Matlab that easily implements matrix exponentials using function *expm*. In components form we have

$$u(\boldsymbol{x},t) = \int_0^t \mathrm{d}t'\, G_{11}(t')\psi(\boldsymbol{x},t-t') + G_{11}(t)u(\boldsymbol{x},0) + G_{12}(t)a(\boldsymbol{x},0), \tag{4.1.7}$$

$$a(\boldsymbol{x},t) = \int_0^t \mathrm{d}t'\, G_{21}(t')\psi(\boldsymbol{x},t-t') + G_{21}(t)u(\boldsymbol{x},0) + G_{22}(t)a(\boldsymbol{x},0), \tag{4.1.8}$$

where the 2-by-2 matrix G has components G_{ij}, $i,j = 1,2$. If the matrix A has real eigenvalues, we obtain

$$\lambda_\pm = \frac{\mathrm{Tr}\ A \pm \sqrt{(\mathrm{Tr}\ A)^2 - 4\mathrm{Det}\ A}}{2}, \tag{4.1.9}$$

that satisfies $Av_\pm = \lambda_\pm v_\pm$ with eigenvectors $v_\pm \in \mathbb{R}$. We can express $G(t)$ as a *Jordan Normal Form* matrix, in the form of $G(t) = Pe^{\Upsilon t}P^{-1}$, where $\Upsilon = \mathrm{diag}[\lambda_+, \lambda_-]$ and $P = [v_+, v_-]$. If the matrix A has complex eigenvalues, $\lambda_\pm = \xi_R \pm i\xi_I$, we find $Av_\pm = (\xi_R + i\xi_I)v_\pm$ with the corresponding complex eigenvector $v_\pm \in \mathbb{C}$. In this setting we consider $G(t) = \mathrm{e}^{\xi_R t}PK(\xi_I t)P^{-1}$, where $P = [\mathrm{Im}(v_+), \mathrm{Re}(v_+)]$ and

$$K(\phi) = \begin{bmatrix} \cos\phi & -\sin\phi \\ \sin\phi & \cos\phi \end{bmatrix}, \qquad P = \begin{bmatrix} 0 & -g \\ \xi_I & \xi_R + 1 \end{bmatrix}. \tag{4.1.10}$$

The components of $G(t)$ are explicitly given in Appendix B1.

4.2 INTERFACE DYNAMICS

Using the results from Chapter 3, we can now construct an extension of the interface dynamics in two-dimensional neural fields with spike frequency adaptation. Here it is convenient to recall the original neural field model with adaptation given in §4.1:

$$u_t(\boldsymbol{x},t) = -u(\boldsymbol{x},t) + \psi(\boldsymbol{x},t) - ga(\boldsymbol{x},t), \tag{4.2.1}$$

$$\tau a_t(\boldsymbol{x},t) = \widetilde{\alpha}u(\boldsymbol{x},t) - a(\boldsymbol{x},t), \tag{4.2.2}$$

where ψ is the non-linear term (second term on the right hand side of equation (4.1.1)). Similar to the case for $g = 0$, the normal velocity along the contour of an active area of synaptic activity for a neural field with adaptation ($g \neq 0$) is given by

$$c_n \equiv \mathbf{n} \cdot \frac{\mathrm{d}}{\mathrm{d}t}\partial\Omega_+ = \frac{y}{|z|}, \tag{4.2.3}$$

where we write $(y,z) = (\partial u(\mathbf{x},t)/\partial t, \nabla_{\mathbf{x}} u(\mathbf{x},t))\,|_{\mathbf{x}=\partial\Omega_+(t)}$. Here

$$y(\mathbf{x},t) = G'_{11}(t)u_0(\mathbf{x}) + G'_{12}(t)a_0(\mathbf{x}) + \frac{\partial}{\partial t}\int_0^t \mathrm{d}t' G_{11}(t')\psi(\mathbf{x},t-t'), \tag{4.2.4}$$

$$z(\mathbf{x},t) = G_{11}(t)\nabla_{\mathbf{x}}u_0(\mathbf{x}) + G_{12}(t)\nabla_{\mathbf{x}}a_0(\mathbf{x}) + \int_0^t \mathrm{d}t' G_{11}(t')\nabla_{\mathbf{x}}\psi(\mathbf{x},t-t'), \tag{4.2.5}$$

with $u_0(\mathbf{x}) = u(\boldsymbol{x},0)$, $\boldsymbol{x} \in \mathbb{R}^2$. To compute the derivative of the non-linear term (third term on the right hand side of (4.2.4)) in terms of line integrals, the key step is to apply Reynolds' transport theorem (two-dimensional Leibnitz rule), namely

$$\frac{\mathrm{d}}{\mathrm{d}t}\int_{\Omega_+} F(\boldsymbol{r},t)\mathrm{d}\boldsymbol{r} = \oint_{\partial\Omega_+} (c_n \cdot \boldsymbol{n})F\,\mathrm{d}s + \int_{\Omega_+} \frac{\partial F(\boldsymbol{r},t)}{\partial t}\,\mathrm{d}\boldsymbol{r}, \tag{4.2.6}$$

where Ω_+ denotes the time dependent excited domain. Using the above information we obtain

$$\frac{\partial}{\partial t}\int_0^t \mathrm{d}t' G_{11}(t')\psi(\mathbf{x}, t-t') \tag{4.2.7}$$

$$= \int_0^t \mathrm{d}t' G_{11}(t')\frac{\partial \psi}{\partial t}(\mathbf{x}, t-t') + G_{11}(t)\psi(\mathbf{x}, 0), \tag{4.2.8}$$

$$= \int_0^t \mathrm{d}t' G_{11}(t') \oint_{\partial\Omega_+(t-t')} \mathrm{d}s w(|\mathbf{x}-\boldsymbol{\gamma}(s,t)|)\frac{\mathrm{d}}{\mathrm{d}t}\boldsymbol{\gamma}(s,t-t')\cdot\mathbf{n}(s,t-t')$$

$$+ G_{11}(t)\psi(\mathbf{x},0).$$

Hence, to evaluate the right hand side of equations (4.2.4) and (4.2.5), it is enough to consider

$$\frac{\partial \psi(\boldsymbol{x},t)}{\partial t} = \oint_{\partial\Omega_+} w(|\boldsymbol{x}-\boldsymbol{\gamma}(s,t)|)\boldsymbol{n}(s,t)\cdot\frac{\mathrm{d}\boldsymbol{\gamma}}{\mathrm{d}t}(s,t)\mathrm{d}s, \tag{4.2.9}$$

$$= \oint_{\partial\Omega_+} w(|\boldsymbol{x}-\boldsymbol{\gamma}(s,t)|)c_n(s,t)\mathrm{d}s, \tag{4.2.10}$$

and

$$\nabla_{\boldsymbol{x}}\psi(\boldsymbol{x},t) = -\oint_{\partial\Omega_+} w(|\boldsymbol{x}-\boldsymbol{\gamma}(s,t)|)\boldsymbol{n}(s,t)\mathrm{d}s, \tag{4.2.11}$$

where $\boldsymbol{\gamma} = \boldsymbol{\gamma}(s,t)$ denotes points on the contour parametrised by s at time t, namely $\boldsymbol{\gamma}(s,t) \in \partial\Omega_+$. Using the above combination we find

$$y(s,t) = \int_0^t \mathrm{d}t'\, G_{11}(t') \oint_{\partial\Omega_+(t-t')} \mathrm{d}s'\, w(|\boldsymbol{\gamma}(s,t)-\boldsymbol{\gamma}(s',t')|)c_n(s',t-t') + y_0(s,t), \tag{4.2.12}$$

$$z(s,t) = -\int_0^t \mathrm{d}t'\, G_{11}(t') \oint_{\partial\Omega_+(t-t')} \mathrm{d}s'\, w(|\boldsymbol{\gamma}(s,t)-\boldsymbol{\gamma}(s',t')|)\boldsymbol{n}(s',t-t') + z_0(s,t), \tag{4.2.13}$$

where

$$y_0(s,t) = \left[G'_{11}(t)u(\boldsymbol{x},0) + G'_{12}(t)a(\boldsymbol{x},0) + G_{11}(t)\psi(\boldsymbol{x},0)\right]\big|_{\boldsymbol{x}=\boldsymbol{\gamma}(s,t)}, \tag{4.2.14}$$

$$z_0(s,t) = \nabla_{\boldsymbol{x}}\left[G_{11}(t)u(\boldsymbol{x},0) + G_{12}(t)a(\boldsymbol{x},0)\right]\big|_{\boldsymbol{x}=\boldsymbol{\gamma}(s,t)}, \tag{4.2.15}$$

$$G'(t) = A\,G(t) \text{ with } G(t=0) = I \text{ (identity matrix)}. \tag{4.2.16}$$

4.3 LOCALISED STATES: LABYRINTHINE STRUCTURES

Recalling the simple neural field with adaptation given by (4.1.1) and (4.1.2), a closed form of the pair (u, a) can be alternatively written by integrating (4.2.1) and (4.2.2) from $-\infty$ to t (and dropping transients):

$$u(\boldsymbol{x}, t) = \int_{-\infty}^{t} \mathrm{d}t' G_{11}(t - t')\psi(\boldsymbol{x}, t'), \tag{4.3.1}$$

$$a(\boldsymbol{x}, t) = \int_{-\infty}^{t} \mathrm{d}t' \mathrm{e}^{-(t-t')} u(\boldsymbol{x}, t). \tag{4.3.2}$$

Here, G_{11} is given in (B1.1), and for a Heaviside firing rate, the non-linear term becomes

$$\psi(\boldsymbol{x}, t) = \int_{\Omega_+(t)} w(\boldsymbol{x} - \boldsymbol{x}')\mathrm{d}\boldsymbol{x}'. \tag{4.3.3}$$

We now consider a mathematically convenient synaptic connectivity of the form

$$w(r) = \sum_{i=1}^{N} \widehat{A}_i K_0(\vartheta_i r), \quad \widehat{A}_i \in \mathbb{R} \text{ and } \sigma_i > 0, \tag{4.3.4}$$

where $K_a(\cdot)$ is the modified Bessel function of the second kind of order a. Here for an appropriate choice of the parameters for A_i and ϑ_i, Mexican hat connectivity can be described as

$$w(r) = \frac{2\varrho}{3\pi}\left(K_0(r) - K_0(2r) - \frac{1}{\gamma}\left(K_0(\beta r) - K_0(2\beta r)\right)\right), \quad \varrho, \gamma, \beta > 0, \tag{4.3.5}$$

as shown in Fig. 4.1. Here γ, ϱ and β are constants.

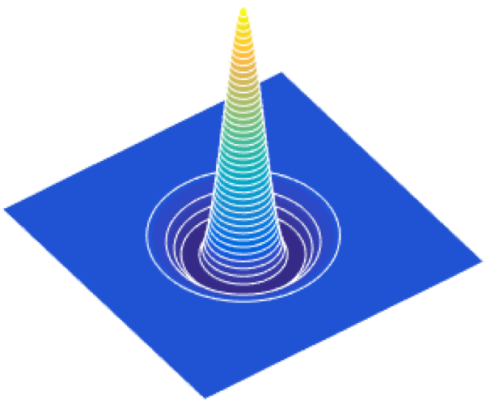

Fig. 4.1: An illustration of Mexican hat connectivity function (4.3.5), describing the interactions among neurons with local excitation and lateral inhibition for $\beta = 0.2$, $\varrho = 1$ and $\gamma = 4$.

The components of normal velocity (4.2.3) can be computed in an identical manner as for the velocity formula we computed for neural field models with no adaptation in Chapter 3. To evaluate the right hand side of (4.2.4) and (4.2.5) in terms of the line integrals, the double integral ψ can be reduced to

$$\psi(\boldsymbol{x},t) = \frac{1}{\vartheta_i}\sum_{i=1}^{N}\widehat{A}_i \oint_{\partial\Omega_+} \mathrm{d}s\boldsymbol{n}(s)\cdot\frac{\boldsymbol{x}-\boldsymbol{\gamma}_c(s)}{|\boldsymbol{x}-\boldsymbol{\gamma}_c(s)|}K_1(\vartheta_i|\boldsymbol{x}-\boldsymbol{\gamma}_c(s)|) + C\frac{2\pi}{\vartheta_i^2}, \tag{4.3.6}$$

where γ_c denotes points on the contour $\partial\Omega_+$. Here $C = 1$ if $x \in \Omega_+$, $C = 0.5$ if $\boldsymbol{x} \in \partial\Omega_+$ and $C = 0$ if $\boldsymbol{x} \in \Omega_-$.

An example of the direct simulation of a localised labyrinthine structure and the evolution of its interface dynamics are shown in Fig. 4.2, where destabilisation to azimuthal instability with a four fold symmetry emerging from an initial spot is observed. Once again compared to the full space-time model for neural dynamics,

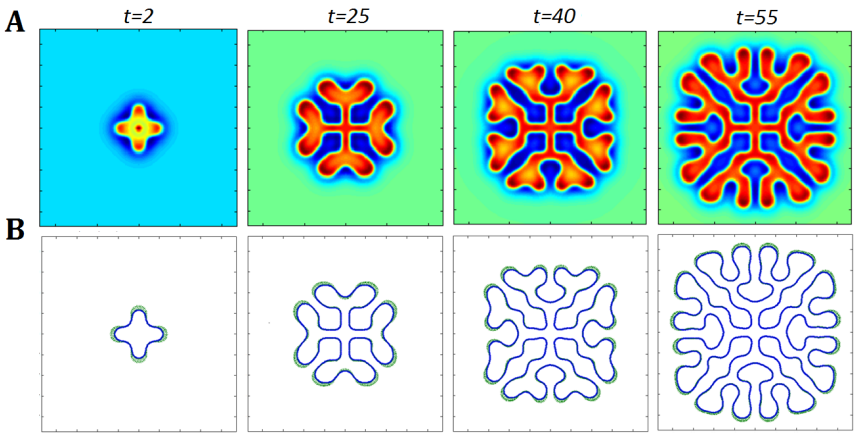

Fig. 4.2: Direct numerical simulations of a spreading labyrinthine structure governed by the space-time model (4.2.1) and (4.2.2) with a Heaviside firing rate and Mexican hat kernel (4.3.5) on a domain of size $[-L,L]\times[-L,L]$ (**A**), and their corresponding interface dynamics (**B**) at fixed times. Parameters are $\widetilde{\alpha} = 1$, $\kappa = 0.003$, $\varrho = 1$, $g = 0.05$, $\tau = 1$, $\gamma = 4$, $\beta = 0.5$, $L = 15\pi$.

the interface description is reduced, yet requires no approximations.

As for the neural fields with no adaptation in Chapter 3, stationary circular spot solutions, which we denote by $U(r)$, can be easily analysed in two-dimensional neu-

ral fields with an adaptation variable, where a spot radius is obtained by replacing κ with $\kappa(1+\widetilde{\alpha}g)$, and ψ is written as

$$U(r)=\frac{\psi(r)}{(1+\widetilde{\alpha}g)},\qquad \psi(r)=\int_0^R\int_0^{2\pi} w(|\boldsymbol{r}-\boldsymbol{r'}|)r'\mathrm{d}\theta\mathrm{d}r', \tag{4.3.7}$$

where $\boldsymbol{r}=(r,\theta)$. Here a saddle-node bifurcation can be found at a critical value of a radius R for a stationary spot, suggesting that $\psi'(R)=0$ $(\mathrm{d}U/\mathrm{d}r=0)$. This also implies the existence of stationary spots under the condition $\kappa<\psi(R)/(1+\widetilde{\alpha}g)$. As in Chapter 3 we can follow the Evans function approach to determine stability. A difference between perturbed and unperturbed spots gives rise to a perturbation $\delta u=\widetilde{u}-u$, with a corresponding change in the radius [11, 76] that we write as $\widetilde{R}=R+\delta R(\theta,t)$. Using (4.3.1), we obtain

$$\delta u=\int_0^t \mathrm{d}t' G_{11}(t')\left\{\sum_{i=1}^N \widehat{A}_i\int_0^{2\pi}\mathrm{d}\theta'\left(\int_0^{\widetilde{R}(\theta',t-t')} K_0(\vartheta_i|\boldsymbol{r}-\boldsymbol{r'}|)r'\mathrm{d}r'\Big|_{\boldsymbol{r}=(\widetilde{R}(\theta,t),\theta)}\right.\right.$$
$$\left.\left.-\int_0^R K_0(\vartheta_i|\boldsymbol{r}-\boldsymbol{r}|)r'\mathrm{d}r'\Big|_{\boldsymbol{r}=(R,\theta)}\right)\right\}, \tag{4.3.8}$$

which reduces to

$$\delta u=\int_0^t \mathrm{d}t' G_{11}(t')\sum_{i=1}^N \widehat{A}_i\int_0^{2\pi}\mathrm{d}\theta'\left\{U'(R)\delta R(\theta,t)+RK_0(\vartheta_i\mathcal{Q}(\theta))\delta R(\theta'-\theta,t-t')\right\}.$$

The equation $\delta u=0$ has a solution in the form $\delta R(\theta,t)=\delta\cos(m\theta)\mathrm{e}^{\lambda_m t}$, leading to the eigenvalue problem

$$\lambda_m=-1+\mathcal{W}_m, \tag{4.3.9}$$

where

$$\mathcal{W}_m=\frac{R}{U'(R)}\sum_{i=1}^N \widehat{A}_i\left\{\int_0^{2\pi}\mathrm{d}\theta\cos(m\theta)K_0(\vartheta_i\mathcal{Q}(\theta))\right\}, \tag{4.3.10}$$

with $\mathcal{Q}(\theta)=R\sqrt{2(1-\cos(\theta))}$. Here, a spot is stable when $\lambda_m<0$ and an m-mode pattern instability is obtained when $\lambda_m>0$. In addition, the mode with $m=1$ is always expected to exist due to rotational invariance (and would give rise to a zero eigenvalue for all parameter values). This agrees with previous results for Mexican hat connectivities on domains where no boundary condition is used, see [11, 76, 107, 142] for further discussions.

4.4 BREATHERS

The inclusion of a linear spike frequency adaptation has a strong effect on the emergence of more exotic patterns, such as breathers. In Fig. 4.3 we show the direct numerical simulations of such a spatially localised periodic oscillation, as well as the evolution of the corresponding interface dynamics. It is worth mentioning that the very slight discrepancy in phases/amplitudes, as seen in Fig. 4.3**C**, should be expected, where the time stepper for the interface is only first order accurate in time, as opposed to the one used for the space-time formulation, which is fourth order. Also the spatial accuracies of the two schemes are different. Linear stability analysis

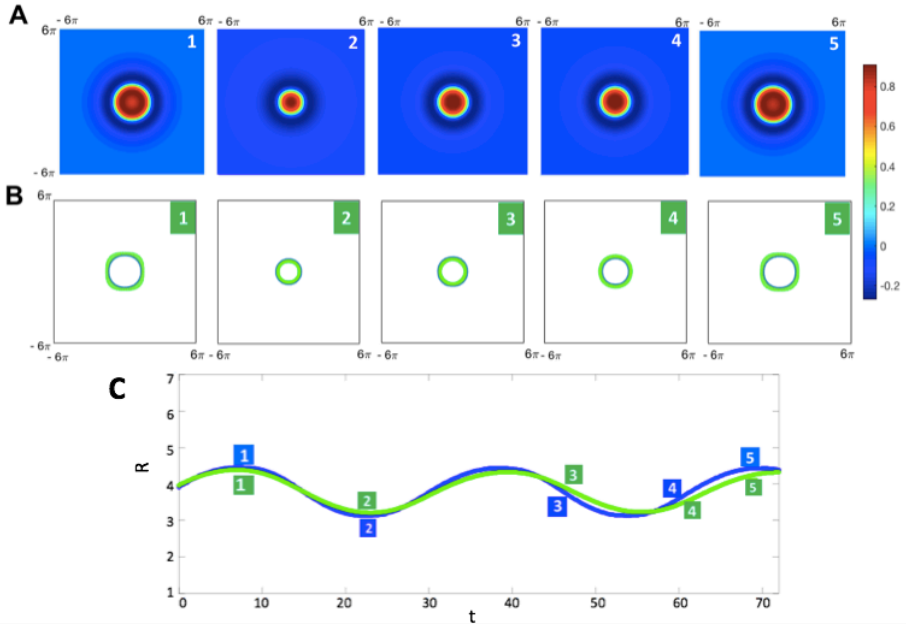

Fig. 4.3: Row (**A**): direct numerical simulation for a breathing instability for the model (4.2.1) and (4.2.2) with Mexican hat kernel (4.3.5) and Heaviside firing non-linearity. Row (**B**): the equivalent evolution using interface (blue line) dynamics due to normal velocity (green arrows) given in equation (4.2.3). Row (**C**) : comparison of radii as a function of time. Parameters are $\widetilde{\alpha} = 0.5$, $\varrho = 5$, $\tau = 5$, $g = 1$, $\gamma = 4$, $\beta = 0.5$, $L = 6\pi$.

of these non-stationary states is performed using an Evans function approach. Here

eigenvalues are determined by the equation $\delta u = 0$ for perturbations in the form $\delta R(\theta, t) = \delta \cos(m\theta) e^{\lambda_m t}$, for which the Evans function $\mathcal{E}_m(\lambda)$ is written as

$$\mathcal{E}_m(\lambda) = \frac{1}{\widetilde{G}_{11}(\lambda)} - (1 + \widetilde{\alpha} g)\mathcal{W}_m = 0, \tag{4.4.1}$$

where $\mathcal{W}_m$ is given in (4.3.10) and $\widetilde{G}_{11}$ denotes the Laplace transform of G_{11} (B1.1), that can be explicitly computed as

$$\widetilde{G}_{11}(\lambda) = \left(\lambda + \frac{1}{\tau}\right) \frac{1}{(\lambda - \lambda_+)(\lambda - \lambda_-)}. \tag{4.4.2}$$

Here a breathing instability can be obtained by considering the $m = 0$ case. Moreover, the eigenvalues for $m = 1$ can be found using $\widetilde{G}_{11}(\lambda) = 1/(1 + \widetilde{\alpha} g)$, where two solutions, from (4.4.2), are determined as $\lambda_1 = 0$ and $\lambda_2 = \widetilde{\alpha} g - 1/\tau$. In this section, breathers are studied in a network of excitation and inhibition using equation (4.3.5); however, they may also arise in a purely excitable system with the inclusion of a localised external input [129]. These oscillatory localised patterns are also supported with a sigmoidal firing rate, the steepness of which has a considerable impact on the existence and stability of breathers. Coombes *et al.* showed that breathers generated with a sigmoidal firing rate have smaller amplitudes compared to ones found using a Heaviside firing rate [12]. Moreover, for a small threshold parameter, a steep sigmoid and a Heaviside non-linearity lead to persistent and vanishing breathers respectively. Although we only focus on an adaptive neural field model with the inclusion of excitatory and inhibitory interactions, there are other metabolic mechanisms which can allow the generation of time periodic and radially symmetric breathers, as well as nonradially symmetric dynamic instabilities. These include threshold accommodation [111], axonal delays [143] and synaptic depression [115]. For a comprehensive review of the dynamics of breathers we refer the reader to [12, 129].

In a very similar fashion to the work described in Chapter 3, it is straightforward to develop a theory of an interface description for these stationary (Fig. 4.2) and non-stationary (Fig. 4.3) localised states in the presence of Dirichlet boundary conditions, and their stability can be similarly determined.

4.5 JACOBIAN OF A LOCALISED SOLUTION (INTERFACE DESCRIPTION) AROUND ITS BOUNDARY

In §4.2, we addressed the stability of circularly symmetric solutions; however, one can also develop a more general approach for an arbitrary closed curve that is not circular. Moreover, we can also incorporate boundary conditions to ensure the smooth decay of localised solutions as well as enforce biophysical constraints. Now we revisit the synaptic activity described by (4.1.7). One way to impose Dirichlet boundary condition is to find the roots of equation $u(\boldsymbol{x},t)|_{\boldsymbol{x}\in\partial\Omega} = 0$. In this context, one can use a Newton-GMRES method (Generalized Minimal Residual) for imposing a Dirichlet boundary condition. This method is particularly useful when an analytical Jacobian is not known in closed form, or is too large to be stored in memory. Since the analytical construction of the Jacobian is awkward (given the intricate dependency of ψ on the vector of unknowns), we pursue this approach here. For this method, the Jacobian acts on a ghost vector (see equation (4.5.1)), leading to a Jacobian-vector product. One of the most striking properties of the Newton-GMRES method is that it does not store or form the elements of the explicit Jacobian. This is particularly convenient for solving large scale systems in terms of performance, storage and accuracy. For further details about Newton-GMRES method, we refer the reader to the Jacobian-Free Newton-Krylov (JFNK) methods overview in [144, 145]. The Jacobian-vector product around a closed contour γ_c can be calculated using a finite difference technique. Evaluating this on the domain boundary $\partial\Omega$ for (4.1.7) we obtain

$$J(\gamma_D;\gamma_c)\widetilde{\gamma} = \left.\frac{u(\gamma_D;\gamma_c+\epsilon\widetilde{\gamma}) - u(\gamma_D;\gamma_c)}{\epsilon}\right|_{\gamma_c=\gamma_c(s,t)}, \tag{4.5.1}$$

where $\widetilde{\gamma} = \widetilde{\gamma}(s,t)$ is a ghost vector on which the Jacobian acts. Here $\gamma_c \in \partial\Omega_+$ and $\gamma_D \in \partial\Omega$. Using a first-order Taylor expansion, an analytical solution of the Jacobian-vector product (independent from ϵ) is given as

$$J(\gamma_D;\gamma_c)\widetilde{\gamma} = -\int_0^t \mathrm{d}t' G_{11}(t-t') \oint_{\partial\Omega_+} \left[\boldsymbol{n}(s)\cdot\widetilde{\gamma}(s) - \widetilde{\boldsymbol{n}}(s)\cdot\boldsymbol{d}(s)\right] \frac{w(|\boldsymbol{d}(s)|)}{|\boldsymbol{d}(s)|} + q(s)\boldsymbol{n}(s)\cdot\frac{\boldsymbol{d}(s)}{|\boldsymbol{d}(s)|^2}\left[\frac{w(|\boldsymbol{d}(s)|}{|\boldsymbol{d}(s)|} - w'(|\boldsymbol{d}(s)|)\right], \tag{4.5.2}$$

where $\boldsymbol{d}(s) = \gamma_D - \gamma_c(s)$ and $q(s) = (\gamma_D - \gamma_c(s))(\gamma_D - \widetilde{\gamma}(s))^T$. Here $\widetilde{\boldsymbol{n}}$ is the normal of the ghost vector $\widetilde{\gamma}$. We will present examples of this theory for the calculation of Jacobian for spiral waves in the next section.

4.6 SPIRAL WAVES

4.6.1 *Biological Background*

Spiral waves are one of the most common stationary (self-sustained) rotating travelling waves that appear in two-dimensional excitable media [16, 62]. They have been observed in a wide range of biological and physical systems, including calcium oscillations in a frog egg during fertilisation [146], reactions in non-linear homogeneous chemical systems [147, 148], spatial dynamics in insect populations [149], ventricular fibrillations in cardiac systems [15, 16]. In the context of the nervous system, they have been clearly seen in Electroencephalography (EEG) recordings in an isolated chicken retina [150] and voltage-sensitive dye imaging of electrical activity in a turtle visual cortex [151]. Since self-sustained activity of the spirals usually overrides and prevents the natural propagation of other cortical waves, long-lasting spirals are usually linked to pathological conditions. For example, spiral waves have been thought to occur during epileptic seizures, where a short episode of a large group of overly synchronised firing of neurons may trigger the emergence of recurrent spiral waves [16, 152]. Rotating spirals have been also reported as pat-

terns of visual hallucinations, where they are experienced as hallucinatory images [62, 153, 154].

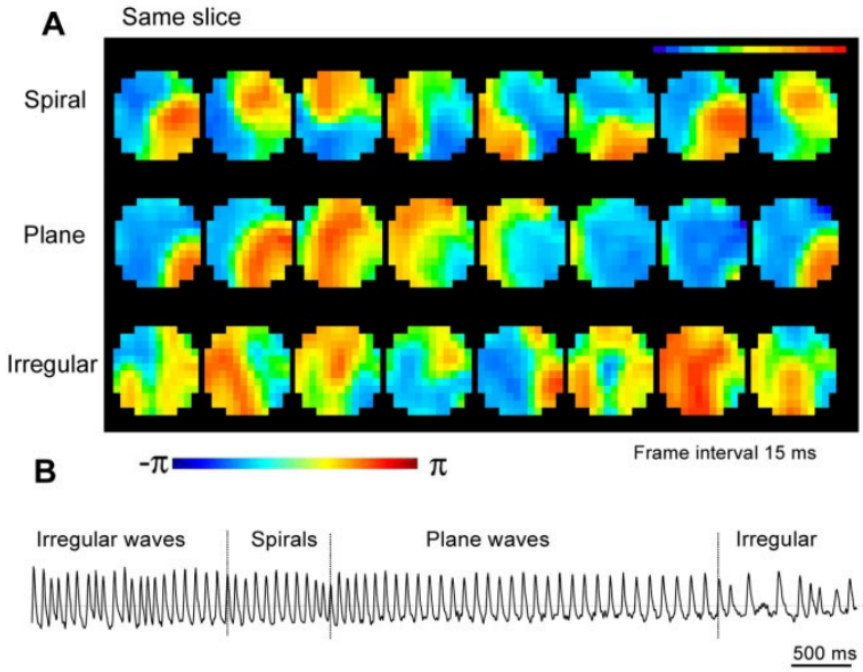

Fig. 4.4: Wave patterns in a tangential slice of a rat neocortex. Panel (**A**): alternation of three different wave patterns: spiral, plane and irregular waves. Panel (**B**): oscillation which shows the wave transition. Image taken from [155].

Although spiral waves have been seen in many systems, they were not observed in a mammalian cortex until a pioneering experiment performed by Huang *et al.* on rodent cortical slices [155]. Figure 4.4 shows the results of Huang *et al.*'s experiments, where the spiral waves alternating between both plane and irregular waves are obtained from the same field of a 500 μm thick tangential slice of a disinhibited cortical layer in a rat neocortex. The activity in Fig. 4.4 is imaged using a voltage-sensitive dye. It is also reasonable to assume that cortical activity induced by spiral waves in an intact brain may differ from that in brain slices: Further work by Huang (2010) has shown the emergence of spirals in an intact mammalian (rat) cortex, where the activity was measured during sleep-like states or during pharmacologically induced oscillations to ensure a purely excitatory state [156]. These two works by Huang *et al.* indicate that the duration and persistence of spiral waves are

shorter for waves in intact brains compared to those in brain slices, albeit with a faster drifting of the spiral core in intact brains. This implies that the cortex might have an internal mechanism to control spiral location and life time in pathological cases [156]. Although all of these findings are interesting, the evolution of spiral waves and their effect on cortical activity has not yet been fully understood.

4.6.2 *Theoretical Background*

From a mathematical point of view, Wiener and Rosenblueth (1946) proposed the first analysis for spiral waves in an excitable cardiac muscle during cardiac arrhythmia (irregular heartbeat) [157]. Almost 15 years later, Anatol Zhabotinsky, known as the father of non-linear chemical dynamics, revisited the seminal work of Boris Belousov, whose attempts on modelling the citric acid (Kreb's) cycle led to the discovery of a new oscillating reaction [158]. Their pioneering work on non-linear chemical dynamics showed the evolution of complex spiral waves, and is named as BZ reaction. Later on, in the 1970s, Winfree published the first systematic mathematical work for spiral wave formation in the BZ reaction [147]. Since then, spiral waves have been primarily found and modelled with modified Fitzhugh Nagumo models [159, 160], Hodgkin Huxley type systems [161, 162], and particularly with reaction-diffusion equations [163–166]. The bifurcation analysis of spiral waves in reaction-diffusion equations on the plane was performed by Sandstede *et al.* [167] and Scheel [168], and the analysis of oscillatory reaction-diffusion equations on a disk was performed by Paullet *et al.* [169], etc. Although all the aforementioned models have been used to observe a wide range of spiral dynamics, e.g. spiral breakup [159], meandering [170] and drifting spirals [165, 171], the only mathematical work which has been performed to understand the theory behind the structure of spirals in planar neural fields is that of Laing [16, 95].

4.6.3 *The PDE Model*

In this section, we revisit the work of Laing [16], where the neural fields with a particular choice of synaptic kernel can be expressed in terms of a system of partial differential equations (PDEs) [16, 17]. Formally, if the Fourier transform of the synaptic kernel $F[w](s)$ is a rational function of a transform variable s, the convolution structure in equation (4.1.1) can be transformed into a PDE. Reproducing Laing's [16] results, an example of a spiral wave in a non-local continuum planar model, (4.1.1) and (4.1.2), with a smooth sigmoidal firing rate function is shown in Fig. 4.6. Here, a non-negative and decaying connectivity function, for which the system of equations (4.2.1) and (4.2.2) can be rearranged in terms of Fourier transforms [16], is

$$w(r) = \int_0^\infty \frac{\zeta s J_0(rs)\mathrm{d}s}{s^4 + \ell_1 s^2 + \ell_2}, \tag{4.6.1}$$

where J_0 denotes the modified Bessel function of the first kind of order zero, and ζ is a scaling parameter. A sigmoidal firing rate function is chosen as

$$f(u) = \frac{1}{1 + e^{-\mu(u-\kappa)}}, \tag{4.6.2}$$

where $\mu > 0$ is the steepness parameter and κ is the activity threshold.

Here the kernel in equation (4.6.1) can be exploited for transforming the non-local continuum model (4.1.1) and (4.1.2) into an equivalent system of fourth order PDEs, allowing the use of computationally inexpensive and well developed algorithms. We refer reader to [16, 17, 113, 127] for further discussion on numerical methods for PDEs. An image of a purely excitatory kernel is depicted in Fig. 4.5.

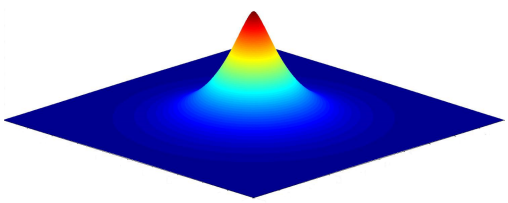

Fig. 4.5: A plot of a purely excitatory kernel. Synaptic interactions are only positive for all range distance.

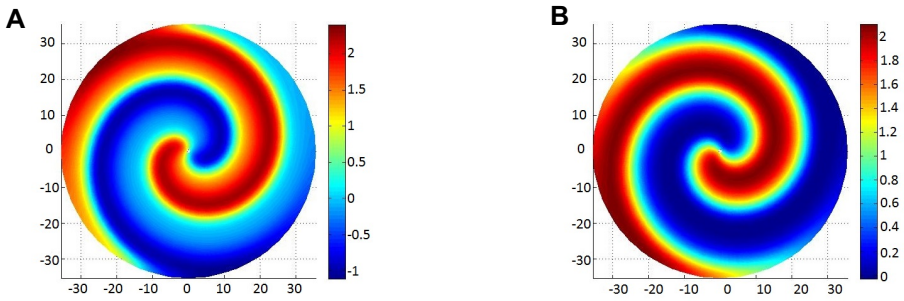

Fig. 4.6: A snapshot of the direct numerical simulations of synaptic activity u (**A**) and recovery variable a (**B**) with a monotonically decaying positive kernel (4.6.1) on a domain of radius $R = 35$. Rigidly rotating spiral waves are obtained in the clockwise direction. Red and blue regions represent excited and quiescent states, respectively. Parameters are $\widetilde{\alpha} = 1.7$, $\zeta = 3.5$, $\ell_1 = 1$, $\ell_2 = 1$, $\mu = 20$, $\tau = 5$, $\kappa = 0.2$, at time= 300 with a Neumann boundary condition. Reproduced from [16] using a smooth sigmoidal firing rate (4.6.2) .

Here we aim to simulate dynamics of spiral waves using a continuum neural field model [155]. Initial conditions for spiral waves are chosen in polar coordinates in the form

$$u(r,\theta,0) = \begin{cases} 1, & \text{if } \theta \in [0,\pi] \\ 0, & \text{otherwise} \end{cases},$$

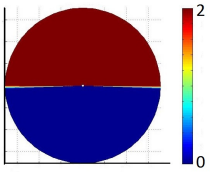

$$a(r,\theta,0) = \begin{cases} 1, & \text{if } \theta \in \left[\frac{\pi}{2},\frac{3\pi}{2}\right] \\ 0, & \text{otherwise} \end{cases},$$

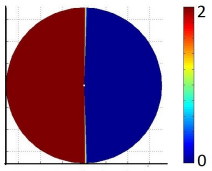

where red and blue regions represent the excited and quiescent states, respectively. As seen, we initiate the simulations in such a way that the top half of the synaptic drive and left half of the adaptation are excited. There are two particular reasons for considering initial conditions in this form. First, we believe that there should be a delay between the activity of the neuron population and negative feedback in a real

tissue. This may arise because neurons are exposed to high dynamical activity just before the adaptation variable recovers them back to their resting states. Second, the initial conditions chosen above may reduce computational effort in the case that spiral wave rotates in the clockwise direction (as in our case). Note that the effect of coupled excitatory neurons is much greater than the effect of inhibitory neurons, so inhibition is assumed to be blocked (as in the experiments performed by Huang *et al.* [155]). This can be also seen in the model, in which variable a is not an inhibitory activity so there is no convolution term for equation (4.1.2), and τ decelerates the effect of the recovery variable a. Spiral wave patterns observed here and by Laing [16] using equations (4.1.1) and (4.1.2) are consistent with the spiral waves obtained in experiments conducted by Huang *et al.* [155].

A two-dimensional Fourier transform, $F[\cdot]$, is applied to both sides of equation (4.1.1)

$$F[u_t + u + g\ a](s) = F[w](s)F[f(u)](s), \tag{4.6.3}$$

where

$$F[w](s) = \frac{\zeta}{s^4 + \ell_1 s^2 + \ell_2}. \tag{4.6.4}$$

The spatial Fourier transforms of $u''(x)$ and $u''''(x)$ are $-s^2F[u]$ and $s^4F[u]$, respectively. Here primes represent derivatives in spatial coordinates. Plugging these expressions into equation (4.6.3) and taking the inverse Fourier transform, we obtain a PDE system of the form

$$\left[\bigtriangledown^4 - \ell_1 \bigtriangledown^2 + \ell_2\right]\left(\frac{\partial u(\boldsymbol{x},t)}{\partial t} + u(\boldsymbol{x},t) + g\ a(\boldsymbol{x},t)\right) = \zeta f(u(\boldsymbol{x},t)), \tag{4.6.5}$$

$$\tau\frac{\partial a(\boldsymbol{x},t)}{\partial t} = \widetilde{\alpha}u(\boldsymbol{x},t) - a(\boldsymbol{x},t). \tag{4.6.6}$$

We transform the above equations into polar coordinates using a standard change of coordinates $\boldsymbol{x} = (r\cos\theta, r\sin\theta)$. The domain for a spiral wave is taken to be a disk D of radius R with a Neumann boundary condition in Laing [16], see Fig. 4.6. However, we choose boundary conditions:

$$u(R,\theta,t) = \left.\frac{\partial^2 u(r,\theta,t)}{\partial^2 r^2}\right|_{r=R} = 0, \tag{4.6.7}$$

leading to a closed pattern. In practice, the adaptation variable a can be written as a function of u, and is also subject to a boundary condition of the form (4.6.7) for all θ and t. As a side note, equations (4.1.1) and (4.6.5) are equivalent.

Snapshots for two examples of constantly rotating spiral waves with a steep sigmoidal firing rate can be seen in Fig. 4.7 and Fig. 4.8. Figure 4.8 is also an example of Archimedean spiral where the distance between successive parallel turns are constant and ≈ 0.49. As mentioned earlier, the parameters κ, τ, $\widetilde{\alpha}$, and μ repre-

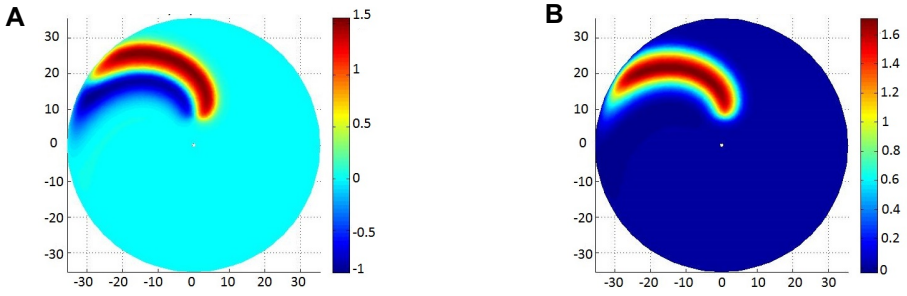

Fig. 4.7: Direct numerical simulations of two representative spiral fingers for the synaptic drive u (**A**) and adaptation variable a (**B**), governed by the model (4.6.5) and (4.6.6) with a very steep sigmoidal firing rate (4.6.2). Red and blue parts denote active and passive states respectively. Parameters are $\widetilde{\alpha} = 2.8,\ \zeta = 10.5,\ \tau = 7,\ \kappa = 0.5,\ , \mu = 200,\ R = 35$ at time$= 300$.

sent threshold for the synaptic activity, time constant for the adaptation, adaptation strength, and steepness parameter of the firing rate function, respectively. These parameters are related in a certain sense that increasing connectivity parameter ζ or time constant τ corresponds to decreasing $\widetilde{\alpha}$. The domain becomes completely active (excited) with large values of ζ, and small values of $\widetilde{\alpha}$ and κ, whereas the domain becomes fully passive (quiescent) for small values of ζ, and large values of $\widetilde{\alpha}$ and κ. Varying κ is associated with wave density of the active region. With the exception of Fig. 4.6 which is recovered from [16], all figures are created with the very steep sigmoidal firing rate that mimics the Heaviside firing rate non-linearity.

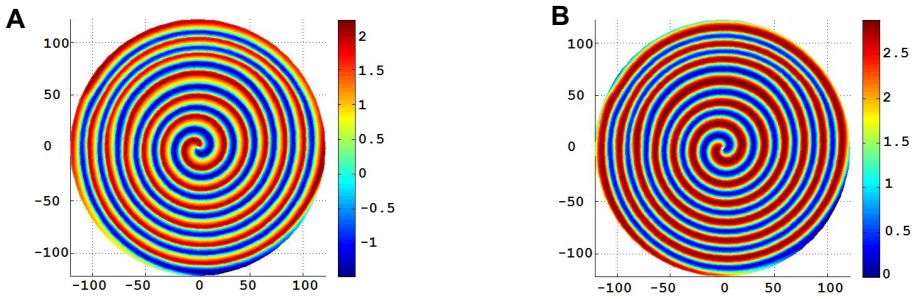

Fig. 4.8: Direct numerical simulations of the synaptic drive u (**A**) and adaptation variable a (**B**) governed by the model (4.6.5) and (4.6.6) with a steep sigmoidal firing rate for a large domain of radius R. Parameters are $\widetilde{\alpha} = 3.7,\ \ell_1 = 5,\ \ell_2 = 4,\ \zeta = 14.4,\ \tau = 8,\ \mu = 200,\ \kappa = 0.25,\ R = 120$ at time $= 150$.

Once a rigidly rotating spiral wave is obtained, we can observe transitions into meandering motion, or spiral break-up under a suitable choice of the parameters and initial conditions, as seen in Fig. 4.9. In Figure 4.9, parameter variation is used to monitor the behaviour of an one -armed spiral, allowing the formation of rigidly rotating spiral (**A**), meandering spiral (**B**) and spiral break-ups (**C**). Rigid rotation refers to the preservation of the spiral shape as it rotates, that is the tip traces out a circle. Meandering spirals are distinguished from stationary spirals by their more complicated tip motion. The shape and core location of a one-armed spiral may change with time when it meanders. This leads to a non-stationary spiral in a co-rotating frame, as in Fig. 4.9**B**. Quasi periodic tip motion of the inwardly and outwardly meandering spirals leads to a very interesting flower-like patterns. For further discussions, we refer the reader to [172, 173] where Barkley and Winfree present their "flower gardens". One should also be aware that a meandering spiral is different from a drifting spiral. Meandering emerges in unperturbed systems whereas drifting results from symmetry breaking perturbations [14]. Spiral break-ups in Fig. 4.9**C** arise from counter rotating spirals, where the wave trains collide and give rise to the emergence of other spiral cores. Note that the synaptic drive

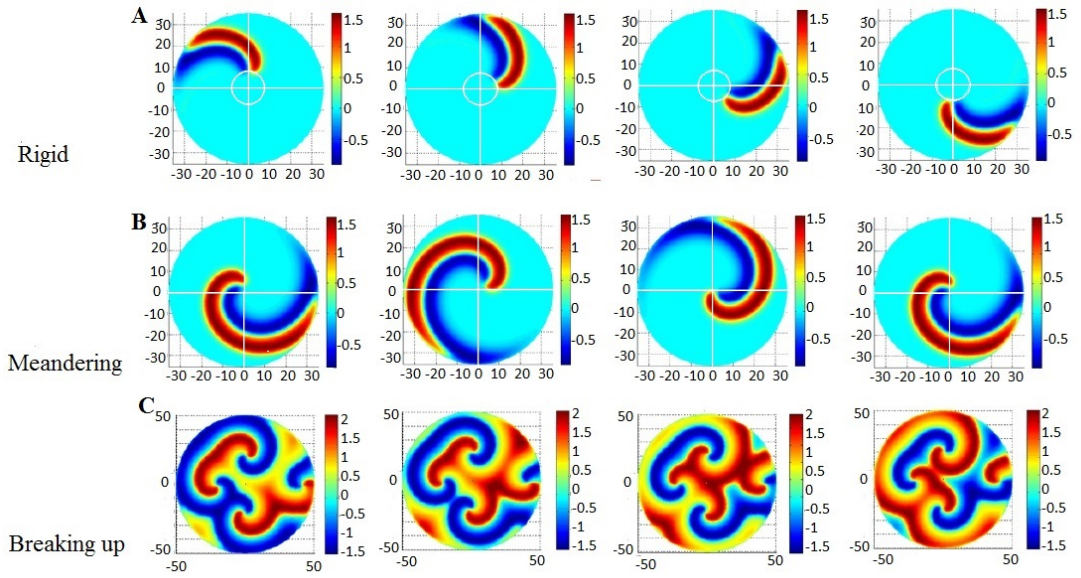

Fig. 4.9: Direct numerical simulations of various spirals waves are shown every 10 time units (after transients), governed by the model (4.6.5) an (4.6.6) with a steep sigmoid firing rate. Panel (**A**): a rigidly rotating spiral wave, where its core tracing out a circle, is shown with parameters $\widetilde{\alpha} = 2.8,\ \zeta = 10.5,\ \tau = 7,\ \kappa = 0.5,\ R = 35$. Panel (**B**): spiral wave, rigidly rotating with $\widetilde{\alpha} = 2.8$, is replaced by meandering motion for $\widetilde{\alpha} = 2.5$. Panel (**C**): spiral break-up are seen with parameters $\widetilde{\alpha} = 3.8,\ \mu = 200,\ \zeta = 14.4,\ \tau = 8,\ \kappa = 0.25,\ R = 50$.

with active 1st and 3rd quadrants, and adaptation with 2nd and 4th have been used to initiate spiral break-up.

4.6.4 *Stability*

The stability of spiral waves has been treated by several authors, and see [16] for an overview. Consider the evolution equations (4.6.5) and (4.6.6) in a rotating frame

$$-\omega\frac{\partial u}{\partial\theta} = -u + \mathcal{L}^{-1}f(u) - ga, \tag{4.6.8}$$

$$-\omega\frac{\partial a}{\partial\theta} = \frac{\widetilde{\alpha}}{\tau}u - \frac{1}{\tau}a, \tag{4.6.9}$$

where $u(r,\theta,t) = u(r,\theta-\omega t)$ with a rotation speed ω. Here $\mathcal{L}$ is the linear operator and f is the firing rate function. The eigenvalues λ for stability is constructed according to the eigenvalue problem

$$\mathrm{J}(u)\cdot \mathrm{v} = \lambda\cdot \mathrm{v}, \tag{4.6.10}$$

where the Jacobian for a spiral solution is

$$\mathrm{J}(u) = \begin{bmatrix} \omega\dfrac{\partial}{\partial\theta} - I + \mathcal{L}^{-1}f'(u) & -gI \\ \dfrac{\widetilde{\alpha}I}{\tau} & \omega\dfrac{\partial}{\partial\theta} - \dfrac{I}{\tau} \end{bmatrix}. \tag{4.6.11}$$

Here $\mathrm{v} = (\partial u/\partial\theta, \partial a/\partial\theta)$ denotes a non-zero eigenvector and f' is the derivative of the firing rate function, that is $f'(u) = \mu f(u)(1-f(u))$ for a firing rate given in the form of (4.6.2). The family of the spiral solutions can be found by first writing equation (4.6.9) in terms of u, that is

$$\left(I - \omega\tau\frac{\partial}{\partial\theta}\right)a(r,\theta,t) = \widetilde{\alpha}u(r,\theta,t), \tag{4.6.12}$$

then plugging this into equation (4.6.8), we write

$$0 = \mathcal{L}\left(\widetilde{\alpha}g\left(I - \omega\tau\frac{\partial}{\partial\theta}\right)^{-1}u + I - \omega\frac{\partial}{\partial\theta}\right) - f(u). \tag{4.6.13}$$

The rotation speed ω in (4.6.13) is treated as another unknown. To find the pair (u,ω) in the above equation, we consider an extra condition which pins the phase

of the spiral. The pinning condition is chosen such that the average of u (over θ) at $r = R/2$ (where R is the radius of the domain) is equal to the value of u at a fixed point on the circle. The rotation speed ω as a function of $\widetilde{\alpha}$ and ζ are shown in Fig. 4.10 for a smooth sigmoidal firing rate. Here the solutions of (4.6.8) and (4.6.9) as well as corresponding eigenvalues at three points marked in Fig. 4.10**A** are shown in Fig. 4.11.

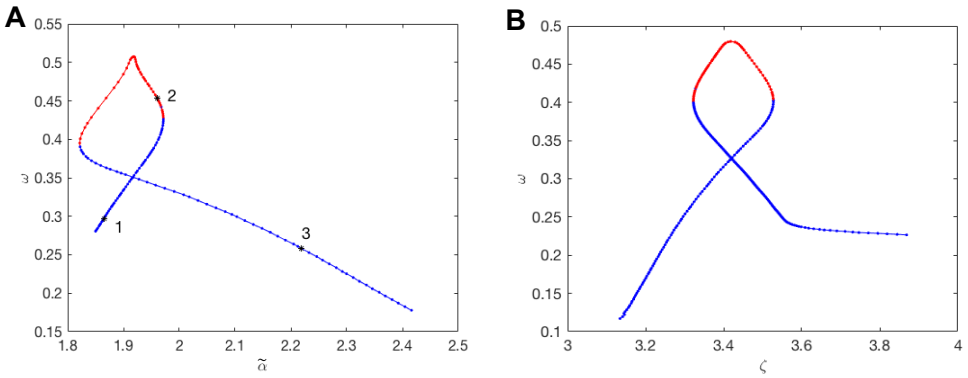

Fig. 4.10: Rotational speed ω is plotted as a function of parameters $\widetilde{\alpha}$ (**A**), and ζ (**B**) for the model (4.6.8) and (4.6.9) with synaptic kernel (4.6.1) and smooth sigmoidal firing rate (4.6.2) . Blue regions are stable solutions, while red ones indicate unstable. Parameters are $\zeta = 3.5$, $\kappa = 0.6$ (**A**), $\widetilde{\alpha} = 2$, $\kappa = 0.6$ (**B**), with $\mu = 20,\ \tau = 3,\ \ell_1 = 1,\ \ell_2 = 1,\ R = 35$. Recalculated from [10].

Similarly, the rotation speed ω as a function of $\widetilde{\alpha}$ and ζ are shown in Fig. 4.12 for a system with a steep sigmoidal firing rate. Here the solutions of (4.6.8) and (4.6.9) as well as the corresponding eigenvalues at three points marked in Fig. 4.12**A** are shown in Fig. 4.13. It is worth mentioning that the qualitative similarities between Amari models and those with a steep sigmoidal firing rate are well known [127].

Here we have performed the numerical continuation analysis of spiral waves using neural fields with a smooth as well as steep sigmoidal firing rate and determined their stabilities under parameter variation. Since the model with a steep sigmoidal firing rate function shows qualitatively similar behaviour to a Heaviside firing rate function, this may open up the possibility of studying numerical continuation using

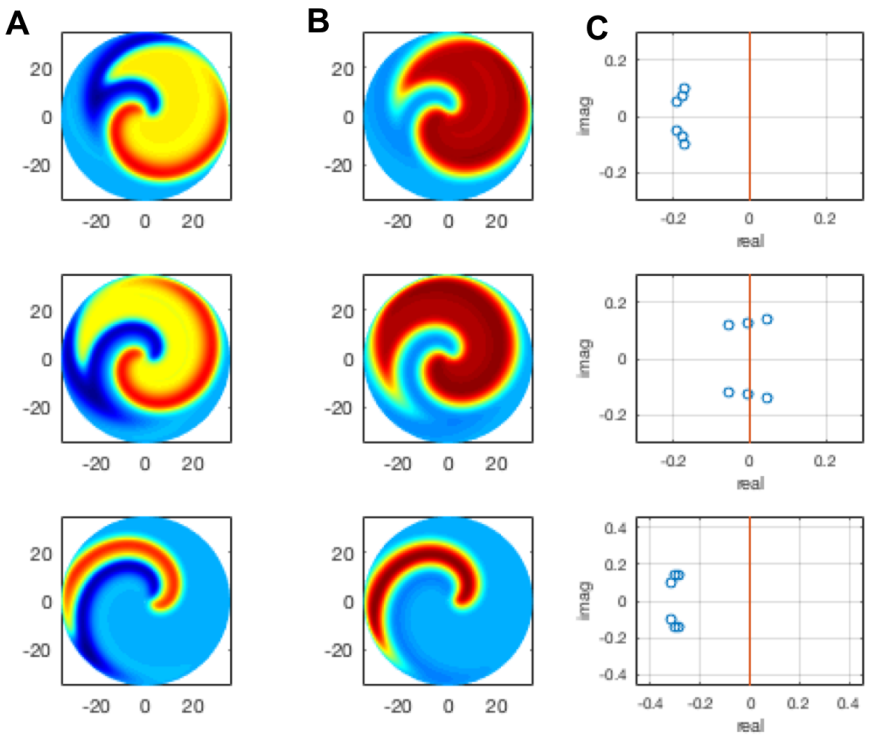

Fig. 4.11: The solutions for synaptic activity u (column **A**), adaptation a (column **B**) and the twelve eigenvalues (column **C**) with non-zero smallest magnitudes are shown for the stability of a spiral at points marked as 1, 2 and 3 in Fig. 4.10**A**.

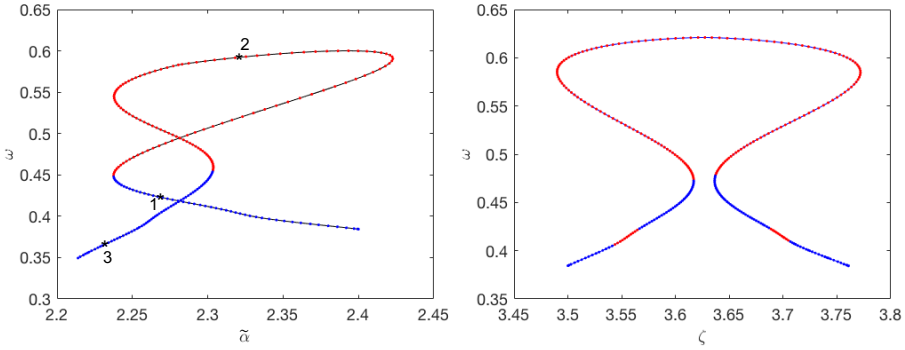

Fig. 4.12: Rotational speed ω is plotted as a function of parameters $\widetilde{\alpha}$ (**A**) and ζ (**B**) for the model (4.6.8) and (4.6.9) with synaptic kernel (4.6.1) and steep sigmoidal firing rate (4.6.2). Blue regions are stable solutions, while red ones indicate unstable. Parameters are $\zeta = 10.5$, $\kappa = 0.4$ (**A**), $\widetilde{\alpha} = 2.4$, $\kappa = 0.4$ (**B**), with $\mu = 60$, $\tau = 3, \ell_1 = 5$, $\ell_2 = 4$, $R = 35$.

one-dimensional interface dynamics. Note that the synaptic kernel (4.6.1) can be rewritten in terms of a linear combination of zeroth order modified Bessel functions of the second kind using the Hankel transform. For example, for a particular choice of $\ell_1 = 5$ and $\ell_2 = 4$,

$$w(r) = \zeta \left(\int_0^\infty \frac{sJ_0(rs)\mathrm{d}s}{s^2+1} - \int_0^\infty \frac{sJ_0(rs)\mathrm{d}s}{s^2+4} \right), \tag{4.6.14}$$

$$= \frac{\zeta}{6\pi} \left(K_0(r) - K_0(2r) \right). \tag{4.6.15}$$

Hence the line integral representation of the non-linear term ψ is given as

$$\psi(\gamma_c(s,t);t) = -\frac{\zeta}{6\pi} \oint_{\partial\Omega_+(t)} \mathbf{n}(s') \cdot \mathcal{A}(s,s')\mathrm{d}s', \tag{4.6.16}$$

where

$$\mathcal{A}(s,s') = \frac{\gamma_c(s) - \gamma_c(s')}{|\,\gamma_c(s) - \gamma_c(s')\,|} \left[K_1(|\,\gamma_c(s) - \gamma_c(s')\,|) - \frac{1}{2} K_1(2\,|\,\gamma_c(s) - \gamma_c(s')\,|) \right],$$

and $\gamma_c \in \partial\Omega_+$. An application of the theory from §4.5, where we determined the linearisation of a steady state around an arbitrary contour, can be made to the spiral waves. In Figure 4.14, the numerical (4.5.1) and theoretical (4.5.2) results for the Jacobian are compared. Fig. 4.14**A** and Fig. 4.14**B** show that there is an

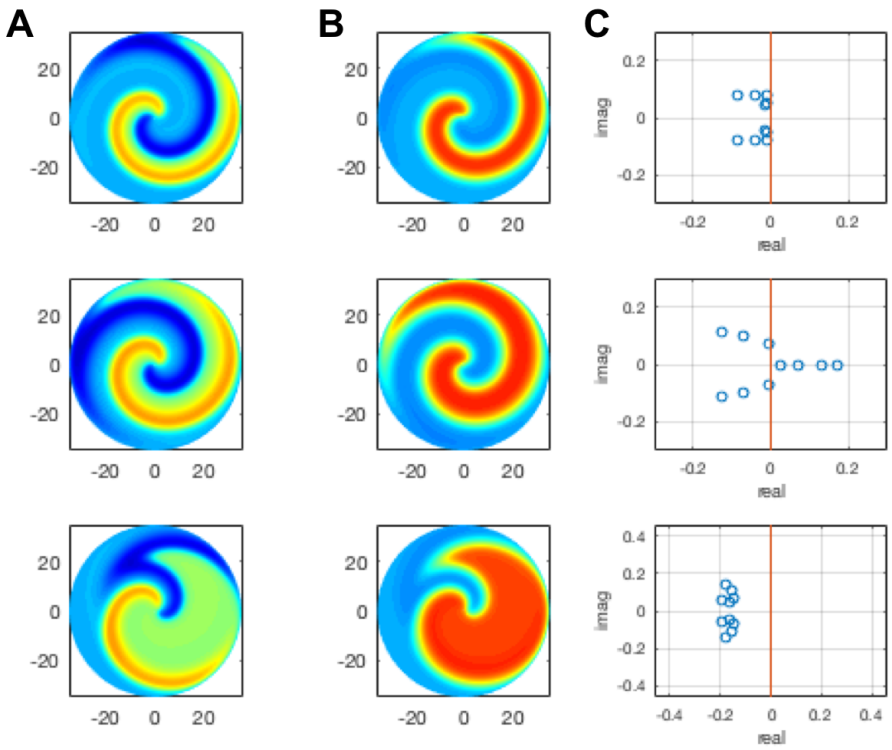

Fig. 4.13: The solutions for synaptic activity u (column **A**), adaptation a (column **B**) and the twelve eigenvalues (column **C**) with non-zero smallest magnitudes are shown for the stability of a spiral at points marked as 1, 2 and 3 in Fig. 4.12**A**.

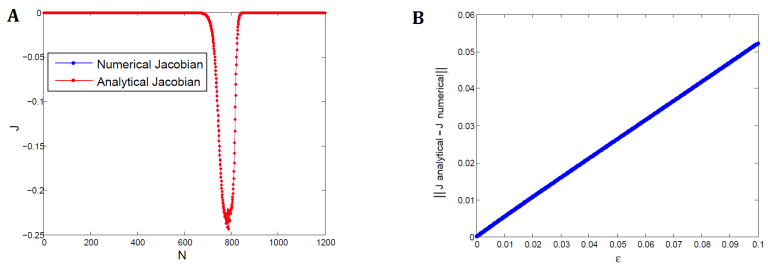

Fig. 4.14: A comparison of the results from numerical (4.5.1) and theoretical (4.5.2) Jacobian (**A**) for a spiral wave, and 2-norm of these quantities as a function of a small ϵ (**B**).

excellent agreement between the numerical and theoretical Jacobian. This suggests that a computationally efficient spectral analysis for the interface dynamics can be developed as opposed to a standard large matrix stability calculation.

4.7 NUMERICAL SCHEME

We discretise the domain in polar coordinates using 160 points in the angular direction and 80 points in the radial direction. The Laplacian matrix, $\mathbf{M}= \left[\nabla^4 - \ell_1\nabla^2 + \ell_2\right]$ in equation (4.6.5), is obtained using a Kronecker tensor product [174], and evaluated in a sparse form, by which only non-zero elements and their position is stored in the system. In this setting the Laplacian formula in polar coordinates is explicitly constructed using

$$\nabla^2 = \boldsymbol{D}_{rr} \otimes \boldsymbol{I}_\theta + \frac{1}{\boldsymbol{R}}\boldsymbol{D}_r \otimes \boldsymbol{I}_\theta + \frac{1}{\boldsymbol{R}^2} \otimes \boldsymbol{D}_{\theta\theta}, \tag{4.7.1}$$

where $\boldsymbol{R} = \mathrm{diag}(r)$. Here $\boldsymbol{D}_{\theta\theta}$, $\boldsymbol{D}_r$ and $\boldsymbol{D}_{rr}$ denote spatial derivatives that are computed using finite difference methods in the r and θ direction, and $\boldsymbol{I}_\theta$ denotes an identity matrix in the θ direction. Here the system of differential equations in (4.6.5) and (4.6.6) is solved in terms of a Mass matrix ($\mathbf{M}$) in the form of $\mathbf{M}\dot{u} = F(u)$, instead of $\dot{u} = \mathbf{M}^{-1}F(u)$, to avoid the computation of matrix inverse ($\mathbf{M}^{-1}$). The numerical continuation of (4.6.13) as parameters are varied, shown in Fig. 4.10 and Fig. 4.12, can be performed using a secant continuation code with MATLAB's *fsolve* function [131]. Since the system of equations for dimensionally reduced interface dynamics is restricted to the case of Heaviside firing rate function, we show the evolution of spiral waves using a very steep sigmoidal firing rate mimicking such non-linearities. However, it is worth mentioning that decreasing the steepness parameter μ in the sigmoidal firing rate (4.6.2) substantially increases the computation speed. Owing to the memory constraints, the numerical code for a rigidly rotating spiral wave is run for a 40-50 time units after it is initiated, then final state is saved and used as an initial condition for the following 40-50 time units, and this

process is repeated. The numerical scheme for interface dynamics of labyrinthine structures and breathers for a neural field model with adaptation was developed in Chapter 3. Once more, we present here the implementation used in our numerical experiments, which were found to be in excellent agreement with the full spatio-temporal simulation.

4.8 CONCLUSION & DISCUSSION

In this Chapter we have shown that the addition of an adaptation variable to a neural field model not only supports the emergence of spreading localised structures, e.g. labyrinths, but also allows the generation of breathers and travelling waves, e.g. spirals. Coombes *et al.* [11] developed an interface description for two-dimensional neural field with no adaptation in unbounded domains, and discussed how the model in the presence of adaptation could support a range of localised states, travelling waves as well as breathers. However, they did not developed an equivalent interface description of these models with adaptation. In this Chapter, we developed a theory for interface dynamics for neural fields with adaptation on a domain without boundary conditions, and showed that they are in an excellent numerical agreement with direct numerical simulations for labyrinthine structures and breathers. We also employed the numerical continuation of spiral waves in the PDE form of the neural field equation with a smooth as well as steep sigmoidal firing rate, and their stabilities were determined under parameters variation. Since the model with a very steep sigmoidal firing rate exhibits qualitatively similar behaviour to one with a Heaviside firing rate, it would be nice to develop the numerical continuation techniques that merges the stability and the interface approach in a single computational framework. Note that boundary conditions are known to have a strong impact on the evolution of spiral waves [16, 175]. In this

Chapter, we presented all the ingredients for treating continuation directly from interface framework with an imposed Dirichlet boundary condition.

Regarding the imposition of boundary conditions ($u(\boldsymbol{x},t)|_{\boldsymbol{x}\in\partial\Omega} = 0$) as in Chapter 3, here the influence of different paths, that connect points on the contour to points on the domain boundary, could also be explored. For a spiral solution using Newton-GMRES iterative method, Figure 4.15 shows two trials regarding different distribution of points on the disk.

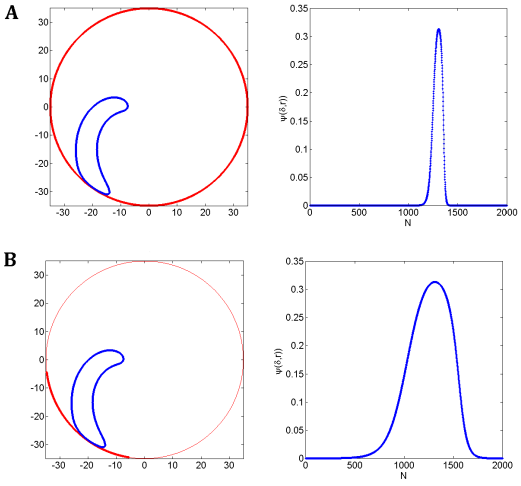

Fig. 4.15: The first column shows a spiral contour (blue) and two different distributions for points (red) along the disk, with Dirichlet boundary conditions. The evaluation of the non-linear term ψ for each case is shown in the second column. Here $N = 570$ with uniformly distributed points.

As seen in Fig. 4.15**A**, apart from a small region, the synaptic activity on the disk boundary is near zero, implying that most of the equations in the system are linearly dependent. To avoid this ill-conditioning, the equations can be chosen from the region where the boundary conditions are violated most, as seen in Fig. 4.15**B**. With this choice, Fig. 4.16 shows that Newton-GMRES method is very efficient for solving very large number of equations in a few iterations.

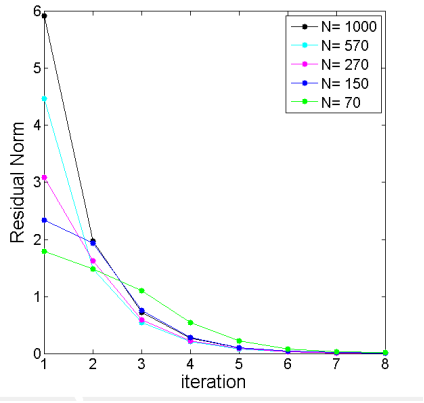

Fig. 4.16: Minimal norm residual computed for different number of points along contour to solve $\psi(\delta;\gamma) = 0$ for boundary conditions. N represents the number of points along the disk.

However, a related point to consider is that root finding of the system may converge to a solution that is away from the level-set (on the boundary of the active region). Therefore, in addition to boundary conditions, one should consider the level-set condition as a constraint to the Newton- GMRES algorithm to find a solution of a spiral wave which respects the Dirichlet boundary condition.

In this Chapter we have also investigated various parameter sets and initial conditions to compute rigidly rotating spirals, as well as meandering spiral waves and spiral break-ups. Due to their changing tip motion, meandering spirals are analytically much more complicated than rigidly rotating spirals. Barkley has used an efficient theoretical approach to determine bifurcation theory for quasi-periodic dynamics of meandering spirals in reaction-diffusion systems, where phase diagrams or a so-called *bifurcation loci* are classified depending on inward-pointing and outward-pointing petals for meandering spiral tip motion [170]. As we have shown that neural field model with an adaptation allows the generation of meandering spirals, a possible extension of this work is to further investigate the existence of meandering spirals, as well as their bifurcation theory in a neural field framework. In addition we only concentrate on an uniform medium but a real tissue is highly heterogeneous, and may lead to spatially drifting spiral waves. Such spiral waves were previously observed in a heart tissue and modelled using reaction diffusion systems [165, 171]. Thus, a neural field model with an inclusion of a symmetry breaking perturbation in the non-uniform media might be another possible route

to analyse drifting motion of spiral waves. Note that this will arise naturally in a model when w is not radially symmetric, namely $w(|\boldsymbol{x}-\boldsymbol{x}'|) \to w(\boldsymbol{x},\boldsymbol{x}')$. Recent research has shown that there may be distinctive differences between flat planar and folded cortex for travelling waves [176]. The structure of the cerebral cortex is highly wrinkled so that more complex and realistic geometries are needed. Since cortical folding is important for changing the structural and functional capacity of the cortex, it also presumably plays a crucial role in describing the dynamics of spirals. The interface description can be amended to higher dimensions. Thus, another possible extension is to analyse the evolution of spiral waves as well as the corresponding interface dynamics on a sphere or more general and realistic geometries. More discussion on neural field models in general geometries will be given in Chapter 6.

5

ORIENTATION BUMPS AND STRIPES IN A COUPLED RING MODEL

In the previous Chapters we mainly discussed the evolution of spatially localised solutions and travelling waves in two-dimensional neural field models. We also showed how a small perturbation at the boundary (at a threshold crossing) or at all values (rather than just at the threshold crossings) can destabilise these solutions, see sections 3.2 and 4.3. The models supporting these solutions, such as (2.3.1), are assumed to be spatially homogeneous and thus the system of integro-differential equations is translationally invariant. This is reflected by the fact that the synaptic kernel w in standard neural field models is chosen based on the Euclidean distance between interacting neurons, namely $w(\boldsymbol{x}|\boldsymbol{x}') = w(|\boldsymbol{x} - \boldsymbol{x}'|)$. However, from the anatomical point of view, the micro-structure of the cortex is far from homogeneous [92, 177].

The visual areas of the cortex comprise almost two third of the brain, and the primary visual cortex (V1), where cortical maps are found, is the most studied of these visual processing areas. Cortical maps are associated with specific visual features in V1, where cells in adjacent locations (in V1) have similar orientation preference [178–180]. Therefore a straightforward implication of feature maps is to consider interactions between post-synaptic and pre-synaptic neurons by a more general function, that is $w(\boldsymbol{x}, \boldsymbol{x}') = w(|\boldsymbol{x} - \boldsymbol{x}'|)J(\theta(\boldsymbol{x}) - \theta(\boldsymbol{x}'))$ [18]. Here the angular compo-

nent $\theta(\boldsymbol{x})$ represents an orientation preference. One challenge in this approach is that the orientation preference map has a non-trivial dependence on position [181]. An alternative way is to replace the position $\boldsymbol{x}$ by the pair $(\boldsymbol{x}, \theta)$, suggesting that the hypercolumn is labelled at position x and the orientation preference of neurons within the hypercolumn is labelled by θ [92]. Thus the activity component in a neural field model can be replaced by $u(\boldsymbol{x}, \theta, t)$ with a generic weight function in the form of $w(\boldsymbol{x}|\boldsymbol{x}') = w(\boldsymbol{x}, \theta, \boldsymbol{x}', \theta')$. This mathematical approach has motivated the development of several recent studies on the primary visual cortex (V1), such as [18, 91, 92, 106, 182], where spatial heterogeneities in neural fields were analysed.

From the pioneering work of Mountcastle [2] (see §2.1.3 in Chapter 2), we know that the cortex is organised in a columnar structure; arranged in sheets which are perpendicular to the surface, so that neurons with similar receptive fields are perpendicularly grouped together. This seminal work also motivated Hubel & Wiesel's discoveries (1962) on the primary visual cortex (V1) of cats and primates, where the orientation map for simple and complex cells were found to be arranged in cortical columns, and neurons in a column preferentially responded to edge of a particular orientation [50, 51, 183]. Motivated by these experimental studies, there has been a great interest in developing rigorous mathematical theories of dynamical systems in V1, including analytical techniques for understanding geometric visual hallucinations [18, 91, 154], image processing of visual cell populations [184], as well as orientation tuning [182, 185, 186]. A notable work is that of Bressloff *et al.* [92], who used a two-dimensional coupled ring model for studying the dynamics of periodic patterns and orientation bumps in V1. This model was developed from a standard neural field model (see Chapter 3), and previously used for understanding geometrical aspects of rich patterns of cortical activity in V1, see also [18, 102, 187]. A coupled two-dimensional ring model with a Heaviside firing rate non-linearity used by Bressloff *et al.* [92] is given by

$$\frac{\partial u(x,\theta,t)}{\partial t} = -u(x,\theta,t) + \int_{\mathbb{R}} \int_{\mathcal{S}} \mathcal{W}(x,\theta,x',\theta') H(u(x',\theta',t)) \mathrm{d}\theta' \mathrm{d}x', \tag{5.0.1}$$

where we treat a non-homogeneous weight distribution in the form

$$\mathcal{W}(x,\theta,x',\theta') = w(\theta-\theta')J(|x-x'|), \tag{5.0.2}$$

with $(x,\theta) \in \mathbb{R} \times \mathcal{S}$, $\mathcal{S} = (-\pi/2, \pi/2]$. Here $u(x,\theta,t)$ represents the activity of populations of interacting neurons in V1 at position x with an orientation preference θ. The kernel J represents horizontal connections which are reinforced in patches over the cortical surface and establishes links between neurons with similar orientation preferences, and $w(\theta)$ denotes a synaptic kernel by which a cell interacts with other cells depending upon the orientation differences.

We begin with an overview of V1 in §5.1, and introduce a coupled ring model with a Heaviside firing rate in §5.2. Here, it is of particular interest to extend the work of Bressloff *et al*. [92] in several directions. We first recover direct numerical solutions for orientation bumps presented in [92], and then develop a new analysis using an interface approach. We also characterise travelling wave solutions of orientation bumps and determine their linear stability analysis using the level set description. Since there are various metabolic processes which can modulate the properties of visual receptive fields, next in §5.3, we consider the coupled ring model with the addition of a linear spike frequency adaptation variable. In this case, destabilisation of the varicose, sinusoid and horizontal stripe solutions can be readily observed. Note that these localised stripe patterns are mostly linked to image translations during visual hallucinations, see [119, 154] for a further discussion. Here, we only investigate the instabilities that arise of a vertical stripe. Orientation independent solutions, where the bifurcation diagrams for homogeneous oscillatory and non-oscillatory spatial distribution, as well as those for heterogeneous spatial distribution are discussed in §5.4. Finally, in §5.5, we construct solutions for multiple stripes, and conclude this Chapter by giving a brief summary and some possible extensions.

5.1 PRIMARY VISUAL CORTEX (V1)

In order to better understand the dynamical behaviour of neurons in V1, it is worthwhile to overview its structure and pathways. The primary visual cortex located toward the rear of the head, is a part of the cerebral cortex. It is the first cortical region where visual signals are processed. As seen in Fig. 5.1, each eye can only see a part of visual field (orange-blue regions).

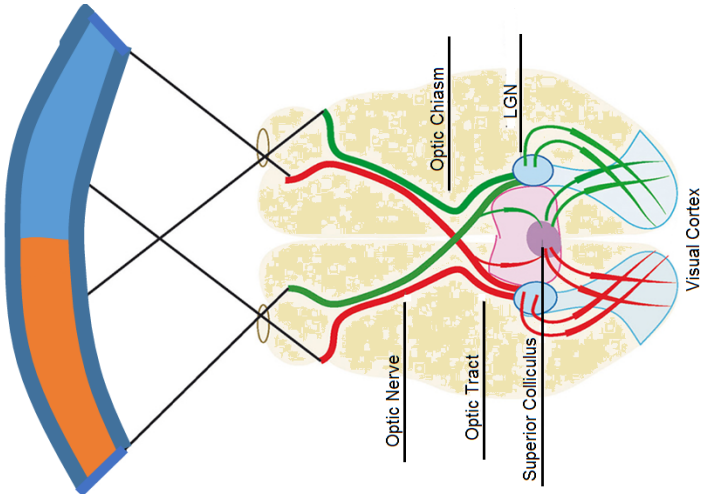

Fig. 5.1: A schematic picture for image projection. Image modified from [188].

The output from each retina is carried by axons of retinal ganglion cells via optic nerves. In human, axons from the nasal retina (part of the retina that is close to the nose) cross over to the other side of the brain in the *optic chiasm* [189], see Fig. 5.1. After crossing the *optic chiasm*, the axons which are collectively called *optic tract* terminate in the lateral geniculate nucleus (LGN), namely the visual part of the thalamus [82, 188]. However, axons from the temporal retina (the part of retina close to the temple) are projected to their own side of the brain so that visual information is directly conveyed to LGN [188]. V1 also projects visual information to the other parts of the cerebral cortex involved in complex visual perception. For example, axons of neurons in LGN also project to the *superior colliculus*, rapid eye movements like saccades are coordinated [190].

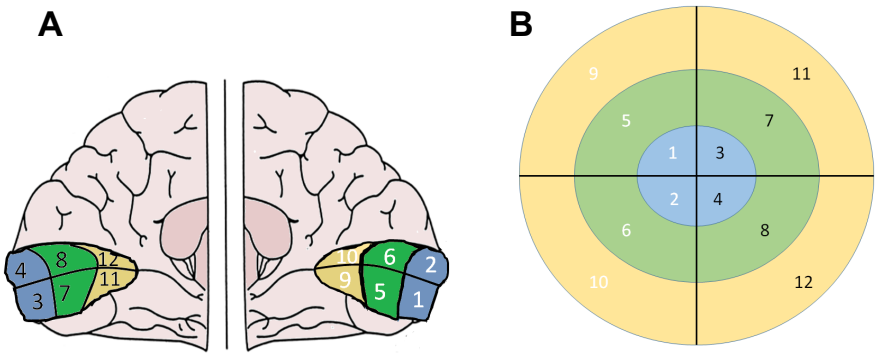

Fig. 5.2: An illustration of a brain slice, showing different regions of visual cortex in the left and right hemifields (**A**) as if opened up looking directly at the back of the head. Regions interpreted with different colours (and indexed numbers) (**B**) are mapped to those in the cortex (**A**). Here 1, 2, 3, and 4 are regions of the central retina, 5, 6, 7, and 8 represent regions of the near peripheral visual fields, and regions 9, 10, 11, and 12 represent regions of the far peripheral visual fields. Modified from [191].

As mentioned earlier, V1 comprises grids of columns that are organised with similar properties and serves as a map of the retina. Visual hemispheres are mapped to the right and left portions of the visual cortex as shown in Fig. 5.2. This topographic way of working, initiated in the left and right retinas (Fig. 5.2B), is nicely summarised by Cowan & Bressloff [104]:

" *...the visual world is mapped onto the cortical surface in a topographic manner, which means neighbouring points in a visual image evoke activity in a neighbouring regions of visual cortex. Moreover, one finds that the central region of the visual field has a larger representation in V1 than the periphery... partly due to a non-uniform distribution of the retinal ganglion cells [104]*".

Depending on the orientation of the input received from LGN, the receptive field of a single V1 neuron may evoke various responses, shown in Fig. 5.3. One of the inter-

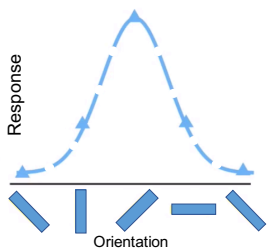

Fig. 5.3: Orientation tuning curve.

esting phenomena about orientation selectivity is that nearby cells tend to organise themselves with the same tuning, which in turn induces those cells to excite each other [192]. On the contrary, cells further apart from each other tend to have different orientation preference which encourages them to inhibit each other. Therefore the regions known as *orientation columns* naturally emerge throughout the surface of V1. Several physiological studies suggested that neurons that are not within the same hypercolumn (up to several mm apart from each other) but have similar orientation preferences may interact via long-range horizontal connections which ramify in periodic patches across the surface of V1 [92, 193, 194].

The orientation preference of a neuron in primary visual cortex continuously changes as its spatial location changes, except at singular points, known as *pinwheel centers*; when neighbouring neurons do not share similar orientation preferences [193, 195]. The studies on these singularities were initiated by Hubel & Wiesel [50, 51]. These experiments showed the existence of smooth and continuous changes of orientation preference between pinwheels, with an underlying periodic or quasi-periodic organisation in the micro-structure of V1 [92]. Note that cells in V1 possess elongated receptive fields. The periodicity of orientation preference is often studied over the ranges of either $\theta \in (0, \pi]$ or $(-\pi/2, \pi/2]$ because bars of orientation θ and $\pi - \theta$ can not be distinguished without cells that respond to edges (elongated stimuli) of a particular orientation. The reason for emergence of these singularities has remained elusive, yet they are thought to be developmental artifacts of the visual field or evolutionary adaptations to keep the volume of the cortex to a minimum [196].

5.2 ORIENTATION BUMPS IN A RING MODEL WITH NO ADAPTATION

An important finding obtained by Bressloff *et al.* [92] is that periodic feature maps and patchy horizontal interactions can lead to spatial patterns of activity for orientation tuning, under the assumption that the synaptic kernel is separable, that is, a product of a function in $|x - x'|$ and one in $\theta - \theta'$. In this section we will recover their results for an orientation bump emerging from a travelling front, and develop an alternative mathematical framework based upon an interface approach.

5.2.1 *Interface Dynamics of Orientation Bumps in V1*

Turning our attention to equation (5.0.1) with a Heaviside firing rate, a parametrisation of a curve on a cylinder is given by

$$\Omega = \{(x,\theta) \in \mathbb{R} \times \mathcal{S} |\ \theta = s, x = \varphi(s,t)\}\,, \tag{5.2.1}$$

where $s \in (-\pi/2, \pi/2]$, $\forall t \geq 0$. This parametrisation is particularly helpful when describing waves: since the orientation component in the above parametrisation is time independent, an orientation bump has a velocity only in the spatial direction. Differentiating the level set condition $u(x,\theta,t) = u(\varphi(s,t),s,t) = \kappa$ with respect to x and t generates a velocity rule:

$$\dot{x} = -\left.\frac{u_t}{u_x}\right|_{x=\varphi(s,t)}. \tag{5.2.2}$$

Here, we use the notation $\Omega_+ = \{(x,\theta)|u(x,\theta) > \kappa\}$ and $\partial\Omega_+ = \{(x,\theta)|u(x,\theta) = \kappa\}$. A closed form expression for u can be found by integrating (5.0.1) to give

$$u(x,s,t) = u_0(x,s)\mathrm{e}^{-t} + \int_0^t \mathrm{d}t'\ \mathrm{e}^{t'-t} \int_{\Omega_+(t')} \mathcal{W}(x,s,x',s')\mathrm{d}x'\mathrm{d}s' \Big|_{x=\varphi(s,t)}, \tag{5.2.3}$$

where the synaptic activity on a finite domain $[-L, L]$ and without boundary conditions is

$$\int\limits_{\Omega_+(t)} \mathcal{W}(x,\theta,x',\theta')\mathrm{d}x'\mathrm{d}\theta' = \int\limits_{-\pi/2}^{\pi/2}\int\limits_{-L}^{\varphi(s',t)} w(s-s')J(|\varphi(s,t)-x'|)\mathrm{d}x'\mathrm{d}s'. \tag{5.2.4}$$

Here L is the half domain length in the spatial direction.

Since long range horizontal connections in V1 are supported by the axons of excitatory pyramidal neurons [92], horizontal connections which ramify in periodic patchy columns are usually assumed to be excitatory, and thus can be expressed by a positive decaying function (J). In addition, depending on the stimulus, a standard choice of Mexican hat function (positive for small values of θ and negative for large values of θ) can be considered for local interactions (w). Following the work of Bressloff *et al.* [92], we chose an exponential weight distribution for patchy horizontal connections and a periodic kernel in the angular direction in the form of

$$J(x) = \frac{1}{2\sigma}\mathrm{e}^{-|x|/\sigma}, \qquad w(\theta) = \frac{1}{\pi}\left[w_0 + 2w_2\cos(2\theta)\right], \tag{5.2.5}$$

where $w_0, w_2 > 0$.

Figure 5.4**A** shows (the results of) direct numerical simulations of the model (5.0.1). The simulations were started from an initial condition in the form of a uniform travelling front solution with the addition of a small random perturbation. As seen from Fig. 5.4, model (5.0.1) effectively demonstrates the emergence of synaptic activity with a preferred orientation in the visual cortex. In Fig. 5.4**B**, a numerical simulation of a travelling orientation bump prescribed by the interface method is shown. Here, an excellent agreement is found between two figures. The solutions for a front with various fixed angle and locations are shown in Fig. 5.5. See [92, 182] for a recent overview of orientation bumps and their instabilities.

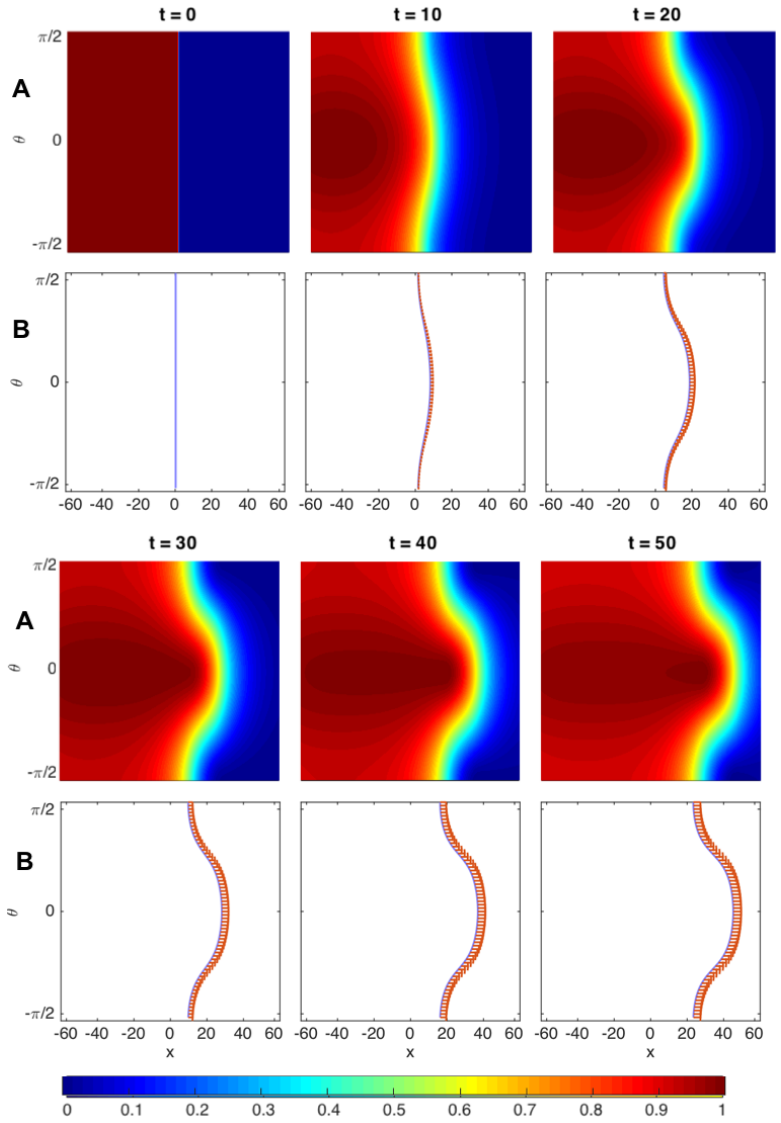

Fig. 5.4: Snapshots from space-time simulations of the full model (5.0.1) for synaptic activity $u(x,\theta,t)$ with synaptic kernels (5.2.5) are shown. Panel (**A**): direct numerical simulations for an orientation bump that emerges from a travelling front. Panel (**B**): equivalent interface dynamics (blue line). The orange arrows shows the normal velocity (5.2.2) of the moving interface (**B**), on a domain of $[-L,L]\times(-\pi/2,\pi/2]$. The contour is updated only in the x direction due to the zero velocity in the angular direction. Parameters are $w_0 = 0.5$, $w_2 = 0.55$, $\kappa = 0.235$, $\sigma = 10$, $L = 60$.

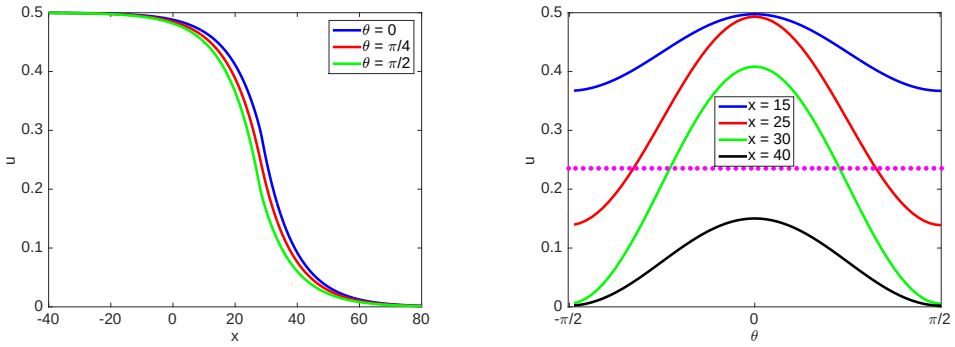

Fig. 5.5: Travelling wave solutions of the model (5.0.1) with synaptic kernels described by (5.2.5) for different fixed values of θ (left) and x (right) at time $t = 45$. Dotted line represents threshold value. Parameters are $w_0 = 0.5$, $w_2 = 0.55$, $\kappa = 0.235$, $\sigma = 10$.

5.2.2 *Travelling Wave Solution*

We now derive solutions for travelling waves using an interface approach. Travelling waves with a single threshold crossing (fronts) are described by $\varphi(s,t) = x_*(t) = ct$, $\forall s \in \mathcal{S}$. Substituting this expression into (5.2.2) for $\dot{x}_*(t) = c$, yields

$$c = \frac{\kappa - \int_{-\pi/2}^{\pi/2} \int_{-L}^{ct} \mathcal{W}(ct, 0, x', s') \mathrm{d}x' \mathrm{d}s'}{\partial_x u_0(ct, s) \mathrm{e}^{-t} + \int_0^t \mathrm{d}t' \, \mathrm{e}^{t'-t} \int_{-\pi/2}^{\pi/2} \int_{-L}^{ct'} \partial_x \mathcal{W}(ct, 0, x', s') \mathrm{d}x' \mathrm{d}s'}, \tag{5.2.6}$$

$$= \frac{\kappa - \frac{w_0}{2}\left(1 - \mathrm{e}^{-(ct+L)/\sigma}\right)}{\partial_x u_0(ct, s)\mathrm{e}^{-t} + \frac{w_0}{2\sigma}\left(\left(1 - \mathrm{e}^{-t}\right)\mathrm{e}^{-(ct+L)/\sigma} - \frac{\sigma}{\sigma + c}\left(1 - \mathrm{e}^{-(\sigma+c)t/\sigma}\right)\right)}. \tag{5.2.7}$$

See Appendix C1 for computing the integrals in (5.2.6). Using the translational invariance of the model and taking $t \to \infty$ and $|L| \to \infty$ into account, equation (5.2.7) simplifies to

$$c = \frac{\sigma}{2\kappa}(w_0 - 2\kappa), \tag{5.2.8}$$

where $c > 0$. This recovers the formula for the wave speed computed by Bressloff *et al.* using an alternative approach, see [92] for further details. The comparison of

time dependent speed formula (5.2.7) with its asymptotic value (5.2.8) is shown in Fig. 5.6.

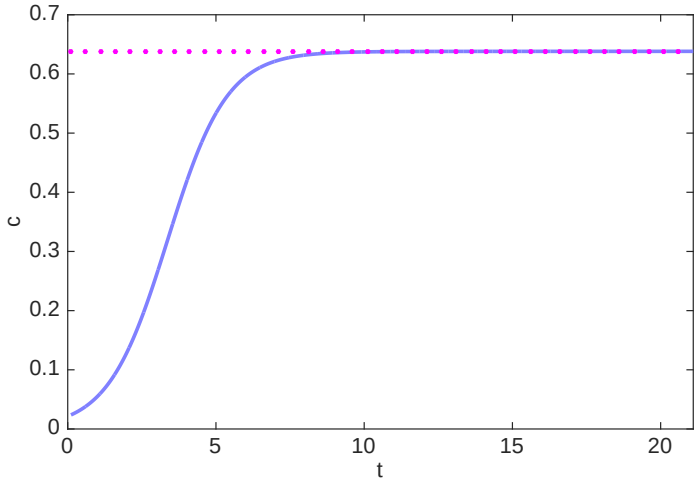

Fig. 5.6: Wave speed (5.2.7) is plotted as a function of time. Here time dependent velocity obtained from equation (5.2.7) saturates at $c = 0.6383$ at $t = 20$ (given by (5.2.8)) on a large domain of size $L = 200$. Dotted lines represent the asymptotic value for the speed of a front. Parameters are as in Fig. 5.4.

5.2.3 *Threshold Condition*

Before we develop a stability analysis for a travelling front using a level set description, it is informative to begin with an explicit calculation of the threshold crossing condition. The original model (5.0.1) in an unbounded domain takes the form

$$u_t(x,s,t) = -u(x,s,t) + \int_{-\pi/2}^{\pi/2} \int_{-\infty}^{\varphi(s',t)} \mathcal{W}(x,s,x',s')\mathrm{d}x'\mathrm{d}s', \tag{5.2.9}$$

where $\mathcal{W}(x,s,x',s') = w(s-s')J(|x-x'|)$.

Making a change of variable ($x' = x - x'$), equation (5.2.9) can be rewritten as

$$u_t(x,s,t) = -u(x,s,t) + \int_{-\pi/2}^{\pi/2} \mathrm{d}s' w(s-s') \int_{x-\varphi(s',t)}^{\infty} \mathrm{d}x' J(x'). \tag{5.2.10}$$

Introducing $z = u_x$ and differentiating (5.2.10) with respect to x yields

$$z_t(x,s,t) = -z(x,s,t) - \int_{-\pi/2}^{\pi/2} \mathrm{d}s' w(s-s') J(x - \varphi(s',t)). \tag{5.2.11}$$

Integrating equation (5.2.11) and dropping all the intermediate steps, we find

$$z|_{x=ct} = -w_0 \int_0^\infty \mathrm{d}t' \mathrm{e}^{-t'} J(ct'). \tag{5.2.12}$$

Following the work of Coombes *et al.* [11] (for a one-dimensional neural field), we introduce a function

$$\widetilde{J}(\lambda) = \int_0^\infty \mathrm{d}t' \mathrm{e}^{-\lambda t'} J(t'), \tag{5.2.13}$$

and thus equation (5.2.12) for an interface to study $x(t) = ct$ with speed $c > 0$ can be rewritten as

$$z|_{x=ct} = -\frac{w_0}{c} \widetilde{J}\left(\frac{1}{c}\right). \tag{5.2.14}$$

Using equation (5.2.10), the change in the activity of the population is

$$u_t|_{x=ct} = -\kappa - \int_{-\pi/2}^{\pi/2} \mathrm{d}s' w(s-s') \int_0^\infty \mathrm{d}x' J(x'), \tag{5.2.15}$$

$$= -\kappa + w_0 \widetilde{J}(0). \tag{5.2.16}$$

Plugging the expressions (5.2.14) and (5.2.16) into (5.2.2), and using the fact that

$$\int_{-\pi/2}^{\pi/2} \cos(2m(s-s'))\mathrm{d}s' = 0, \ \forall s, \tag{5.2.17}$$

we obtain a threshold condition given by

$$\kappa = w_0 \left[\widetilde{J}(0) - \widetilde{J}\left(\frac{1}{c}\right)\right], \tag{5.2.18}$$

where (5.2.13) can be explicitly computed as

$$\widetilde{J}(\lambda) = \frac{1}{2(\lambda\sigma + 1)}. \tag{5.2.19}$$

Note that the exponential weight distribution (5.2.5) is symmetric. Hence, using equations (5.2.18) and (5.2.19), one finds the speed of the travelling front

$$c = \frac{\sigma}{2\kappa}(w_0 - 2\kappa), \tag{5.2.20}$$

for $0 < \kappa < w_0/2$.

5.2.4 *Linear Stability Analysis*

Although the velocity of the front is only in the spatial (x) direction (see page 108), the presence of the ring structure may affect stability [92]. Hence the stability of an orientation bump should be determined considering a perturbation of the boundary in both angular and spatial directions. Integrating (5.2.10) and omitting the intermediate steps for brevity, a closed form for the activity is computed as

$$u(x,s,t) = \int_0^\infty \mathrm{d}t' \mathrm{e}^{-t'} \int_{-\pi/2}^{\pi/2} \mathrm{d}s' w(s-s') \int_{x-\varphi(s',t-t')}^{\infty} \mathrm{d}x' J(x') \Big|_{x=\varphi(s,t)}. \tag{5.2.21}$$

Evaluating at $\varphi(s,t) = ct$ gives

$$u|_{\varphi=ct} = w_0 \int_0^\infty \mathrm{d}t' \mathrm{e}^{-t'} \int_{ct'}^{\infty} \mathrm{d}x' J(x'). \tag{5.2.22}$$

To determine stability of the travelling front we consider a relationship between a perturbed interface $\partial\widetilde{\Omega}_+$ and perturbed front $\widetilde{\Omega}_+$. We refer the reader to [11] for an overview of details for stability analysis using interface dynamics, and also see Chapter 3. The perturbation in the activity can be associated to the perturbation in the interface using a level set, namely

$$u(x_*,s,t) = \widetilde{u}(\widetilde{x}_*,s,t) = \kappa. \tag{5.2.23}$$

Thus, the difference between perturbed and unperturbed quantities:

$$\delta u(s,t) = \widetilde{u}|_{x=\widetilde{x}_*(s,t)} - u|_{x=x_*(t)}, \tag{5.2.24}$$

is determined using the condition $\delta u(s,t) = 0$. Let us consider the perturbed quantity in the form of

$$\widetilde{x}_*(s,t) = ct + \epsilon\widetilde{\varphi}(s,t), \tag{5.2.25}$$

where $\widetilde{\varphi}(s,t) = \mathrm{e}^{\lambda t}\sum_m \cos(2ms)$. Hence the perturbed activity of the population is found as

$$\widetilde{u}(x,s,t) = \int_0^\infty \mathrm{d}t' \mathrm{e}^{-t'} \int_{-\pi/2}^{\pi/2} \mathrm{d}s' w(s-s') \int_{x-\widetilde{x}_*(s',t-t')}^{\infty} \mathrm{d}x' J(x'), \tag{5.2.26}$$

where the construction of $\delta u(s,t)$ results in

$$\begin{aligned}\delta u &= \int_0^\infty \mathrm{d}t' \mathrm{e}^{-t'} \int_{-\pi/2}^{\pi/2} \mathrm{d}s' w(s-s') \left[\int_{\widetilde{x}_*(s,t)-\widetilde{x}_*(s',t-t')}^{\infty} - \int_{x_*(t)-x_*(t-t')}^{\infty} \right] \mathrm{d}x' J(x'), \\ &= \int_0^\infty \mathrm{d}t' \mathrm{e}^{-t'} \int_{-\pi/2}^{\pi/2} \mathrm{d}s' w(s-s') \left[\epsilon\widetilde{\varphi}(s',t-t') - \epsilon\widetilde{\varphi}(s,t) \right] \int_{ct'}^{\infty} \mathrm{d}x' J'(x'), \\ &= \frac{1}{c} \int_0^\infty \mathrm{d}t' \mathrm{e}^{-t'/c} \int_{-\pi/2}^{\pi/2} \mathrm{d}s' w(s-s') J(t') \left[\epsilon\widetilde{\varphi}(s,t) - \epsilon\widetilde{\varphi}(s',t-t'/c) \right]. \end{aligned} \tag{5.2.27}$$

Substituting $\widetilde{\varphi}(s,t) = \mathrm{e}^{\lambda t} \sum_m \cos(2ms)$ in (5.2.27) yields

$$\delta u(s,t) = \frac{1}{c} \int_0^\infty \mathrm{d}t' \mathrm{e}^{-t'/c} J(t') \int_{-\pi/2}^{\pi/2} \mathrm{d}s' w(s-s') \sum_m \left[\cos(2ms) - \mathrm{e}^{\lambda t'/c} \cos(2ms') \right] \epsilon \mathrm{e}^{\lambda t}.$$

Here using the fact

$$\sum_{m=1}^{\infty} \frac{\sin(m\pi)}{m\pi} = 0, \tag{5.2.28}$$

and considering the components of the connectivity, $\mathcal{W}(x,s,x',s') = w(s-s')J(|x-x'|)$ with the slightly more general choice:

$$J(x) = \frac{1}{2\sigma} \mathrm{e}^{-|x|/\sigma} \quad \text{and} \quad w(\theta) = \frac{1}{\pi} \left[w_0 + 2 \sum_{m=1}^{\infty} w_{2m} \cos(2m\theta) \right], \tag{5.2.29}$$

we obtain the following Evans function for the travelling front solution ,

$$\mathcal{E}_m(\lambda) = w_0 \widetilde{J}\left(\frac{1}{c}\right) - w_{2m} \widetilde{J}\left(\frac{\lambda+1}{c}\right), \tag{5.2.30}$$

where $\widetilde{J}(\lambda) = 1/[2(\lambda\sigma+1)]$ was described in (5.2.19). It can be seen from equation (5.2.30) that the zeros of the Evans function satisfy $\mathcal{E}_0(0) = 0$ with $w_0 = w_{2m}$. Hence using (5.2.19) the eigenvalue equation can be explicitly calculated as

$$\lambda_m = \frac{w_{2m} - w_0}{w_0} \left(1 + \frac{c}{\sigma}\right). \tag{5.2.31}$$

This recovers the results obtained in [92] for $m = 1$ using an alternative approach, suggesting that

- $\lambda > 0$ (unstable) , if $w_2 > w_0$,
- $\lambda \leq 0$ (stable), if $w_2 \leq w_0$ or $w(\theta) = w_0$.

These results of the stability analysis are also supported in Fig. 5.4, where orientation bump emerges from an unstable front. Note that, as expected, the zero eigenvalue leads to a neutrally stable state.

5.3 STRIPES IN A RING MODEL WITH ADAPTATION

The direct numerical simulations that arise from instabilities (for a standard neural field model without features or adaptation) of a stripe were previously shown by Coombes *et al*. [11]. As discussed in Chapter 4, the spike frequency adaptation (a negative feedback process) is often included in neural field models to diminish sustained firing. Since we consider patchy horizontal connections between pre-and post-synaptic neurons to be only excitatory, the adaptation variable becomes an important mechanism to moderate synaptic activity. Before we introduce a new approach for stripe solutions in a coupled ring model with adaptation, we recall some findings of the previous Chapters. We consider the standard neural field model with adaptation,

$$\tau u_t = -u + \psi - ga, \qquad a_t = u - a, \tag{5.3.1}$$

where the non-linear term ψ involves a non-homogeneous kernel given by

$$\psi(\cdot,t) = \int_{\mathbb{R}} \int_{S} \mathcal{W}(\cdot,x',\theta') H(u(x',\theta',t) - \kappa) \mathrm{d}\theta' \mathrm{d}x'. \tag{5.3.2}$$

Here, the parameter τ denotes the time constant for the synaptic activity. As calculated in §4.1, the solutions (u,a) are given in closed form as

$$u(\cdot,t) = \int_{-\infty}^{t} \mathrm{d}t' G_{11}(t') \psi(\cdot,t-t'), \tag{5.3.3}$$

$$a(\cdot,t) = \int_{-\infty}^{t} \mathrm{d}t' \mathrm{e}^{-t'} u(\cdot,t-t'), \tag{5.3.4}$$

where G_{11} is the first element of the matrix $G = \mathrm{e}^{At}$ and is calculated in a similar fashion as in (B1.1).

So far we have considered an orientation preference map which is periodic (see equation (5.2.5)), where neurons with similar orientation preferences interact strongly with each other. However we can analyse other scales in the absence of this periodic structure. In the rest of this Chapter, we consider generalised kernels of the form

$$w(s) = w_0 + w_2 \cos(2ps), \tag{5.3.5}$$

$$J(x) = \frac{1}{2\sigma} \cos(2kx) \mathrm{e}^{-|x|/2\sigma}, \tag{5.3.6}$$

where $p, k, \sigma > 0$. The kernel J represents horizontal connections which consist of a natural choice of short-range excitation and long-range inhibition, and w denotes the existence of regularly repeating (when $p > 1$) feature maps. Considering $k > 1$ in kernel (5.3.6) leads to oscillations whose amplitude decays in the spatial distribution and also provides inhibitory interactions, parameter σ controls the rate at which the oscillations in $J(x)$ decay with distance, and parameter p is associated with frequency, namely the number of oscillations (cycles) that occur between $-\pi/2$ and $\pi/2$ in the orientation preference map. Although the choice of $p > 1$ is not relevant to periodic orientation maps ($p = 1$), it might be a proxy for less preferred interactions as seen in salt-and-pepper orientation preference maps (more random orientation preference) without periodic structures [197, 198]. This functional architecture is more likely to be the case for animals that do not have an orientation preference map, particularly rodents. Thus we now construct a coupled ring model of visual cortex where orientation selectivity is not random but rather oscillatory, in which there is also strong preferred interactions for angles differing by π/p. This can arise for feature map connectivity with $p > 1$ in equation (5.3.5). Figure 5.7 shows illustrations of weight kernels for the feature map connectivity (5.3.5) and horizontal connectivity (5.3.6), respectively.

In a scalar neural field model of Amari type (posed on two dimensions), azimuthal instabilities of different modes (m) which deform circular solutions can emerge on the solution branches according to $R \to R + \epsilon \cos(ms)$, where $s \in [0, 2\pi)$, $m \in$

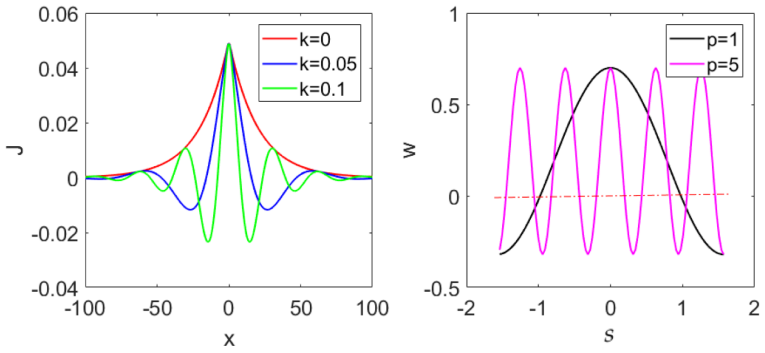

Fig. 5.7: Plots of the kernels given in equation (5.3.5) and (5.3.6) for various parameters of k and p, respectively. Other parameters are $w_0 = 0.19$, $w_2 = 0.51$, $\sigma = 10$.

$\mathbb{N}$ and $|\epsilon| \ll 1$. For example, instabilities of modes $m = 2, 3, 4...$ which deform localised states with a smooth Mexican hat connectivity were shown in Fig. 3.7**A**. However, in a coupled ring model described by (5.0.1), (5.3.5) and (5.3.6) the type of the mode for a stripe instability is determined by parameter p. In other words, stripes can undergo only a single type of azimuthal instability, the mode of which is pre-determined. We shall investigate the properties of these instabilities in more detail in the following sub-sections.

In Figures 5.8 and 5.9, we show the results of direct numerical simulations at fixed times for a ring model (5.3.1) with non-homogeneous kernels (5.3.5) and (5.3.6). These simulations show the emergence of varicose (rows **A**) and sinusoidal (rows **B**) instabilities ($k = 0.1$), where the initial stripe is perturbed with $\pm\cos(2p\theta)$, as seen in Fig. 5.8. The horizontal stripe instabilities with a five fold symmetry can also be obtained with a purely excitatory kernel (5.3.6) ($k = 0$), as shown in Fig. 5.9. These suggest that the stripe is unstable to an azimuthal instability with $m = p = 5$.

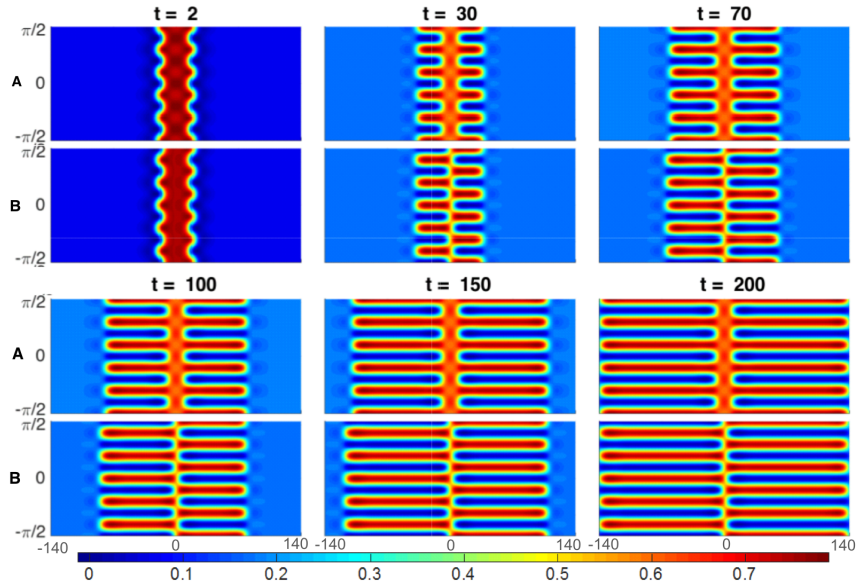

Fig. 5.8: Direct numerical simulations of varicose (rows **A**) and sinusoidal (rows **B**) instabilities, governed by the model (5.3.1) and (5.3.2), with synaptic kernels (5.3.5) and (5.3.6). Here the stripe is initiated with a width of $D = 26.3557$ (obtained from (5.3.7)), and perturbed with $\pm\cos(2p\theta)$ for varicose and sinusoidal instabilities, respectively. A plot of the stripe width as a function of the firing threshold is shown in Fig. 5.10. Parameters are $w_0 = 0.19$, $w_2 = 0.51$, $g = 0.6$, $\kappa = 0.2271$, $k = 0.1$ and $p = 5$.

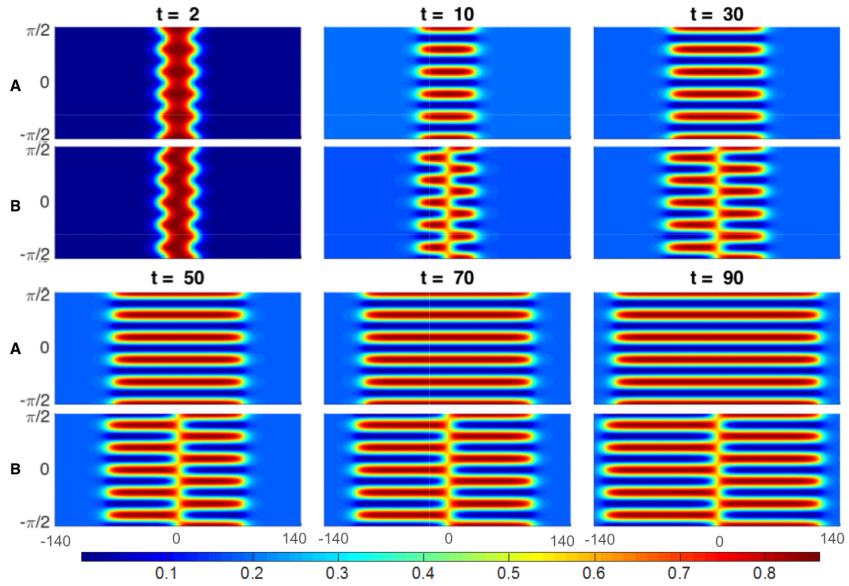

Fig. 5.9: Direct numerical simulations of horizontal stripes (rows **A**) and sinusoidal (rows **B**) instabilities, governed by the model (5.3.1) and (5.3.2), with synaptic kernels (5.3.5) and (5.3.6). The stripe is initiated with the width $D = 25.9769$ obtained from (5.3.7), and perturbed with $\pm\cos(2p\theta)$. A plot of the stripe width as a function of the firing threshold is shown in Fig. 5.10. Parameters are $w_0 = 0.19$, $w_2 = 0.51$, $g = 0.6$, $\kappa = 0.3725$, $k = 0$ and $p = 5$.

5.3.1 *Stripe Construction*

A stripe may be described as a long and narrow active area in between two stationary fronts. Let $x = x_1$ and $x = x_2$ to be two interfaces separating active and quiescent regions of a vertical stripe. Considering the time independent solutions of (5.3.1):

$$u(x,s) = \frac{1}{1+g} \int_{-\pi/2}^{\pi/2} \mathrm{d}s' w(s-s') \int_{x-x_2}^{x-x_1} \mathrm{d}x' J(x'), \tag{5.3.7}$$

the level set condition for a stripe of width D can be written as

$$u(x_1,s) = \kappa = u(x_1+D,s), \tag{5.3.8}$$

where $x_1 = 0$ is chosen to be a reference point for the first interface, and thus $x_2 = x_1 + D$ is readily obtained. Hence, equation (5.3.7) reduces to

$$\kappa = \frac{1}{1+g} \int_{-\pi/2}^{\pi/2} \mathrm{d}s' w(s-s') \int_{0}^{D} \mathrm{d}x' J(x'), \tag{5.3.9}$$

that can be explicitly computed as

$$\kappa(1+g) = \begin{cases} \dfrac{w_0\pi}{4\sigma AB}\left[A(1-\mathrm{e}^{-BD}) + B(1-\mathrm{e}^{-AD})\right], & \text{if } p \in \mathbb{Z} \\ \dfrac{(w_0 p\pi + w_2 \sin(p\pi))}{4p\sigma AB}\left[A(1-\mathrm{e}^{-BD}) + B(1-\mathrm{e}^{-AD})\right], & \text{otherwise} \end{cases}$$

where $A, B = (1 \pm 4\sigma ik)/2\sigma$.

5.3.2 *Stability Analysis*

In order to perform linear stability analysis of a single stripe, we recall time dependent solutions of (5.3.1):

$$u(x,s,t) = \frac{1}{1+g} \int_{-\pi/2}^{\pi/2} \mathrm{d}s' w(s-s') \int_{x-x_2(t)}^{x-x_1(t)} \mathrm{d}x' J(x'), \tag{5.3.10}$$

and determine the relationship between perturbed and unperturbed quantities, that are defined by $u(x,s,t) = \widetilde{u}(\widetilde{x},s,t) = \kappa$. Hence introducing $\delta u_i = u_i|_{x=\varphi_i(s,t)} -$

$\widetilde{u}_i|_{\widetilde{x}=\widetilde{\varphi}_i(s,t)}$ we write the condition $\delta u_i(t) = 0$, $i = 1,2$ for $\forall t$. The solution for each interface of the stripe is given according to

$$u_i(\varphi_i(s,t),s,t) = \int_0^\infty \mathrm{d}t' G_{11}(t') \int_{-\pi/2}^{\pi/2} \mathrm{d}s' w(s-s') \int_{\varphi_i(s,t)-\varphi_2(s',t-t')}^{\varphi_i(s,t)-\varphi_1(s',t-t')} \mathrm{d}x' J(x'), \quad (5.3.11)$$

where $i = 1,2$ with $\varphi_1 = 0$ and $\varphi_2 = D$. Considering perturbations in each of the stripe boundaries of the form $\widehat{\varphi}_i(s,t) = \varphi_i + \epsilon_i \widetilde{\varphi}(s,t)$ one finds

$$\begin{aligned}\delta u_i &= \int_0^\infty \mathrm{d}t' G_{11}(t') \int_{-\pi/2}^{\pi/2} \mathrm{d}s' w(s-s') \left[\int_{\widehat{\varphi}_i(s,t)-\widehat{\varphi}_2(s',t-t')}^{\widehat{\varphi}_i(s,t)-\widehat{\varphi}_1(s',t-t')} - \int_0^D \right] \mathrm{d}x' J(x'), \\ &= \int_0^\infty \mathrm{d}t' G_{11}(t') \int_{-\pi/2}^{\pi/2} \mathrm{d}s' w(s-s') \left[\int_{\epsilon_i\widetilde{\varphi}(s,t)-\epsilon_2\widetilde{\varphi}(s',t-t')}^{D+\epsilon_i\widetilde{\varphi}(s,t)-\epsilon_1\widetilde{\varphi}(s',t-t')} - \int_0^D \right] \mathrm{d}x' J(x'). \quad (5.3.12)\end{aligned}$$

Using the above expressions we see that $\delta u_i(t) = 0$ has solutions of the form $\widetilde{\varphi}_i(s,t) = \cos(2ms)\mathrm{e}^{\lambda t}$. Here

$$\int_0^\infty \mathrm{d}t' G_{11}(t') \Theta_i(t') = 0, \quad (5.3.13)$$

where we describe

$$\begin{bmatrix} \Theta_1 \\ \Theta_2 \end{bmatrix} = \mathcal{A} \begin{bmatrix} \epsilon_1 \\ \epsilon_2 \end{bmatrix} = 0,$$

with

$$\mathcal{A} = \begin{bmatrix} [\mathcal{K}(0,0) - \mathcal{K}(0,D)] - \mathcal{K}(m,0)\mathrm{e}^{-\lambda t'} & \mathcal{K}(m,D)\mathrm{e}^{-\lambda t'}, \\ \mathcal{K}(m,D)\mathrm{e}^{-\lambda t'} & [\mathcal{K}(0,0) - \mathcal{K}(0,D)] - \mathcal{K}(m,0)\mathrm{e}^{-\lambda t'} \end{bmatrix},$$

and

$$\mathcal{K}(m,D) = \int_{-\pi/2}^{\pi/2} \mathrm{d}s' w(s') J(D) \cos(2ms'). \quad (5.3.14)$$

The difference between perturbed and unperturbed states can be constructed considering only one of the contour equations, e.g. $\delta u_1(t) = 0$. Imposing equal amplitudes of perturbations, $|\epsilon_1| = |\epsilon_2| = \epsilon$, or demanding non-trivial solutions of (5.3.13) we find

$$\delta u_1 = \int_0^\infty \mathrm{d}t' G_{11}(t') \left\{ \epsilon_1 \left(\mathcal{K}(0,D) - \mathcal{K}(0,0) \right) - \epsilon_2 \mathcal{K}(m,D)\mathrm{e}^{-\lambda t'} + \epsilon_1 \mathcal{K}(m,0)\mathrm{e}^{-\lambda t'} \right\}. \quad (5.3.15)$$

Substituting G_{11} (B1.1) into (5.3.15), we obtain

$$\frac{\epsilon_1 \left(\mathcal{K}(0,D) - \mathcal{K}(0,0)\right)}{\lambda_+\lambda_-} = \frac{(\lambda+1)\left(\epsilon_2\mathcal{K}(m,D) - \epsilon_1\mathcal{K}(m,0)\right)}{(\lambda-\lambda_+)(\lambda-\lambda_-)}. \tag{5.3.16}$$

Assuming that $(\epsilon_1, \epsilon_2) = \epsilon(1, \pm 1)$, one finds

$$\frac{\mathcal{K}(0,0) - \mathcal{K}(0,D)}{\lambda_+\lambda_-} = \frac{(\lambda+1)\left(\mathcal{K}(m,0) \pm \mathcal{K}(m,D)\right)}{(\lambda-\lambda_+)(\lambda-\lambda_-)}. \tag{5.3.17}$$

Hence, solving the following two quadratic equations

$$\lambda^2 - \lambda\left(\lambda_+ + \lambda_- + \lambda_+\lambda_-\widetilde{M}_\pm\right) + \lambda_+\lambda_-\left(1 - \widetilde{M}_\pm\right) = 0, \tag{5.3.18}$$

with

$$\widetilde{M}_\pm(m,D) = \frac{\mathcal{K}(m,0) \mp \mathcal{K}(m,D)}{\mathcal{K}(0,0) - \mathcal{K}(0,D)}, \tag{5.3.19}$$

leads to two pairs of eigenvalues:

$$\lambda_{1,2} = \frac{-B_+ \pm \sqrt{B_+^2 - 4C_+}}{2}, \tag{5.3.20}$$

$$\lambda_{3,4} = \frac{-B_- \pm \sqrt{B_-^2 - 4C_-}}{2}, \tag{5.3.21}$$

where

$$B_\pm = -\left(\lambda_+ + \lambda_- + \lambda_+\lambda_-\widetilde{M}_\pm(m,D)\right), \tag{5.3.22}$$

$$C_\pm = \lambda_+\lambda_-\left(1 - \widetilde{M}_\pm(m,D)\right). \tag{5.3.23}$$

The branch with $\lambda = \lambda_{1,2}$ corresponds to sinusoidal perturbations with $(\epsilon_1, \epsilon_2) = \epsilon(1,1)$ and the branch with $\lambda = \lambda_{3,4}$ corresponds to varicose perturbations with $(\epsilon_1, \epsilon_2) = \epsilon(1,-1)$. Here, $\lambda_{2,4}$ are always negative leading to a stable activity. When $\lambda_3 > \lambda_1$, varicose instabilities dominates over sinusoidal instabilities. Note that a trivial eigenvalue $\lambda = 0$ is found when $\widetilde{M}_\pm = 1$.

The function given in the equation (5.3.14) can be explicitly computed as,

$$\frac{\mathcal{K}(0,D)}{J(D)} = w_0\pi + w_2\frac{\sin(\pi p)}{p}, \tag{5.3.24}$$

$$\frac{\mathcal{K}(m,D)}{J(D)} = w_0\frac{\sin(\pi m)}{m} + w_2\mathcal{C}, \tag{5.3.25}$$

where

$$\mathcal{C} = \begin{cases} \pi, & \text{if} \quad m = p = 0 \\ \pi/2, & \text{if} \quad m = p \neq 0 \\ 0, & \text{if} \quad m \neq p \end{cases} \cdot$$

Stripes solutions have instabilities of modes with $m = p$. In Fig. 5.10, we show that sufficiently small (large) values of w_0 in (5.3.5) lead to unstable (stable) branches respectively. Solid lines represent stable branches and dashed lines represent instabilities of a p-mode ($m = p$) which deform a stripe.

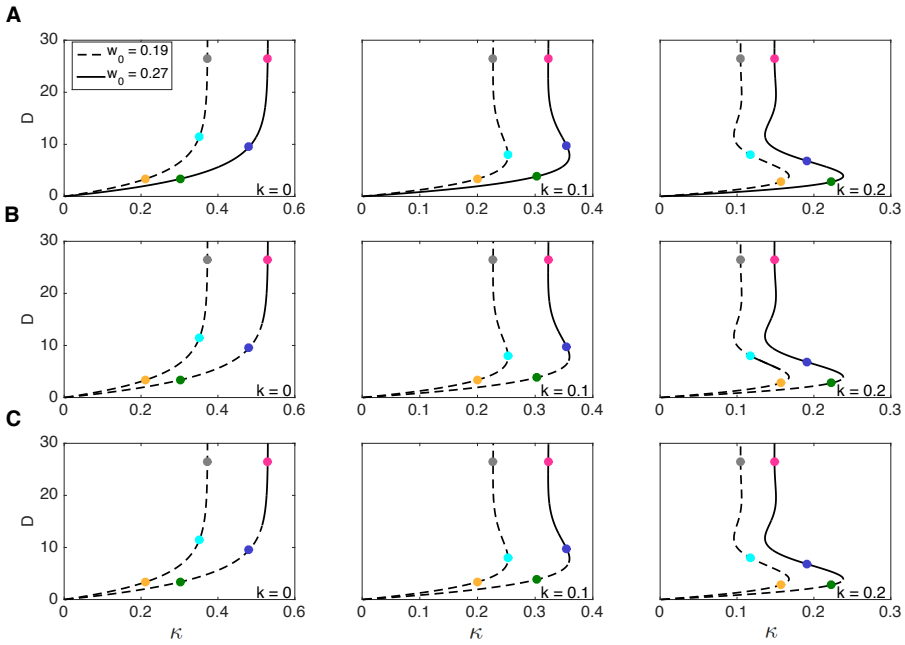

Fig. 5.10: Stripe widths (D) as a function of threshold (κ), using the time independent model (5.3.7) with synaptic kernels (5.3.5) and (5.3.6), are shown with sinusoid (**A**) and varicose (**B**) perturbations for different values of $k = 0, 0.1, 0.2$ (from left to right). Row (**C**) represents the overall stability with combination of row (**A**) and row (**B**). The points indexed by different colour spots will be referred in Figures 5.11, 5.12 and 5.13. Parameters are $w_2 = 0.51$, $\sigma = 2$, $g = 0.6$, $p = 5$.

In Fig. 5.11, another bifurcation structure is shown for stripe width as a function of the parameter w_0 for various points of interest (indexed by different colour spots

shown in Fig. 5.10). As for the results in Fig. 5.10, the solution for a vertical stripe tends to be more stable for large values of w_0 in (5.3.5).

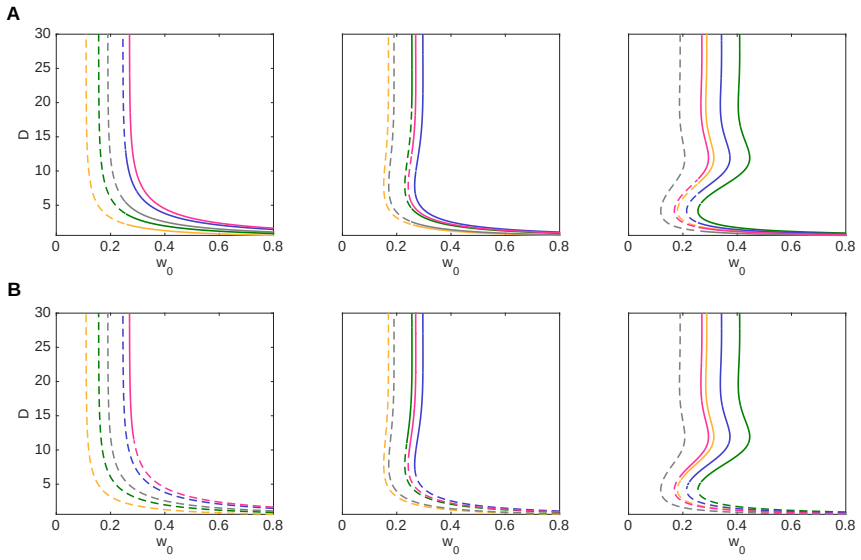

Fig. 5.11: Stripe widths (D) as a function of w_0, using the time independent model (5.3.7) and synaptic kernels (5.3.5) and (5.3.6), are shown with respect to sinusoidal (row **A**) and varicose (row **B**) perturbations for various threshold values of κ. The values of κ are taken from Fig. 5.10. Solid and dashed lines correspond to the stable and unstable branches respectively. Parameters are $w_2 = 0.51$, $\sigma = 2$, $p = 5$.

Here lower branches of the bifurcation diagrams (small values of D) are found to be stable to sinusoid perturbations (row **A**) and unstable to varicose perturbations (row **B**). So far we have used the threshold κ and w_0 in (5.3.5) as the main bifurcation parameters. The results are complemented by the findings in Fig. 5.12, where we apply this framework for a two-parameter diagram. Here we concentrate on the case where the adaptation parameter g is plotted as a function of decay parameter σ in (5.3.6) by solving (5.3.9) for each κ indexed by colour spots in Fig. 5.10. Here, we find that the system is always unstable for a sufficiently small w_0 without depending on the level of adaptation; however, the same degree of adaptation may induce further stability for sufficiently large values of w_0.

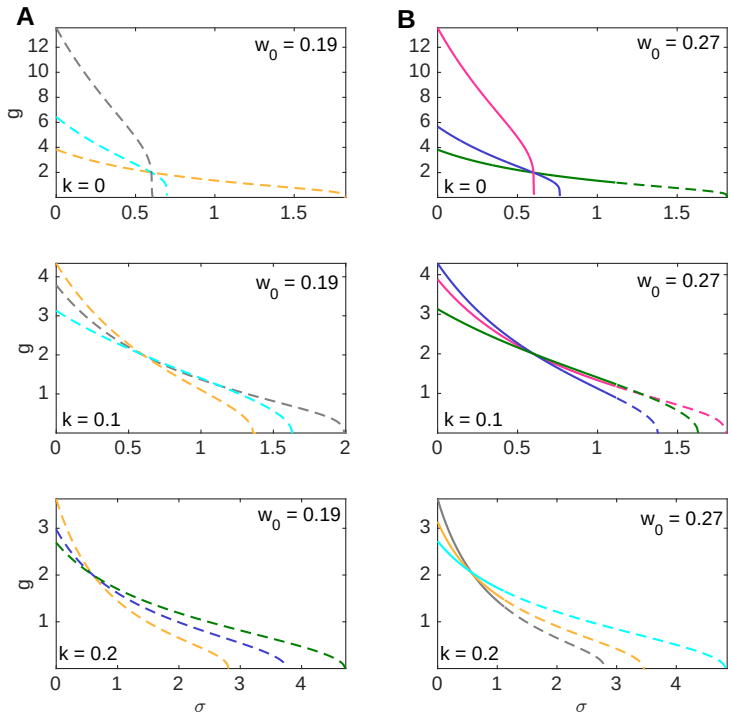

Fig. 5.12: The adaptation parameter g for a stripe solution is plotted as a function of σ with $w_0 = 0.27$ (column **A**) and $w_0 = 0.19$ (column **B**). Here only sinusoidal perturbations are considered for the model (5.3.7) with synaptic kernels (5.3.5) and (5.3.6). Solid and dashed lines correspond to the stable and unstable branches respectively. Parameters are $w_2 = 0.51$, $\sigma = 2$, $p = 5$.

Eigenvalues that arise from sinusoidal and varicose instabilities with a 5-mode instability are plotted in Fig. 5.13. Simulations are initiated with two points of interest taken from Fig. 5.10, that are $(\kappa, D) = (0.2271, 21.596)$ (left) and $(\kappa, D) = (0.1998, 3.3688)$ (right). As seen, the varicose instability dominates over the sinusoidal instability for small values of active region width, and this agrees the direct numerical simulations shown in Fig. 5.8 and Fig. 5.9.

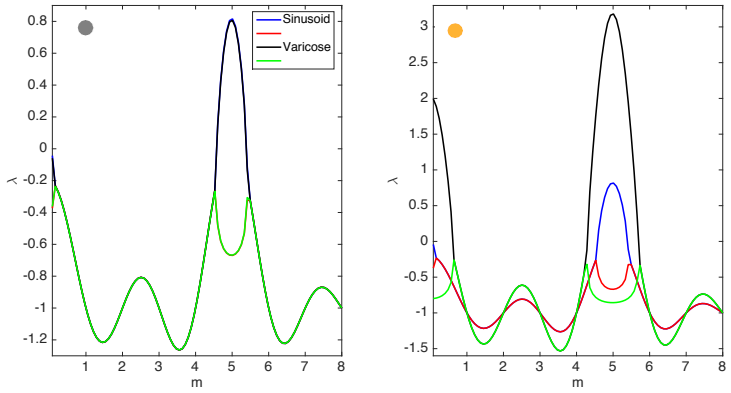

Fig. 5.13: Spectra showing 5-mode instability for solutions shown in Fig. 5.10, indexed by the gray and yellow colour spots. Parameters: $k = 0.1$, $w_0 = 0.19$, $w_2 = 0.51$, $g = 0.6$, $\sigma = 2$.

5.4 ORIENTATION-INDEPENDENT SOLUTIONS

Direction selectivity is no doubt one of the most important characteristics of the cells in V1. However, the results obtained by Chen *et al*. showed that in addition to the well established orientation dependent mechanism, there exist also some sort of orientation independent mechanism underlying the direction selectivity in V1 [199]. Here we investigate orientation independent steady state solutions, and show how homogeneous oscillatory, homogeneous non-oscillatory and inhomogeneous forms of pathcy horizontal connectivity (in the spatial direction) give rise to different bifurcation structures. The (non)oscillatory kernel is determined depending upon the

parameter k in (5.3.6), where taking $k = 0$ blocks oscillatory behaviour in spatial distribution. Depending upon the control parameters, solutions can be organised in snaking, damped snaking and non-snaking branches. The term *snaking* refers that the solution branches of spatially localised (steady) structures oscillates backward and forward [131, 200]. The localised patterns of cortical activity through the mechanism of homoclinic snaking has been previously associated with orientation selective activity in V1 [131].

Considering $w_2 = 0$ in (5.3.5) for an orientation independent solution, time dependent equation (5.3.7) becomes

$$u(x) = \frac{w_0 \pi}{1+g} \int_{x-x_2}^{x-x_1} \mathrm{d}x' J(x'), \tag{5.4.1}$$

where J (5.3.6) denotes patchy horizontal connections. Here, the level set condition is given as

$$u(x_1) = \kappa = u(x_1 + D). \tag{5.4.2}$$

Now we construct the explicit solutions of (5.4.1) with homogeneous and inhomogeneous choices of patchy horizontal kernel (5.3.6).

5.4.1 *Homogeneous Non-oscillatory Spatial Distribution*

Considering two threshold crossings x_1 and x_2 for a stripe, here we show how purely excitatory horizontal connections lead to a non-snaking bifurcation diagram. Using equations (5.4.1) and (5.3.6) with $x_{1,2} = \mp D/2$, one obtains

$$\frac{u(x)}{\widetilde{\rho}} = \begin{cases} 1 - \mathrm{e}^{-D/4\sigma} \cosh\left(\dfrac{x}{2\sigma}\right), & \text{if } |x| < \dfrac{D}{2} \\ \mathrm{e}^{-x/2\sigma} \sinh\left(\dfrac{D}{4\sigma}\right), & \text{otherwise} \end{cases}$$

where $\widetilde{\rho} = 2w_0\pi/(1+g)$. Note that, for now, we take $k = 0$ in equation (5.3.6), blocking oscillations in the spatial distribution of patchy horizontal connections. In this setting, the threshold condition is $\kappa = \widetilde{\rho}\left(1 - \mathrm{e}^{-D/2\sigma}\right)/2$.

In order to determine stability for an orientation independent stripe with homogeneous non-oscillating kernel, we consider perturbations of the form $\widehat{x_i} = x_i + \epsilon_i e^{\lambda t}$ with $i = 1, 2$ and follow the similar approach as in §5.3.2. Here δu_1 can be calculated as the difference between perturbed and unperturbed quantities:

$$\delta u_1 = w_0 \pi \int_0^\infty \mathrm{d}t' G_{11}(t') \left\{ \epsilon_1 \left[J(D) - J(0) \right] - \epsilon_2 J(D) e^{-\lambda t'} + \epsilon_1 J(0) e^{-\lambda t'} \right\},$$

where using G_{11} in (B1.1), the quadratic equations

$$\lambda^2 - \lambda(\lambda_+ + \lambda_- + \lambda_+ \lambda_- \widetilde{M}) + \lambda_+ \lambda_- (1 - \widetilde{M}) = 0, \tag{5.4.3}$$

$$\lambda \left(\lambda - (\lambda_+ + \lambda_- + \lambda_+ \lambda_-) \right) = 0, \tag{5.4.4}$$

leads two pairs of eigenvalues arise from sinusoid and varicose perturbations respectively. Here

$$\widetilde{M} = \frac{J(0) + J(D)}{J(0) - J(D)}. \tag{5.4.5}$$

The ideas previously presented by Avitabile *et al.* [201], to analyse non-snaking bifurcation diagram for localised bumps in a one-dimensional neural field with no adaptation, remain valid for an orientation independent coupled ring model with adaptation. We plot the solutions and their bifurcation diagram in Fig. 5.14, where a purely unstable branch (to sinusoidal perturbations) is shown. Here a non-snaking bifurcation branch has a vertical asymptote, due to $\lim_{\kappa \to w_0 \pi/(1+g)} D = \infty$. The vertical stripe emerging from varicose instabilities is found either stable or neutral (not shown).

5.4.2 *Homogeneous Oscillatory Spatial Distribution*

We will now concentrate on the more complicated and interesting case of $k > 0$, $k \in \mathbb{N}$ in the kernel of patchy horizontal connections (5.3.6), by which inhibitory interactions with different strengths are included in the spatial distribution. Depending on the modulatory parameter k in (5.3.6) and orientation parameter w_2 in (5.3.5), snaking branches occur with a damped symmetry in stripe width D.

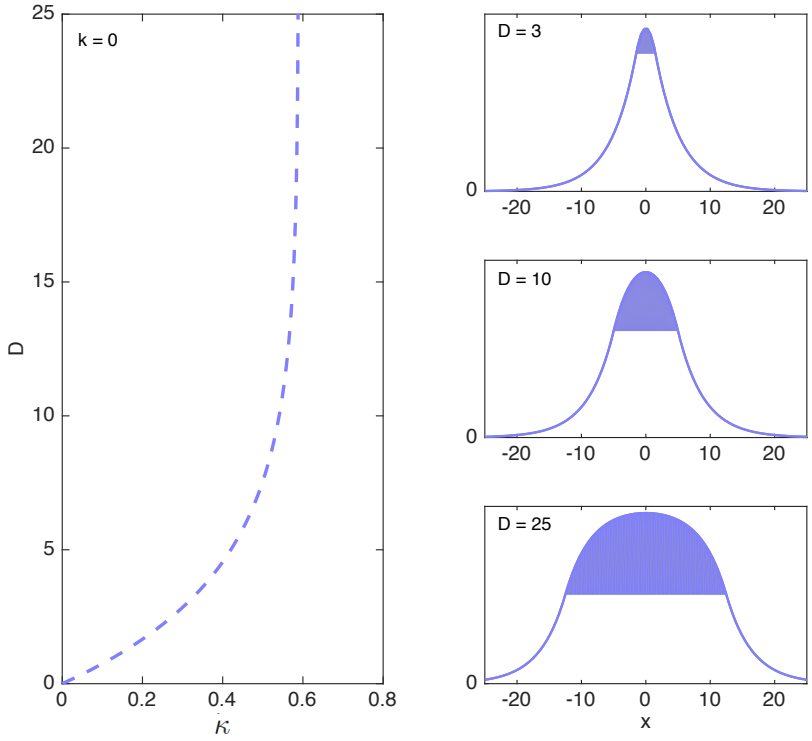

Fig. 5.14: Bifurcation diagram for an orientation independent solution (5.4.1) with a homogeneous spatial kernel J (5.3.6). Only unstable fronts are obtained with $k = 0$ and $w_2 = 0$ (left) . Here D denotes the width of the active region, that is $D = x_2 - x_1$. Selected profiles along the branch are shown (right). Shading areas in profiles represent the activity above the synaptic threshold. Parameters are $w_0 = 0.3$, $\sigma = 2$, $g = 0.6$, $\tau = 1$.

We can explicitly construct stationary solutions for a non-zero modulation parameter k given by

$$\frac{u(x)}{\widetilde{\rho}} = \begin{cases} 2 - Ae^{-BD/4\sigma}\cosh\left(\frac{Bx}{2\sigma}\right) - Be^{-AD/4\sigma}\cosh\left(\frac{Ax}{2\sigma}\right), & \text{if } |x| < \frac{D}{2} \\ Ae^{-Bx/2\sigma}\sinh\left(\frac{BD}{4\sigma}\right) + Be^{-Ax/2\sigma}\sinh\left(\frac{AD}{4\sigma}\right), & \text{if } x > \frac{D}{2} \\ Ae^{Bx/2\sigma}\sinh\left(\frac{BD}{4\sigma}\right) + Be^{Ax/2\sigma}\sinh\left(\frac{AD}{4\sigma}\right), & \text{if } x < -\frac{D}{2} \end{cases}$$

where $\widetilde{\rho} = w_0\pi/(AB(1+g))$ with $A, B = 1 \pm 4\sigma ik$. Here, the threshold condition takes the form

$$\kappa = \frac{\widetilde{\rho}}{2}\left(4 - A\left(1 + e^{-BD/2\sigma}\right) - B\left(1 + e^{-AD/2\sigma}\right)\right). \tag{5.4.6}$$

Figure 5.15 shows that larger values of k lead to snaking behaviour which decreases in κ-range as stripe width D increases. The stability for orientation independent stripes with a homogeneous oscillatory kernel ($k > 0$) can be similarly performed as in §5.4.1, where we consider small perturbations at the threshold crossings. Moreover, destabilisation to multiple stripes can arise as a result of more than two threshold crossings with $k > 0.2$, shown in the profile for $D = 10$ in Fig. 5.15. Since the turning points between these branches become difficult to distinguish for large values of D, stationary points where the stability changes can be explicitly found according to

$$\frac{d\kappa}{dD} = \frac{w_0\pi}{2\sigma(1+g)}\left(e^{-BD/2\sigma} + e^{-AD/2\sigma}\right) = 0. \tag{5.4.7}$$

This can also be seen from the spectral equations in (5.4.3) and (5.4.5), where $\widetilde{M} = 1$ for $\lambda = 0$ is obtained with

$$J(D) = 0. \tag{5.4.8}$$

Note that there is a proportional relationship between (5.4.7) and (5.4.8):

$$\frac{d\kappa}{dD} = \frac{w_0\pi}{1+g}J(D), \tag{5.4.9}$$

which implies that the change in the threshold with respect to the stripe width linearly depends upon the synaptic kernel of patchy horizontal connections evaluated at the stripe width D.

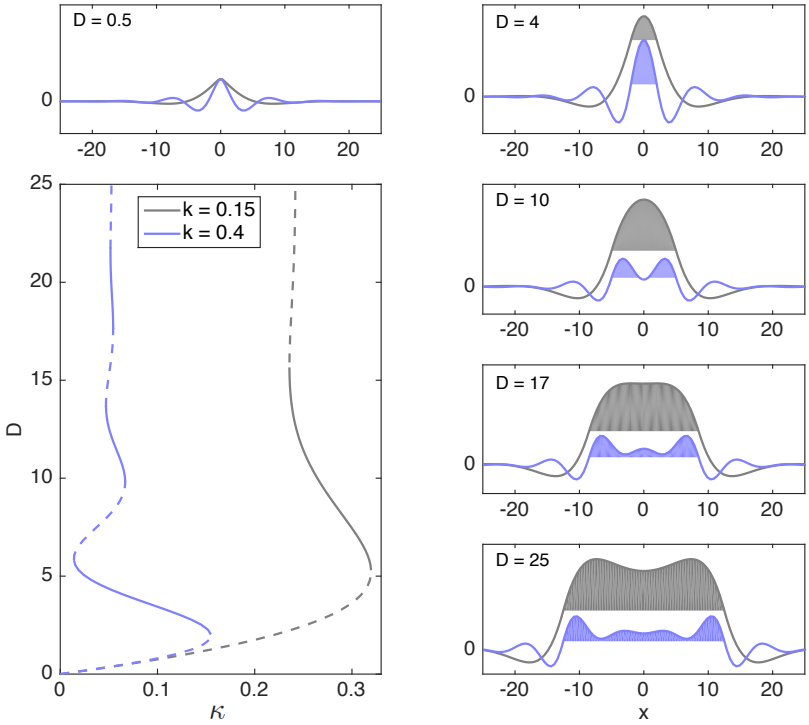

Fig. 5.15: Bifurcation diagram for an orientation independent solution (5.4.1) with an oscillatory homogeneous spatial kernel J ($k > 0$) (5.3.6), exhibiting sinusoid perturbations. Here the width of the active region D is plotted as a function of threshold κ using equation (5.4.6). Depending on the parameter k, snaking branches are seen with a damped symmetry. Selected profiles are shown along the branch for $k = 0.15$ and $k = 0.4$ (right). Parameters are $w_0 = 0.3$, $\sigma = 2$, $g = 0.6$, $\tau = 1$.

5.4.3 *Heterogeneous Spatial Distribution*

The patchy horizontal connections (5.3.6) that only depend on the Euclidean distance allows the generation of homogeneous solutions with a translational invariance. Incorporating a simple harmonic function ($J \to J \cdot \mathcal{A}$) ensures the modulation of patchy horizontal connections, which in turn breaks the translational invariance. In this case we find stationary solutions in the form

$$u(x) = \frac{w_0 \pi}{1+g} \int_{x_1}^{x_2} \mathrm{d}x' J(x-x') \mathcal{A}(x'), \tag{5.4.10}$$

where $\mathcal{A}$ is a periodic modulation function given as

$$\mathcal{A}(y) = 1 + \widetilde{\zeta} \cos(y). \tag{5.4.11}$$

Here, $\widetilde{\zeta}$ represents the amplitude of the harmonic modulation. The stationary solutions for the spatially heterogeneous system take the form

$$\frac{u(x)}{\widetilde{\rho}} = \begin{cases} \widetilde{\zeta}\left[\mathcal{J}(x;\widetilde{A}) + \mathcal{J}(x;\widetilde{B})\right] - 2\mathrm{e}^{-D/4\sigma}\cosh\left(\dfrac{x}{2\sigma}\right) + 2, & \text{if } |x| < \dfrac{D}{2} \\ \widetilde{\zeta}\mathrm{e}^{-x/2\sigma}\sinh\left(\dfrac{D}{4\sigma}\right)\left(\dfrac{2}{\widetilde{\zeta}} + \dfrac{\mathrm{e}^{\widetilde{A}}}{\widetilde{A}} + \dfrac{\mathrm{e}^{\widetilde{B}}}{\widetilde{B}}\right), & \text{if otherwise} \end{cases}$$

where

$$\mathcal{J}(x;z) = \frac{1}{z}\cosh(x) - \frac{1}{z}\mathrm{e}^{-Dz/4\sigma}\cosh\left(\frac{x}{2\sigma}\right), \tag{5.4.12}$$

with $\widetilde{\rho} = w_0\pi/(1+g)$ and $\widetilde{A}, \widetilde{B} = 1 \pm 2\sigma i k$. Here we consider $k = 0$ for simplicity. Following our standard stability analysis we obtain, for example

$$\begin{aligned} \delta u_2 = w_0 \pi \int_0^\infty \mathrm{d}t' G_{11}(t') \Big\{ & \epsilon_1 \mathrm{e}^{-\lambda t'} \widetilde{F}_1(-\infty; D) + \left[\epsilon_2 - \epsilon_1 \mathrm{e}^{-\lambda t'}\right] \widetilde{F}_2(-\infty; D) \Big\} \\ & + \Big\{ -\epsilon_2 \mathrm{e}^{-\lambda t'} \widetilde{F}_1(-\infty; 0) - \left[\epsilon_2 - \epsilon_2 \mathrm{e}^{-\lambda t'}\right] \widetilde{F}_2(-\infty; 0) \Big\}, \end{aligned} \tag{5.4.13}$$

where $(\epsilon_1, \epsilon_2) = \epsilon(1,1)$ and $(\epsilon_1, \epsilon_2) = \epsilon(1,-1)$ denote sinusoidal and varicose perturbations respectively. Here,

$$\widetilde{F}_1(x;z) = \int_x^z \mathrm{d}y J(y) \mathcal{A}'(D/2 - y), \tag{5.4.14}$$

$$\widetilde{F}_2(x;z) = \int_x^z \mathrm{d}y J'(y) \mathcal{A}(D/2 - y). \tag{5.4.15}$$

Here f' represents derivative of a function f. Using G_{11} in (B1.1), the quadratic equations

$$\lambda^2 - \lambda(\lambda_+ + \lambda_- + \lambda_+\lambda_-\widetilde{M}_1) + \lambda_+\lambda_-(1 - \widetilde{M}_1) = 0, \tag{5.4.16}$$

$$\lambda^2 - \lambda(\lambda_+ + \lambda_- + \lambda_+\lambda_-\widetilde{M}_2) + \lambda_+\lambda_-(1 - \widetilde{M}_2) = 0, \tag{5.4.17}$$

lead to two pairs of eigenvalues corresponding to sinusoidal and varicose perturbations, respectively. Here,

$$\widetilde{M}_1 = \frac{\widetilde{F}_2(0;D) - \widetilde{F}_1(0;D)}{\widetilde{F}_2(0;D)}, \tag{5.4.18}$$

$$\widetilde{M}_2 = \frac{[\widetilde{F}_1 - \widetilde{F}_2](-\infty;D) + [\widetilde{F}_1 - \widetilde{F}_2](-\infty;0)}{\widetilde{F}_2(0;D)}. \tag{5.4.19}$$

Note that the parameter k in (5.3.6) is fixed to zero for analytical tractability. In Figure 5.16, snaking behaviour emerges with a consistent non-shrinking symmetry. As for the oscillatory homogeneous case in §5.4.2, the heterogeneous spatial distribution allows the instabilities resulting from multiple threshold crossings for larger values of modulation parameter k (not shown). As reported in [200], there exist intertwined snaking branches with different symmetries (even/odd branches), which have not been computed here for brevity.

The work presented here is also in tune with the results for snaking bifurcations constructed using the Swift-Hohenberg equation, see [200, 201] for further discussion. It should be noted that the imposition of different type of perturbations may affect the spatio-temporal evolution of a stripe and the conditions for its dynamic instability. For example, in Fig. 5.16, we have only shown the analysis with a sinusoidal perturbation; however, the results of the stability may differ for a varicose perturbation.

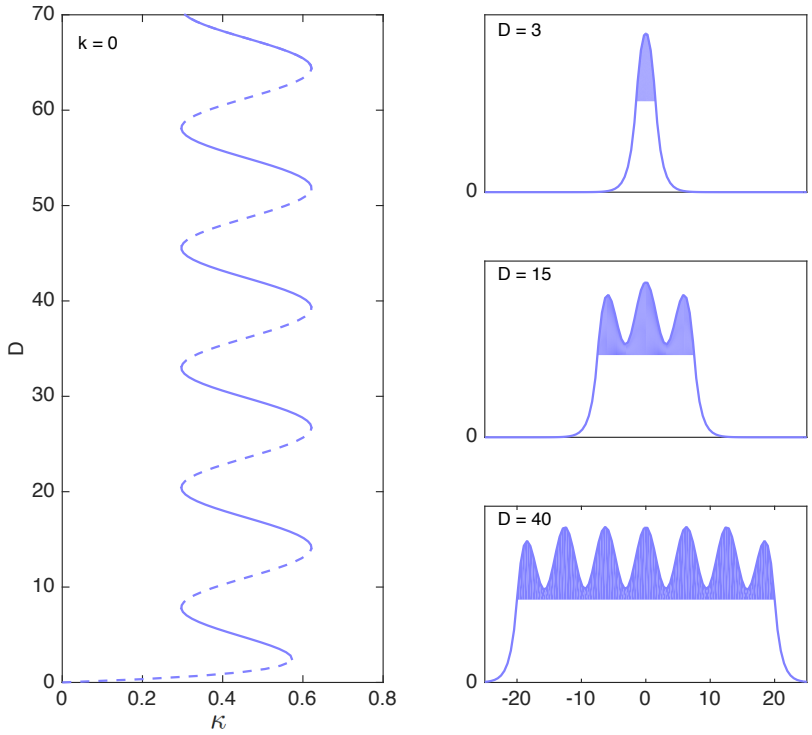

Fig. 5.16: Bifurcation diagram for orientation independent solutions with a heterogeneous spatial kernel, where patchy horizontal connections (5.3.6) are modulated with $\mathcal{A}$ (5.4.11), exhibiting instabilities (left) with sinusoidal perturbations. D represents the width of the active region. Snaking branches are seen with a consistent symmetry. Selected profiles along the branch for $k = 0$ are shown (right). Parameters are $k = 0$, $w_0 = 0.19$, $\sigma = 1/2$, $g = 0.3$, $\tau = 1$, $\widetilde{\zeta} = 0.5$.

5.5 ANALYSIS OF NON-LOCALISED STRIPES

As mentioned in §5.1, there is a topographic map from the visual images captured in the eyes to the neural activity in visual cortex. Non-localised striped visual patterns are one of the most typical patterns of neural activity that have been commonly seen during this image translation from the eyes to the visual cortex, for instance in the case of visual hallucinations [91] (see page 139). In this section we explicitly construct solutions for these patterns and discuss their stability. An illustration of a multiple stripe solution is shown in Fig. 5.17.

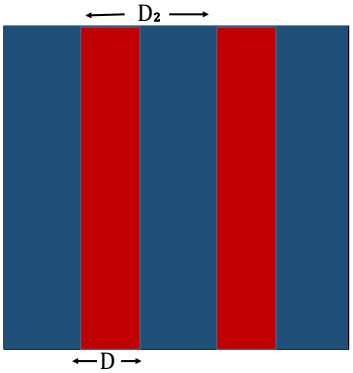

Fig. 5.17: An illustration of two consecutive stripes. D is the width of the active regions and D_2 is the distance between first (second) interfaces of each successive stripes.

Considering an infinite number of stripes, the time independent solution takes the form,

$$u(x,s) = \frac{1}{1+g} \int_{-\pi/2}^{\pi/2} \mathrm{d}s' w(s-s') \sum_{m\in\mathbb{Z}} \int_{x_1+mD_2}^{x_2+mD_2} \mathrm{d}x' J(x-x'). \tag{5.5.1}$$

Taking the system with $x_1 = 0$ and $x_2 = D$ into account, we can obtain two equations resulting from both interfaces; however, due to the symmetry of kernel J, the only existence equation is found to be

$$\kappa = \frac{1}{1+g} \int_{-\pi/2}^{\pi/2} \mathrm{d}s' w(s-s') \sum_{m} \int_{mD_2}^{D+mD_2} \mathrm{d}x' J(x'). \tag{5.5.2}$$

An example for spatio-temporal solutions for stationary multi stripes are shown in Fig. 5.18. Once again we note that the nature of the kernels in spatial (5.3.6) and

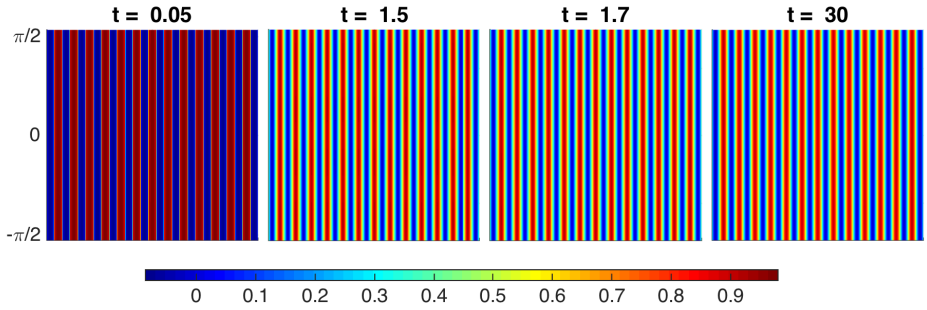

Fig. 5.18: Direct numerical simulations for the emergence of stationary multiple stripes , governed by the model (5.3.1) and (5.3.2), with synaptic kernels (5.3.6) and (5.3.5). Here, the initial conditions are found solving equation (5.5.2) for $D = 3.6189$, $D2 = 7.4428$. Parameters are $w_0 = 0.8$, $\kappa = 0.11$, $\sigma = 2$, $g = 0.8$, $k = 0.35$.

angular direction (5.3.5) substantially simplifies the calculation in equation (5.5.2), that is

$$\begin{aligned}\int_{mD_2}^{D+mD_2} \mathrm{d}x J(x) &= \sum_{m=-\infty}^{-1} \int_{mD_2}^{D+mD_2} \mathrm{d}x \frac{1}{2\sigma} \cos(2kx) \mathrm{e}^{x/2\sigma} + \sum_{m=0}^{\infty} \int_{mD_2}^{D+mD_2} \mathrm{d}x \frac{1}{2\sigma} \cos(2kx) \mathrm{e}^{x/2\sigma}, \\ &= \frac{\mathrm{e}^{AD}-1}{4\sigma A} \left[\sum_{m=-\infty}^{-1} \mathrm{e}^{AmD_2} + \frac{1}{\mathrm{e}^{AD}} \sum_{m=0}^{\infty} \mathrm{e}^{-AmD_2} \right] \\ &+ \frac{\mathrm{e}^{BD}-1}{4\sigma B} \left[\sum_{m=-\infty}^{-1} \mathrm{e}^{BmD_2} + \frac{1}{\mathrm{e}^{BD}} \sum_{m=0}^{\infty} \mathrm{e}^{-BmD_2} \right], \end{aligned} \tag{5.5.3}$$

where $A, B = (1 \pm 4\sigma ik)/2\sigma$. Using properties for a geometric progression, we write

$$\sum_{m=-\infty}^{-1} \mathrm{e}^{AmD_2} = \frac{1}{\mathrm{e}^{AD_2}} \sum_{m=0}^{\infty} \mathrm{e}^{-AmD_2} = \frac{1}{\mathrm{e}^{AD_2}-1}. \tag{5.5.4}$$

Substituting equations (5.5.3) and (5.5.4) in (5.5.2), the existence condition reduces to

$$\kappa = \frac{(w_0 p\pi + w_2 \sin(p\pi))}{p(1+g)} \left[F(A) + F(B) \right]. \tag{5.5.5}$$

Here

$$F(x) = \frac{1}{4\sigma x \left(\mathrm{e}^{D_2 x}-1\right)} \left[\left(\mathrm{e}^{Dx}-1\right) + \left(1-\mathrm{e}^{-Dx}\right) \mathrm{e}^{D_2 x} \right]. \tag{5.5.6}$$

Figure 5.19 shows a bifurcation structure for multiple stripes, where solutions are

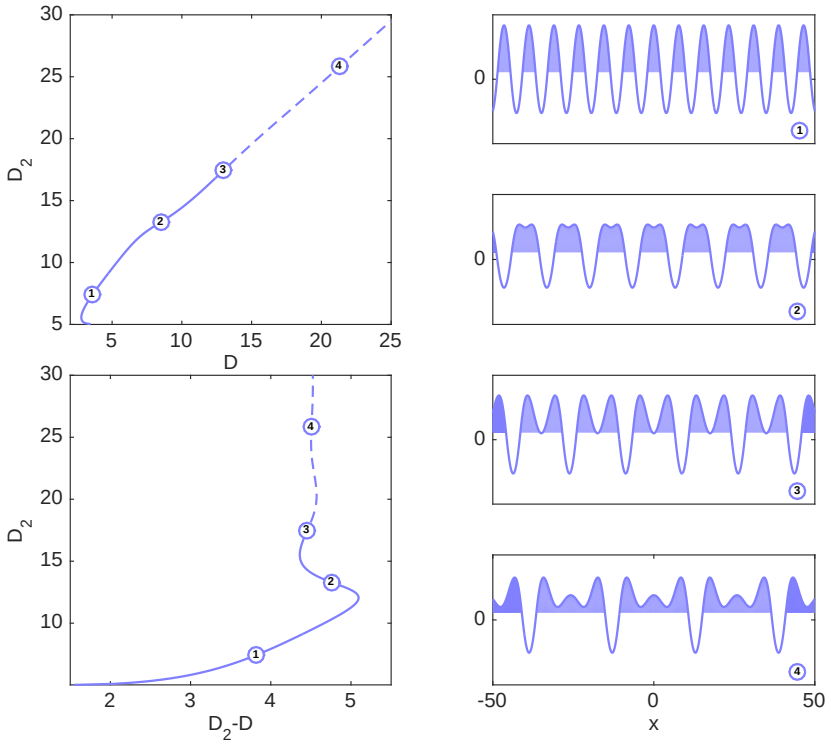

Fig. 5.19: Bifurcation diagrams for multi-stripe solutions (left), where D_2 is plotted as a function of D and $D_2 - D$. Solid and dashed lines represent stationary solutions and multiple stripe instabilities respectively. Selected profiles along the branches are shown (right). For each periodic oscillation in Profile (3), two additional threshold crossings lead to an another multi stripe instability. Parameters are $w_0 = 0.8$, $\kappa = 0.11$, $\sigma = 2$, $g = 0.8$, $k = 0.35$.

stationary for small values of D and D_2 (solid branch). This can be also seen from Fig. 5.18, where direct numerical simulations of Profile (1) (indexed in bifurcation diagrams in Fig. 5.19) shows stable activity. However, in Fig. 5.20**A**, initial stripes which are wider than some threshold break into stripes with smaller width, implying that another multiple stripe instability is formed. For instance, in Fig. 5.19 (Profile 3), the threshold crossing at $D = 12.3$ is found by local minima using $u_x = 0$, $u_{xx} > 0$.

Studies indicate that there is a topographic map between neural activity in primary visual cortex and the visual field where objects are captured as a two-dimensional image in the eye. This retino-cortical map was first modelled by Ermentrout *et al.* [91] using a coordinate transformation interpreted as a log- polar transformation, namely $(x, y) = (ln(r), \theta)$. For example if a point in the visual field is described by (r, θ) in polar coordinates, the corresponding point (via a logaritmic map) in the V1 is described as (x, y) in cartesian coordinates [91, 119]. Figure 5.20**B** shows that the vertical stripes of neural activity in the V1 are mapped to circles in the visual field.

5.6 CONCLUSION & DISCUSSION

In this Chapter, we have extended the work of Bressloff *et al.* [92] for patterns of orientation using a coupled ring model of neural fields with a Heaviside firing rate. Focusing on the interface dynamics, we have developed a one-dimensional description of orientation bumps using the level set method. We have also considered the effects of spike frequency adaptation to investigate varicose and sinusoidal instabilities emerging from a vertical stripe. Although many different parameters are involved in the model and kernels, variations in parameters k (which controls the oscillations in the spatial distribution kernel (5.3.6)) and p (which controls the oscillations in the orientation preference map (5.3.5)) have a particular impact on the

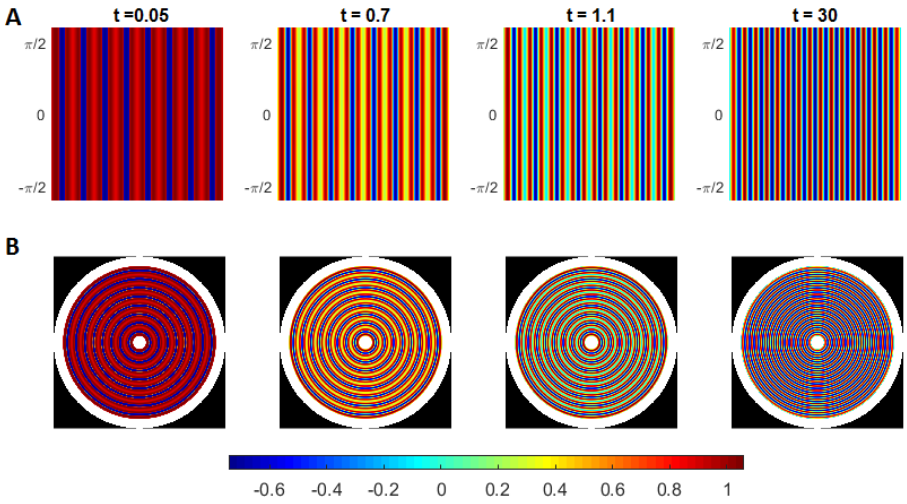

Fig. 5.20: Direct numerical simulations for the instabilities of vertical stripes, governed by the model (5.3.1) and (5.3.2), with synaptic kernels (5.3.6) and (5.3.5). Row (**A**): multi stripe instabilities of the neural activity in V1 emerging from an initially regular stripes with a larger width. Row (**B**): the stripes of neural activity are translated to corresponding circles in the visual field. Data has been taken from Profile (3) in Fig. 5.19, where more than two threshold crossings occur for $D = 13.0140$, $D2 = 17.4682$. Parameters are $w_0 = 0.8$, $\kappa = 0.11$, $\sigma = 2$, $g = 0.8$, $k = 0.35$, $L = 80$.

dynamical behaviour of stripes. We have shown that increasing the parameter k in horizontal connectivity (5.3.6) leads to an enhanced snaking bifurcation structure. Moreover, the parameter p in (5.3.5) gives rise to azimuthal instabilities of p-mode, and any other instabilities are not seen along the solution branches of a stripe.

We have indicated that multiple threshold crossings may occur with $k > 0.2$, and this results into multiple stripes spreading across the domain. There are two potential directions for further examining the evolution of multiple stripes. One is to study stationary multiple stripes after they have been fully formed and the other is to analyse multiple stripes that evolve from a single stripe. The stability analysis of the former case can be similarly performed as in §5.3.1, albeit for eigenvalues computed using a sum over each stationary stripe. The stability analysis of the latter case is not straightforward as each stripe in the system can be treated with different forms of perturbations.

In this Chapter we have only studied pattern formation in the spatial direction, hence it would also be interesting to analyse patterning in the orientation direction. An investigation of new solutions such as oscillatory patterns, and a further analysis for their interface dynamics can also be another route for exploring such high dimensional models with a product structure. Another natural extension of the work in this Chapter is to analyse neural fields posed on $\mathbb{R}^2 \times S$, incorporating two spatial dimensions with an additional dimension that reflects the hyper-columnar structure with orientation preference. In this case it would be interesting to analyse how the extra spatial dimension affects the conditions for stability in a neural field model with a Heaviside firing rate. Moreover, in the primary visual cortex of mammals, patchy horizontal connections link V1 neurons with similar orientation preferences. However, this is not always the case. Rodents have orientation selective cells but do not have orientation maps [193]. Hence, another extension would be to investigate the behaviour of a coupled ring model of neural field in the absence of patchy horizontal connections in primary visual cortex. Furthermore, it

would be interesting to develop stochastic forms of the ring model in neural field theories we considered here, and see how an inclusion of the noise function affects the dynamics of orientation bumps and patterns of visual processing.

6

NEURAL FIELD MODELS ON CURVED GEOMETRIES

So far we have studied neural field models posed on one- or two- dimensional flat spaces. However, our brain, which looks like a wrinkled walnut, is far from being flat. Due to the limited size of our skull, and given the laminar structure of cortex, the brain encapsulates more cortical area as it gets more wrinkles, and in turn it can accommodate more neurons and synapses. Therefore, from the first weeks of embryonic development, folding in the cerebral cortex is seen as a key phenomenon for the emergent of higher order functions such as intelligence and cognition [202, 203]. Perhaps the first attempt on modelling the bio-mechanical development of the folded cortex (six-layered architecture) is due to Richman *et al.* [204], who showed that cortical folding emerges as a result of differential growth rate, where upper cortical layers (layers I-III) grow faster than lower cortical layers (layers IV-VI). Although the model presented by Richman *et al.* is able to explain a mechanical transformation from a planar surface to a realistic folded surface, its reliance on the differences in the growth rates between cortical layers, without any reference to neocortical and functional organisation in the cortex, has been thought of as unrealistic by the scientific community [205]. Before Richman *et al.*'s studies, several hypotheses were proposed about the source of cortical folding; for example, one hypothesis is that gyri and sulci patterns are first formed by a

chemical morphogen, then cortical folding occur when gyri (on top) grow more than sulci [206, 207]. No proof has been found for this hypothesis.

Here, we study the propagation of a travelling front solution in a standard neural field model posed on domains with curvature. An idealised Amari model (2.3.1) posed on a generic manifold with a Heaviside firing rate takes the form

$$\frac{\partial u(\boldsymbol{r},t)}{\partial t} = -u(\boldsymbol{r},t) + \int_{\mathcal{M}} W(\boldsymbol{r},\boldsymbol{r}')H(u(\boldsymbol{r}',t)-\kappa)\mathrm{dm}(\boldsymbol{r}'), \tag{6.0.1}$$

where connectivity is described as $W(\boldsymbol{r},\boldsymbol{r}') = w(d(\boldsymbol{r},\boldsymbol{r}'))$ on the cortical manifold $\mathcal{M}$ (with distance measure dm). Here if $\mathcal{M}$ is planar, the natural description for a distance between points is $\mathrm{d}(\boldsymbol{r},\boldsymbol{r}') = ||\boldsymbol{r}-\boldsymbol{r}'||_2$. This choice leads to idealised neural field equations that are invariant with respect to Euclidean translation. However, if $\mathcal{M}$ is a curve in $\mathbb{R}^2$ then the distance between points is described as $d(\boldsymbol{r},\boldsymbol{r}') = ||\boldsymbol{r}-\boldsymbol{r}'||_{\mathcal{M}_g}$ and the curved geometry $\mathcal{M} \subseteq \mathbb{R}^2$ can be written by the parametrisation:

$$\mathcal{M} = \{\boldsymbol{r} = (x,y) \in \mathbb{R}^2 | x = \varphi(s), y = \varsigma(s), s \in [0,1]\}. \tag{6.0.2}$$

Here the distance function can be expressed as $d(\boldsymbol{r}(s),\boldsymbol{r}(s')) = |l(s)-l(s')|$ where $l(s) = \int_0^s \mathrm{d}\alpha \sqrt{\varphi'(\alpha)^2+\varsigma'(\alpha)^2}$. This choice leads to a neural field model that is invariant on manifold $\mathcal{M}$, if $\mathcal{M}$ is a closed curve.

In §6.1, we overview the structural and functional properties of a folded brain, as well as the functional interactions between grooves and ridges that make the folds. Based on the biologically relevant assumptions that we make for possible neural interactions in a folded cortex in §6.2, the main focus will be on spatio-temporal synaptic activity on non-planar geometries. For example, in §6.3, we discuss (6.0.1) a circular domain of radius R, where the connectivity function depends solely on the arclength distance between interacting neurons. This in fact mimics the dynamics of the standard Amari model posed on a real plane with a translationally invariant synaptic kernel (dependent on the Euclidean distance). Then we extend our model to include heterogeneity and adaptation on a circular domain, where we describe reflection and compression phenomenon in travelling pulses (§6.4).

Considering gyrus (sulcus) as a part of the circumference (arc), next in §6.5, we begin modelling the activity of cortical ridges, as well as the combination of cortical ridges and grooves that mimic folds in the cortex. Lastly in §6.6 we incorporate the effects of curvature in the synaptic kernel in (6.0.1) and discuss the dynamics of a travelling front.

6.1 BIOLOGICAL BACKROUND

The ridges and grooves which make the cortex (grey matter) folded are called gyri and sulci respectively [208], and the process forming the cortical folding is known as gyrification. A recent experiment performed by Mahadevan *et al.* [207] has shown that varying size, number and position of the neurons during brain development result in the expansion of grey matter relative to white matter. Neuron bodies and synapses (axon terminals) are located in the grey matter, whilst axons mostly sit in the white matter of the brain and allow the communication between neurons [207]. In Figure 6.1, a comparison of different mammalian brains (at the same scale) shows that animals with a small brain have a smoother brain, whereas those with a large brain have different degrees of wrinkling [209]. For example, a human brain cortex has ~ 2500 cm^2 surface area, whereas a shrew has only ~ 0.8 cm^2 [209], see Fig. 6.1. Thus, although the shape and the degree of folding are essential, the influence of the size of the brain on its functional organisation cannot be denied. Here we ignore the differences in brain volume, and discuss how the folded structure of the cortex with neural interactions varying between gyri and sulci influences the structure and nature of synaptic travelling waves. See [208] for a recent comprehensive overview about molecular and cellular factors that affect cortical size and folding.

There is now strong evidence that intelligence and learning are most often associated with the gyrification in the cortex. For example, when body size against brain

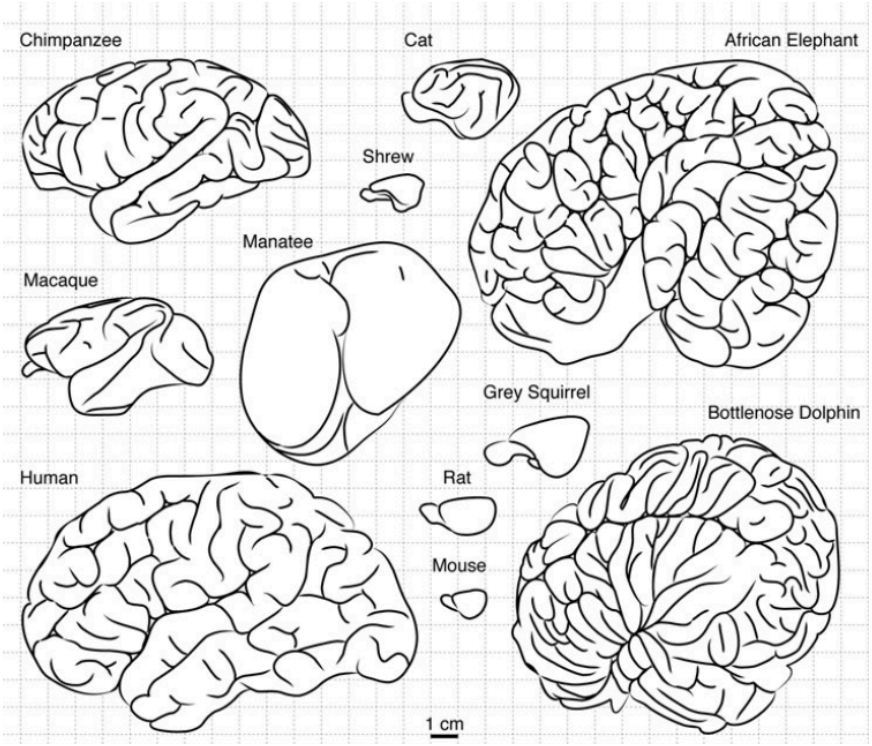

Fig. 6.1: Schematic pictures of various mammalian brains plotted at the same scale. As seen, shrew, rat and squirrel brains are quite smooth compared to notably wrinkled dolphin brains, that appear to be almost twice as folded as a human brain. Picture reproduced from [209].

volume is scaled, mammalian brains have more gyrification than non-mammalian brains, and the most wrinkled of all these is found to be a human brain, see Fig. 6.1. The high gyrification in a small volume helps the human brain to generate more connections and perform higher order functions that distinguish us from other species [210]. However, abnormal alterations in brain folding may cause significant limitations in brain functioning, including intellectual disabilities (difficulties in learning, problem solving and decision making) [209, 211]. Some people are born with a disease called lissencephaly (smooth brain syndrome), where they suffer from severe mental retardation, muscle spasms, learning difficulty, speech disturbance and the majority die before the age of ten [208, 209, 212]. In addition, considering the body size and the brain volumes of the mammals presented in Fig. 6.1, it is often not straightforward to understand if there is an evolutionary lissencephaly. One interesting example (as an exception) could be that the body size of the manatee is comparable with that of Bottlenose dolphin; however the brain size of the manatee is comparable with that of an chimpanzee [209]. This implies that the manatee has a smooth (lissencephalic) brain in comparison to other mammals measured at the same scale. Note that cortical layers of a normal brain are much thinner than that of a smooth brain where enormous number of neurons accumulate in thickened layers with a limited lateral expansion that makes the cortex difficult to bend and form wrinkles [213].

It is known that brain function decreases in the elderly and that short term memory seems to fade. Although there are various other reasons (e.g reduction in cerebral blood flow [214]), this may mostly result from the shrinkage of brain tissue in general: widening of sulci and shrinkage or the gradual thinning of gyri. Abnormalities in cortical folding have been linked to many chronic long-term fatal conditions. For example, there are several studies that report a considerable folding reduction in both hemispheres of patients with chronic schizophrenia [215, 216]. Alterations or malformations in cortical folding have also been linked to intractable epilepsy in humans [217, 218]. In addition, it has been shown that cortical gyrification is

decreased in patients with severe Alzheimer's disease, where the width of sulci is found to be greater compared to controls [219]. As a counter example, preliminary studies of MRI scans shows that the patients with autism tend to have increased patterns of gyrification, and this increase will be more notable in children and teenagers than in adults [220].

6.2 LOCAL CORTICAL INTERACTIONS IN A FOLDED CORTEX

In planar neural field models, it is often assumed that synaptic connectivity is translationally invariant, namely that it depends on Euclidean distance. However, since axon terminals lie close to the cortical surface, the synaptic connectivity on a folded brain mostly relies on geodesic distance [221]. In this sense, we expect differences between dynamics of planar and non-planar neural tissue.

There have been a few papers addressing how neural interactions via geodesic paths or shortcuts affect the activity of a neural population. For example, as required for the information processing in the histological studies of grey matter, Lo *et al.* proposed a model of intrinsic grey matter connectivity using data from a human brain to explain the importance of maximum clustering and minimum path length between neurons, where excessively long geodesic paths are ignored, and shortcut interactions are taken into account with a signed distance method to detect spurious connections [222]. In their setting, the connectivity function was considered with several constraints: (i) two neurons are connected if they lie within a specific Euclidean distance. In other words, a circle of a radius R (ambient space) is drawn around a neuron which should only connect to its target cell within the circle, (ii) the neurons that are nearby in ambient space but excessively distant on the cortical surface (geodesically) have non-physical connections and their interactions are ignored. Comparing the cortical activity obtained on a folded domain with that of an inflated (smooth) domain, Lo *et al.* found that activity of an in-

flated structure is much slower [222]. Here, the radius R of the ambient space is a key factor, because as R is increased, the neural network will include more distant connections, implying more folds extending into the white matter [222]. Therefore, small R would trigger dense and short-range connections, and large R would trigger sparse and long-range connections. Although the connectivity function in such simple cortical network models interpolates between standard Euclidean and geodesic distance metrics, it can still provide insight into the effect of brain morphology on dynamics. Now we discuss some factors that may affect neural interactions and the consequences for waves travelling across gyri and sulci.

In real brain, axons of neurons usually tend to follow the surface of the cortex. Namely, if axons travel for a large distance they usually follow the contour surface of grey matter; however, neurons may also connect via shortcuts, particularly for very local (short-range) interactions [222, 223]. This implies that, although neurons in close proximity are more likely to connect using shortcuts and geodesic paths, spatially separated neurons tend to connect on geodesic paths. Note that neurons and brain regions that are spatially close have a relatively high probability of being connected, whereas connections between spatially remote regions are less likely [224].

Local cortical connections may be myelinated as well as unmyelinated. The speed of conduction for unmyelinated nerve fibres is $0.5 - 2$ mm/sec, whereas that for the myelinated ones is $4 - 70$ mm/sec [225]. The fibres along the neurons that are far from each other are most likely to be myelinated. Hence long-range connections may trigger cortical waves to move faster, while short-range connections may lead to slower wave propagation. However, the neural field activity is the sum of the great number of individual neurons which often involve a mixture of myelinated and unmyelinated connections. Therefore, further research is needed to model the tissue with the mixture of fibre types.

Hence, cortical waves which travel along myelinated fibres propagate faster than those travel along unmyelinated fibres, implying that the velocity of cortical waves is expected to be slow in regions where neurons are locally connected. Thus a potential implication is that long-range connections may trigger cortical waves to move faster, while short-range connections lead to slower wave activity in the cortex.

Another important factor which affects local cortical connections is the thickness between brain wrinkles. For example, the thickness of a gyrus in human cerebral cortex (2.7 ± 0.3 mm on average) is found to be greater than that of sulci (2.2 ± 0.3 mm on average), and the number of neurons is found to be larger in gyri compared to that in sulci [122, 226, 227]. Moreover, recent analyses of DTI (diffusion tensor imaging) and HARDI (high angular resolution diffusion imaging) data by Deng *et al.* have confirmed that gyral regions are connected by much denser fibre tracks than sulcal regions, where stronger interactions occur in gyri [228, 229]. Inspired by these findings and motivated by the fact that DTI derived fibres determine the structural organisation for functional connectivity, Deng *et al.* hypothesise that gyri serve as global functional interaction units, whereas sulci are seen as local functional units [228, 230]. In addition, their experimental results demonstrated that there are differences in terms of functional connectivity strengths, where interactions among gyral-gyral regions is strong, is weak among sulcal-sulcal regions, and moderate between gyral and sulcal regions [228]. A straightforward implication of these results is that gyri are mostly seen as central units of functional connections, that communicate with neighbouring sulci as well as distant gyri and other distant cortical areas, while sulci are able to exchange information with neighbouring gyri as well as other areas of the cortex through gyri (indirectly), see [228–230] for further discussion. All these findings are summarised in Fig. 6.2.

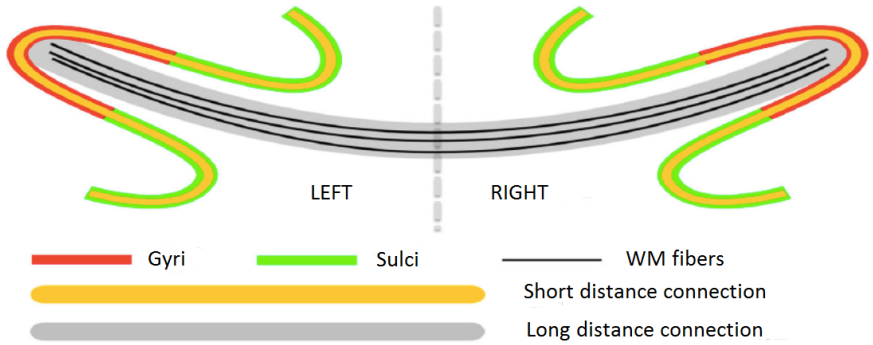

Fig. 6.2: A diagram illustrating functional connections between gyri and sulci. Interactions are strong within gyri (red), weak within sulci (green), and moderate between them (grey). Gyri can make long-range connections through fibres (black lines), as well as short-range connections among neighbouring gyri and sulci. Sulci, on the other hand, make short-range connections with their neighbouring cortical regions. Image reproduced from [228].

6.3 TRAVELLING PULSES IN NEURAL FIELDS ON CIRCULAR DOMAINS

Before we analyse the properties of neural field models posed on non-planar domains with a Heaviside rate, it is informative to start with a discussion for neural fields posed on a circle, for which (6.0.1) can be written as

$$u_t(\theta,t) = -u(\theta,t) + \psi(\theta,t), \qquad \psi(\theta,t) = R\int_{\Omega_+(t)} \mathrm{d}\theta' w(R(\theta-\theta')), \tag{6.3.1}$$

where $\Omega_+ = \{\theta | u(\theta,t) > \kappa\}$. Here R is the radius of the circle, $\theta \in [-\pi,\pi]$ and $t \in \mathbb{R}^+$. We point out that, in this case, the model is still translation-invariant, therefore we expect that a travelling pulse can be achieved either in the presence of an adaptation variable, or in the presence of an asymmetric synaptic kernel. Here we consider a horizontally shifted Mexican hat connectivity as

$$w(\theta) = \frac{1}{2\pi}\left(\mathrm{e}^{-|\theta+\theta_s|} - \frac{1}{\gamma}\mathrm{e}^{-\beta|\theta+\theta_s|}\right), \tag{6.3.2}$$

where θ_s is the shifting parameter (the kernel is shifted right if $\theta_s < 0$, and left if $\theta_s > 0$). Hence a time dependent solution for a pulse with two threshold crossings at $\theta_1(t)$ and $\theta_2(t)$ on a circular domain is given by

$$q(\theta, t) = R \int_{\theta-\theta_2(t)}^{\theta-\theta_1(t)} w(R\theta' - \theta_s) \mathrm{d}\theta'. \tag{6.3.3}$$

Here the pulse width is $\Delta_\theta = \theta_2(t) - \theta_1(t)$. Considering $q(\theta_2) = q(\theta_1) = \kappa$, the threshold condition takes the form

$$\frac{\kappa}{R} = \int_0^{\Delta_\theta} \mathrm{d}\theta w(R\theta - \theta_s) = W(\Delta_\theta) - W(0), \tag{6.3.4}$$

where

$$W(\theta) = \int_{-\infty}^{\theta} w(R\theta' - \theta_s) \mathrm{d}\theta'. \tag{6.3.5}$$

The profile $u(\theta)$ for the pulse solution is given by the formula

$$\frac{u(\theta)}{R} = W(\theta - \theta^*(t) + \Delta_\theta/2) - W(\theta - \theta^*(t) - \Delta_\theta/2), \tag{6.3.6}$$

where $\theta^* = \theta^*(t)$ is the time dependent center of the pulse. In Figure 6.3 we show time simulations of the model (6.3.1) with periodic boundary conditions, where a slight decrease in the threshold value κ leads to a transition from a travelling pulse to an inverted travelling pulse. In Figure 6.4, we show solution branches for the pulse width as a function of firing rate threshold and radius on a circular domain, and we obtain similar results to one-dimensional neural fields posed on a real line (see Chapter 3).

Considering a pulse center at $\theta = \theta^*$ allows us to define two threshold crossings at $\theta_1 = \theta^* - \Delta_\theta/2$ and $\theta_2 = \theta^* + \Delta_\theta/2$. As seen from (6.3.6), the activity at the center of the pulse is $u(\theta^*) = R\left[W(-\Delta_\theta/2) - W(\Delta_\theta/2)\right]$. Note that the size and shape of the pulse does not change as it travels in the θ direction. A global maximum exists for a symmetrical yet shifted kernel, if $q'(\theta) = 0$ and

$$\frac{q''(\theta)}{R} = w'\left(R(\theta - \theta^* + \Delta_\theta/2) - \theta_s\right) - w'\left(R(\theta - \theta^* - \Delta_\theta/2) - \theta_s\right) < 0.$$

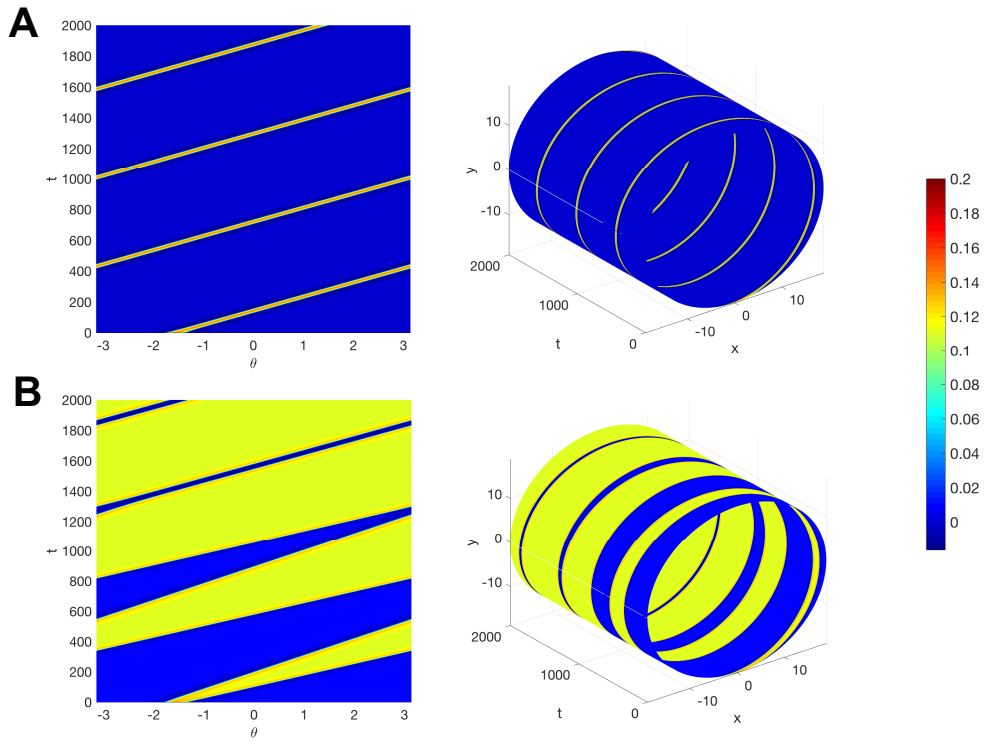

Fig. 6.3: Time simulations of the model (6.3.1) with synaptic connectivity function (6.3.2) and Heaviside firing rate simulated on a circle of radius $R = 6\pi$ with periodic boundary conditions. Panels (**A**): a travelling pulse with $\kappa = 0.06$. Panels (**B**): transition into an inverted travelling pulse (that settles after $t = 1000$) with $\kappa = 0.05$. Right panels: time simulations shown on a cylinder. Other parameters are $\beta = 0.5$, $\gamma = 3$, $\theta_s = -0.2$ with a mesh of $N = 2^{10}$ points.

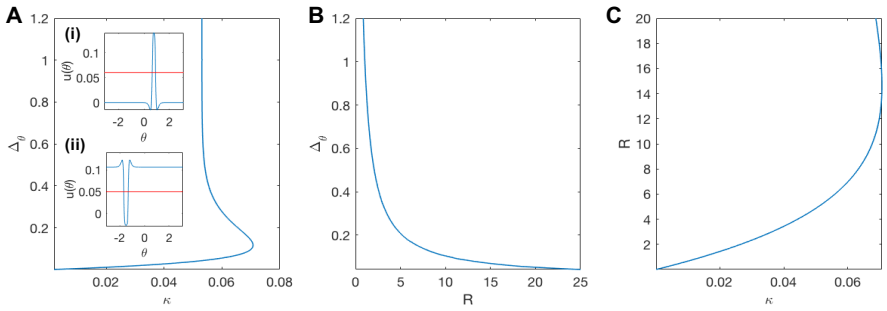

Fig. 6.4: Panel (**A**): full solution branches of the pulse width Δ_θ as function of firing threshold κ for a fixed radius of $R = 6\pi$. Panel (**B**): pulse width Δ_θ as a function of radius R for a fixed threshold $\kappa = 0.06$. A saddle node bifurcation occur at the turning point which separates stable (upper) and unstable (lower) branches (**A**). In panel (**C**) the radius R of the circle is shown as a function of firing threshold for a fixed pulse width $\Delta_\theta = 0.1$. The insets in (**A**) show the profiles of a pulse for $R = 6\pi$ with $\kappa = 0.06$ **(i)** and $\kappa = 0.05$ **(ii)** time= 2000. The initial condition used in the simulations is $u = 2/\cosh(10\theta)$. Parameters are $\beta = 0.5$, $\gamma = 3$ and $\theta_s = -0.2$.

However, depending on the parameter space, a local minimum with $q''(\theta) > 0$ can be found at the center of a sufficiently wide pulse.

As discussed in Chapter 3, an interface between active and quiescent regions can also be described by the level set condition $u(\theta_i(t), t) = \kappa$. The propagation velocity is then obtained by differentiation as

$$c_i = \frac{R\left[W(\theta_i - \theta_1) - W(\theta_i - \theta_2)\right] - \kappa}{u_{\theta_i}}. \tag{6.3.7}$$

Here W is given by (6.3.5) and the denominator is

$$\frac{u_{\theta_i}(t)}{R} = \int_0^\infty \mathrm{e}^{-s}\left[w(R(\theta_i(t-s) - \theta_1(t)) - \theta_s) - w(R(\theta_i(t-s) - \theta_2(t)) - \theta_s)\right] \mathrm{d}s.$$

For a single pulse, it is also possible to calculate the change in the pulse width $\Delta_\theta(t) = \theta_2(t) - \theta_1(t)$ with respect to time, that is

$$\frac{\mathrm{d}\Delta_\theta(t)}{\mathrm{d}t} = \frac{\mathrm{d}\theta_2(t)}{\mathrm{d}t} - \frac{\mathrm{d}\theta_1(t)}{\mathrm{d}t} \tag{6.3.8}$$

$$= R\left(\frac{1}{u_{\theta_2}} - \frac{1}{u_{\theta_1}}\right)\left(W(0) - W(\Delta_\theta) - \kappa\right). \tag{6.3.9}$$

Here if u_{θ_1} and u_{θ_2} are constant, the equilibrium solution to (6.3.4) is stable when

$$\frac{\mathrm{d}}{\mathrm{d}\Delta_\theta}\int_0^{\Delta_\theta} w(R\theta - \theta_s)\mathrm{d}\theta = w(R\Delta_\theta - \theta_s) < 0. \tag{6.3.10}$$

6.4 REFLECTION AND COMPRESSION ON CIRCULAR DOMAINS

The heterogeneities in the cortex may result in changes in the nature of wave propagation. For example reflection and compression behaviour in cortical waves have been found by Weifeng *et al.*[231] in their pioneering experiments performed on rat's visual cortex, where they state

"A primary wave originated in the monocular area of V1 and was compressed when propagating to V2. A reflected wave initiated after compression and propagated backward into V1. The compression occurred at the V1/V2 border, and local $GABA_A$ inhibition is important for the compression [231]."

Goulet *et al.* studied reflection and compression behaviour of waves using a three component planar neural field model that is obtained from the combination of the Pinto - Ermentrout model (where inhibition is blocked) and the Wilson - Cowan equations [135]. Here numerical studies were performed with a smooth sigmoidal firing rate. In this section we explore the reflection and compression of cortical waves using a simple neural field model with adaptation and a Heaviside firing rate posed on a circular domain, that is

$$\tau u_t = -u + \psi - ga, \qquad a_t = u - a, \tag{6.4.1}$$

where

$$\psi(\theta,t) = \int_{\Omega} w(d(\theta,\theta'))A(\theta')H(u(\theta',t)-\kappa)\,\mathrm{d}\Omega(\theta'), \tag{6.4.2}$$

with

$$w(\theta) = \frac{1}{2\pi}\left(\mathrm{e}^{-|\theta|} - \frac{1}{\gamma}\mathrm{e}^{-\beta|\theta|}\right), \quad A(\theta) = \begin{cases} a_m, & \text{if } \theta \in R_1 \\ a_p, & \text{if } \theta \in R_2 \end{cases}. \tag{6.4.3}$$

Here R_1 and R_2 denote the regions where the excitability of the synaptic drive (ψ) changes according to a piece-wise constant function A in (6.4.3). This is demonstrated in Fig. 6.5, where reflection and compression patterns for a travelling pulse are shown for periodic boundary conditions. Considering a travelling wave propagating from region R_1 to region R_2 (or vice versa), partial block of excitability in the medium leads to compression on the border between R_1 and R_2, as shown in Fig. 6.5**A**. In this setting, region R_1 is less excitable relative to R_2. As the wave is being compressed (Fig. 6.5**A**), for which the width of the active region in R_1 (low excitability) is thinner than that is in R_2 (high excitability), a small delay occurs in the synaptic activity. If the delay is sufficiently long, the activity in R_2 may be re-excited and the wave propagating from R_2 to R_1 can reflect backwards as shown in Fig. 6.5**B**. The latency in reflected and compressed cortical waves have been previously discussed by Ermentrout *et al.* [135, 232], who suggests that the characterisation of the excitable behaviour of the medium (Class I or Class II) can be determined by understanding how the wave switches between rest and oscillation. Although the system with Class I excitability (one equilibrium) becomes oscillatory in the presence of high input, the system with Class II excitability undergoes a saddle node bifurcation, where the saddle node point indicates that the spike can be generated with an arbitrarily long latency, see [135, 232] for a further discussion.

In Figure 6.6, we show the change in the pulse width as a function of time for compressed and reflected pulses respectively. As seen from Fig. 6.6**B** the pulse is compressed for a small time period (with a decreasing velocity) before it reflects backward.

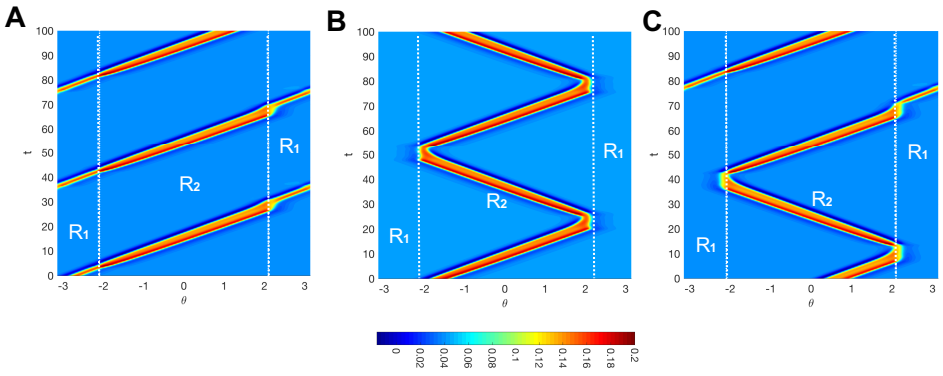

Fig. 6.5: Wave propagation in an inhomogeneous neural field model (6.4.1) and (6.4.2) posed on a circular medium with a Heaviside firing rate and periodic boundary conditions. The borders between R_1 (less excitable) and R_2 (more excitable) regions occur at $\theta_1 = -2\pi/3$ and $\theta_2 = 2\pi/3$. Panel (**A**): pulse compression, where the pulse width decreases (increases) as it travels from high (low) excitable region R_2 (R_1) to low (high) excitable region R_1 (R_2). Panel (**B**): pulse reflection, where the pulse is reflected backwards as it attempts to enter from region R_2 to R_1. Panel (**C**): reflection pattern for a pulse is followed by a compression. Parameter values are $\kappa = 0.03$, $g = 1$, $\tau = 0.2$, $k = -0.2$, $\gamma = 4$, $\beta = 0.4$, $R = 5\pi$, $a_p = 1$, and $a_m = 0.8$ (**A**), $a_m = 0.5$ (**B**), $a_m = 0.75$ (**C**), with a mesh of $N = 2^{10}$ points.

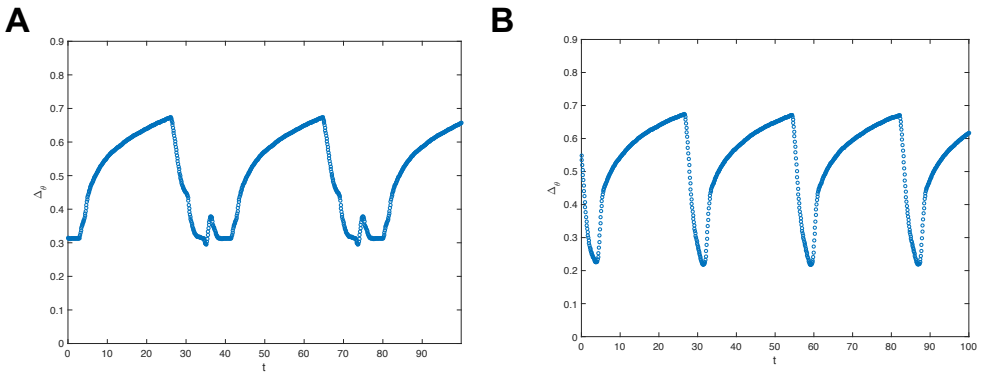

Fig. 6.6: The change in the pulse widths for compressed and reflective waves shown in Fig. 6.5**A** and Fig. 6.5**B** respectively. Parameters are same as Fig. 6.5. For a sufficiently large domain, we expect saturation in the speed and pulse width of a reflected wave.

6.5 GYRAL-SULCAL CIRCULAR SEGMENTS

Now we move away from circular domain and consider the gyrus and sulcus as parts of the circumference (arc) that is cut off from a circle by a chord.

In Fig. 6.7, we show a real line incorporated with an upward circular narrowing (**A**), downward circular narrowing (**C**) as well as their combination (**D**) posed on a large domain $[-L, L]$. As an example, a geometric interpretation for an upward circular narrowing of radius R, with a central angle of θ_g between the line defined by $(-l, 0)$ and $(l, 0)$ is shown in Appendix D1. Here the combination of planar and folded geometries, e.g. $\mathcal{M} = \mathcal{M}_- \cup \mathcal{M}_g \cup \mathcal{M}_+$, can be given by the parametrisations:

$$\begin{aligned}
\mathcal{M}_- &= \{\boldsymbol{r} = (x, y) | x = s,\ y = 0,\ \ s \in [-L, -l]\},\\
\mathcal{M}_g &= \{\boldsymbol{r} = (x, y) | x = R\cos(s),\ y = R\sin(s) + h_0,\ s \in [\theta_1, \theta_2]\},\\
\mathcal{M}_+ &= \{\boldsymbol{r} = (x, y) | x = s,\ y = 0,\ \ s \in [l, L]\},
\end{aligned}$$

with

$$\theta_1 = -\frac{\pi - \theta_g}{2} \ \text{ and } \ \theta_2 = \pi - \theta_1,$$

where $\theta_g = 2\sin^{-1}(l/R)$, see Appendix D1. Now we consider the model (6.0.1) with a simple exponentially decaying synaptic connectivity $W(\boldsymbol{r}, \boldsymbol{r}') = w(d(\boldsymbol{r}, \boldsymbol{r}'))$ where

$$w(d(\boldsymbol{r}, \boldsymbol{r}')) = \frac{1}{2\sigma} \mathrm{e}^{-d(\boldsymbol{r}, \boldsymbol{r}')/\sigma}, \tag{6.5.1}$$

where σ is the decay parameter and d is the distance function. An example of how one can introduce heterogeneity along the manifold is given in equation (6.5.2). Here the connectivity kernel can be described as a combination of arclength (with a strength Y) and Euclidean distance (with a strength $1 - \mathrm{Y}$). The list below gives

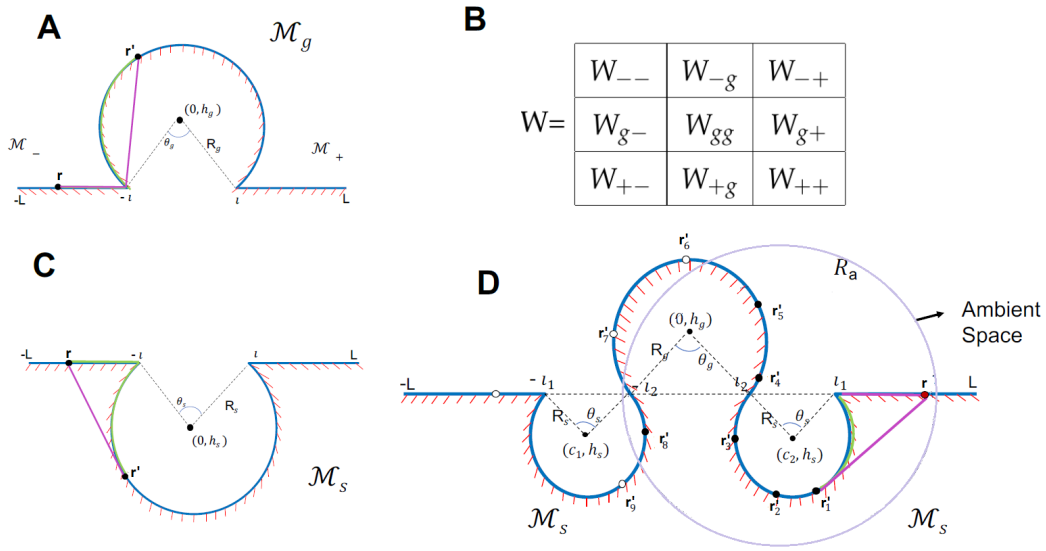

Fig. 6.7: Schematic illustrations of upward and downward circular narrowings combined with planar domains from both sides. Panel (**A**) and Panel (**C**) respectively show upward and downward narrowings, where $\boldsymbol{r}$ and $\boldsymbol{r}'$ points may connect through Euclidean distance, as well as arclength distance. Panel (**B**): total synaptic strength computed for points interacting in between each region of the domain (in Panel **A**); each of them is written in equation (6.5.2). For example W_{-g} is a synaptic connectivity matrix between $\boldsymbol{r} \in \mathcal{M}_-$ and $\boldsymbol{r}' \in \mathcal{M}_g$. Panel (**D**) : a combination of the upward and downward circular narrowings with radii of R_g and R_s respectively. Here the circle of radius R_a denotes the ambient space, by which two neurons are only connected if they lie within a specific Euclidean or arclength distance (see §6.2). The heights h_g and h_s denote apothems (see §D1) of the circles with radii R_g and R_s for gyri and sulci, respectively.

the components of the connectivity function shown in Fig. 6.7**B** on the domain shown in Fig. 6.7**A**.

$$\begin{cases} W_{--} = \|\boldsymbol{r}_1 - \boldsymbol{r}'_1\|_2 \\ W_{-g} = \|\boldsymbol{r}_1 - \xi_1\|_2 + \Upsilon\|\xi_1 - \boldsymbol{r}'_2\|_{\mathcal{M}_g} + (1-\Upsilon)\|\xi_1 - \boldsymbol{r}'_2\|_2 \\ W_{-+} = \|\boldsymbol{r}_1 - \xi_1\|_2 + \Upsilon\|\xi_1 - \xi_2\|_{\mathcal{M}_g} + (1-\Upsilon)\|\xi_1 - \xi_2\|_2 + \|\xi_2 - \boldsymbol{r}'_3\|_2 \\ W_{gg} = (1-\Upsilon)\|\xi_2 - \boldsymbol{r}'_2\|_2 + \Upsilon\|\xi_2 - \boldsymbol{r}'_2\|_{\mathcal{M}_g} \\ W_{g+} = \Upsilon\|\boldsymbol{r}_2 - \xi_2\|_{\mathcal{M}_g} + (1-\Upsilon)\|\boldsymbol{r}_2 - \xi_2\|_2 + \|\xi_2 - \boldsymbol{r}'_3\|_2 \\ W_{+-} = W_{-+}, \;\; W_{+g} = W_{g+}, \;\; W_{g-} = W_{-g} \\ W_{++} = \|\boldsymbol{r}_3 - \boldsymbol{r}'_3\|_2. \end{cases} \tag{6.5.2}$$

Here $\xi_1 = (-l, 0)$ and $\xi_2 = (l, 0)$, and $\|\cdot\|_2$ and $\|\cdot\|_{\mathcal{M}_g}$ denote Euclidean and arclength distances respectively. At this point it is evident that translation invariance is no longer present in the model for $\Upsilon < 1$ in (6.5.2), as the distance $d(\boldsymbol{r}, \boldsymbol{r}')$ is effectively heterogeneous. Once more it should be pointed out that even though the connectivity matrix W is described in a piece-wise manner, the connections that only depend on the arclength distance ($\Upsilon = 1$) allow the generation of solutions with a translation invariance along the manifold, if the manifold is a closed curve. In the rest of the chapter, we will only consider cases in which connectivity along the manifold is homogeneous ($\Upsilon = 1$). Figure 6.8 shows time simulations of the model (6.0.1) with no adaptation, posed on a domain with a combination of real lines ($\mathcal{M}_-$ and $\mathcal{M}_+$) and upward oriented narrowings ($\mathcal{M}_g$) with periodic boundary conditions. We find a wave front that propagates with constant speed *along the manifold*, but that slows down considerably on both sides of the upward narrowing when speed is considered purely from the point of view of an observer tracking movement in the x-direction. This distinction clarifies that the point of view and particular measure taken by an observer changes the observed wave speed.

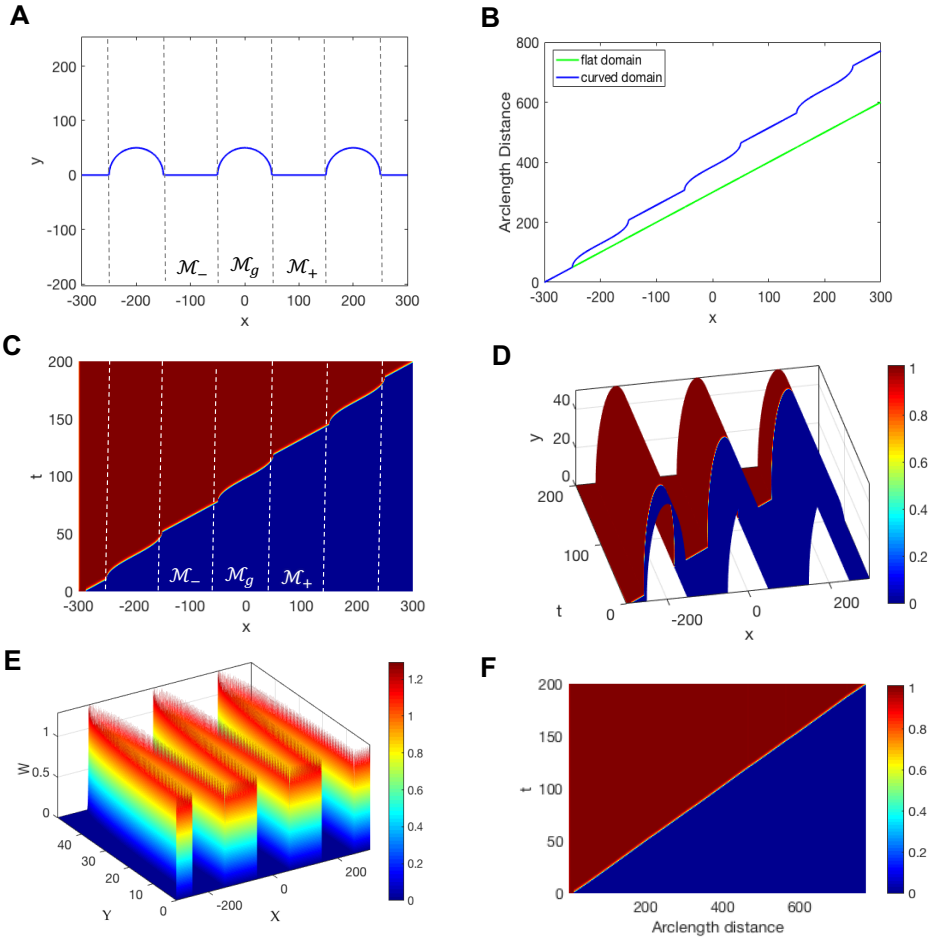

Fig. 6.8: Simulations of the model (6.0.1) with synaptic kernel (6.5.1) and Heaviside firing rate, posed on a large domain $[-L, L]$ with periodic boundary conditions. The synaptic kernel is described as a function of the arclength distance. Panel (**A**): a domain with a series of flat lines and upward circular narrowings. Panel (**B**): distance from the left boundary as a function of space is compared between planar (green) and curved (blue) domain. Panel (**C** & **D**) : space-time simulations for a front solution which travels with a time dependent speed for a specific observer tracking the movement in the x-direction. Panel (**E**): synaptic kernel matrix W is plotted as a function of two-dimensional grid coordinates X and Y, that are based on the coordinates contained in vectors x and y. Panel (**F**): arclength distance is presented as a function of time, where a travelling wave propagating with a constant speed along the manifold can be observed. Parameters are $R_g = 50$, $h_g = 0$, $\sigma = 1$, $\kappa = 0.1$, $L = 300$, with a mesh of 2^{10} points.

6.5.1 *Heterogeneities in the Synaptic Interactions*

In this section, we study neural fields (6.0.1) with a Heaviside firing rate and synaptic modulation posed on a domain with gyri and sulci (shown in Fig. 6.7**D**). The model (6.0.1) with modulation takes the form

$$\frac{\partial u(\boldsymbol{r},t)}{\partial t} = -u(\boldsymbol{r},t) + \int_{\mathcal{M}} w(d(\boldsymbol{r},\boldsymbol{r}'))H(u(\boldsymbol{r}',t)-\kappa)\widetilde{A}(\boldsymbol{r}')\mathrm{dm}(\boldsymbol{r}'), \tag{6.5.3}$$

where

$$w(r) = \frac{1}{2\sigma}\mathrm{e}^{-|r|/\sigma}, \qquad \widetilde{A}(\boldsymbol{r}) = \begin{cases} a_m, & \text{if } \boldsymbol{r} \in \mathcal{M}_s \\ a_p, & \text{if } \boldsymbol{r} \in \mathcal{M}_g \\ a_o, & \text{if } \boldsymbol{r} \in \mathcal{M}_+ \text{ and } \boldsymbol{r} \in \mathcal{M}_- \end{cases}. \tag{6.5.4}$$

Here, $\widetilde{A}$ is a piece-wise constant modulation, and $\mathcal{M}_s$, $\mathcal{M}_g$ and $\mathcal{M}_{+,-}$ denote sulci, gyri and flat domains, respectively. We consider the parametrisation of the model as in (6.0.2). The synaptic kernel described in equation (6.5.2) for an upward narrowing can be extended to include a combination of gyri and sulci. Here we numerically explore how the piece-wise constant modulation $\widetilde{A}$ in (6.5.4) affects the local and overall speed of a front solution.

In Figure 6.9, time simulations of the model (6.5.3) whose associated kernel solely depends on arclength distance ($\mathrm{Y} = 1$ in (6.5.2)) posed on a domain with gyri and sulci (given in Fig. 6.7**D**) are shown. Simulations without any constraints (with an arclength dependent homogeneous kernel) are presented in Fig. 6.9**A**, where the propagation speed significantly decays on both edges of upward and downward narrowings for an external observer tracking the movement in the x direction. As discussed in §6.2, an ambient space is described by a circle of radius R_a. The interactions between neurons that are excessively away from each other, namely the neurons that do not lie within the same ambient space, are ignored in Fig. 6.9**B**, and we find that causes a slower overall wave propagation in the system. As mentioned in §6.2 the gyri are dense, namely stronger neural interactions are

considered in manifold $\mathcal{M}_g$ (increased a_p in (6.5.4)). Thus, a considerably faster propagation is observed in the upward narrowing, when the excitability (synaptic efficacy) is increased by 20% through a piece-wise constant modulation (6.5.4) as shown in Fig. 6.9**C**. On the contrary, increased excitation in sulci and decreased in gyri (opposite to the literature) in Fig. 6.9**D** lead to slower propagation in gyri. Note that the piece-wise modulation $\widetilde{A}$ affects the speed at which a wave travels along the manifold. Since there are two sulci and one gyrus in the system, increased excitation in gyri and decreased excitation in sulci lead to a slower overall front propagation, whereas decreased excitation in gyri, increased in sulci result in a faster overall front propagation. The change in the connectivity function for each of these cases is shown in Fig. 6.10. Although there is a lack of clear evidence in the literature to prove that waves are slow in sulci and fast in gyri, Deng *et al.* showed that gyri are denser with strong neural interactions [228] and Lo *et al.* pointed out that, compared to an inflated domain, activation of the network is significantly faster in a folded cortical domain, and that is due to strong neural interactions [222]. Combining the ideas presented in [222] and [228], where strong neural interactions lead to faster wave propagation, we suggest that cortical waves may be faster in gyri compared to those in sulci.

6.6 CURVATURE

Curvature has been widely used as a fundamental property in pattern classifications in the cortex [233]. This includes a curvature based mesh model for analysing gyrification of the cortical surface [234]. Moreover, the results obtained by Lo *et al.* [222] indicated that the network activation, as well as connectivity structure in the grey matter, is closely associated with the local curvature of the population network. The curvature is calculated as the reciprocal of the osculating circle radius (the radius of the curvature) at every point on a curve, see Fig. 6.11. In a generic

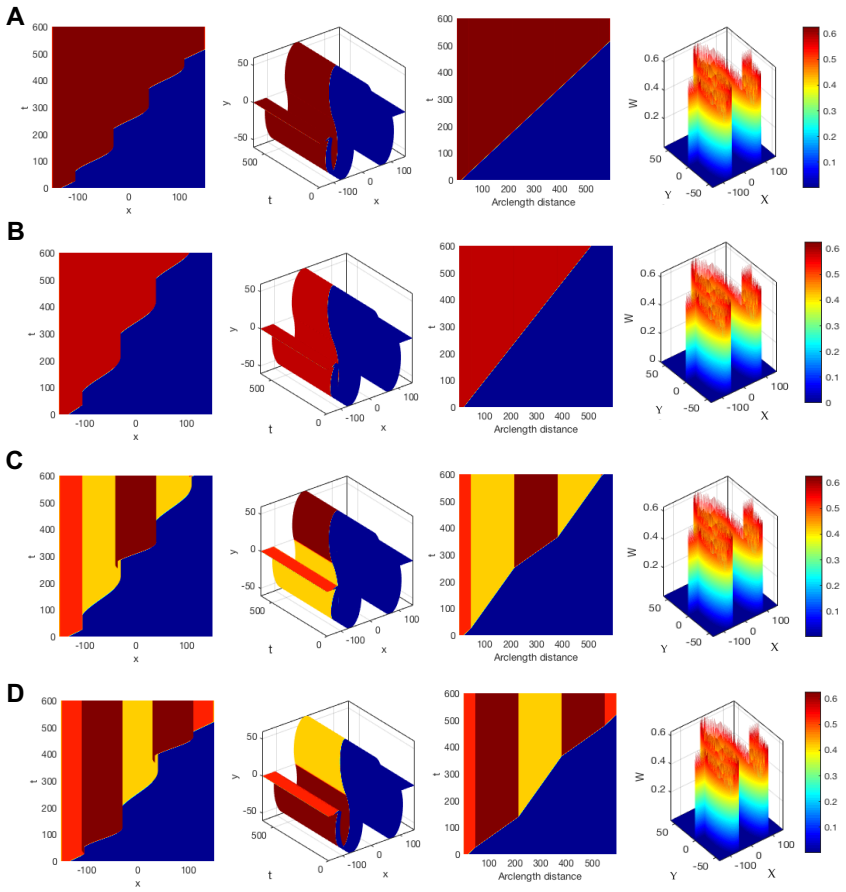

Fig. 6.9: Time simulations of the model (6.5.3) for a front solution with synaptic kernel (6.5.4) and Heaviside firing rate, posed on a large manifold $\mathcal{M} = \mathcal{M}_- \cup \mathcal{M}_s \cup \mathcal{M}_g \cup \mathcal{M}_s \cup \mathcal{M}_+$ on a domain $[-L, L]$, shown in Fig. 6.7**D**. Here the synaptic kernel is chosen to be only a function of arclength distance. Panel (**A**): time simulations of the model without any constraints (control). Panel (**B**): excessively long geodesic distances are not connected in the model, namely $w(\boldsymbol{r}, \boldsymbol{r}') = w(d(\boldsymbol{r}, \boldsymbol{r}'))$ if $d(\boldsymbol{r}, \boldsymbol{r}') < R_a$ and $w(\boldsymbol{r}, \boldsymbol{r}') = 0$ otherwise, where $d(\boldsymbol{r}, \boldsymbol{r}')$ denotes the arclength distance between $\boldsymbol{r}$ and $\boldsymbol{r}'$. Panel (**C**): the excitation in downward circular narrowing $\mathcal{M}_s$ is decreased compared to that in upward circular narrowing $\mathcal{M}_g$ using a piece-wise modulation (6.5.4) where $a_m = 0.8$ and $a_p = 1.2$. Panel (**D**): the excitation in downward circular narrowing $\mathcal{M}_s$ is increased compared to that in upward circular narrowing $\mathcal{M}_g$ where $a_m = 1.2$ and $a_p = 0.8$. Other parameters are $a_o = 1$, $R_g = R_s = 40$, $h_g = h_s = 20$, $\kappa = 0.2$, $\sigma = 0.8$, $L = 150$, with a mesh $N = 2^{10}$ points.

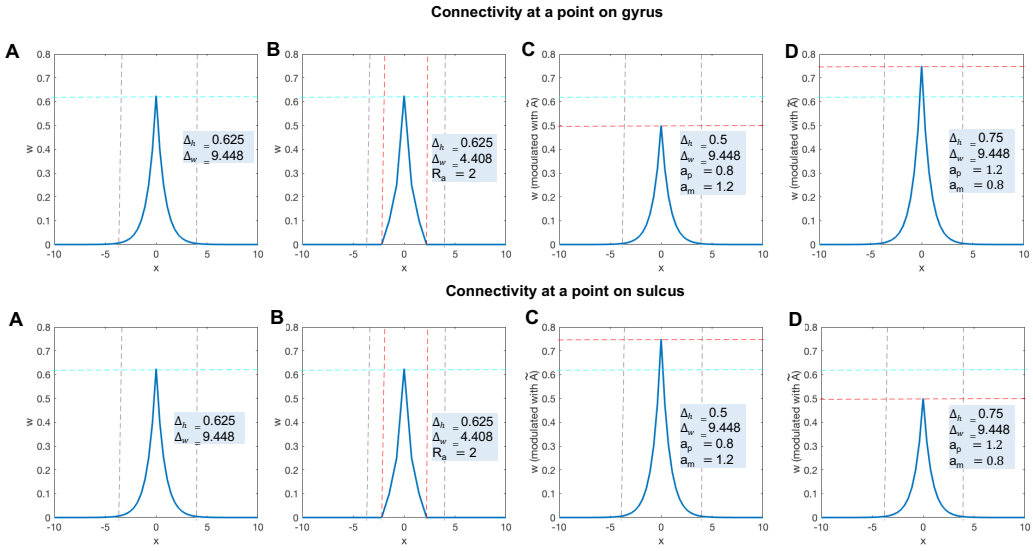

Fig. 6.10: Connectivity functions (6.5.4) are plotted for two individual points (one in the gyrus shown in the first row and the other in the sulcus shown in the second row) in the x direction in the presence of various constraints. Here dashed lines show the changes (height: Δ_h and weight: Δ_w) in connectivity depending on (i) the ambient space R_a and (ii) piece-wise constant modulation $\widetilde{A}$ (6.5.4). Panels (**A**): control case where simulations are performed for a synaptic kernel w in (6.5.4) as a function of arclength distance. Panels (**B**): synaptic kernel with an ambient space of radius $R_a = 2$, where a smaller spreading (compared to **A**) is observed. Panels (**C**): connectivity for denser sulci (opposite to the literature), where excitation is increased by 20% in sulci and decreased by 20% in gyri compared to flat domain in which $a_o = 1$. Panels (**D**): connectivity for denser gyri, where excitation is decreased by 20% in sulci, and increased by 20% in gyri. Note that $\boldsymbol{r} = (x, y) = (-70, -50)$ and $\boldsymbol{r} = (0, 50)$ are the spatial locations of the points in sulcus and gyrus respectively, and the domain is truncated for plotting purposes.

sense, for a tangent line which is drawn in a way that it makes an angle ϕ with the positive x axis, the curvature ($\mathcal{K}$) can be described as the rate of change in ϕ with respect to arclength. Thus using the formula of the arclength, one can find the rate $\mathcal{K}$ at which the tangent line turns. For example, for a given equation $y = f(x)$ we write

$$\mathcal{K} = \frac{d\phi}{ds} = \frac{f''(x)}{[1 + f'(x)^2]^{3/2}}. \tag{6.6.1}$$

The propagation of cortical waves on a folded brain may be characterised by the

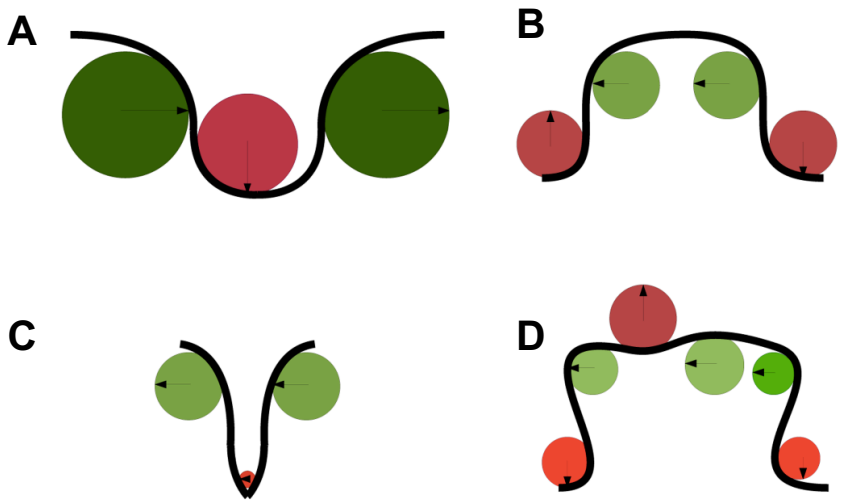

Fig. 6.11: An illustration of the concept of curvature at particular points in a curve, where curvature is measured as the reciprocal of the radii of osculating circles at those points. Green and red colours in circles represent negative and positive displacement, respectively. Image taken from [235].

curvature [235, 236]. Thus, in this section, we study the propagation of a travelling front solution using the neural field model (6.0.1) posed on a real cortical domain.

In Figure 6.12 we show the real data extracted from a human cortical slice. Here one-dimensional data from left and right superior frontal gyrus of a labeled brain scan (created using the methods in [237]) is discretised using the image reading features of Matlab and the software GetData Graph Digitizer [238], see Fig. 6.12(**B** & **C**). We note that the resulting curve (blue line in Fig. 6.12**C**) has a different aspect ratio with respect to the original cortical manifold (pink line in Fig. 6.12**B**). A small

stretching along the y-axis has been used to amplify slightly the effects of curvature on the speed of the cortical activity, so that the variations in speed are more clearly visible.

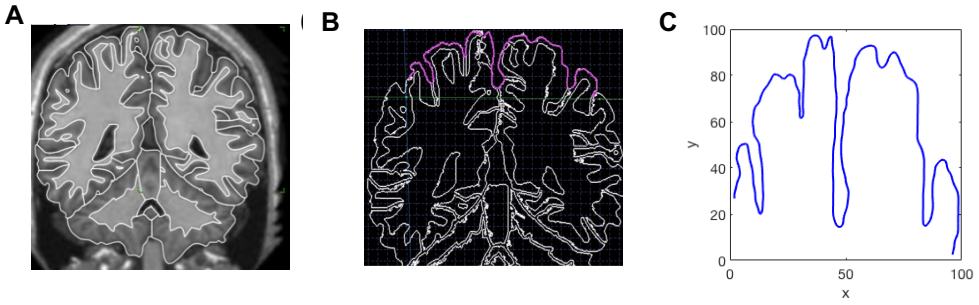

Fig. 6.12: The one-dimensional data extracted from the left and right superior frontal gyrus of an adult human brain. Panel (**A** & **B**): the labeled brain scan created by The Scalable Brain Atlas (*Neuromorphometrics, Inc*) [237]. Panel (**C**): one-dimensional data obtained from the region of the left and right superior frontal gyrus shown in pink in Panel (**B**). Note that the aspect ratio of the curve in panel **C** is different from that in panel **B**. In panel **C**, we consider a stretch in the y-axis so that the effects of curvature on the propagation speed of a wave are clearly visible.

We now consider a synaptic kernel whose decay parameter depends on the signed curvature at each point, that is

$$w(d(\boldsymbol{r}(s),\boldsymbol{r}(s')),s') = \frac{1}{2\sigma_1(s')}\mathrm{e}^{-d(\boldsymbol{r}(s),\boldsymbol{r}(s')))/\sigma_2(s')}, \tag{6.6.2}$$

where σ_1 and σ_2 are given by curvature dependent functions:

$$\sigma_1(s) = \beta_{11}\mathcal{K}(s) + \beta_{21}, \tag{6.6.3}$$

$$\sigma_2(s) = \beta_{12}\mathcal{K}(s) + \beta_{22}, \tag{6.6.4}$$

with a signed curvature described using the parametrisation (6.0.2) as:

$$\mathcal{K}(s) = \frac{\varphi'(s)\varsigma''(s) - \varsigma'(s)\varphi''(s)}{\sqrt{\varphi'(s)^2 + \varsigma'(s)^2}}. \tag{6.6.5}$$

Here β_{11} and β_{12} are curvature scaling parameters and β_{22} is used to impose a constant decay in the synaptic kernel if curvature radius gets infinitely large (e.g. $\mathcal{K} \approx 0$ for almost planar regions). Illustrations of curvature $\mathcal{K}$ and curvature dependent decay length scale σ_2 are shown in Fig. 6.13.

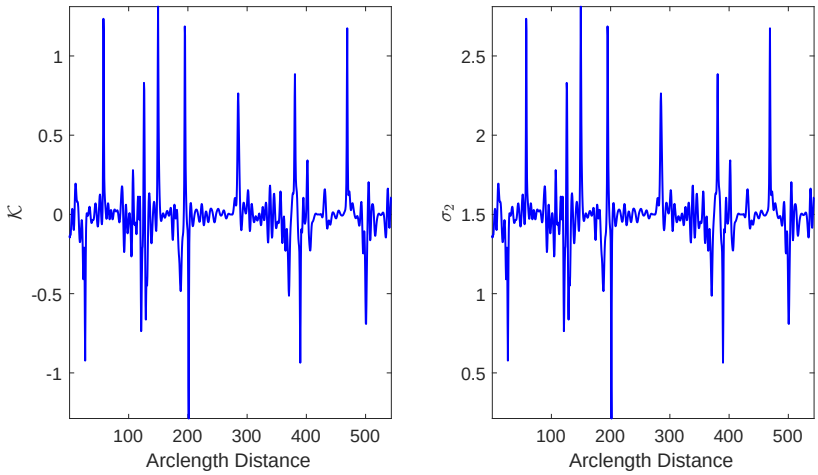

Fig. 6.13: Plots of the curvature $\mathcal{K}$ (6.6.5), and curvature dependent decay length scale σ_2 (6.6.4) in the synaptic kernel (6.6.2). Since the synaptic kernel is subject to exponential decay, one should choose appropriate parameter values for β_{12} and β_{22} such that σ_2 is always positive. Here we choose $\beta_{12} = 1$ and $\beta_{22} = 1.5$.

In Fig. 6.14 we show time simulations for three different cases to explore the effects of constant and curvature dependent functions of σ_1 and σ_2 in the synaptic kernel (6.6.2), and assume there exist no difference in terms of local cortical interactions between gyri and sulci. As seen from Fig. 6.14**A**, we find a wave front that propagates with a constant speed along the cortical manifold, where $\beta_{11} = \beta_{12} = 0$ and $\beta_{21} = \beta_{22} = \sigma_0$ (σ_0 is a constant) in (6.6.3) and (6.6.4). Fig. 6.14**B** shows time simulations where decay length scale σ_2 in the kernel (6.6.2) is curvature dependent. This effectively induces heterogeneity in the model. In Fig. 6.14**C**, time simulations of the model (6.0.1) for the weight kernel (6.6.2), where both σ_1 and σ_2 depend on curvature. In this case (Fig. 6.14**B** & **C**) the weight kernel depends on the position

due to varying curvature along the cortical surface, and thus the speed at which the wave travels should also change along the surface. Since the decay length scale σ_2 is a decreasing function of curvature $\mathcal{K}$, high curvature should give short decay lengths (shorter range kernel) and slower propagation even along the cortical manifold. This can be also observed from Fig. 6.15, where time as a function of arclength distance is plotted for each case in Fig. 6.14 (last column) and the speed of the front is seen to be curvature dependent due to the heterogeneous synaptic kernel.

6.7 CONCLUSION & DISCUSSION

Over the past two decades, there has been a growing interest in understanding how the cortex develops and gets its folds. The studies on cortical gyrification particularly have shed a light on important pathways underlying many neurological disorders [207]. This includes the cases where people born with a smooth (lissencephalic) brain, as well as people with a severe Alzheimer's disease where folding decreases after a certain age. Although planar neural field models provide a good approximation for the spatio-temporal evolution of synaptic activity in neuron populations, in this Chapter, we have been interested in studying how neural activity propagates through more realistic geometries, and how it differs from the activity on planar domains. Here the most obvious extension is to develop stability analysis of stationary solutions in (one- and two-dimensional) neural field models on non-planar geometries, and compare them with the stability of solutions in flat neural field models.

The wrinkles of our brain are not uniformly distributed. For instance the back of the neocortex is much less folded than the front lobe of neocortex [209], where highly folded cortical areas are usually linked to higher cognitive functions such as learning and decision making. On the other hand, less folded cortical areas such

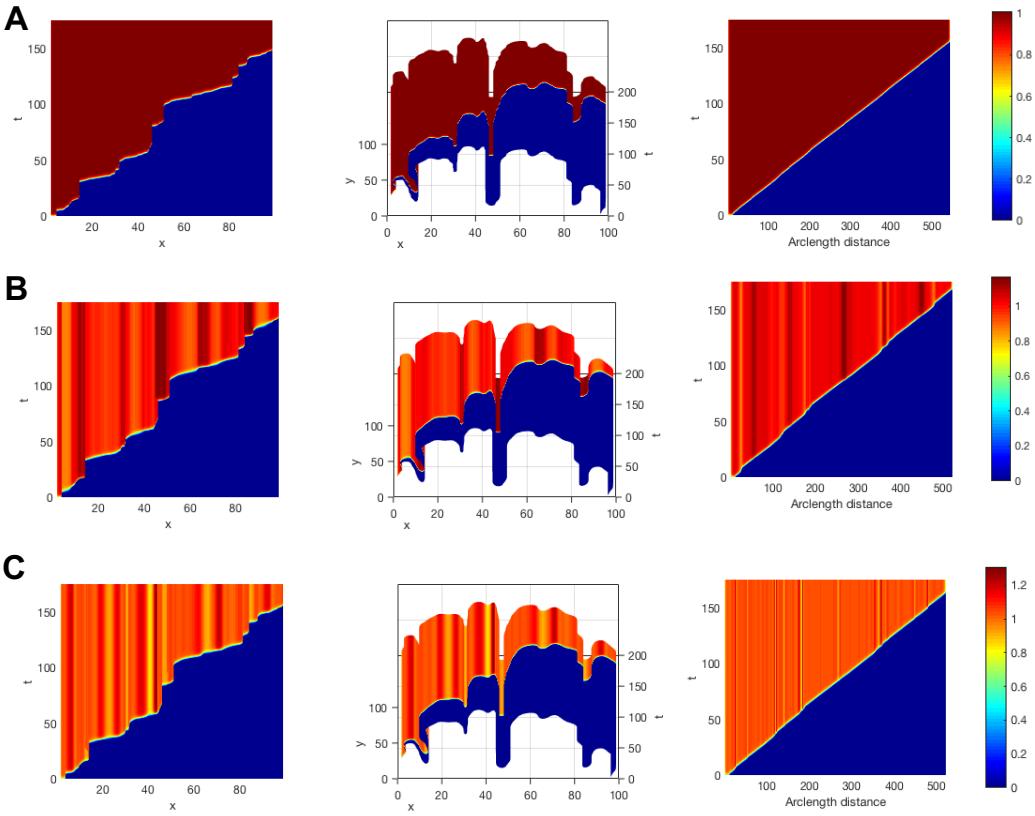

Fig. 6.14: The model (6.0.1) is simulated for one-dimensional data extracted from the left and right superior frontal gyrus of an adult human brain. Panel (**A**): time simulations for a homogeneous kernel where σ_1 and σ_2 in (6.6.2) are constants with $\beta_{11} = \beta_{12} = 0$ and $\beta_{21} = \beta_{22} = \sigma_0$. Here the arclength distance as a function of time is a straight line (as expected) for a front propagating with a constant speed along the cortical manifold. Panel (**B**): time simulations for a heterogeneous synaptic kernel (6.6.2) where σ_2 (6.6.4) is a curvature dependent function and σ_1 (6.6.3) is a constant with $\beta_{11} = 0$ and $\beta_{21} = \sigma_0$. Panel (**C**): time simulations for a heterogeneous synaptic kernel where σ_1 (6.6.3) and σ_2 (6.6.4) are both curvature dependent along the manifold. Parameters are $\sigma_0 = 1.5$ (**A**), $\sigma_0 = 1.5$, $\beta_{12} = 1$, $\beta_{22} = 1.5$ (**B**), $\beta_{11} = \beta_{12} = 1$, $\beta_{21} = \beta_{22} = 1.5$ (**C**) for a fixed threshold $\kappa = 0.15$, with a mesh of 2^{10} points.

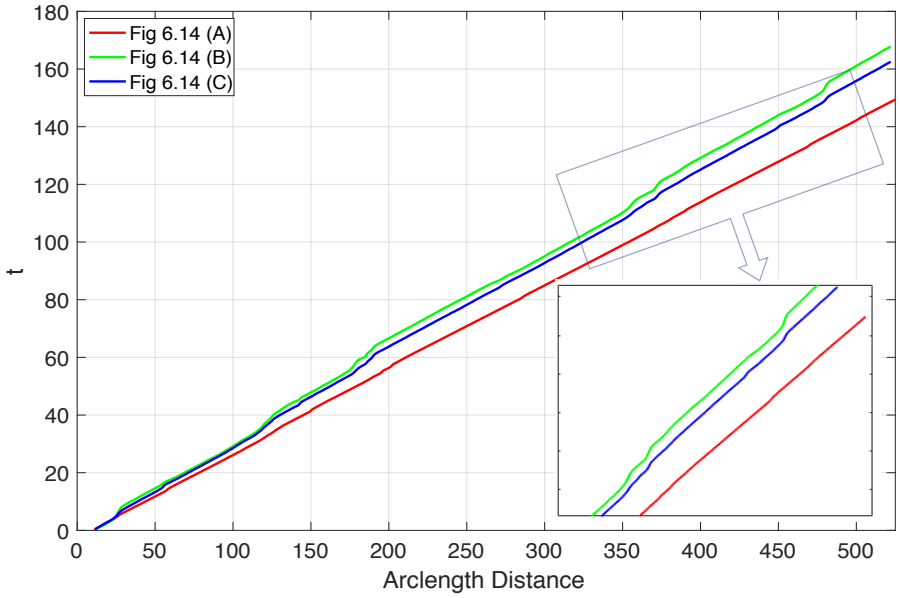

Fig. 6.15: The times for threshold crossing as a function of arclength distance for the three different cases presented in Fig. 6.14, where a wave travelling with a constant speed (red line), and waves with slower propagation (blue and black lines) along the manifold can be observed with homogeneous (constant σ_1 and σ_2) and heterogeneous kernels (curvature dependent σ_1 and σ_2 in (6.6.2)), respectively.

as primary visual cortex can be an easier application area for understanding how the geometrical structure (curvature) of the domain affects pattern formation. Note that the planar neural field model presented in Chapter 5 for the primary visual cortex, where the feature space is defined by orientation, can be easily extended to general geometries. Hence it would be interesting to see how curvature affects the stability and existence of an orientation bump, using a neural field model incorporating feature space.

A human embryo has a tiny smooth brain in its early stage of development, yet cortical folding is completed as it reaches 40 weeks [209]. Hence we do not get more wrinkles as we grow and learn. Although we do not develop new gyri and sulci, the connections between neurons in our brain keeps changing with various electrochemical processes. This process is attributed to cortical plasticity as mentioned in §2.3.3. Therefore, it would be interesting to analyse the planar neural field model of synaptic depression and recovery, presented by Kilpatrick and Bressloff [115], on geometrically more realistic domains.

There is a considerable literature on travelling depression waves in migraines that result in visual hallucinations called *auras* which propagate across the visual field, see [236, 239] for further details. The visual auras are interesting features in itself since the hallucinatory impressions help to improve the understanding of human cortical organization [236, 240]. Dahlem *et al.* pointed out that depression waves march slowly (minutes to hours) across the visual field and their velocity changes depending on the wave-front curvature [236]. Similar to the wave-front curvature, the folded geometry of the cortex is known to affect the speed at which a wave travels. It has been revealed that a wave moves faster in the region of increasing curvature, and it propagates slowly in the region with decreasing curvature [236, 241]. Therefore, studying neural field models on folded geometries becomes a worthwhile future direction to better understand the existence and velocity of depression waves in migraine aura that propagates across the gyri and sulci.

One should note that studying realistic geometries is only one of the main stages of cortical folding. Other phenomenons such as cortical growth, development and accommodation should also be considered in more realistic models. For example see [209] for a computational model that addresses some of these key elements of brain growth.

7

CONCLUSION

7.1 SUMMARY OF THE RESULTS

In this Thesis, we have studied dynamic features of localised states and travelling waves in neural field models on bounded domains in the presence and absence of Dirichlet boundary conditions. We have been interested in the behaviour of both one- and two-dimensional models as well as their dimensionally reduced interface descriptions. Therefore, we have split this Thesis into four main parts: (i) spatio-temporal activity of localised structures and their interface dynamics in flat neural fields with Dirichlet boundary conditions, (ii) interface dynamics in flat neural fields with a linear spike frequency adaptation supporting localised states, breathers and travelling waves (including spiral waves), (iii) patterns of orientation bumps and stripes in inhomogeneous neural fields that incorporate feature selectivity, (iv) dynamics of travelling fronts and pulses in neural fields posed on non-flat geometries.

In Chapter 2, we reviewed some of the well known single neuron models, and discussed various aspects of Amari type neural field models such as those with spike frequency adaptation, threshold accommodation and plasticity. This is particularly useful for understanding later Chapters. The study of Amari type neural

field models with a Heaviside firing rate remains a topic of interest in mathematical neuroscience. After showing some numerical results of the full space-time simulations, our aim was to write the normal velocity in terms of the shape of the boundary between active and quiescent regions. This level-set approach for interface dynamics in neural fields with no boundary conditions was initially developed by Coombes *et al.* [11] with a particular choice of synaptic kernel (a linear combination of modified Bessel function of the second kind zeroth order). Here we have extended their theory in Chapter 3 to construct interface dynamics for a generic synaptic kernel, as well as with an imposed Dirichlet boundary condition. The two-dimensional integral term is reduced to a line integral along the interface. The key point for this reduced formulation is the use of Green's theorem for the model without adaptation and the Reynold's transport theorem for the model with adaptation. Hence, we can list the important contributions of Chapter 3 as: (i) the generation and understanding of labyrinthine structures in neural fields with an imposed Dirichlet boundary condition, (ii) the derivation of the motion of their interface dynamics via a level-set condition, (iii) simplified calculations for localised states with piece-wise constant caricatures of the synaptic kernel. The techniques presented in this Chapter are generic and applicable to a broad range of problems in which interface dynamics and boundary conditions can be explored, see Chapter 7.2.

In Chapter 4 we treated neural fields with a linear spike frequency adaptation variable that allows the generation of breathers and travelling waves such as spiral waves. Spiral waves are rotating travelling waves that occur in excitable media, where their persistence is often strongly dependent on the choice of boundary conditions. The key contributions of this Chapter can be listed as (i) developing a theory for interface dynamics for neural fields with adaptation, where we show that there exists an excellent numerical agreement between two-dimensional space-time simulations and one-dimensional interface dynamics for labyrinthine structures and breathers in infinite domains, (ii) performing the numerical contin-

uation of spiral waves using the numerical eigenvalues of the full Jacobian matrix for a two-dimensional PDE neural field, (iii) presenting the constituent parts for developing the continuation problem using an interface approach with an imposed Dirichlet boundary condition. Since the system with a very steep sigmoidal firing rate shows qualitatively similar behaviour to a Heaviside firing rate, a straightforward extension would be to develop the numerical continuation techniques that merges the stability and the interface approach in a single computational framework. In this context, testing the theory presented in §4.5 on a spiral solution, we have already opened up the possibility to determine stability directly from the interface dynamics.

In Chapter 5, we studied neural field equations that take orientation features into account in a model of primary visual cortex. Here, the first part was dedicated to the existence and the stability of orientation bumps and the second part centered on the study of single and multiple stripe solutions in a ring model of neural fields. Here we extended the work of Bressloff *et al.* [92] by studying (i) a new analysis of orientation bumps using an interface approach, (ii) a characterisation of travelling wave solutions of orientation bumps and their stability using a level set description, (iii) the analysis of stripe solutions and their instabilities using neural fields with adaptation, where we consider orientation preference map with strong preferred interactions for angles differing by π/p ($p > 1$), (iv) orientation independent solutions with homogeneous oscillatory, homogeneous non-oscillatory as well as heterogeneous patchy horizontal connectivities.

Due to the brain being far from flat, formulating neural field models on non-flat geometries was the topic of Chapter 6. Since axons lie close to the cortical surface, neurons mostly interact via geodesic distances on a folded cortex. If the connectivity kernel depends only on geodesic distances, the neural field model is translation-invariant on a manifold $\mathcal{M}$ (if $\mathcal{M}$ is a closed curve). One can also introduce heterogeneity on the manifold by considering a combination of Euclidean and

geodesic distance, namely $Y < 1$ in equation (6.5.2). In this case, the assumption of translation invariance is no longer sensible. Another way to introduce heterogeneity on the manifold is to modulate the strength and spatial decay of synaptic input (see pages 162 and 166), where we multiply the kernel w by a piece-wise modulation $\widetilde{A}$ and consider the decay length scale σ as a function of curvature. For a homogeneous kernel that depends on the arclength distance, the speed at which the wave propagates varies in the x-coordinate; yet it is constant in the arclength coordinate. If the neural field model is modulated, then we expect to see change in the wave speed even along the manifold in the arclength coordinate. In this Chapter we analysed (i) travelling pulses in homogeneous and inhomogeneous neural field models on a circular domain (a circle of radius R), where it is possible to observe reflection and compression patterns, (ii) several aspects of folded brain geometry, including heterogeneity in the cell density and curvature for neural field models posed on folded structures.

7.2 FUTURE DIRECTIONS

In addition to possible future work described at the end of each Chapter, we list here some other possible research directions building on the work presented in this Thesis.

In the last part of Chapter 3, we investigated neural fields with piece-wise constant Top hat and piece-wise constant Mexican hat kernels. One can further consider doubly periodic solutions with $u(\boldsymbol{r} + \boldsymbol{l}_{1,2}, t) = u(\boldsymbol{r}, t)$, for linearly independent vectors $\boldsymbol{l}_{1,2} \in \mathbb{R}^2$. From equation (3.6.3) the doubly periodic stationary solution is given by

$$U(r) = \sum_{m,n\in\mathbb{Z}} \iint_{|\boldsymbol{r}'+m\boldsymbol{l}_1+n\boldsymbol{l}_2|<R} w\left(|\boldsymbol{r}-\boldsymbol{r}'|\right) \mathrm{d}\boldsymbol{r}', \tag{7.2.1}$$

subject to the constraint $U(R) = \kappa$.

Note that one obvious caveat to all of the Chapters is that the interface approach is restricted to Amari style models with a Heaviside firing rate. Nonetheless the qualitative similarities between Amari models and those with a steep sigmoidal firing rate are well known. In Figure 7.1, numerical solutions of the full neural field model with a sigmoidal firing rate show the evolution of patterns starting from doubly periodic solutions. For example in 7.1**A**, we observe destabilisation of a hexagonal tiling into an overlapping concentric circular-like pattern. In Figure 7.1**B** the pattern destabilises to large spots that are compressed and trapped by surrounding small spots. We see a regularly deforming pattern which looks like a chequered flag in Figure 7.1**C**, and lastly the initial conditions destabilise to a star-like pattern in Figure 7.1**D**. A further analysis of doubly periodic solutions can be performed, including the use of numerical continuation methods to determine solutions and their stabilities by considering the ideas in [131], with a focus on numerical continuation.

In Chapter 4, we investigated various parameter sets and initial conditions to compute rigidly rotating spirals, meandering spirals and spiral break-ups. Since meandering spirals are prominent due to their quasi-periodic motion, a possible extension of this work is to further investigate their existence and behaviour in a neural field model with adaptation. To characterise the behaviour of the spiral, the system of equations for the dynamics of the spiral tip should be derived. Following the ideas presented by Foulkes [14], who derived the equations of the spiral tip motion that depend on rotational as well as translational speed, one can further investigate meandering spirals in neural field models. Moreover, for spiral waves, we have only concentrated on an uniform medium but a real tissue is highly heterogeneous, and may lead to spatially drifting spiral waves. Such spiral waves have previously been observed in heart tissue and modelled using reaction diffusion systems [165, 171]. Thus, a neural field model with the inclusion of a symmetry breaking perturbation in the non-uniform media might be another possible mechanism to generate the drifting motion of spiral waves.

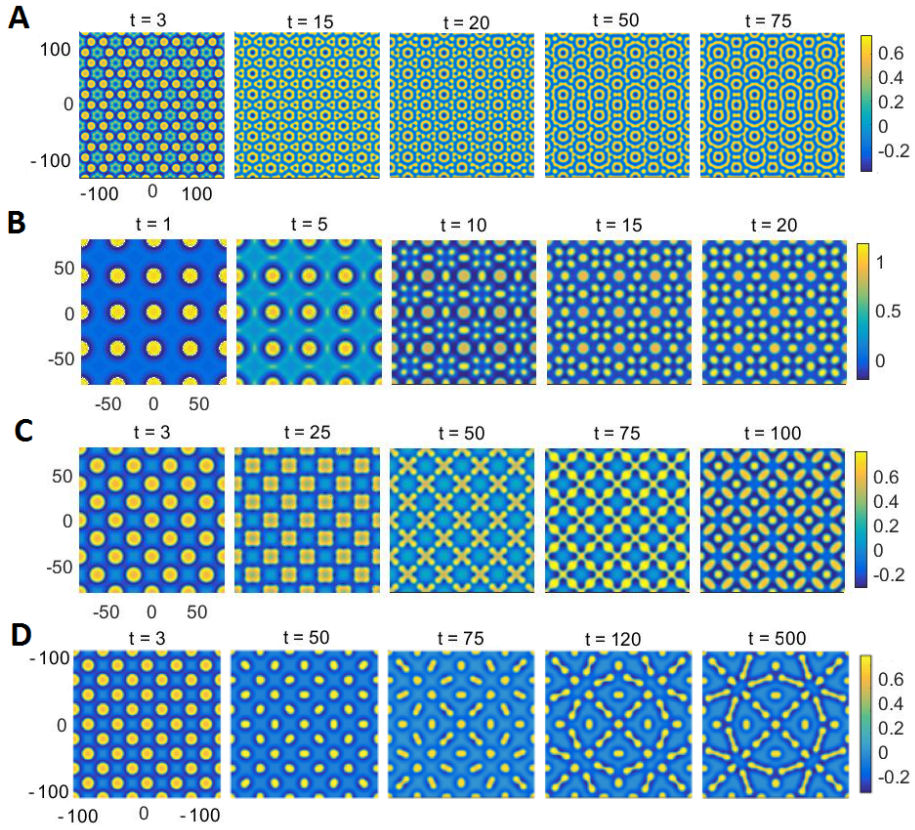

Fig. 7.1: Various space time simulations of two-dimensional neural field model with a piece-wise constant Mexican hat kernel posed on a large domain $[-L, L]$ with periodic boundary conditions. Panels (**A**) and (**B**) are simulated with a sigmoidal firing rate function of the form $F(u) = 1/(1 + e^{-\mu(u-h)})$. Panels (**C**) and (**D**) are simulated with a Heaviside firing rate. Parameters are (**A**): $w_+ = 0.1$, $w_- = -0.004$, $\mu = 6$, $\sigma_1 = 2$, $\sigma_2 = 10$, $h = 0.12$, with $L = 150$, (**B**): $w_+ = 0.1$, $w_- = -0.004$, $\mu = 10$, $\sigma_1 = 2$, $\sigma_2 = 10$, $h = 0.23$, with $L = 80$, (**C**): $w_+ = 0.1$, $w_- = -0.004$, $\sigma_1 = 2$, $\sigma_2 = 10$, $h = 0.14$, with $L = 80$, (**D**): $w_+ = 0.1$, $w_- = -0.004$, $\sigma_1 = 2$, $\sigma_2 = 10$, $h = 0.283$, with $L = 100$.

In Chapter 5, we studied the coupled ring model of neural fields posed on $\mathbb{R} \times S$. The analysis of the model posed on $\mathbb{R}^2 \times S$, namely incorporating two spatial dimensions with an additional dimension that reflects the hyper-columnar structure with an orientation preference, is a natural extension. In this case, we mentioned in Chapter 5 that it would be interesting to analyse how the extra spatial dimension affects the conditions for solution stability. Since the state variable on $\mathbb{R}^2 \times S$ is periodic in the angular direction and not periodic in the spatial directions, a standard matrix-vector multiplication is needed to evaluate the relevant integral operator. However, computing and storing a full matrix in three dimensions may result in practical memory constraints, and we thus require better numerical techniques. Apart from Chapter 4, we have mainly worked with localised patterns that have only one connected region of activity. However, neural field models also support multiple patterns which may be either connected to each other or disconnected from each other, e.g. multiple bumps. A potential future extension is to study the construction and stability of these type of solutions. For example, considering the model given by (5.3.1) and (5.3.2) with initial conditions different from a vertical stripe (that we have focused on, in Chapter 5), we expect to observe various instabilities, leading to the evolution of spreading connected multi bumps as shown in Fig. 7.2. In addition, one can also expand the ideas presented in Chapter 3 to tackle the problem of interface dynamics of multiple bumps in the presence and absence of boundary conditions.

Finally it is worth pointing out that the curved nature of the brain may affect the existence and stability of waves and patterns. For example a pulse which is stable on a flat domain may lose its stability in a non-flat domain, since dynamics of neural field models may change with a kernel that depends on the curvature. Moreover, the level set condition leads to an interface that may not have a constant normal velocity on a curved domain. Since cortical folding is important for changing the structural and functional capacity of the cortex, it also plays a crucial role in the dynamics of spirals. Interestingly the interface dynamics is not limited to the line or

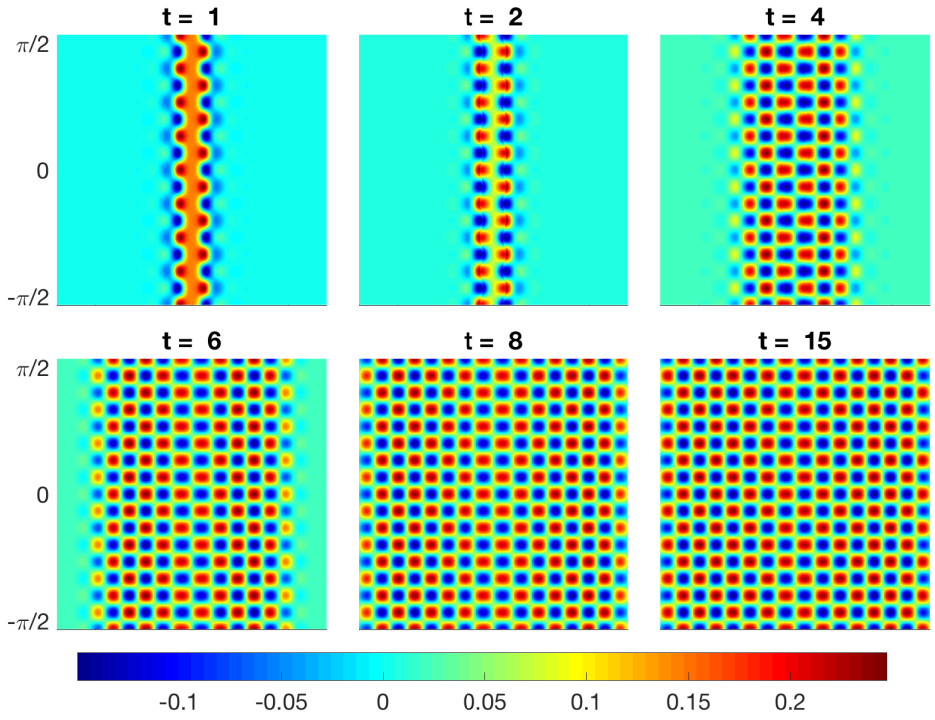

Fig. 7.2: Time simulations of the model given by (5.3.1) and (5.3.2) with synaptic kernels (5.3.5) and (5.3.6), and a Heaviside firing rate posed on a large domain $[-L, L] \times (-\pi/2, \pi/2]$. Connected multiple bumps fill the domain over time. Parameters are $D = 23.5619$, $w_0 = 0.1$, $w_2 = 0.49$, $\kappa = 0.053$, $\sigma = 4$, $g = 0.5$, $k = 0.1$ with $L = 140$.

plane and can be generalised to other manifolds. Thus, another possible extension is to analyse the evolution of spiral waves as well as the corresponding interface dynamics on a sphere or more general and realistic geometries. Moreover, the extension of folded neural field models to include space dependent delays is another possible direction. Space dependent delays arising from axonal interactions in flat neural fields are studied in [242, 243] and delays arising from dendritic interactions are comprehensively studied in [244, 245]. Hence there is no substantial difficulty in formulating non-flat neural field models with delay, such as in the recent work of Visser *et al.* [246] for spheres.

In summary the treatment of neural fields with boundary conditions is a relatively unexplored area of mathematical neuroscience whose further study should pay dividends for the understanding of neuroimaging data that shows functional segregation of activity. As discussed in [9] a natural way to achieve this in a neural field setting is to use Dirichlet boundary conditions. Moreover, deriving dimensionally reduced equations of the full non-linear integral equations allows a spatially reduced but exact formulation of these dynamics. Neural field theory remains a vibrant part of mathematical neuroscience, and I look forward to making further contributions, in the areas outlined above.

A

APPENDIX

A1 EXPRESSING ψ IN TERMS OF CONTOUR INTEGRALS

In this Appendix, we derive the identities (3.3.9) and (3.3.10). This allows us to represent the double integral for the non-local input $\psi(\boldsymbol{x}, t)$ given by (3.3.6) as an equivalent line-integral. We recall divergence theorem for a generic vector field $\boldsymbol{F}$ on a domain $\mathcal{B}$ with boundary $\partial\mathcal{B}$,

$$\int_{\mathcal{B}} (\nabla \cdot \boldsymbol{F})\, \mathrm{d}\boldsymbol{x} = \oint_{\partial\mathcal{B}} \boldsymbol{F} \cdot \boldsymbol{n} \mathrm{d}s, \tag{A1.1}$$

where $\boldsymbol{n}$ is the unit normal vector on $\partial\mathcal{B}$. We consider a rotationally symmetric two-dimensional synaptic weight kernel $w(\boldsymbol{x}) = w(r)$ which satisfies $\int_{\mathbb{R}^2} \mathrm{d}\boldsymbol{x} w(\boldsymbol{x}) = \mathcal{K}$, for some finite constant $\mathcal{K}$, and we introduce a function $g(\boldsymbol{x}) : \mathbb{R}^2 \to \mathbb{R}$ such that

$$w(\boldsymbol{x}) = (\nabla \cdot \boldsymbol{F})(\boldsymbol{x}) + g(\boldsymbol{x}). \tag{A1.2}$$

Now considering a function $\varphi(r) : \mathbb{R}^+ \to \mathbb{R}$ which satisfies the condition $\lim_{r\to\infty} r\varphi(r) = 0$, the vector field can be written using polar coordinates, that is $\boldsymbol{F} = \varphi(r)(\cos\theta, \sin\theta) =$

$\varphi(r)\,\boldsymbol{x}/|\boldsymbol{x}|$ with $\boldsymbol{x} = r(\cos\theta, \sin\theta)$. Transforming the expressions $\mathcal{K}$ and g into polar coordinates, integrating equation (A1.2), and using the divergence theorem, yields

$$\mathcal{K} = \int_0^\infty \int_0^{2\pi} rw(r,\theta)\,\mathrm{d}\theta\mathrm{d}r = \int_0^\infty \int_0^{2\pi} r\left[\nabla\cdot\boldsymbol{F} + g\right](r,\theta)\,\mathrm{d}\theta\mathrm{d}r, \tag{A1.3}$$

$$= \oint \boldsymbol{F}\cdot\boldsymbol{n}\,\mathrm{d}s + \int_0^\infty \int_0^{2\pi} rg(r,\theta)\,\mathrm{d}\theta\mathrm{d}r, \tag{A1.4}$$

where the line integral is described over a circle of radius $R \to \infty$. Therefore, the weight kernel can be written in the form

$$\mathcal{K} = 2\pi \lim_{R\to\infty} R\,\varphi(R) + \int_0^\infty \int_0^{2\pi} rg(r,\theta)\,\mathrm{d}\theta\mathrm{d}r. \tag{A1.5}$$

Since the line integral vanishes, we may set $g(\boldsymbol{x}) = \mathcal{K}\,\delta(\boldsymbol{x})$. We can now deduce the equation for $\varphi(r)$ by writing

$$\begin{aligned} w(r) &= \frac{\partial}{\partial r}\left[\varphi(r)\cos\theta\right]\frac{\partial r}{\partial x} + \frac{\partial}{\partial\theta}\left[\varphi(r)\cos\theta\right]\frac{\partial\theta}{\partial x} \\ &\quad + \frac{\partial}{\partial r}\left[\varphi(r)\sin\theta\right]\frac{\partial r}{\partial y} + \frac{\partial}{\partial\theta}\left[\varphi(r)\sin\theta\right]\frac{\partial\theta}{\partial y}, \\ &= \frac{\partial\varphi}{\partial r}(r) + \frac{1}{r}\varphi(r), \qquad r > 0. \end{aligned} \tag{A1.6}$$

The integration of (A1.6) yields

$$\varphi(r) = \frac{1}{r}\int_\infty^r xw(x)\mathrm{d}x. \tag{A1.7}$$

Using the above results means that (3.3.6) can be evaluated as

$$\begin{aligned} \psi(\boldsymbol{x},t) &= \int_{\Omega_+(t)} \mathrm{d}\boldsymbol{y}\, w(|\boldsymbol{x}-\boldsymbol{y}|) \\ &= \oint_{\partial\Omega_+(t)} \mathrm{d}s\boldsymbol{F}(|\boldsymbol{x}-\boldsymbol{\gamma}(s)|)\cdot\boldsymbol{n}(s) + \mathcal{K}\int_{\Omega_+(t)} \mathrm{d}\boldsymbol{y}\,\delta(\boldsymbol{x}-\boldsymbol{y}) \\ &= \oint_{\partial\Omega_+(t)} \mathrm{d}s\,\varphi(|\boldsymbol{x}-\boldsymbol{\gamma}(s)|)\frac{\boldsymbol{x}-\boldsymbol{\gamma}(s)}{|\boldsymbol{x}-\boldsymbol{\gamma}(s)|}\cdot\boldsymbol{n}(s) + \mathcal{K}C. \end{aligned} \tag{A1.8}$$

Here $\boldsymbol{\gamma} \in \partial\Omega_+$, and the integration over the Dirac-delta function gives $C = 1$ if $\boldsymbol{x}$ is within Ω_+, $C = 0$ if $\boldsymbol{x}$ is outside Ω_+, and $C = 1/2$ if $\boldsymbol{x}$ is on the boundary of Ω_+.

A2 AN ALTERNATIVE DERIVATION FOR NORMAL VELOCITY

The results obtained in §3.4 can also be established using a first order Taylor expansion and fundamental theorem of calculus. Here following the techniques described in §3.2 we write

$$\boldsymbol{u}(\boldsymbol{x},t) = u_{BC} + \int\limits_{\Gamma(\Omega_+(t))} \nabla_{\boldsymbol{y}} \boldsymbol{u}(\boldsymbol{y},t)\mathrm{d}\boldsymbol{y}. \tag{A2.1}$$

Considering the level set condition $u(\Omega_+(t),t) = \kappa$ and $u_{BC} = 0$, and differentiating (A2.1) with respect to time yields

$$\frac{\partial}{\partial_t} \int\limits_{\Gamma(\Omega_+(t))} \nabla_{\boldsymbol{y}} u(\boldsymbol{y},t)\mathrm{d}\boldsymbol{y} = 0, \tag{A2.2}$$

with

$$\int\limits_{\Gamma(\Omega_+(t+dt))} \boldsymbol{z}(\boldsymbol{y},t+dt)\cdot \mathrm{d}\boldsymbol{y} = \int\limits_{\Gamma(\Omega_+(t+dt))} \left(\boldsymbol{z}(\boldsymbol{y},t) + \partial_t \boldsymbol{z}(\boldsymbol{y},t) + \mathcal{O}(dt^2)\right)\cdot \mathrm{d}\boldsymbol{y}. \tag{A2.3}$$

This leads to

$$\begin{aligned}
0 &= \partial_t \int\limits_{\Gamma(\Omega_+(t))} \nabla_{\boldsymbol{y}} \boldsymbol{u}(\boldsymbol{y},t)\mathrm{d}\boldsymbol{y}, \\
&= \lim_{\mathrm{d}t\to 0} \frac{1}{\mathrm{d}t}\left[\int\limits_{\Gamma(\Omega_+(t+\mathrm{d}t))} \boldsymbol{z}(\boldsymbol{y},t+\mathrm{d}t)\cdot\mathrm{d}\boldsymbol{y} - \int\limits_{\Gamma(\Omega_+(t))} \boldsymbol{z}(\boldsymbol{y},t)\cdot\mathrm{d}\boldsymbol{y}\right], \\
&= \int\limits_{\Gamma(\Omega_+(t))} \boldsymbol{z}_t(\boldsymbol{y},t)\cdot\mathrm{d}\boldsymbol{y} + \lim_{\mathrm{d}t\to 0}\frac{1}{\mathrm{d}t}\left[\int\limits_{\Gamma(\Omega_+(t+\mathrm{d}t))} \boldsymbol{z}(\boldsymbol{y},t)\cdot\mathrm{d}\boldsymbol{y} - \int\limits_{\Gamma(\Omega_+(t))} \boldsymbol{z}(\boldsymbol{y},t)\cdot\mathrm{d}\boldsymbol{y}\right], \\
&= \int\limits_{\Gamma(\Omega_+(t))} \boldsymbol{z}_t(\boldsymbol{y},t)\cdot\mathrm{d}\boldsymbol{y} + \lim_{\mathrm{d}t\to 0}\frac{1}{\mathrm{d}t}\left[\boldsymbol{u}(\Omega_+(t+\mathrm{d}t),t) - \boldsymbol{u}(\Omega_+(t),t)\right], \\
&= \int\limits_{\Gamma(\Omega_+(t))} \boldsymbol{z}_t(\boldsymbol{y},t)\cdot\mathrm{d}\boldsymbol{y} + \lim_{\mathrm{d}t\to 0}\left[\boldsymbol{u}(\Omega_+(t)+c_n\mathrm{d}t+\mathcal{O}(\mathrm{d}t^2),t) - \boldsymbol{u}(\Omega_+(t),t)\right], \\
&= \int\limits_{\Gamma(\Omega_+(t))} \boldsymbol{z}_t(\boldsymbol{y},t)\cdot\mathrm{d}\boldsymbol{y} + c_n\cdot\nabla\boldsymbol{u}(\Omega_+(t),t).
\end{aligned}$$

The velocity formula is obtained as

$$c_n\cdot\boldsymbol{z}(\Omega_+(t),t) = -\int\limits_{\Gamma(\Omega_+(t))} \boldsymbol{z}_t(\boldsymbol{y},t)\cdot\mathrm{d}\boldsymbol{y}. \tag{A2.4}$$

A3 CIRCULAR GEOMETRY FOR A PIECE-WISE CONSTANT TOP HAT KERNEL

Consider a portion of a disk whose upper boundary is an (circular) arc and whose lower boundary is a chord making a central angle $\phi_0 < \pi$, illustrated as the shaded region in Fig. A.1**A**.

The area $A = A(r_0, \phi_0)$ of the (shaded) segment is then simply given by the area of the circular sector (the entire wedge-shaped portion) minus the area of an isosceles triangle, namely

$$A(r_0, \phi_0) = \frac{\phi_0}{2\pi}\pi r_0^2 - \frac{1}{2} r_0 \sin(\phi_0/2) r_0 \cos(\phi_0/2) = \frac{1}{2} r_0^2 (\phi_0 - \sin\phi_0)\,. \qquad \text{(A3.1)}$$

The area of the overlap of two circles, as illustrated in Fig. A.1**B**, can be constructed

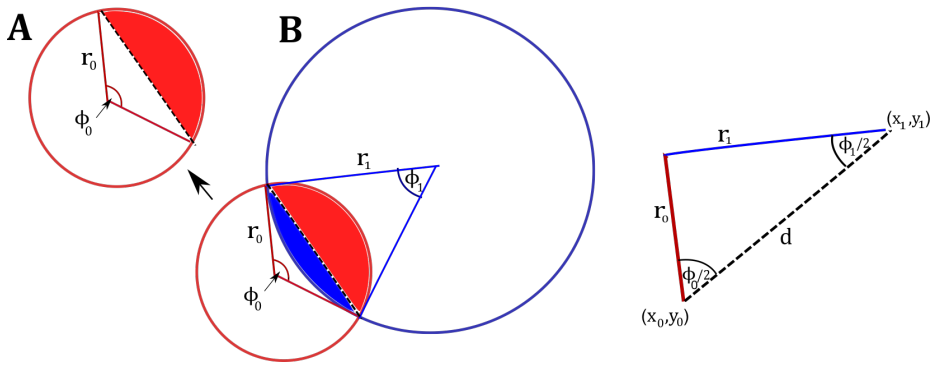

Fig. A.1: The area of the total shaded segment is $r_0^2(\phi_0 - \sin\phi_0)/2$ (**A**). Overlap of two circles shows the area of active region (**B**).

as the total area of $A(r_0, \phi_0) + A(r_1, \phi_1)$. To determine the angles $\phi_{0,1}$ in terms of the centres, (x_0, y_0) and (x_1, y_1), and radii, r_0 and r_1, of the two circles we use the cosine formula that relates the lengths of the three sides of a triangle formed by joining the centres of the circles to a point of intersection. Denoting the distance between the two centres by d where $d^2 = (x_0 - x_1)^2 + (y_0 - y_1)^2$ so that

$$r_1^2 = r_0^2 + d^2 - 2r_0 d\cos(\phi_0/2), \qquad r_0^2 = r_1^2 + d^2 - 2r_1 d\cos(\phi_1/2). \qquad \text{(A3.2)}$$

Hence

$$\phi_0(d, r_1) = 2\cos^{-1}\left(\frac{r_0^2 + d^2 - r_1^2}{2r_0 d}\right), \qquad \phi_1(d, r_1) = 2\cos^{-1}\left(\frac{r_1^2 + d^2 - r_0^2}{2r_1 d}\right). \tag{A3.3}$$

B

APPENDIX

B1 COMPONENTS OF G MATRIX

Real eigenvalues satisfy $Av_\pm = \lambda_\pm v_\pm$ with eigenvectors $v_\pm \in \mathbb{R}$. Here matrix A is given in equation (4.1.5), and $G(t)$ in equation (4.1.6) is computed as a *Jordan Normal Form* matrix, namely in the form of $G(t) = Pe^{\Upsilon t}P^{-1}$ where $\Upsilon = \text{diag}[\lambda_+, \lambda_-]$ and $P = [v_+, v_-]$.

We can explicitly compute the components of $G(t)$ for real eigenvalues of matrix A (4.1.5):

$$G_{11}(t) = \frac{1}{\lambda_+ - \lambda_-}\left\{\left(\lambda_+ + \frac{1}{\tau}\right)e^{\lambda_+ t} - \left(\lambda_- + \frac{1}{\tau}\right)e^{\lambda_- t}\right\}, \tag{B1.1}$$

$$G_{12}(t) = \frac{\alpha}{\tau(\lambda_- - \lambda_+)}(e^{\lambda_+ t} - e^{\lambda_- t}), \tag{B1.2}$$

$$G_{21}(t) = \frac{\tau}{\alpha(\lambda_+ - \lambda_-)}\left(\lambda_+ + \frac{1}{\tau}\right)\left(\lambda_- + \frac{1}{\tau}\right)\left\{e^{\lambda_+ t} - e^{\lambda_- t}\right\}, \tag{B1.3}$$

$$G_{22}(t) = \frac{1}{\lambda_+ - \lambda_-}\left\{\left(\lambda_+ + \frac{1}{\tau}\right)e^{\lambda_- t} - \left(\lambda_- + \frac{1}{\tau}\right)e^{\lambda_+ t}\right\}, \tag{B1.4}$$

with

$$\lambda_\pm = \frac{\text{Tr } A \pm \sqrt{(\text{Tr } A)^2 - 4\text{Det } A}}{2}. \tag{B1.5}$$

If the matrix A has complex eigenvalues, $\lambda_\pm = \xi_R \pm i\xi_I$, we find $Av_\pm = (\xi_R + i\xi_I)v_\pm$ with the corresponding complex eigenvector $v_\pm \in \mathbb{C}$. In this setting we consider $G(t) = e^{\xi_R t} P K(\xi_I t) P^{-1}$, where $P = [Im(v_+), Re(v_+)]$ and

$$K(\phi) = \begin{bmatrix} \cos\phi & -\sin\phi \\ \sin\phi & \cos\phi \end{bmatrix}, \qquad P = \begin{bmatrix} 0 & -g \\ \xi_I & \xi_R + 1 \end{bmatrix}. \tag{B1.6}$$

Thus the eigenvalues of the matrix A is complex, the components of $G(t)$ is found as $G_{ij} = H_{ij}(t)e^{\xi_R t}/g\xi_I$ where

$$H_{11}(t) = -\xi_I(\xi_R + 1)\sin(\xi_I t) + g\xi_I \cos(\xi_I t), \tag{B1.7}$$

$$H_{12}(t) = \left(-g^2 - (\xi_R + 1)^2\right)\sin(\xi_I t), \tag{B1.8}$$

$$H_{21}(t) = \xi_I^2 \sin(\xi_I t), \tag{B1.9}$$

$$H_{22}(t) = \xi_I(\xi_R + 1)\sin(\xi_I t) + g\xi_I \cos(\xi_I t). \tag{B1.10}$$

C

APPENDIX

C1 WAVE SPEED USING INTERFACE DYNAMICS

For a coupled ring model (5.0.1) with a synaptic kernel given by equation (5.2.5), the velocity rule for the interface approach becomes semi-analytical, in that many of the terms required for the computation of the normal velocity can be calculated by hand rather than have to be found numerically. Hence, an explicit calculation for the components of the velocity in (5.2.6) can be written as

$$\begin{aligned}\int_{-\pi/2}^{\pi/2}\int_{-L}^{ct}\mathcal{W}(ct,0,x',s')\mathrm{d}x'\mathrm{d}s', &= \frac{1}{2\sigma\pi}\int_{-\pi/2}^{\pi/2}\mathrm{d}s'\left[w_0+2w_2cos(2s')\right]\int_{-L}^{ct}e^{-|ct-x'|/\sigma}\mathrm{d}x',\\ &= \frac{w_0}{2\sigma}\int_{-L}^{ct}e^{-|ct-x'|/\sigma}\mathrm{d}x',\\ &= \frac{w_0}{2}\left(1-\mathrm{e}^{-(ct+L)/\sigma}\right), c\geq 0. \end{aligned} \tag{C1.1}$$

Denominator of the velocity formula in equation (5.2.7) is given as

$$\begin{aligned}\int_{-\pi/2}^{\pi/2}\int_{-L}^{c\tau}\partial_x\mathcal{W}(ct,0,x',s')\mathrm{d}x'\mathrm{d}s', &= \frac{w_0}{2\sigma^2}\int_{-L}^{c\tau}\frac{(ct-x')e^{-|ct-x'|/\sigma}}{|ct-x'|}\mathrm{d}x',\\ &= \frac{w_0}{2\sigma}e^{-ct/\sigma}\left(\mathrm{e}^{-L/\sigma}-\mathrm{e}^{c\tau/\sigma}\right), \end{aligned} \tag{C1.2}$$

where

$$\int \frac{(ct-x')e^{-|ct-x'|/\sigma}}{|ct-x'|}\mathrm{d}x' = \frac{\sigma}{2}\left[\mathrm{e}^{(ct-x')/\sigma}\left(\mathrm{sgn}(ct-x')-1\right)\right.$$
$$\left.-\mathrm{e}^{(x'-ct)/\sigma}\left(\mathrm{sgn}(ct-x')+1\right)\right]. \qquad \text{(C1.3)}$$

D

APPENDIX

D1 CIRCULAR NARROWING

Here we study a planar domain combined with a circumference of radius R as seen in Fig. D.1, where $(-l, 0)$ and $(l, 0)$ denote the points at which the circumference intersects the real line. Considering an apothem h_0 from the center of the circle to the midpoint of the chord (drawn from $-l$ to l), one can easily see that $l = \sqrt{R^2 - {h_0}^2}$. Here using the geometrical properties of an circle we find

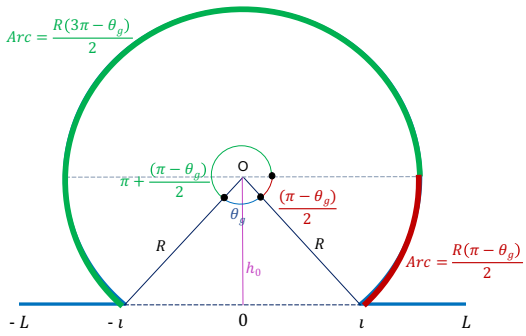

Fig. D.1: A cartoon for an upward circular narrowing.

$$\theta_g = 2\sin^{-1}\left(\frac{l}{R}\right). \tag{D1.1}$$

Here a part of the circumference (arc) is parametrised from $(\pi - \theta_g)/2$ to $\pi - \theta_1$.

Similar calculations can simply be written or downward circular narrowings that mimics sulci, as well as for negative values of h_0, implying a decrease in the amplitude of the arc.

BIBLIOGRAPHY

[1] Alan L Hodgkin, Andrew F Huxley, and B Katz. Measurement of current-voltage relations in the membrane of the giant axon of loligo. *The Journal of Physiology*, 116(4), 1952.

[2] Vernon B Mountcastle. Modality and topographic properties of single neurons of cat's somatic sensory cortex. *Journal of neurophysiology*, 20(4), 1957.

[3] Patricia Revest. Neuroscience methods: A guide for advanced students, 1998.

[4] Hugh R Wilson and Jack D Cowan. Excitatory and inhibitory interactions in localized populations of model neurons. *Biophysical Journal*, 12(1), 1972.

[5] Hugh R Wilson and Jack D Cowan. A mathematical theory of the functional dynamics of cortical and thalamic nervous tissue. *Biological Cybernetics*, 13(2), 1973.

[6] Shun-Ichi Amari. Homogeneous nets of neuron-like elements. *Biological cybernetics*, 17(4):211–220, 1975.

[7] Shun-ichi Amari. Dynamics of pattern formation in lateral-inhibition type neural fields. *Biological cybernetics*, 27(2), 1977.

[8] Paul L Nunez. The brain wave equation: a model for the EEG. *Mathematical Biosciences*, 21(3), 1974.

[9] Jean Daunizeau, Stefan J Kiebel, and Karl J Friston. Dynamic causal modelling of distributed electromagnetic responses. *NeuroImage*, 47(2), 2009.

[10] Stephen Coombes, Peter beim Graben, Roland Potthast, and James Wright. *Neural Fields: Theory and Applications*. Springer, 2014.

[11] Stephen Coombes, Helmut Schmidt, and Ingo Bojak. Interface dynamics in planar neural field models. *The Journal of Mathematical Neuroscience*, 2(1), 2012.

[12] Stephen Coombes, Helmut Schmidt, and Daniele Avitabile. Spots: breathing, drifting and scattering in a neural field model. In *Neural Fields*. Springer, 2014.

[13] Michael J Herrmann, Hecke Schrobsdorff, and Theo Geisel. Localized activations in a simple neural field model. *Neurocomputing*, 65, 2005.

[14] Andrew J Foulkes. Drift and meander of spiral waves. *ArXiv Preprint:* 0912.4247, 2009.

[15] Jorge M Davidenko, Arcady V Pertsov, et al. Stationary and drifting spiral waves of excitation in isolated cardiac muscle. *Nature*, 355(6358), 1992.

[16] Carlo R Laing. Spiral waves in nonlocal equations. *SIAM Journal on Applied Dynamical Systems*, 4(3), 2005.

[17] Carlo R Laing and William C Troy. PDE methods for nonlocal models. *SIAM Journal on Applied Dynamical Systems*, 2(3), 2003.

[18] Paul C Bressloff. Spatiotemporal dynamics of continuum neural fields. *Journal of Physics A: Mathematical and Theoretical*, 45(3), 2011.

[19] James J Wright and David TJ Liley. Dynamics of the brain at global and microscopic scales: Neural networks and the EEG. *Behavioral and Brain Sciences*, 19(02), 1996.

[20] Andrew Koob. The root of thought: what do glial cells do. *Scientific American*, 4, 2009.

[21] Alfonso Araque and Marta Navarrete. Glial cells in neuronal network function. *Philosophical Transactions of the Royal Society of London B: Biological Sciences*, 365(1551), 2010.

[22] Marian C Diamond, Arnold B Scheibel, Greer M Murphy, and Thomas Harvey. On the brain of a scientist: Albert Einstein. *Experimental Neurology*, 88(1), 1985.

[23] Antonia Vernadakis. Glia-neuron intercommunications and synaptic plasticity. *Progress in Neurobiology*, 49(3), 1996.

[24] Frederico AC Azevedo, Ludmila RB Carvalho, Lea T Grinberg, José Marcelo Farfel, Renata EL Ferretti, Renata EP Leite, Roberto Lent, Suzana Herculano-Houzel, et al. Equal numbers of neuronal and nonneuronal cells make the human brain an isometrically scaled-up primate brain. *Journal of Comparative Neurology*, 513(5), 2009.

[25] Suzana Herculano-Houzel. The glia/neuron ratio: how it varies uniformly across brain structures and species and what that means for brain physiology and evolution. *Glia*, 62(9), 2014.

[26] Alexei Verkhratsky and Arthur Morgan Butt. *Glial physiology and pathophysiology*. John Wiley & Sons, 2013.

[27] Douglas R Fields. The other brain. *Simon & Schuster: New York. Rizzoli SO, Betz WJ (2005). Synaptic vesicle pools. Nat Rev Neurosci*, 6(1), 2009.

[28] XueJuan Zhang and Jianfeng Feng. Computational modeling of neuronal networks. In *Encyclopedia of Biophysics*. Springer, 2013.

[29] Henry C Tuckwell. *Introduction to Theoretical Neurobiology: Volume 2, Nonlinear and Stochastic Theories*, volume 8. Cambridge University Press, 2005.

[30] Ruchi Parekh and Giorgio A Ascoli. Neuronal morphology goes digital: a research hub for cellular and system neuroscience. *Neuron*, 77(6), 2013.

[31] Rodney A Rhoades and David R Bell. *Medical physiology: Principles for clinical medicine*. Lippincott Williams & Wilkins, 2012.

[32] Stephen Coombes. Neuronal networks with gap junctions: A study of piecewise linear planar neuron models. *SIAM Journal on Applied Dynamical Systems*, 7(3), 2008.

[33] Q Ashton Acton. *Issues in Biomedical Engineering Research and Application*. ScholarlyEditions, 2012.

[34] Paul C Bressloff. Stochastic neural field theory and the system size expansion. *SIAM Journal on Applied Mathematics*, 70(5), 2009.

[35] Berend Snijder and Lucas Pelkmans. Origins of regulated cell-to-cell variability. *Nature Reviews Molecular Cell Biology*, 12(2), 2011.

[36] Pawel Paszek, Sheila Ryan, Louise Ashall, Kate Sillitoe, Claire V Harper, David G Spiller, David A Rand, and Michael RH White. Population robustness arising from cellular heterogeneity. *Proceedings of the National Academy of Sciences*, 107(25), 2010.

[37] Premananda Indic, William J Schwartz, Erik D Herzog, Nicholas C Foley, and Michael C Antle. Modeling the behavior of coupled cellular circadian oscillators in the suprachiasmatic nucleus. *Journal of Biological Rhythms*, 22(3), 2007.

[38] Thomas Bollinger and Ueli Schibler. Circadian rhythms-from genes to physiology and disease. *Swiss Med Wkly*, 144(w13984), 2014.

[39] Charna Dibner, Ueli Schibler, and Urs Albrecht. The mammalian circadian timing system: organization and coordination of central and peripheral clocks. *Annual review of physiology*, 72, 2010.

[40] Douglas J Mar, Carson C Chow, Wulfram Gerstner, Ralf W Adams, and JJ Collins. Noise shaping in populations of coupled model neurons. *Proceedings of the National Academy of Sciences*, 96(18), 1999.

[41] Wulfram Gerstner and Werner M Kistler. *Spiking neuron models: Single neurons, populations, plasticity*. Cambridge university press, 2002.

[42] Stephen Coombes. Large-scale neural dynamics: simple and complex. *NeuroImage*, 52(3), 2010.

[43] Grégory Faye. *Symmetry breaking and pattern formation in some neural field equations*. PhD thesis, Nice, 2012.

[44] Jonathan C Horton and Daniel L Adams. The cortical column: a structure without a function. *Philosophical Transactions of the Royal Society of London B: Biological Sciences*, 360(1456), 2005.

[45] Javier DeFelipe, Henry Markram, and Kathleen S Rockland. The neocortical column. *Frontiers in Neuroanatomy*, 6, 2012.

[46] Y Daniel, Charles D Gilbert Ts'o, and N Wiesel Torsten. Relationships between horizontal interactions and functional architecture in cat striate cortex as revealed by cross-correlation analysis. *Journal of Neuroscience*, 6, 1986.

[47] Charles Gilbert and Torsten N Wiesel. *Columnar specificity of intrinsic horizontal and corticocortical connection in cat visual cortex*. Society for Neuroscience, 1989.

[48] Klaus Obermayer and Gary G Blasdel. Geometry of orientation and ocular dominance columns in monkey striate cortex. *Journal of Neuroscience*, 13(10), 1993.

[49] Geoffrey J Goodhill and Miguel Á Carreira-Perpiñán. Cortical columns. *Encyclopedia of Cognitive Science*, 2002.

[50] David H Hubel and Torsten N Wiesel. Sequence regularity and geometry of orientation columns in the monkey striate cortex. *Journal of Comparative Neurology*, 158(3), 1974.

[51] David H Hubel and Torsten N Wiesel. Uniformity of monkey striate cortex: a parallel relationship between field size, scatter, and magnification factor. *Journal of Comparative Neurology*, 158(3), 1974.

[52] Daniel P Buxhoeveden and Manuel F Casanova. The minicolumn hypothesis in neuroscience. *Brain*, 125(5), 2002.

[53] Francois Grimbert. *Mesoscopic models of cortical structures*. PhD thesis, University of Nottingham, UK, 2008.

[54] Peiji Liang, Si Wu, and Fanji Gu. *An Introduction to Neural Information Processing*. Springer, 2015.

[55] Richard FitzHugh. Impulses and physiological states in theoretical models of nerve membrane. *Biophysical Journal*, 1(6), 1961.

[56] Louis Lapicque. Recherches quantitatives sur l'excitation électrique des nerfs traitée comme une polarisation. *J. Physiol. Pathol. Gen*, 9(1), 1907.

[57] Larry F Abbott. Lapicque ' s introduction of the integrate-and-fire model neuron (1907). *Brain Research Bulletin*, 50(5), 1999.

[58] Gary G Matthews. Electrical properties of cells. *Cellular Physiology of Nerve and Muscle, Fourth Edition*, 2002.

[59] Christof Koch. *Biophysics of computation: information processing in single neurons*. Oxford university press, 2004.

[60] Bertil Hille et al. *Ion channels of excitable membranes*, volume 507. Sinauer Sunderland, MA, 2001.

[61] Mark Nelson and John Rinzel. The Hodgkin & Huxley model. In *The book of genesis*. Springer, 1998.

[62] James Keener and James Sneyd. *Mathematical Physiology, Interdisciplinary Applied Mathematics 8*. Springer-Verlag, New York, 1998.

[63] Jinichi Nagumo, Suguru Arimoto, and Shuji Yoshizawa. An active pulse transmission line simulating nerve axon. *Proceedings of the Institute of Radio Engineers*, 50(10), 1962.

[64] Rose T Faghih, Ketan Savla, Munther A Dahleh, and Emery N Brown. The Fitzhugh-Nagumo model: Firing modes with time-varying parameters & parameter estimation. In *Engineering in Medicine and Biology Society (EMBC), 2010 Annual International Conference of the IEEE*. IEEE, 2010.

[65] Matthias Ringkvist. *On dynamical behaviour of FitzHugh-Nagumo systems*. Department of mathematics, Stockholm university, 2006.

[66] Leah Edelstein-Keshet. *Mathematical models in biology*. SIAM, 2005.

[67] Balth Van der Pol. LXXXVIII. on a relaxation-oscillations. *The London, Edinburgh, and Dublin Philosophical Magazine and Journal of Science*, 2(11), 1926.

[68] Gautam Reddy and Chaitanya Murthy. Coherence resonance in the fitzhugh-nagumo system. *Physics 210B: Nonequilibrium Statistical Physics, Student Project, University of California, San Diego*, 2013.

[69] A Liénard. Etude des oscillations entretenues. *Revue générale de l'électricité*, 23(21), 1928.

[70] Eugene M Izhikevich. *Dynamical systems in neuroscience*. MIT press, 2007.

[71] Anthony N Burkitt. A review of the integrate-and-fire neuron model: I. homogeneous synaptic input. *Biological Cybernetics*, 95(1), 2006.

[72] Matthew Philip James. *Dynamics of synaptically interacting integrate and fire neurons*. PhD thesis, Loughborough University, 2002.

[73] Brent Doiron, John Rinzel, and Alex Reyes. Stochastic synchronization in finite size spiking networks. *Physical Review E*, 74(3), 2006.

[74] Po Hsiang Chu, John G Milton, and Jack D Cowan. Connectivity and the dynamics of integrate-and-fire neural networks. *International Journal of Bifurcation and Chaos*, 4(01), 1994.

[75] David Horn and Irit Opher. Solitary waves of integrate-and-fire neural fields. *Neural Computation*, 9(8), 1997.

[76] Helmut Schmidt. *Interface Dynamics in Neural Field Models*. PhD thesis, University of Nottingham, UK, 2012.

[77] Eugene M Izhikevich. Simple model of spiking neurons. *IEEE Transactions on neural networks*, 14(6), 2003.

[78] Raymond L Beurle. Properties of a mass of cells capable of regenerating pulses. *Philosophical Transactions of the Royal Society B: Biological Sciences*, 240 (669), 1956.

[79] J So Griffith. A field theory of neural nets: I: Derivation of field equations. *The Bulletin of Mathematical Biophysics*, 25(1), 1963.

[80] J So Griffith. A field theory of neural nets: II . Properties of the field equations. *The Bulletin of Mathematical Biophysics*, 27(2), 1965.

[81] Laurence J Garey. *Brodmann's localisation in the cerebral cortex*. World Scientific, 1994.

[82] Rand S Swenson. Review of clinical and functional neuroscience. *Educational Review Manual in Neurology*, 2006.

[83] David J Pinto and Bard G Ermentrout. Spatially structured activity in synaptically coupled neuronal networks: I. Traveling fronts and pulses. *SIAM journal on Applied Mathematics*, 62(1), 2001.

[84] Jonathan B Levitt, David A Lewis, Takashi Yoshioka, and Jennifer S Lund. Topography of pyramidal neuron intrinsic connections in macaque monkey

prefrontal cortex (areas 9 and 46). *Journal of Comparative Neurology*, 338(3), 1993.

[85] Boris S Gutkin, Bard G Ermentrout, and Joseph O'Sullivan. Layer 3 patchy recurrent excitatory connections may determine the spatial organization of sustained activity in the primate prefrontal cortex. *Neurocomputing*, 32, 2000.

[86] Amanda Jane Elvin. *Pattern formation in a neural field model*. PhD thesis, PhD thesis, 2008.

[87] Carlo R Laing, William C Troy, Boris Gutkin, and Bard G Ermentrout. Multiple bumps in a neuronal model of working memory. *SIAM Journal on Applied Mathematics*, 63(1), 2002.

[88] Stephen Coombes. Waves, bumps, and patterns in neural field theories. *Biological Cybernetics*, 93(2), 2005.

[89] Grégory Faye and Jonathan Touboul. Pulsatile localized dynamics in delayed neural field equations in arbitrary dimension. *SIAM Journal on Applied Mathematics*, 74(5), 2014.

[90] K Kishimoto and S Amari. Existence and stability of local excitations in homogeneous neural fields. *Journal of Mathematical Biology*, 7(4), 1979.

[91] Bard G Ermentrout and Jack D Cowan. A mathematical theory of visual hallucination patterns. *Biological Cybernetics*, 34(3), 1979.

[92] Paul C Bressloff and Samuel R Carroll. Spatiotemporal dynamics of neural fields on product spaces. *SIAM Journal on Applied Dynamical Systems*, 13(4), 2014.

[93] Patricia S Goldman-Rakic. Cellular basis of working memory. *Neuron*, 14(3), 1995.

[94] Xiao-Jing Wang. Synaptic reverberation underlying mnemonic persistent activity. *Trends in Neurosciences*, 24(8), 2001.

[95] Carlo R Laing. PDE methods for two-dimensional neural fields. In *Neural Fields*. Springer, 2014.

[96] Martin A Giese. *Dynamic neural field theory for motion perception*, volume 469. Springer Science & Business Media, 2012.

[97] James Rankin, Andrew Isaac Meso, Guillaume S Masson, Olivier Faugeras, and Pierre Kornprobst. Bifurcation study of a neural field competition model with an application to perceptual switching in motion integration. *Journal of Computational Neuroscience*, 36(2), 2014.

[98] Andrew Isaac Meso, James Rankin, Olivier Faugeras, Pierre Kornprobst, and Guillaume S Masson. The relative contribution of noise and adaptation to competition during tri-stable motion perception. *Journal of vision*, 16(15), 2016.

[99] Paul C Bressloff. Neural field model of binocular rivalry waves. In *Waves in Neural Media*. Springer, 2014.

[100] Matthew A Webber and Paul C Bressloff. The effects of noise on binocular rivalry waves: a stochastic neural field model. *Journal of Statistical Mechanics: Theory and Experiment*, 2013(03), 2013.

[101] Dimitris Pinotsis, Peter Robinson, Peter beim Graben, and Karl Friston. Neural masses and fields: modeling the dynamics of brain activity. *Frontiers in Computational Neuroscience*, 8, 2014.

[102] Bard G Ermentrout. Neural networks as spatio-temporal pattern-forming systems. *Reports on Progress in Physics*, 61(4), 1998.

[103] Stephen Coombes and Markus R Owen. Bumps, breathers, and waves in a neural network with spike frequency adaptation. *Physical Review Letters*, 94 (14), 2005.

[104] Paul C Bressloff. *Waves in Neural Media: From Single Neurons to Neural Fields*. Springer, 2014.

[105] Stephen Coombes. Large-scale neural dynamics: Simple and complex. *NeuroImage*, 52, 2010.

[106] Paul C Bressloff. From invasion to extinction in heterogeneous neural fields. *The Journal of Mathematical Neuroscience*, 2(1), 2012.

[107] Bard G Ermentrout, Stefanos E Folias, and Zachary P Kilpatrick. Spatiotemporal pattern formation in neural fields with linear adaptation. In *Neural Fields*. Springer, 2014.

[108] Jan Benda and Andreas VM Herz. A universal model for spike-frequency adaptation. *Neural Computation*, 15(11), 2003.

[109] Romain Veltz and Olivier Faugeras. Local/global analysis of the stationary solutions of some neural field equations. *SIAM Journal on Applied Dynamical Systems*, 9(3), 2010.

[110] Archibald V Hill. Excitation and accommodation in nerve. *Proceedings of the Royal Society of London. Series B, Biological Sciences*, 119(814), 1936.

[111] Stephen Coombes and Markus R Owen. Exotic dynamics in a firing rate model of neural tissue. In *Fluids and Waves: Recent Trends in Applied Analysis*, volume 440. American Mathematical Soc., 2007.

[112] Carlo Laing and Stephen Coombes. The importance of different timings of excitatory and inhibitory pathways in neural field models. *Network: Computation in Neural Systems*, 17(2), 2006.

[113] Zachary Peter Kilpatrick. *Spatially structured waves and oscillations in neuronal networks with synaptic depression and adaptation*. PhD thesis, The University of Utah, 2010.

[114] Robert S Zucker and Wade G Regehr. Short-term synaptic plasticity. *Annual review of Physiology*, 64(1), 2002.

[115] Zachary P Kilpatrick and Paul C Bressloff. Effects of synaptic depression and adaptation on spatiotemporal dynamics of an excitatory neuronal network. *Physica D: Nonlinear Phenomena*, 239(9), 2010.

[116] Catherine Morris and Harold Lecar. Voltage oscillations in the barnacle giant muscle fiber. *Biophysical Journal*, 35(1), 1981.

[117] James L Hindmarsh and RM Rose. A model of neuronal bursting using three coupled first order differential equations. *Proceedings of the Royal Society of London B: Biological Sciences*, 221(1222), 1984.

[118] Antonio Galves and Eva Löcherbach. Infinite systems of interacting chains with memory of variable length a stochastic model for biological neural nets. *Journal of Statistical Physics*, 151(5), 2013.

[119] Paul C Bressloff, Jack D Cowan, Martin Golubitsky, Peter J Thomas, and Matthew C Wiener. Geometric visual hallucinations, euclidean symmetry and the functional architecture of striate cortex. *Philosophical Transactions of the Royal Society of London B: Biological Sciences*, 356(1407), 2001.

[120] Marcelo Camperi and Xiao-Jing Wang. A model of visuospatial working memory in prefrontal cortex: recurrent network and cellular bistability. *Journal of Computational Neuroscience*, 5(4), 1998.

[121] Bard G Ermentrout and Bryce J McLeod. Existence and uniqueness of travelling waves for a neural network. *Proceedings of the Royal Society of Edinburgh: Section A Mathematics*, 123(03), 1993.

[122] Bruce Fischl and Anders M Dale. Measuring the thickness of the human cerebral cortex from magnetic resonance images. *Proceedings of the National Academy of Sciences*, 97(20), 2000.

[123] Paul L Nunez and Ramesh Srinivasan. *Electric fields of the brain: the neurophysics of EEG*. Oxford University Press, USA, 2006.

[124] John G Taylor. Neural bubble dynamics in two dimensions: Foundations. *Biological Cybernetics*, 80, 1999.

[125] Herrad Werner and Tim Richter. Circular stationary solutions in two-dimensional neural fields. *Biological Cybernetics*, 85(3), 2001.

[126] Stephen Coombes and Markus R Owen. Evans functions for integral neural field equations with Heaviside firing rate function. *SIAM Journal on Applied Dynamical Systems*, 34, 2004.

[127] Markus R Owen, Carlo R Laing, and Stephen Coombes. Bumps and rings in a two-dimensional neural field: splitting and rotational instabilities. *New Journal of Physics*, 9(10), 2007.

[128] Norman J Zabusky, MH Hughes, and KV Roberts. Contour dynamics for the euler equations in two dimensions. *Journal of Computational Physics*, 135(2), 1997.

[129] Stefanos E Folias and Paul C Bressloff. Breathers in two-dimensional neural media. *Physical Review Letters*, 95(20), 2005.

[130] Paul C Bressloff and Stephen Coombes. Neural bubble dynamics revisited. *Cognitive Computation*, 5, 2013.

[131] James Rankin, Daniele Avitabile, Javier Baladron, Gregory Faye, and David JB Lloyd. Continuation of localized coherent structures in nonlocal neural field equations. *SIAM Journal on Scientific Computing*, 36(1), 2014.

[132] Lloyd N Trefethen. *Spectral methods in MATLAB*, volume 10. SIAM, 2000.

[133] John D'Errico. Interparc, matlab central file exchange. URL http://www.mathworks.com/matlabcentral/fileexchange/34874. [Retrieved from Feb 01, 2012].

[134] Raymond E Goldstein, David J Muraki, and Dean M Petrich. Interface proliferation and the growth of labyrinths in a reaction-diffusion system. *Physical Review E*, 53(4), 1996.

[135] Julie Goulet and Bard G Ermentrout. The mechanisms for compression and reflection of cortical waves. *Biological Cybernetics*, 105(3), 2011.

[136] Stephen Coombes and Helmut Schmidt. Neural fields with sigmoidal firing rates: approximate solutions. *Discrete and Continuous Dynamical Systems. Series S*, 2010.

[137] David A Brown and Paul R Adams. Muscarinic suppression of a novel voltage-sensitive K+; current in a vertebrate neurone. *Nature*, 283(5748), 1980.

[138] Manfred J Oswald, Dorothy E Oorschot, Jan M Schulz, Janusz Lipski, and John NJ Reynolds. Ih current generates the after hyperpolarisation following activation of subthreshold cortical synaptic inputs to striatal cholinergic interneurons. *The Journal of Physiology*, 587(24), 2009.

[139] Richard K Ellerkmann, Vladimir Riazanski, Christian E Elger, Bernd W Urban, and Heinz Beck. Slow recovery from inactivation regulates the availability of voltage-dependent na+ channels in hippocampal granule cells, hilar neurons and basket cells. *The Journal of Physiology*, 532(2), 2001.

[140] DJ Pinto. Computational, experimental, and analytic explorations of neuronal circuits in the cerebral cortex (phd thesis). *University of Pittsburgh, Pittsburgh, PA*, 1997.

[141] D Hansel and H Sompolinsky. Modeling feature selectivity in local cortical circuits. in: Koch, c., segev, i. (eds.) methods in neuronal modeling: From ions to networks, chap. 13. 1998.

[142] Paul C Bressloff and Zachary P Kilpatrick. Two-dimensional bumps in piecewise smooth neural fields with synaptic depression. *SIAM Journal on Applied Mathematics*, 71(2), 2011.

[143] Ingo Bojak and David TJ Liley. Axonal velocity distributions in neural field equations. *PLoS Computational Biology*, 6(1), 2010.

[144] Kathryn Turner and Homer F Walker. Efficient high accuracy solutions with GMRES(m). *SIAM Journal on Scientific and Statistical Computing*, 13(3), 1992.

[145] Dana A Knoll and David E Keyes. Jacobian-free Newton-Krylov methods: a survey of approaches and applications. *Journal of Computational Physics*, 193 (2), 2004.

[146] James Lechleiter, Steven Girard, Ernest Peralta, and David Clapham. Spiral calcium wave propagation and annihilation in Xenopus laevis oocytes. *Science*, 252(5002), 1991.

[147] Arthur T Winfree. Spiral waves of chemical activity. *Science*, 175(4022), 1972.

[148] Vladimir K Vanag and Irving R Epstein. Inwardly rotating spiral waves in a reaction-diffusion system. *Science*, 294(5543), 2001.

[149] Michael P Hassell, Hugh N Comins, and Robert M May. Spatial structure and chaos in insect population dynamics. *Nature*, 353(6341), 1991.

[150] Markus A Dahlem and Stefan C Müller. Self-induced splitting of spiral-shaped spreading depression waves in chicken retina. *Experimental Brain Research*, 115(2), 1997.

[151] JC Prechtl, LB Cohen, B Pesaran, PP Mitra, and D Kleinfeld. Visual stimuli induce waves of electrical activity in turtle cortex. *Proceedings of the National Academy of Sciences*, 94(14), 1997.

[152] Ivan Osorio, Hitten P Zaveri, Mark G Frei, and Susan Arthurs. *Epilepsy: the intersection of neurosciences, biology, mathematics, engineering, and physics*. CRC Press, 2016.

[153] A David Redish. *The mind within the brain: How we make decisions and how those decisions go wrong*. Oxford University Press, 2013.

[154] Peter Tass. Oscillatory cortical activity during visual hallucinations. *Journal of Biological Physics*, 23(1), 1997.

[155] Xiaoying Huang, William C Troy, Qian Yang, Hongtao Ma, Carlo R Laing, Steven J Schiff, and Jian-Young Wu. Spiral waves in disinhibited mammalian neocortex. *The Journal of Neuroscience*, 24(44), 2004.

[156] Xiaoying Huang, Weifeng Xu, Jianmin Liang, Kentaroh Takagaki, Xin Gao, and Jian Young Wu. Spiral wave dynamics in neocortex. *Neuron*, 68(5), 2010.

[157] Norbert Wiener and Arturo Rosenblueth. The mathematical formulation of the problem of conduction of impulses in a network of connected excitable elements, specifically in cardiac muscle. *Archivos del instituto de Cardiología de México*, 16(3), 1946.

[158] AM Zhabotinskii. Periodic course of the oxidation of malonic acid in a solution (studies on the kinetics of Beolusov's reaction). *Biofizika*, 9, 1963.

[159] Alexandre Panfilov and Pauline Hogeweg. Spiral breakup in a modified FitzHugh-Nagumo model. *Physics Letters A*, 176(5), 1993.

[160] Irina V Biktasheva, Arun V Holden, and Vadim N Biktashev. Localization of response functions of spiral waves in the FitzHugh–Nagumo system. *International Journal of Bifurcation and Chaos*, 16(05), 2006.

[161] Wang Ya-Min, Liu Yong, Wang Jing, and Liu Yu-Rong. Weak field-induced evolution of spiral wave in small-world networks of Hodgkin-Huxley Neurons. *Chinese Physics Letters*, 29(8), 2012.

[162] Jun Ma, Long Huang, HePing Ying, and ZhongSheng Pu. Detecting the breakup of spiral waves in small-world networks of neurons due to channel block. *Chinese Science Bulletin*, 57(17), 2012.

[163] Victor Zykov. Kinematics of rigidly rotating spiral waves. *Physica D: Nonlinear Phenomena*, 238(11), 2009.

[164] Hiroki Yagisita, Masayasu Mimura, and Michio Yamada. Spiral wave behaviors in an excitable reaction-diffusion system on a sphere. *Physica D: Nonlinear Phenomena*, 124(1), 1998.

[165] Irina V Biktasheva, Dwight Barkley, Vadim N Biktashev, and Andrew J Foulkes. Computation of the drift velocity of spiral waves using response functions. *Physical Review E*, 81(6), 2010.

[166] Faridon Amdjadi. Numerical simulation of reaction–diffusion equations on spherical domains. *Communications in Nonlinear Science and Numerical Simulation*, 13(8), 2008.

[167] Björn Sandstede, Arnd Scheel, and Claudia Wulff. Dynamics of spiral waves on unbounded domains using center- manifold reductions. *Journal of Differential Equations*, 141(1), 1997.

[168] Arnd Scheel. Bifurcation to spiral waves in reaction-diffusion systems. *SIAM journal on Mathematical Analysis*, 29(6), 1998.

[169] Joseph Paullet, Bard G Ermentrout, and William Troy. The existence of spiral waves in an oscillatory reaction-diffusion system. *SIAM Journal on Applied Mathematics*, 54(5), 1994.

[170] Dwight Barkley. Spiral meandering. In *Chemical Waves and Patterns*. Springer, 1995.

[171] Vadim N Biktashev, Dwight Barkley, and Irina V Biktasheva. Orbital motion of spiral waves in excitable media. *Physical Review Letters*, 104(5), 2010.

[172] Dwight Barkley. Euclidean symmetry and the dynamics of rotating spiral waves. *Physical Review Letters*, 72(1), 1994.

[173] Arthur T Winfree. Varieties of spiral wave behavior: An experimentalist's approach to the theory of excitable media. *Chaos: An Interdisciplinary Journal of Nonlinear Science*, 1(3), 1991.

[174] Daniele Avitabile, David JB Lloyd, John Burke, Edgar Knobloch, and Björn Sandstede. To snake or not to snake in the planar swift–hohenberg equation. *SIAM Journal on Applied Dynamical Systems*, 9(3), 2010.

[175] Zhao Ying-Kui, Wang Guang-Rui, and Chen Shi-Gang. Breakup of spiral wave under different boundary conditions. *Chinese Physics*, 16(4), 2007.

[176] Ingo Bojak, Thom F Oostendorp, Andrew T Reid, and Rolf Kötter. Connecting mean field models of neural activity to EEG and fMRI data. *Brain Topography*, 23(2), 2010.

[177] Kathleen S Rockland, Jon H Kaas, and Alan Peters. *Cerebral Cortex: Volume 12: Extrastriate Cortex in Primates*, volume 12. Springer Science & Business Media, 2013.

[178] Tobias Fischer. *Model of all known spatial maps in primary visual cortex*. PhD thesis, The University of Edinburgh, UK, 2014.

[179] Michael Connolly and David Van Essen. The representation of the visual field in parvicellular and magnocellular layers of the lateral geniculate nucleus in the macaque monkey. *Journal of Comparative Neurology*, 226(4), 1984.

[180] Gary G Blasdel. Orientation selectivity, preference, and continuity in monkey striate cortex. *The Journal of Neuroscience*, 12(8), 1992.

[181] Paul C Bressloff and Jack D Cowan. The functional geometry of local and horizontal connections in a model of v1. *Journal of Physiology-Paris*, 97(2), 2003.

[182] Paul C Bressloff and Samuel R Carroll. Laminar neural field model of laterally propagating waves of orientation selectivity. *PLoS Computational Biology*, 11(10), 2015.

[183] David H Hubel and Torsten N Wiesel. Receptive fields, binocular interaction and functional architecture in the cat's visual cortex. *The Journal of Physiology*, 160(1), 1962.

[184] David TJ Liley, Peter J Cadusch, and Mathew P Dafilis. A spatially continuous mean field theory of electrocortical activity. *Network: Computation in Neural Systems*, 13(1), 2002.

[185] R Ben-Yishai, R Lev Bar-Or, and H Sompolinsky. Theory of orientation tuning in visual cortex. *Proceedings of the National Academy of Sciences*, 92(9), 1995.

[186] David C Somers, Sacha B Nelson, and Mriganka Sur. An emergent model of orientation selectivity in cat visual cortical simple cells. *The Journal of Neuroscience*, 15(8), 1995.

[187] Lars Schwabe, Klaus Obermayer, Alessandra Angelucci, and Paul C Bressloff. The role of feedback in shaping the extra-classical receptive field of cortical neurons: a recurrent network model. *The Journal of Neuroscience*, 26(36), 2006.

[188] E Herrera and CA Mason. The evolution of crossed and uncrossed retinal pathways in mammals. *Evolution of nervous systems: Mammals. Volume*, 3, 2007.

[189] James V Stone. *Vision and brain: how we perceive the world*. MIT press, 2012.

[190] Mehran Ahmadlou and J Alexander Heimel. Preference for concentric orientations in the mouse superior colliculus. *Nature communications*, 6, 2015.

[191] Eric R Kandel, James H Schwartz, Thomas M Jessell, Steven A Siegelbaum, A James Hudspeth, et al. *Principles of neural science*, volume 4. McGraw-hill New York, 2000.

[192] Trichur R Vidyasagar, Jaikishan Jayakumar, Errol Lloyd, and Ekaterina V Levichkina. Subcortical orientation biases explain orientation selectivity of visual cortical cells. *Physiological Reports*, 3(4), 2015.

[193] Stephen D Van Hooser, J Alexander Heimel, Sooyoung Chung, and Sacha B Nelson. Lack of patchy horizontal connectivity in primary visual cortex of a mammal without orientation maps. *The Journal of Neuroscience*, 26(29), 2006.

[194] Alessandra Angelucci, Jonathan B Levitt, Emma JS Walton, Jean-Michel Hupe, Jean Bullier, and Jennifer S Lund. Circuits for local and global signal integration in primary visual cortex. *The Journal of Neuroscience*, 22(19), 2002.

[195] Matthias Kaschube, Michael Schnabel, and Fred Wolf. Self-organization and the selection of pinwheel density in visual cortical development. *New Journal of Physics*, 10(1), 2008.

[196] Alexei A Koulakov and Dmitri B Chklovskii. Orientation preference patterns in mammalian visual cortex: a wire length minimization approach. *Neuron*, 29(2), 2001.

[197] Joe Corey and Benjamin Scholl. Cortical selectivity through random connectivity. *Journal of Neuroscience*, 32(30), 2012.

[198] Dario L Ringach, Patrick J Mineault, Elaine Tring, Nicholas D Olivas, Pablo Garcia-Junco-Clemente, and Joshua T Trachtenberg. Spatial clustering of tuning in mouse primary visual cortex. *Nature communications*, 7, 2016.

[199] Yao Chen, Bing Li, Baowang Li, and Yuncheng Diao. Directional tunings independent of orientation in the primary visual cortex of the cat. *Science in China Series C: Life Sciences*, 44(5), 2001.

[200] John Burke and Edgar Knobloch. Snakes and ladders: localized states in the swift–hohenberg equation. *Physics Letters A*, 360(6), 2007.

[201] Daniele Avitabile and Helmut Schmidt. Snakes and ladders in an inhomogeneous neural field model. *Physica D: Nonlinear Phenomena*, 294, 2015.

[202] Tao Sun and Robert F Hevner. Growth and folding of the mammalian cerebral cortex: from molecules to malformations. *Nature Reviews Neuroscience*, 15(4), 2014.

[203] Grant R Steen. *Human intelligence and medical illness: Assessing the Flynn effect*. Springer Science & Business Media, 2009.

[204] David P Richman, R Malcolm Stewart, John W Hutchinson, and Verne S Caviness. Mechanical model of brain convolutional development. *Science*, 189(4196), 1975.

[205] Philip V Bayly, LA Taber, and Christopher D Kroenke. Mechanical forces in cerebral cortical folding: a review of measurements and models. *Journal of the Mechanical Behavior of Biomedical Materials*, 29, 2014.

[206] Julien Lefèvre and Jean-François Mangin. A reaction-diffusion model of human brain development. *PLoS Computational Biology*, 6(4), 2010.

[207] Tuomas Tallinen, Jun Young Chung, John S Biggins, and L Mahadevan. Gyrification from constrained cortical expansion. *Proceedings of the National Academy of Sciences*, 111(35), 2014.

[208] Virginia Fernández, Cristina Llinares-Benadero, and Víctor Borrell. Cerebral cortex expansion and folding: what have we learned? *The EMBO Journal*, 2016.

[209] Roberto Toro. On the possible shapes of the brain. *Evolutionary Biology*, 39(4), 2012.

[210] Tonya White, Shu Su, Marcus Schmidt, Chiu-Yen Kao, and Guillermo Sapiro. The development of gyrification in childhood and adolescence. *Brain and Cognition*, 72(1), 2010.

[211] Christopher A Walsh. Neuroscience in the post-genome era: an overview. *Trends in Neurosciences*, 24(7), 2001.

[212] Daniela T Pilz and Oliver W Quarrell. Syndromes with lissencephaly. *Journal of Medical Genetics*, 33(4), 1996.

[213] Richard J Leventer, Renzo Guerrini, and William B Dobyns. Malformations of cortical development and epilepsy. *Dialogues in Clinical Neuroscience*, 10, 2008.

[214] Ruth Peters. Ageing and the brain. *Postgraduate Medical Journal*, 82(964):84, 2006.

[215] Henry A Nasrallah, Samuel Kuperman, Charles G Jacoby, Mona McCalley-Whitters, and Badri J Hamra. Clinical correlates of sulcal widening in chronic schizophrenia. *Psychiatry Research*, 10(4), 1983.

[216] Kaiming Li, Lei Guo, Gang Li, Jingxin Nie, Carlos Faraco, Guangbin Cui, Qun Zhao, L Stephen Miller, and Tianming Liu. Gyral folding pattern analysis via surface profiling. *NeuroImage*, 52(4), 2010.

[217] James A Barkovich, Renzo Guerrini, Ruben I Kuzniecky, Graeme D Jackson, and William B Dobyns. A developmental and genetic classification for malformations of cortical development: update 2012. *Brain*, 135(5), 2012.

[218] Richard J Leventer, Anna Jansen, Daniela T Pilz, Neil Stoodley, Carla Marini, Francois Dubeau, Jodie Malone, L Anne Mitchell, Simone Mandelstam, Ingrid E Scheffer, et al. Clinical and imaging heterogeneity of polymicrogyria: a study of 328 patients. *Brain*, 2010.

[219] Tao Liu, Darren M Lipnicki, Wanlin Zhu, Dacheng Tao, Chengqi Zhang, Yue Cui, Jesse S Jin, Perminder S Sachdev, and Wei Wen. Cortical gyrification and sulcal spans in early stage alzheimer's disease. *PLoS One*, 7(2), 2012.

[220] Antonio Y Hardan, Roger J Jou, Matcheri S Keshavan, Ravi Varma, and Nancy J Minshew. Increased frontal cortical folding in autism: a preliminary mri study. *Psychiatry Research: Neuroimaging*, 131(3), 2004.

[221] Christine Ecker, Lisa Ronan, Yue Feng, Eileen Daly, Clodagh Murphy, Cedric E Ginestet, Michael Brammer, Paul C Fletcher, Edward T Bullmore, John Suckling, et al. Intrinsic gray-matter connectivity of the brain in adults with autism spectrum disorder. *Proceedings of the National Academy of Sciences*, 110(32), 2013.

[222] Yi-Ping Lo, Reuben O ' Dea, Jonathan J Crofts, Cheol E Han, and Marcus Kaiser. A geometric network model of intrinsic grey-matter connectivity of the human brain. *Scientific Reports*, 5, 2015.

[223] Mark Wallace. Personal communication, October 21, 2016.

[224] Ed Bullmore and Olaf Sporns. Complex brain networks: graph theoretical analysis of structural and functional systems. *Nature Reviews Neuroscience*, 10 (3), 2009.

[225] CG Engeland and Phillip Marucha. Neuroimmunology of the skin: Basic science to clinical practice. In *Springer Berlin Heidelberg*, 2009.

[226] Tuo Zhang, Mir Jalil Razavi, Xiao Li, Hanbo Chen, Tianming Liu, and Xianqiao Wang. Mechanism of consistent gyrus formation: an experimental and computational study. *Scientific reports*, 6, 2016.

[227] Claus C Hilgetag and Helen Barbas. Developmental mechanics of the primate cerebral cortex. *Anatomy and embryology*, 210(5-6), 2005.

[228] Fan Deng, Xi Jiang, Dajiang Zhu, Tuo Zhang, Kaiming Li, Lei Guo, and Tianming Liu. A functional model of cortical gyri and sulci. *Brain Structure and Function*, 219(4), 2014.

[229] Jingxin Nie, Lei Guo, Kaiming Li, Yonghua Wang, Guojun Chen, Longchuan Li, Hanbo Chen, Fan Deng, Xi Jiang, Tuo Zhang, et al. Axonal fiber terminations concentrate on gyri. *Cerebral Cortex*, 22(12), 2012.

[230] Hanbo Chen, Tuo Zhang, Lei Guo, Kaiming Li, Xiang Yu, Longchuan Li, Xintao Hu, Junwei Han, Xiaoping Hu, and Tianming Liu. Coevolution of gyral folding and structural connection patterns in primate brains. *Cerebral Cortex*, 2012.

[231] Weifeng Xu, Xiaoying Huang, Kentaroh Takagaki, and Jianyoung Wu. Compression and reflection of visually evoked cortical waves. *Neuron*, 55(1), 2007.

[232] Bard G Ermentrout and John Rinzel. Reflected waves in an inhomogeneous excitable medium. *SIAM Journal on Applied Mathematics*, 56(4), 1996.

[233] Wei-Yang Lin, Yen-Lin Chiu, KerryR Widder, YuHen Hu, and Nigel Boston. Robust and accurate curvature estimation using adaptive line integrals. *EURASIP Journal on Advances in Signal Processing*, 2010(1), 2010.

[234] Eileen Luders, Paul M Thompson, Katherine L Narr, Arthur W Toga, Lutz Jancke, and Christian Gaser. A curvature-based approach to estimate local gyrification on the cortical surface. *NeuroImage*, 29(4), 2006.

[235] Rudolph Pienaar, Bruce Fischl, V Caviness, Nikos Makris, and P Ellen Grant. A methodology for analyzing curvature in the developing brain from preterm to adult. *International Journal of Imaging Systems and Technology*, 18(1), 2008.

[236] Markus A Dahlem and Stefan C Müller. Migraine aura dynamics after reverse retinotopic mapping of weak excitation waves in the primary visual cortex. *Biological cybernetics*, 88(6), 2003.

[237] Inc Neuromorphometrics. T1 MRI scan from the cross-sectional set. URL https://scalablebrainatlas.incf.org/human/NMM1103.

[238] S. Fedorov. Informer technologies, inc. URL http://www.getdata-graph-digitizer.com.

[239] James A Reggia and David Montgomery. A computational model of visual hallucinations in migraine. *Computers in biology and medicine*, 26(2), 1996.

[240] Markus A Dahlem, R Engelmann, S Löwel, and Stefan C Müller. Does the migraine aura reflect cortical organization? *European Journal of Neuroscience*, 12(2), 2000.

[241] VA Davydov and VS Zykov. Kinematics of spiral waves on nonuniformly curved surfaces. *Physica D: Nonlinear Phenomena*, 49(1-2), 1991.

[242] Stephen Coombes, Gabriel J Lord, and Markus R Owen. Waves and bumps in neuronal networks with axo-dendritic synaptic interactions. *Physica D: Nonlinear Phenomena*, 178(3), 2003.

[243] Viktor K Jirsa and Hermann Haken. Field theory of electromagnetic brain activity. *Physical Review Letters*, 77(5), 1996.

[244] Paul C Bressloff and Stephen Coombes. Physics of the extended neuron. *International Journal of Modern Physics B*, 11(20), 1997.

[245] Paul C Bressloff. New mechanism for neural pattern formation. *Physical Review Letters*, 76(24), 1996.

[246] Sid Visser, Rachel Nicks, Olivier Faugeras, and Stephen Coombes. Standing and travelling waves in a spherical brain model: the nunez model revisited. *Physica D: Nonlinear Phenomena*, 349, 2017.